Investigating the Void Lattice Phenomenon in Nuclear Irradiated Materials

Matthew W. Noble

BSc (St And) MSc (Ebor)

Oriel College, Oxford

A thesis presented for the degree of

Doctor of Philosophy

Department of Materials

University of Oxford

Submitted

06 - October - 2023

Abstract

In the 1950s, the pioneering computer scientist and mathematician, Alan Turing proposed a method to describe the observed phenomenon of pattern formation in reaction–diffusion systems: a Turing instability or a reaction–diffusion instability. The mechanism states that two or more species must be present within the system and be able to interact and move around. Pattern formation in these systems can occur when the diffusion rates between two (or more) species significantly differ in magnitude. In liquid chemical reactions, the diffusion rates are similar, so pattern formation within these systems is rare. In the solid state, however, the diffusion rate is $D \propto \exp\left(-E_{mig}/k_B T\right)$, where E_{mig} is the energy of the migration barrier of the species and T is the temperature of the system. As a result, the diffusion rates are enormous, often orders of magnitude apart, and the criteria for pattern formation are satisfied.

Void and gas bubble superlattices are phenomena observed in nuclear-irradiated materials when a random distribution of pre-existing voids or gas bubbles moves and self-order themselves into a long-range periodic superlattice, often mimicking the crystal structure of the host lattice. This transition from a random distribution into a long-range ordered system, at first, would appear to violate the second law of thermodynamics; as such, it stands to reason that there must be one or more mechanisms driving this pattern formation, however, to date, no mechanisms have yet been proven. The mechanism behind the formation of void and gas bubble superlattices remains a mystery.

In this thesis, I propose that a Turing-like instability can explain the emergent

pattern of a void superlattice in a nuclear-irradiated material. I do this in two stages. First, by following the derivation notes of M. Cross and H. Greenside, I perform a linear stability analysis on a pair of Cahn-Hilliard partial differential equations. The equations are coupled by an annihilation term and include a creation term. They describe the evolution of the vacancy and the self-interstitial atom concentrations in a nuclear-irradiated material. I show that such a system will support pattern formation due to the Turing-like instability for a particular selection of parameter values. Secondly, a phase-field model is used to explore the non-linear post-bifurcation regime using the finite-element framework MOOSE (Multiphysics Object Oriented Simulation Environment), allowing me to numerically solve the coupled pair of Cahn-Hilliard partial differential equations via the implicit method of backward Euler time integration, demonstrating the formation and development of a void superlattice.

My model, although simple and minimal, as it neglects features like driving advective terms or refinements such as the elastic interactions between voids or the anisotropic mobility of the self-interstitial atoms, can successfully explain almost all of the qualitative behaviours of a void superlattice, such as their ordered formation from a random distribution of pre-existing voids; their periodicity and structure, which are in agreement with experimental observations, and the temperature window of their formation. Combined, this model suggests that a Turing-like instability is, in fact, the driving mechanism for void superlattices in nuclear-irradiated materials and, given that widely differing mobilities are so typical in solid-state materials, could be the driving mechanism for many of the patterns observed in solid-state systems.

Acknowledgements

0.1 Discussions

I am grateful for discussions with Prof. Chris Grovenor, Prof. Steve Fitzgerald, and Prof. Mike Tonks throughout the course of this project.

0.2 Funding

This DPhil project was funded by Rolls-Royce, whose support is gratefully acknowledged.

0.3 Figures and Tables

Some figures and tables in this thesis have been reproduced from other works. In such cases, permission has been sought and obtained from either the original author or the publisher. All reproduced material is clearly indicated in the thesis text and in the relevant captions. Copies of licences are available upon request.

0.4 Beamery

To my team at Beamery, in particular my friend and manager Ahmad — thank you for your support and understanding as I completed this thesis alongside my role.

0.5 Proofreaders

To my supervisors, colleagues, collaborators, friends, and family — thank you for taking the time to proofread this thesis.

0.6 Personal Support

To my Mam and Dad — thank you for your unwavering love, encouragement, and belief in me throughout this journey. Your support has been the foundation of everything I've achieved. Here's to Mam finally getting to wear her hat!

To Nicole — thank you for your patience, understanding, and constant encouragement. Your presence has meant everything during the highs and lows of this process.

Contents

List of Figures

List of Tables

Chapter 1

Introduction

1.1 Pattern Formation in Nature

Patterns in nature are a beautiful phenomenon and have been discussed, described, and investigated as far back as ancient Greece, with philosophers such as Pythagoras, Empedocles, Plato, and Aristotle all touching upon the phenomenon in their philosophies [1]. Patterns manifest as spots and stripes on animals, the cracks in rocks, the tessellations of repeated structures — such as the honeycomb of a beehive, the spherical shapes of soap bubbles and their collective foams, the rippling ocean waves and desert dunes, the spirals of animal horns and the phyllotaxis [1] of plants, fractal-like tree branches and human veins, and the symmetry of organisms and phenomena like the fivefold symmetry of starfish arms or the sixfold symmetry of snowflake arms [2].

As these patterns were studied over the centuries, scientists started to think about and understand them from a mathematical point of view as the Fibonacci sequence — first introduced in 1202 by Leonardo Fibonacci in his book "Liber Abaci" [3] — and the golden ratio were often observed in many of the phenomena. Mario Livio, in his book "The Golden Ratio: The Story of Phi, the World's Most Astonishing Number" [4], presents several fascinating stories of the interconnected research of pattern formation

[1] The arrangement of leaves on an axis or stem.

over the centuries. Quoting his own words from the inside cover:

> *The Golden Ratio is a captivating journey through art and architecture, botany and biology, physics and mathematics. It tells the human story of numerous phi-fixated individuals, including the followers of Pythagoras who believed that this proportion revealed the hand of God; astronomer Johannes Kepler, who saw phi as the greatest treasure of geometry; such Renaissance thinkers as mathematician Leonardo Fibonacci of Pisa; and such masters of the modern world as Goethe, Cezanne, Bartók, and physicist Roger Penrose.*

As experiments became more sophisticated, pattern formation was observed in fields beyond biology. The phenomena were as diverse as Turing bifurcations and pattern selection in chemical systems [5, 6], electrically driven pattern-forming instabilities in planar nematic liquid crystals [7, 8], the patterns formed in fluid dynamics as a result of non-linear convection [9, 10], the solidification of a dilute binary alloy spontaneously assuming a cellular structure [11], the fingering in thin layer electrodeposition [12], the unstable plastic flow producing pronounced hierarchical structures of dislocations [13, 14], the alignment of voids and gas bubbles under high energy irradiation into long-range periodic superlattices [15, 16], and the evolution of magnetic stripe domains in ferrimagnetic films [17].

With these observations, more advanced mathematics than simply observing the Fibonacci sequence or formalising a nomenclature to group similar patterns was needed to understand the underlying mechanisms and drivers of pattern formation. Of particular relevance to this thesis are Turing patterns — named after the computer scientist Alan Turing. In his 1952 paper, "The Chemical Basis of Morphogenesis" [18], Turing proposed a mechanism to explain the phenomenon of pattern formation in reaction–diffusion systems. This mechanism would go on to be named a "Turing instability". The mechanism proposes that the pattern formation results from the competing behaviours of the smoothing diffusion effect and the non-linear reaction terms. He showed that in a reaction–diffusion system with two or more separate concentrations, the system can create bifurcations that will drive pattern formation if the species exhibit

sufficiently different mobilities. As the equations' parameters change, different wavelengths and pattern types can be driven and constructed, respectively.

1.2 Nuclear Energy

1.2.1 Nuclear Fission

Overview

Nuclear fission was discovered in 1938 by the German chemists Otto Hahn and Fritz Strassmann when they discovered bombarding uranium with neutrons would create lighter elements [19]. Their results were explained a year later, in 1939, by the Austro-Swedish physicist Lise Meitner and her nephew, the Austro-British physicist Otto Robert Frisch [20]. The story of nuclear energy, from the initial discovery of uranium in 1789 by the German chemist Martin Klaproth [21] through to the Manhattan Project in 1942 and beyond, was littered with contributions from some of the greatest physicists to have lived, including Antoine Henri Becquerel, Marie Curie, Ernest Rutherford, James Chadwick, Niels Bohr, Albert Einstein, and Richard Feynman — among many others. It is a fascinating historical account worthy of further exploration [22, 23].

Neils Bohr and John Archibald Wheeler wrote the original paper describing the overall process of nuclear fission from uranium in 1939 [24]. Today, originating from the nuclear weapons programmes of World War II, nuclear fission plays a vital role in energy production by harnessing the energy released from the splitting of the U-235 atom to drive turbines and create electricity [25].

The Pressurised Water Reactor (PWR) is the most common reactor design, seeing deployment in both commercial electricity generation and the engines of naval vessels. It consists of fuel rods containing the enriched uranium fuel capable of undergoing fission. A set of control rods slow down the reaction by absorbing neutrons; these prevent runaway reactions. In the case of a PWR, the moderator used to slow the neutrons is the coolant, regular water. The coolant generates steam in a secondary system via a heat exchanger. The coolant is kept under immense pressure, around

150 atmospheres, preventing it from boiling and allowing it to reach temperatures of approximately 325 °C. PWR designs are capable of generating around 1,000 MW of electricity with an efficiency of approximately 33% [25].

Many atoms undergo nuclear fission reactions naturally, but the process with U-235 is induced when the atom of U-235 is bombarded with a slow-moving neutron (≈ 0.025 eV). The absorption of this neutron causes the U-235 to split. There is not a unique set of binary fission products, but a distribution of products ranging between $80 \leq Z \leq 160$; some of the most common are listed in Equations 1.1 [26, 27]. The average energy output of these reactions is approximately 200 MeV [25].

$$
\begin{aligned}
{}^{235}_{92}U + {}^{1}_{0}n &\rightarrow {}^{144}_{56}Ba + {}^{90}_{36}Kr + 2\,{}^{1}_{0}n \\
{}^{235}_{92}U + {}^{1}_{0}n &\rightarrow {}^{141}_{56}Ba + {}^{92}_{36}Kr + 3\,{}^{1}_{0}n \\
{}^{235}_{92}U + {}^{1}_{0}n &\rightarrow {}^{90}_{38}Sr + {}^{144}_{54}Xe + 2\,{}^{1}_{0}n \\
{}^{235}_{92}U + {}^{1}_{0}n &\rightarrow {}^{96}_{37}Rb + {}^{137}_{55}Cs + 3\,{}^{1}_{0}n \\
{}^{235}_{92}U + {}^{1}_{0}n &\rightarrow {}^{137}_{52}Te + {}^{97}_{40}Zr + 2\,{}^{1}_{0}n \\
{}^{235}_{92}U + {}^{1}_{0}n &\rightarrow {}^{139}_{52}Te + {}^{94}_{40}Zr + 3\,{}^{1}_{0}n
\end{aligned}
\tag{1.1}
$$

Additionally, lighter nuclei are possible via the process of ternary fission. Although rare, when it occurs, it creates positive fragments between $1 \leq Z \leq 18$. This allows isotopes such as helium to be present within the reactor environment and bombard the reactor materials [28].

1.2.2 Nuclear Fusion

Overview

Nuclear fusion is often described as harnessing the power of the Sun whilst putting it inside a box. The theoretical foundations began between 1929 and 1939 with the work of R. E. Atkinson and F. G. Houtermans [29], M. L. E. Oliphant, P. Harteck, and E. Rutherford [30], and H. A. Bethe [31]. Their papers focused on understanding the cores

of stars. Creating fusion on Earth is challenging primarily because of the difficulty of plasma confinement rather than its generation. In September 1958, at the Second United Nations Conference on the Peaceful Uses of Atomic Energy held in Geneva, Switzerland, four concepts for building a magnetic confinement device and controlling thermonuclear fusion were unveiled: the tokamak, the pinch [2], the magnetic mirror, and the stellarator [33].

The tokamak is a large torus which uses the magnetic fields created by its central solenoid and outer poloidal coils to confine the plasma. The pinch, now distinguished as the "Z-pinch", passes an electric current through the plasma, generating a magnetic field to contain the plasma. The magnetic mirror uses two reflective magnetic fields to reflect and control the plasma between the two magnetic mirrors. Finally, the stellarator uses external magnetic fields to contain the plasma, but unlike the tokamak, it is in the form of a twisted helix configuration that operates without a central solenoid [33, 34]. The tokamak emerged as the front-runner design for sustainable fusion energy.

Several literature reviews are available for the study of fusion reactors, with the latest by Samuele Meschini et al. in 2023 [35] looking to bridge the failings — in their opinion — of the previous reviews, arguing that they were either outdated and no longer appropriate [36–38]; or were too restrictive, focussing only on specific confinement approaches such as inertial confinement fusion [39] or magnetic confinement fusion [40]; or were even more restrictive, focussing on specific reactor material and component choices [41, 42]; or were too restrictive in that they only concentrated on specific geographical regions like Europe [43, 44], the US [45] or Japan [46].

Nuclear fusion is a thermonuclear reaction that forces two nuclei together, overcoming the strong repulsive electrostatic force and fusing them, forming a heavier element. The energy released from fusion is enormous. Equations 1.2 represent some of the most widely studied reactions for the application of energy production; they generate 4.03 MeV, 3.27 MeV, 17.6 MeV, 8.68 MeV, and 12.86 MeV of energy, respectively. Controlling for equal mass, fusion produces approximately four times the

[2]This term is also referenced in science fiction, such as the Halo franchise. The pinch fusion reactors power the ships of the Covenant Empire, though this connection is incidental. [32].

energy output of fission reactions [35, 47].

$$
\begin{aligned}
{}^{2}_{1}H + {}^{2}_{1}H &\rightarrow {}^{3}_{1}H + {}^{1}_{1}p \\
{}^{2}_{1}H + {}^{2}_{1}H &\rightarrow {}^{3}_{2}He + {}^{1}_{0}n \\
{}^{2}_{1}H + {}^{3}_{1}H &\rightarrow {}^{4}_{2}He + {}^{1}_{0}n \\
{}^{1}_{1}p + {}^{11}_{5}B &\rightarrow 3\,{}^{4}_{2}He \\
{}^{3}_{2}He + {}^{3}_{2}He &\rightarrow {}^{4}_{2}He + 2\,{}^{1}_{1}p
\end{aligned}
\tag{1.2}
$$

Fusion environments are, therefore, similar to fission environments in terms of the damage caused to the confinement materials by irradiation. They produce large amounts of helium atoms, protons, and neutrons, which cause damage to the metal structures and introduce impurities.

1.3 Pattern Formation in Irradiated Solid-State Materials

When a material is irradiated with high-energy particles, such as neutrons and ions, as experienced during the regular operating conditions of a nuclear reactor, the underlying crystal structure will become damaged, creating point defects such as vacancies and self-interstitial atoms and introducing impurities in the case of ion irradiation [48]. Pattern formation and defect self-organisation occur when a system is externally driven into regimes far from equilibrium [49–51]; the continuous irradiation by high energy particles provide such an environment for defect self-organisation.

Evidence of irradiation-induced defect self-organisation into superlattices includes the labyrinthine concentration patterns in alloy systems [52]; the alignment of Ga nanodroplets on a GaAs surface [53]; the alignment of stacking fault tetrahedra (SFT) and dislocation loops [54–59]; the alignment of planar walls of defects [60]; the alignment of Krypton precipitates in Cu, Ni, and Au [61]; and the alignment of voids and gas bubbles into superlattices in nuclear-irradiated materials [15, 16].

1.3.1 Void and Gas Bubble Superlattices

Void and gas bubble superlattices are examples of pattern formation in nuclear-irradiated materials. The voids and gas bubbles formed during irradiation in metals due to ion bombardment or neutron irradiation are usually distributed randomly throughout the host metal. However, they have been observed to self-order and form a long-range periodic superlattice under certain environmental conditions. The voids and gas bubbles composing these superlattices are remarkably stable, with consistent radii and inter-lattice spacings [48].

Since the first discovery of void superlattices by J. H. Evans in 1971 [15] and of gas bubble superlattices by S. L. Sass and B. L. Eyre in 1973 [16], a great deal of experimental, analytical, and simulation work has been undertaken on creating, characterising, and explaining void and gas bubble superlattices under irradiation. There have been several sound reviews of the literature periodically to date. Some of the most prominent literature reviews were done by K. Krishan in 1982 [62], J. H. Evans in 1990 [63], W. Jäger and H. Trinkaus in 1993 [64], P. B. Johnson and D. J. Mazey in 1995 [65], N. M. Ghoniem, D. Walgraef, and S. J. Zinkle in 2002 [66], and Y. Zhang in 2023 [67]. A deep dive into the literature of void and gas bubble superlattices — the experimental observations, their proposed mechanism(s), and the computational simulations — is reserved for the literature review in Chapter 2.

In addition to scientific curiosity, the motivation to understand the phenomenon of void and gas bubble superlattices lies in their relevance to fission and fusion reactor materials. During regular operation, noble gases such as helium, xenon, and krypton are produced and implanted in the materials, agglomerating, and forming noble gas bubbles. These bubbles change the mechanical properties of the reactor materials, leading to problems such as swelling when the gas bubbles grow and interconnect [68, 69] or leading to embrittlement and accelerated mechanical failure when they migrate towards areas of high tensile strain such as grain boundaries [70]. Suppose the reactor operating conditions can be tuned in such a way as to be favourable to the formation of gas bubble superlattices. In that case, it may be possible to sequester away the gas bubbles and store them in a gas bubble superlattice, extending the lifetime of the

reactor components.

Below, I summarise the important experimental results for both void and gas bubble superlattices:

1. Void superlattices form within the approximate temperature window of $0.25T_m < T < 0.5T_m$ where T_m is the material's melting temperature. It is easier to create a void superlattice just below the peak swelling temperature of the material [66]. Gas bubble superlattices typically form at lower temperatures, within the approximate temperature window of $0.15T_m < T < 0.35T_m$. The gas bubble superlattice temperature window appears to be manipulatable. In 2019, C. Sun and D. J. Sprouster et al. showed with helium-irradiated molybdenum that increasing the helium appm:dpa ratio would reduce both the lower temperature bound and the upper temperature bound and broadened the overall temperature window [71].

2. The void superlattice parameter, a_L, is typically between 20–75 nm, but can be as low as 5 nm [72] and as high as 145 nm [73]. The gas bubble superlattice parameter, a_L, is smaller and more consistent, typically between 4–10 nm, even when formed in the same material under similar irradiation conditions. For both void superlattices and gas bubble superlattices, the lattice parameter, a_L, is positively correlated with temperature, negatively correlated with dose rate, and will saturate over dose.

3. Void superlattices typically mimic the structure of the host metal lattice, i.e. face-centred cubic (FCC) in FCC metals, body-centred cubic (BCC) in BCC metals, and form ordered hexagonal arrays parallel to the basal plane in hexagonal close-packed (HCP). However, a notable exception is the body-centred tetragonal (BCT) void superlattice in BCC Cr [74]. Gas bubble superlattices also typically mimic the host metal lattice. Two notable exceptions are the FCC xenon gas bubble superlattice in the BCC U–7%Mo dispersion fuel plate [75] and the BCT helium gas bubble superlattice in BCC molybdenum [76]. This updates the original theory that they were always isomorphic to the host metal lattice [66].

4. In gas bubble superlattices, the critical dose appears to depend on temperature. E. Jossou and A. Schneider et al. found decreasing the temperature required them to increase the dose rate for otherwise identical experimental conditions [77]. A. M. Robinson and P. D. Edmondson et al. found decreasing the temperature initially required them to reduce the dose rate, and further decreasing the temperature increased the dose rate, under otherwise identical experimental conditions [78].

5. Void superlattices demonstrate a more robust ordering of the superlattice structure than gas bubble superlattices. BCC metals demonstrate a more robust ordering of the superlattice structure than FCC and HCP metals for void superlattices.

6. Both void superlattices and gas bubble superlattices form via the following process [71, 79]:

   (a) An initial, randomly distributed population of small voids/gas bubbles is created due to the damage from irradiation.

   (b) The population of established voids/gas bubbles begins to grow — with the larger voids/gas bubbles surviving and growing at the expense of the smaller voids/gas bubbles.

   (c) The larger voids/gas bubbles begin to move and self-order themselves locally into pockets of ordered planar arrays along the close-packed directions but with disordered random populations separating these pockets of local order.

   (d) The areas of locally concentrated ordering expand and interconnect with the other pockets of locally ordered voids/gas bubbles, creating the long-range periodic void/gas bubble superlattice.

   (e) And, uniquely to gas bubble superlattices, there is a fifth stage to the formation, whereby the gas bubbles continue to grow, and small pipe-like structures begin to emerge, connecting the gas bubbles [80].

7. Void superlattices have been observed to form in BCC metals, FCC metals, stainless steel, alkali earth compounds, and form planar arrays in HCP metals whilst being irradiated with electrons, protons, neutrons, and ions. Gas bubble superlattices have been observed in BCC and FCC metals and to form planar arrays in HCP metals whilst being irradiated with neutrons and hydrogen, helium, neon, and krypton ions. This covers all primary irradiation sources and structures, indicating that the formation of a superlattice does not depend on the structure of the host crystal lattice, its bonding nature, or the irradiation source.

8. Void superlattices require a considerably more significant amount of damage, 100–400 dpa, to form in FCC metals than in BCC metals, which can occur with damage as low as 2–5 dpa.

1.4 Proposed Mechanism(s) and Modelling Approaches

The fact that void superlattices and gas bubble superlattices generally mimic the crystal lattice of the host metal (in the case of BCC and FCC) and create planar arrays parallel to the basal plane in HCP metals suggests some manner of a thermodynamic driving force. However, to date, no mechanism has been discovered. The proposed mechanisms that have been put forward are:

1. Elastic interactions between voids
2. Isomorphic decomposition
3. Anisotropic self-interstitial atom diffusion
4. Self-interstitial dislocation loop punching
5. Phase instability

1.4.1 Elastic Interactions Between Voids

Proposed by K. Malen and R. Bullough in 1971 [81], they conjectured that the ordering of void superlattices was because of the elastic cubic anisotropy of voids, with the elastic field being generated by the surface tension at the surface of the voids. They argued that these fields would create energy minima where voids would push themselves away from other voids within the host metal lattice structure, causing the spacing of a periodic lattice. Whilst the void-void elastic interaction is strong, the issue is that the distances between the voids in a void superlattice observed in the literature are too large for this to be applicable [66, 67].

1.4.2 Isomorphic Decomposition

Based on the work by S. G. Khachaturyan in 1969 and expanded upon in the early 1970s [82, 83], Khachaturyan looked at elastic strains during the decomposition of an elastically anisotropic homogenous solid solution. A. J. E. Foreman made the analogy between void superlattices and these precipitate lattices in his 1974 Harwell report [84]. Khachaturyan's work differed considerably from the work of J. W. Cahn and J. E. Hilliard's [85]; he could predict three different types of distribution, the third being a 3D cubic lattice. Again, similar to the issue with elastic interactions above, the distances that these elastic minima would apply over, and hence the spacings predicted, alongside the consideration of different lattice symmetries, did not apply to what was observed in the experimental literature [66, 67].

1.4.3 Anisotropic Self-Interstitial Atom Diffusion

Originating with the work done by A. J. E. Foreman in his 1974 Harwell report [84], he proposed that ordering voids into a void superlattice is due to the anisotropic diffusion of self-interstitial atoms. There were two model variations; one was 1D and the other 2D — although, importantly, the 2D version is not an extension of the 1D version. The 1D version described the preferential migration and alignment along close-packed directions, and the 2D version described the preferential migration and alignment

along close-packed planes.

The argument in 1D was based on the flux of self-interstitial atoms that a void would receive if aligned along the self-interstitial atoms' diffusion paths. The voids which were aligned along these preferential self-interstitial atom paths would shield each other from the self-interstitial atoms and hence receive a smaller flux, allowing them to grow, compared to the voids which existed outside of this alignment, which would receive a higher self-interstitial atom flux, and hence shrink away. Because the diffusion paths of self-interstitial atoms are more likely the close-packed directions of the crystal structure, the voids which were able to grow did so along the close-packed directions.

The 1D version was adapted by C. H. Woo et al. in the late 1980s and early 1990s [86–89] to create a 2D version, although their model did require a specific crowdion configuration. J. H. Evans, at the same time [61, 63, 90–92] created his model of 2D self-interstitial atom diffusion. Like the 1D version, after carefully considering the vacancy and self-interstitial atom fluxes, this time along close-packed planes, Evans showed that a void within one of these planes would experience a smaller flux of self-interstitial atoms than one existing off this plane. As such, the interconnection of these planes would create a void superlattice as the voids on the planes would grow, and the voids external to the planes would shrink.

1.4.4 Self-Interstitial Dislocation Loop Punching

The mechanism proposed by V. I. Dubinko and A. V. Tur et al. in 1989 [93] was based on the elastically induced absorption of self-interstitial dislocation loops by voids. For specific crystal structures, i.e. BCC metals, the self-interstitial dislocation loops can glide along the close-packed directions; they argued that these self-interstitial dislocation loops would, over time, interact with the voids along those close-packed directions, ultimately producing a void superlattice similar to the anisotropic self-interstitial atom diffusion — i.e. along close-packed planes, the balance of vacancy and self-interstitial dislocation loop flux favours void growth, and external to the close-packed planes, the increased flux of self-interstitial dislocation loops favours void

shrinkage. Their proposed mechanism, however, has a few issues: it was dependent on the mobility of defects but not on the production and annihilation rates of those defects, and given irradiation would change the microstructure of the host metal lattice, their mechanism was not stable in a non-equilibrium environment. In contrast, the literature shows that void and gas bubble superlattices grow, order, and remain stable even under continued irradiation [66, 67].

1.4.5 Phase Instability

Originating with the work of K. Krishan in 1980 [94, 95], phase instability mechanisms build rate equations to describe the phenomenon of void and gas bubble superlattice formation as a non-equilibrium phase transition. [3] When irradiation occurs, the energetic particles create damage in the form of vacancy and self-interstitial atom pairs. The rate equations couple each of the individual point defect concentrations, such as the vacancies and the self-interstitial atoms, to the micro-structural sinks, which are defined by the Bullough-Eyre-Krishan (BEK) equations [97]. The system is then linearised about a uniform base state, and solutions are sought that would destabilise this uniformity. This instability drives pattern formation and is a product of the non-equilibrium conditions resulting from neutron and ion irradiation, creating point defects, the differences in mobilities between the slow-moving vacancies and the fast-moving self-interstitial atoms, and the micro-structural sinks. The issue, however, as with many pattern-forming systems, is not just the presence of instability criteria but its evolution in the non-linear post-bifurcation regime [51]. [4]

[3] They are similar to the reaction–diffusion equations proposed by A. Turing [18], which were the basis of J. W. Cahn and J. E. Hilliard's "Cahn-Hilliard" [85] and S. M. Allen and J. W. Cahn's "Allen-Cahn" [96] equations; the Cahn-Hilliard equations being the foundation of the work I present in this thesis.

[4] It is the evolution in this post-bifurcation regime that this thesis explores using MOOSE [98, 99] developed by the Idaho National Laboratory (INL).

1.5 Structure of the Thesis

Chapter 2 presents a comprehensive literature review in which the experimental, theoretical, and computational work on void and gas bubble superlattices is surveyed and critically evaluated. Particular emphasis is placed on instability-driven mechanisms for pattern formation, encompassing both dynamic and thermodynamics-based approaches. These include the foundational Bullough-Eyre-Krishan (BEK) rate equations, which describe defect kinetics under irradiation; the hybrid Cahn-Hilliard/BEK framework proposed by Y. Gao et al. and Y. Zhang et al. [138, 143, 144], which couples thermodynamic forces with kinetic asymmetries; and the novel Turing-like mechanism introduced by the current author, which interprets void superlattice formation as a manifestation of reaction–diffusion instability within a phase-field framework. These models provide a conceptual foundation for the simulations and analyses presented in later chapters.

In Chapter 3, I derive a pair of Cahn-Hilliard partial differential equations following the derivations of M. Cross and H. Greenside [2]. The equations are coupled by an annihilation term and include a creation term. They describe the evolution of the vacancy and the self-interstitial atom concentrations in a nuclear-irradiated material. I then perform a linear stability analysis of the coupled partial differential equations, showing that a Turing-like instability exists within the system for a particular set of parameter conditions. However, I will also show that the range of parameter conditions is, in fact, rather broad. From this solution, the periodicity and the threshold of formation of a stable void superlattice are predictable.

In chapter 4, I implement a phase-field simulation using the open source finite-element framework MOOSE [98, 100–102] to numerically integrate via the implicit method of backward Euler time integration the coupled pair of Cahn-Hilliard partial differential equations derived in Chapter 3.

In Chapter 5, I present the simulation results and corresponding analyses. I begin by demonstrating the formation of a stable void superlattice from an initially random distribution of vacancies and self-interstitial atoms (Experiment 1). I then investigate

the influence of the mobility ratio on pattern formation (Experiment 2), followed by validation of the threshold of formation and lattice periodicity predicted in Chapter 3 (Experiment 3). Next, I explore the effect of domain size (Experiment 4), the impact of introducing a pre-existing population of voids (Experiment 5), and the influence of their initial size (Experiment 6) and initial number (Experiment 7). Finally, in Experiment 8, I compare the proposed model to the standard Cahn-Hilliard formulation.

In Chapter 6, I discuss the work performed and tie it back to its applications in modelling void superlattices in nuclear-irradiated materials while acknowledging the inherent simplifications of the model; for example, I have not yet incorporated elastic interactions of established voids nor the anisotropic mobility of self-interstitial atoms. However, despite this lack of refinements, this thesis underscores the model's efficacy in predicting the formative behaviour and the inherent length scales of ordered void superlattice patterns in nuclear-irradiated materials. The focal point lies in presenting a fundamental and versatile model rather than delving into the specifics of distinct materials. I leave a comprehensive examination of particular metals and irradiation conditions for future work.

Chapter 2

Literature Review

2.1 Experimental Observations of Void Superlattices

2.1.1 Overview

In 1967, C. Cawthorne and E. J. Fulton discovered voids in irradiated metals [103]. In 1971, J. H. Evans observed the first regular void array in high-purity molybdenum irradiated with 2 MeV nitrogen ions at 400 dpa — the void superlattice [15].

During the same year, F. W. Wiffin explored the BCC metals, observing void superlattices in niobium, tantalum, molybdenum, and titanium-molybdenum-zirconium (TMZ) alloy using fission neutrons at both 858 K and 1,063 K at notably smaller doses of 20–36 dpa [104], B. L. Eyre and J. H. Evans filled in the gap and achieved a void superlattice in molybdenum using fission neutrons at 923 K and 30–60 dpa [105], and G. L. Kulcinski, J. L. Brimhall, and H. E. Kissinger achieved a void superlattice in nickel using selenium ions at 798 K and a dose of 400 dpa [106].

The following year, the BCC metals were explored further by J. H. Evans, R. Bullough and A. M. Stoneham using nitrogen ions into molybdenum [107], V. K. Sikka and J. Moteff using neutrons into tungsten and neutrons into TMZ [108, 109],

and G. L. Kulcinski, J. L. Brimhall, and H. E. Kissinger using nickel ions into niobium [106]. Kulcinski et al. subsequently explored FCC metals, and they were the first to observe a void superlattice in nickel, using 5 MeV nickel ions at 798 dpa and 6 MeV selenium ions at 400 dpa; both irradiations were done at 798 K.

The first HCP "lattice" was observed by A. Risbet and V. Levy in 1974 using fission neutrons at 328 K with a dose of 3–6 dpa. I use the term "lattice" because this was the first observation to break away from the observed 3D structure. Instead of forming 3D arrays, HCP metals would form rafts or planes parallel to the basal plane [110].

For non-metals, F. W. Clinard, J. M. Bunch, and W. A. Ranken observed linear strings of cavities perpendicular to the basal plane in neutron irradiated aluminium oxide, Al_2O_3 [111]. Whilst not a void lattice, L. T. Chadderton, E. Johnson, and T. Wohlenberg went on to explore alkaline earth metals and successfully observed an anion void lattice in CaF_2 and SrF_2 using room temperature 0.1 MeV electron irradiation [112, 113]. The anion void lattice in SrF_2 was weaker than CaF_2; it was not possible to form an anion void lattice in BaF_2.

As of 2023, void superlattices have been observed in metals, alloys, and alkaline earth metals of all structures: body-centred cubic (BCC), face-centred cubic (FCC), hexagonal close-packed (HCP), simple cubic (SC), and body-centred tetragonal (BCT) and they have been formed using neutrons, electrons, protons, and ions for a wide range of temperatures and dose [66, 67].

Summary tables for observed void superlattices and partially ordered lattices via electron and proton irradiation, neutron irradiation, and ion irradiation are presented in Tables 2.2 – 2.7. The summary tables include the material matrix, the structure of the void lattice formed, the projectile, the energy of the projectile in MeV, the temperature of the irradiation in K, the ratio of the temperature of irradiation to the melting temperature of the metal, T/T_m, the dose in dpa, the void diameter in nm, and the superlattice lattice parameter, a_L.

Several sound reviews of the literature have been produced periodically to date. Some of the most prominent literature reviews were done by K. Krishan in 1982 [62],

J. H. Evans in 1990 [63], W. Jäger and H. Trinkaus in 1993 [64], P. B. Johnson and D. J. Mazey in 1995 [65], N. M. Ghoniem, D. Walgraef, and S. J. Zinkle in 2002 [66], and Y. Zhang in 2023 [67].

A BCC void superlattice in BCC molybdenum is shown in Figure 2.1; this image is reused with permission and taken from Figure 3 of [15]. An FCC void superlattice in FCC nickel is shown in Figure 2.2; this image is reused with permission and taken from Figure 4 of [106]. Planar void ordering in the basal plane of magnesium is shown in Figure 2.3; this image is reused with permission and taken from Figure 1 of [114].

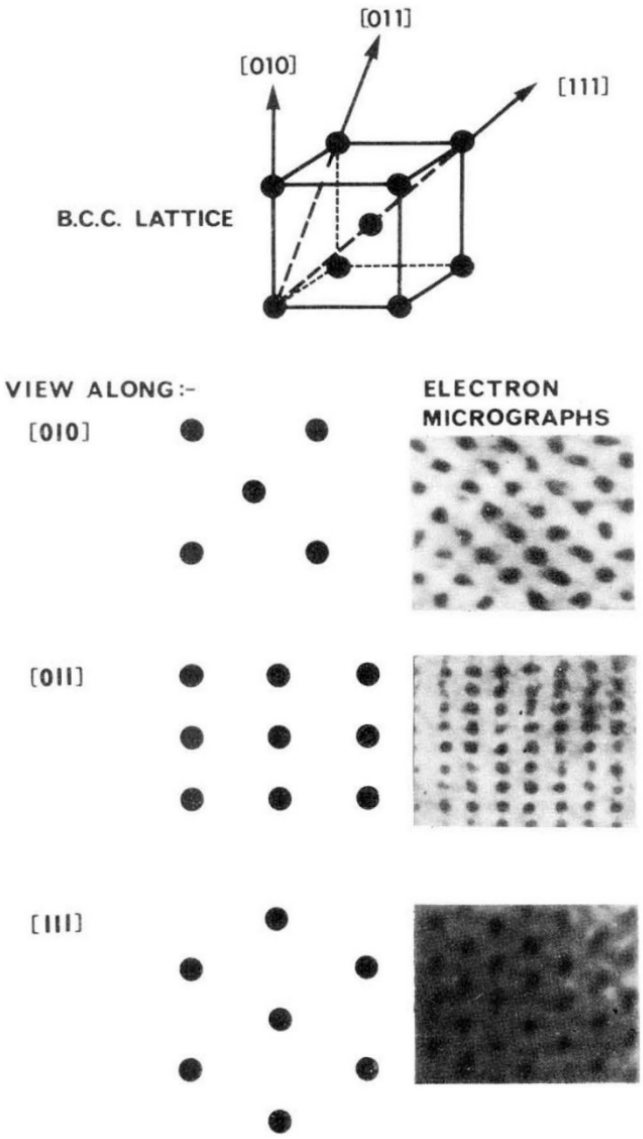

Figure 2.1: Electron micrographs (right) and schematic projections (left) of a BCC void superlattice in BCC molybdenum irradiated with nitrogen ions, viewed along the [010], [011], and [111] directions (top to bottom). Voids appear as black objects. This image is reused with permission and taken from Figure 3 of [15].

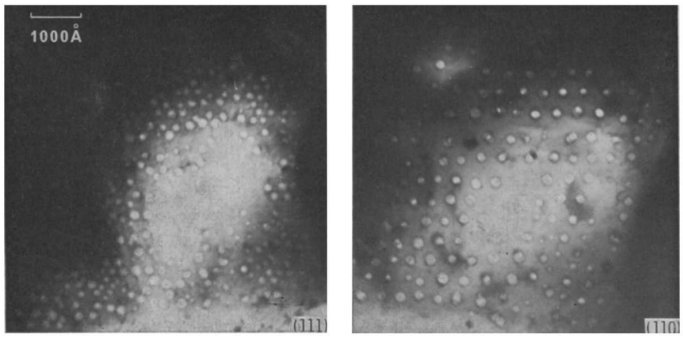

Figure 2.2: Electron micrographs of an FCC void superlattice in FCC nickel irradiated with selenium ions, viewed along the [111] and [110] directions (left and right). Voids appear as white objects. This image is reused with permission and taken from Figure 4 of [106].

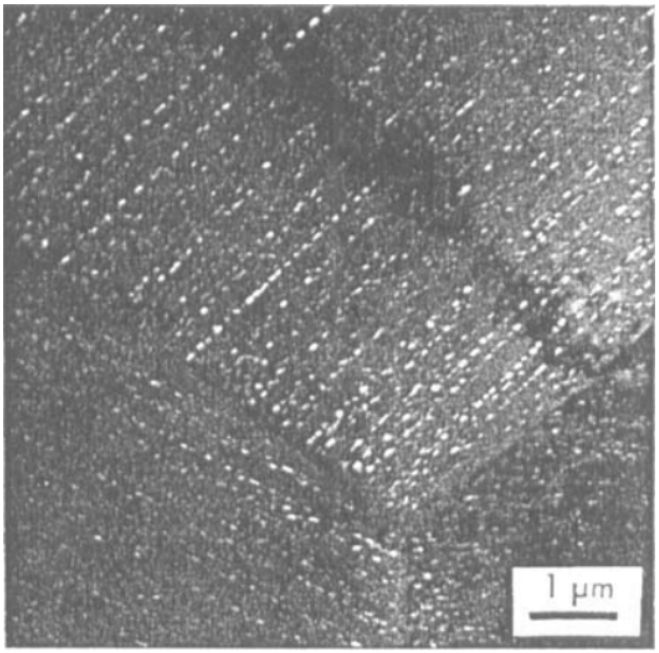

Figure 2.3: Electron micrograph showing planar void ordering in the basal plane of HCP magnesium irradiated with neutrons. Voids appear as white objects. This image is reused with permission and taken from Figure 1 of [114].

2.1.2 Formation and Development

The formation and development of a void superlattice in non-HCP structures proceeds through four stages — assuming the correct irradiation conditions. First, an initial, randomly distributed population of tiny voids is created due to the damage from irradiation; second, the population of established voids begins to grow — with larger voids growing at the expense of the smaller voids; third, the larger voids begin to move and self-order locally into pockets of ordered planar arrays along the close-packed directions but with disordered random populations separating these pockets of local order. Fourth, the areas of locally concentrated ordering expand and interconnect with the other pockets of locally ordered voids, creating the long-range periodic void superlattice [71, 79].

Void superlattices typically develop either partially or fully isomorphically with the target's host crystalline lattice, i.e. they have an FCC structure in FCC metals such as aluminium and nickel and a BCC structure in BCC metals such as niobium, molybdenum, tungsten, and tantalum. In contrast to this 3D structure, HCP metals such as magnesium void "lattices" demonstrate 2D planar ordering in rafts or layers parallel to the basal plane [62–67]. A notable exception, however, is the body-centred tetragonal (BCT) void superlattice in BCC Cr produced by C. Sun et al. in 2022 using 5 MeV Iron ions at 823 K. They produced a void superlattice twice, one at a dose of 100 dpa and another at a dose of 150 dpa [74]. This challenges the earlier assumption that void superlattices always mimic the host metal lattice [66].

In Aluminium [110, 115, 116], Ni-Al alloys [117], stainless steel [118], and Cu-10%Ni [119], imperfect FCC void lattices have been observed with a dose of 10–80 dpa.

Although experiments with up to 100 dpa have been undertaken [104, 120, 121], it has not yet been possible to form a void superlattice in vanadium, despite high void densities.

The simple cubic void superlattice observed by T. H. Ding et al. in 2005 [122] was a return to CaF_2 after almost 40 years. Similar to Chadderton et al., Ding et al. used in-situ electron irradiation, with similar energies of 200 keV compared to

L. T. Chadderton et al.'s 100, 200, and 1,000 keV electron irradiation experiments using in-situ transmission electron microscopy (TEM) [112, 113]. L. T. Chadderton et al. described their structure as an anion lattice; they believed that the damage was purely radiolytic, that it formed on the anion sublattice with anion vacancies and anion interstitials, and left the cation sublattice unaffected. T. H. Ding et al. used calcium elemental mapping obtained from energy-filtered transmission electron microscopy and, in doing so, characterised the voids as cavities without calcium. This suggests both the anion and the cation sublattice were damaged despite the low energy irradiation, contradicting L. T. Chadderton et al.

2.1.3 Temperature Window

The experimental observations suggest there is a temperature window for forming a void superlattice; it is approximately $0.25T_m < T < 0.5T_m$, where T_m is the material's melting temperature [64]. Additionally, it appears to be easier to create a void superlattice just below the peak swelling temperature of the material [66].

2.1.4 Diameter and Superlattice Lattice Parameter

The summary statistics for void diameters and void lattice parameters (a_L) is given in Table 2.1. The void lattice parameter is typically between 3–5 times larger than the void diameter for both BCC and FCC metals and typically one hundred times larger than the atomic lattice parameter. The lattice parameter, a_L, increases with temperature [73, 121, 123], decreases with dose rate, and when increasing the dose, it will initially decrease [73] and then plateau once the void superlattice is established [73, 121, 123, 124]. With continued irradiation, the void diameter to lattice parameter ratio approaches 10 [73, 125].

Metric	Structure	Mean (nm)	Min (nm)	25^{th} Pctl (nm)	Median (nm)	75^{th} Pctl (nm)	Max (nm)
Diameter	BCC	8.73	1.6	4	5.8	6.6	75
a_L	BCC	35.71	6.5	22	30.5	38.5	145
Diameter	FCC	15.7	6.3	10.6	11.9	14	65
a_L	FCC	73.11	36	48.5	60	66	250

Table 2.1: Summary statistics for void diameters and lattice parameters (a_L) in BCC and FCC metals.

2.1.5 Creation Threshold and Ordering

Compared to a BCC metal, FCC metals require significantly higher damage doses to form void superlattices. For pure BCC metals such as molybdenum, tungsten, and niobium, the threshold to create a void superlattice is a dose of a few dpa up to 30 dpa [106, 123, 124], compared to FCC metals like pure nickel, where the dose required is 100–400 dpa [106, 125]. FCC superlattices also exhibit weaker lattice ordering than those in BCC metals.

2.1.6 Effect of Alloying

The effect of alloying on void superlattice formation remains uncertain. Experiments with TMZ demonstrate similar void ordering compared to pure molybdenum [104, 123], and similarly with niobium alloys [73]. Wiffen reported that the alloying in Nb-1%Zr suppressed void ordering [104], however, this might have been due to the oxygen impurities, as Loomis [73] reported being unable to create a void superlattice when oxygen concentrations were below 60 ppm for niobium and 400 ppm for Nb-1%Zr, respectively. However, in Ipatova et al.'s 3 MeV proton irradiation of tantalum, a void superlattice was established over all three irradiations. They reported that the addition of tungsten (Ta-W alloy) inhibited void superlattice formation.

2.1.7 Summary of Experimental Results

Matrix	Structure	Projectile	Energy (MeV)	Temperature (K)	T/T_m	Dose (dpa)	Diameter (nm)	a_L (nm)	Reference	Notes
20/25 stainless steel	—	electron	2	773	0.43	20	8	25	[163]	
CaF_2	SC	electron	0.1	293	0.18	20	2	19.2–28.3	[112, 113]	
CaF_2	SC	electron	0.2	293	0.18	1.5	5	15–20	[122]	
SrF_2	—	electron	0.1	293	0.17	20	—	—	[113]	
Ta	BCC	proton	3	618	0.19	0.25	2	13.2	[72]	(a)
Ta	BCC	proton	3	618	0.19	0.85	2.7	11.3	[72]	(a)
Ta	BCC	proton	3	618	0.19	1.55	2.9	6.5	[72]	(a)

Table 2.2: Experimental observations of void superlattices created through electron and proton irradiation. Table data collated from Table 3 of [62] and Table 1 of [67]. The melting temperatures used to calculate the T/T_m ratio were: 20/25 stainless steel = 1,783.15 K [171], CaF_2 = 1,633.15 K [172], SrF_2 = 1,723.15 K [173], and tantalum = 3,293 K [174]. **Notes:** (a) a_L, was calculated using the $a_L : d$ ratio from [72].

Matrix	Structure	Projectile	Energy (MeV)	Temperature (K)	T/T_m	Dose (dpa)	Diameter (nm)	a_L (nm)	Reference	Notes
Mo	BCC	neutron	> 0.1	703	0.24	5	5.8	21	[121]	
Mo	BCC	neutron	> 0.1	723	0.25	36	6.4	26.5	[104]	
Mo	BCC	neutron	> 0.1	853	0.29	5	5.8	27	[121]	
Mo	BCC	neutron	> 0.1	858	0.30	10	6.2	46	[124]	
Mo	BCC	neutron	> 0.1	858	0.30	36	6.4	26.5	[104]	
Mo	BCC	neutron	> 0.1	873	0.30	30–60	5.4	28	[123]	
Mo	BCC	neutron	> 0.1	923	0.32	30–60	3.8	34	[105]	
Mo	BCC	neutron	> 0.1	953	0.33	5	5.8	30.5	[121]	
Mo	BCC	neutron	> 0.1	988	0.34	30–60	5.7	32.8	[123]	
Mo	BCC	neutron	> 0.1	1,063	0.37	36	7.2	32.8	[104]	
Mo	BCC	neutron	> 0.1	1,073	0.37	5	5.8	40	[121]	
Mo	BCC	neutron	> 0.1	1,153	0.40	30–60	6	37	[123]	
Mo	BCC	neutron	> 0.1	1,173	0.41	30–60	5.8	35.8	[123]	
Mo	BCC	neutron	> 0.1	1,173	0.41	5	5.8	47	[121]	
Mo	BCC	neutron	> 0.1	1,193	0.41	30–60	5.6	39–124	[123]	
Mo	BCC	neutron	> 0.1	1,323	0.46	5	5.8	66	[121]	
TZM	—	neutron	> 0.1	853	0.29	36	4	22	[109]	
TZM	—	neutron	> 0.1	858	0.30	36	6.9	21.5	[104]	
TZM	—	neutron	> 0.1	873	0.30	400	5.2	27.6	[123]	
TZM	—	neutron	> 0.1	988	0.34	400	5.2	30	[123]	
TZM	—	neutron	> 0.1	1,063	0.37	36	7.2	31.5	[104]	
TZM	—	neutron	> 0.1	1,153	0.40	400	5.2	37	[123]	
TZM	—	neutron	> 0.1	1,173	0.41	400	5.9	38.7	[123]	
TZM	—	neutron	> 0.1	1,193	0.41	400	5.1	36.5	[123]	

Table 2.3: Experimental observations of void superlattices created through neutron irradiation – Part 1. Table data collated from Table 1 of [62], Table 1 of [64], Table 2 of [66], and Table 1 of [67]. The melting temperatures used to calculate the T/T_m ratio were: molybdenum = 2,896 K [174] and TZM = 2,896.15 K [175].

Matrix	Structure	Projectile	Energy (MeV)	Temperature (K)	T/T_m	Dose (dpa)	Diameter (nm)	a_L (nm)	Reference	Notes
Al	FCC	neutron	> 0.1	328	0.35	6	65	250	[110]	
Mg	PLANAR	neutron	> 0.1	328	0.36	3–6	14	60–80	[110, 114]	(a)
Nb	BCC	neutron	> 0.1	1,063	0.39	34	18.6	66.5	[104]	
Nb	BCC	neutron	> 0.1	1,073	0.39	34	18.6	68.5	[176]	
Ta	BCC	neutron	> 0.1	858	0.26	20–36	6.1	20.5	[104]	
W	BCC	neutron	> 0.1	823	0.22	15	3	19.5	[121]	
W	BCC	neutron	> 0.1	853	0.23	2	3	19.5	[121]	
W	BCC	neutron	> 0.1	953	0.26	2	—	20	[121]	
W	BCC	neutron	> 0.1	1,023	0.28	1.5	4.7	20	[137]	
W	BCC	neutron	> 0.1	1,073	0.29	2	—	21	[121]	
W	BCC	neutron	> 0.1	1,153	0.31	15	4	25	[108]	
W	BCC	neutron	> 0.1	1,173	0.32	2	4	25	[121]	
W	BCC	neutron	> 0.1	1,323	0.36	2	—	30	[121]	

Table 2.4: Experimental observations of void superlattices created through neutron irradiation – Part 2. Table data collated from Table 1 of [62], Table 1 of [64], Table 2 of [66], and Table 1 of [67]. The melting temperatures used to calculate the T/T_m ratio were: aluminium = 933.5 K [174], magnesium = 922 K [174], niobium = 2,742 K [174], tantalum = 3,293 K [174], and tungsten = 3,695 K [174]. **Notes:** (a) Whilst magnesium demonstrated 2D planar ordering, it was an imperfect lattice.

Matrix	Structure	Projectile	Energy (MeV)	Temperature (K)	T/T_m	Dose (dpa)	Diameter (nm)	a_L (nm)	Reference	Notes
Al	FCC	Al	0.4	323	0.35	40	10	60	[115]	(a)
Al	FCC	Al	0.4	348	0.37	80	14	60–80	[115]	
Cr	110 PLANAR	Fe	5	823	0.39	100	8.1	20	[177]	
Cr	BCT, c/a = 1.127	Fe	5	823	0.39	100	10	20	[74]	
Cr	BCT, c/a = 1.127	Fe	5	823	0.39	150	9.5	20	[74]	
Mo	BCC	Ta	7.5	723	0.25	7.5	2.5	22	[124]	
Mo	BCC	Ta	7.5	723	0.25	18	4.5	22	[124]	
Mo	BCC	Ta	7.5	723	0.25	40	4	22	[124]	
Mo	BCC	Ta	7.5	873	0.30	40	5.4	28	[124]	
Mo	BCC	Ta	7.5	988	0.34	40	5.7	32.8	[124]	
Mo	BCC	Ta	7.5	1,063	0.37	36	7.2	32.8	[104]	
Mo	BCC	N	2	1,143	0.39	100	4	22	[107]	(b)
Mo	BCC	Ta	7.5	1,173	0.41	150	15	46	[124]	
Mo	BCC	Ta	7.5	1,173	0.41	40	5.8	37	[124]	
Mo	BCC	Ta	7.5	1,173	0.41	130	6	31	[124, 125]	
Mo	BCC	Ta	7.5	1,173	0.41	130	6	23	[125]	
Mo TZM	—	N	2	1,143	0.39	400	6	22	[15, 178]	

Table 2.5: Experimental observations of void superlattices created through ion irradiation – Part 1. Table data collated from Table 1 of [62], Table 1 of [64], Table 2 of [66], and Table 1 of [67]. The melting temperatures used to calculate the T/T_m ratio were: aluminium = 933.5 K [174], chromium = 2,130 K [174], molybdenum = 2,896 K [174], and TZM = 2,896.15 K [174]. **Notes:** (a) It was observed that helium doping improved the alignment of the void superlattice. (b) It was reported that gaseous impurities influenced the formation and development of the void superlattice.

Matrix	Structure	Projectile	Energy (MeV)	Temperature (K)	T/T_m	Dose (dpa)	Diameter (nm)	a_L (nm)	Reference	Notes
Nb	BCC	Ta	7.5	1,073	0.39	140	12.5	34	[125, 178]	
Nb	BCC	Ta	7.5	1,073	0.39	290	11	38	[125, 178]	
Nb	BCC	Ta	7.5	1,173	0.43	300	25	75	[125, 178]	
Nb	BCC	Ni	5	1,073	0.39	5	4.5	35	[179]	
Nb	BCC	Ni or V	3.2	923	0.34	30–140	1.6	10	[73]	(a)
Nb	BCC	Ni or V	3.2	923	0.34	30	2	10	[73, 180]	(a)
Nb	BCC	Ni or V	3.2	1,078	0.39	5	2	10	[73, 180]	(a)
Nb	BCC	Ni or V	3.2	1,078	0.39	10	5	24	[73, 180]	(a)
Nb	BCC	Ni or V	3.2	1,078	0.39	40–140	13.5	36	[73, 180]	(a)
Nb	BCC	Ni or V	3.2	1,098	0.40	30	20	48	[73, 180]	(a)
Nb	BCC	Ni or V	3.2	1,198	0.44	20	22.5	58	[73, 180]	(a)
Nb	BCC	Ni or V	3.2	1,198	0.44	40–140	25	62	[73, 180]	(a)
Nb	BCC	Ni or V	3.2	1,283	0.47	30	75	145	[73, 180]	(a)
Nb-1%Zr	—	Ni or V	3.2	923–1,283	—	2–140	2–75	10–145	[73, 180]	(a)
Nb-1%Zr	—	Ni or V	3.2	1,053	—	30–140	7.5	25	[73]	(a)
Nb-1%Zr	—	Ni or V	3.2	1,078	—	30–140	14	35	[73]	(a)
Nb-1%Zr	—	Ni or V	3.2	1,123	—	30–140	10	34	[73]	(a)
Nb-1%Zr	—	Ni or V	3.2	1,198	—	30–140	25	61	[73]	(a)
Nb-1%Zr	—	Ni or V	3.2	1,283	—	30–140	78	145	[73]	(a)

Table 2.6: Experimental observations of void superlattices created through ion irradiation – Part 2. Table data collated from Table 1 of [62], Table 1 of [64], Table 2 of [66], and Table 1 of [67]. The melting temperatures used to calculate the T/T_m ratio were: niobium = 2,742 K [174]. **Notes:** (a) Void superlattices could not be formed in niobium and Nb-1%Zr alloys when oxygen concentrations were below 60 ppm and 400 ppm, respectively.

Matrix	Structure	Projectile	Energy (MeV)	Temperature (K)	T/T_m	Dose (dpa)	Diameter (nm)	a_L (nm)	Reference	Notes
Ni	FCC	Se	6	798	0.46	400	18	66	[106, 179]	
Ni	FCC	Ni	5	798	0.46	360	25	62–66	[179]	(a)
Ni	FCC	Ni	5	798	0.46	360–480	25	62	[106, 125]	
Ni-2%Al	—	N	0.4	773	—	10	17.3	88.7	[117]	(b)
Ni-2%Al	—	N	0.4	773	—	20	13.6	49.9	[117]	(b)
Ni-2%Al	—	N	0.4	773	—	40	11	45.5	[117]	(b)
Ni-2%Al	—	N	0.4	773	—	70	13.9	46.5	[117]	(b)
Ni-2%Al	—	N	0.4	773	—	70	14	65	[117]	(b)
Ni-4%Al	—	N	0.4	773	—	10	11.1	98.5	[117]	(b)
Ni-4%Al	—	N	0.4	773	—	20	13.1	51.3	[117]	(b)
Ni-4%Al	—	N	0.4	773	—	40	11.7	48.5	[117]	(b)
Ni-4%Al	—	N	0.4	773	—	70	11.9	45.2	[117]	(b)
Ni-6%Al	—	N	0.4	773	—	10	10.1	146.3	[117]	(b)
Ni-6%Al	—	N	0.4	773	—	20	10.7	50.2	[117]	(b)
Ni-6%Al	—	N	0.4	773	—	40	6.3	36	[117]	(b)
Ni-6%Al	—	N	0.4	773	—	70	11.6	49.2	[117]	(b)
Ni-8%Al	—	N	0.4	773	—	10	10.6	154.3	[117]	(b)
Ni-8%Al	—	N	0.4	773	—	20	10.5	57	[117]	(b)
Ni-8%Al	—	N	0.4	773	—	40	9.5	45.3	[117]	(b)
Ni-8%Al	—	N	0.4	773	—	70	10	44.3	[117]	(b)

Table 2.7: Experimental observations of void superlattices created through ion irradiation – Part 3. Table data collated from Table 1 of [62], Table 1 of [64], Table 2 of [66], and Table 1 of [67]. The melting temperatures used to calculate the T/T_m ratio were: nickel = 1,726 K [174]. **Notes:** (a) They reported that introducing a helium concentration of 3 ppm had no effect. (b) They reported that they believed an aluminium-depleted region surrounded the voids.

2.2 Experimental Observations of Gas Bubble Superlattices

2.2.1 Overview

The first gas bubble superlattice was observed by S. L. Sass and B. L. Eyre in 1973 by irradiating molybdenum with helium ions at room temperature [16]. They observed that the helium gas bubbles formed a long-range, equally distanced superlattice similar to the void superlattices observed a few years earlier. The gas bubble superlattice had a BCC structure, the same as the host metal molybdenum. The critical difference, though, was the lattice parameter, which was notably smaller at 5 nm, although this was consistent given the large bubble density from the irradiation. Similar to void superlattices, this created a flurry of experimentation, with gas bubble superlattices being discovered in the FCC metals of copper [80, 126, 127], nickel [80, 126, 127], AiSi 321 and 316 stainless steel's [80, 126, 127] and gold [128]; the BCC metals of vanadium, tantalum, and tungsten [65] and the HCP metals of titanium [80, 129] and zirconium [130].

As of 2023, gas bubble superlattices have been observed in metals and alloys of all structures: body-centred cubic (BCC), face-centred cubic (FCC), hexagonal close-packed (HCP), and body-centred tetragonal (BCT) and they have been formed using neutrons and ions for a wide range of temperatures and dose. All of the noble gases — helium, neon, argon, krypton, and xenon — have been observed to form a gas bubble superlattice [66, 67].

A very remarkable result was discovered by P. B. Johnson, R. W. Thomson, and D. J. Mazey when irradiating gold with helium; they discovered the superposition of two gas bubble superlattices [128]. The first gas bubble superlattice was consistent with the other experimental results of the community, with a diameter of 2 nm and a lattice parameter of 8 nm; however, the second gas bubble superlattice had bubble diameters of 70 nm and a lattice spacing of 105 nm. Another double-bubble superlattice has yet to be found.

Summary tables for observed gas bubble superlattices are presented in Tables 2.9 – 2.11. The summary tables include the material matrix, the structure of the gas bubble lattice formed, the projectile, the energy of the projectile in keV, the temperature of the irradiation in K, the ratio of the temperature of irradiation to the melting temperature of the metal, T/T_m, the dose rate in dpa/s, the gas bubble diameter in nm, and the superlattice lattice parameter, a_L. For the irradiations carried out by neutrons, the table values of the dose, the fluence, and the flux are populated.

The same literature reviews done by K. Krishan [62], J. H. Evans [63], W. Jäger and H. Trinkaus [64], P. B. Johnson and D. J. Mazey [65], N. M. Ghoniem, D. Walgraef, and S. J. Zinkle [66], and Y. Zhang [67] cover gas bubble superlattices, however, the community's understanding of gas bubble superlattices has dramatically improved since Ghoniem et al. created their literature review in 2001 [66], with a total of 49 new observations being added to the database [67].

A BCC gas bubble superlattice in BCC tungsten is shown in Figure 2.4; this image is reused with permission and taken from Figure 2 of [70]. An FCC gas bubble superlattice in FCC copper is shown in Figure 2.5; this image is reused with permission and taken from Figure 1 of [131]. Planar gas bubble ordering in the basal plane of zirconium is shown in Figure 2.6; this image is reused with permission and taken from Figure 6 of [132].

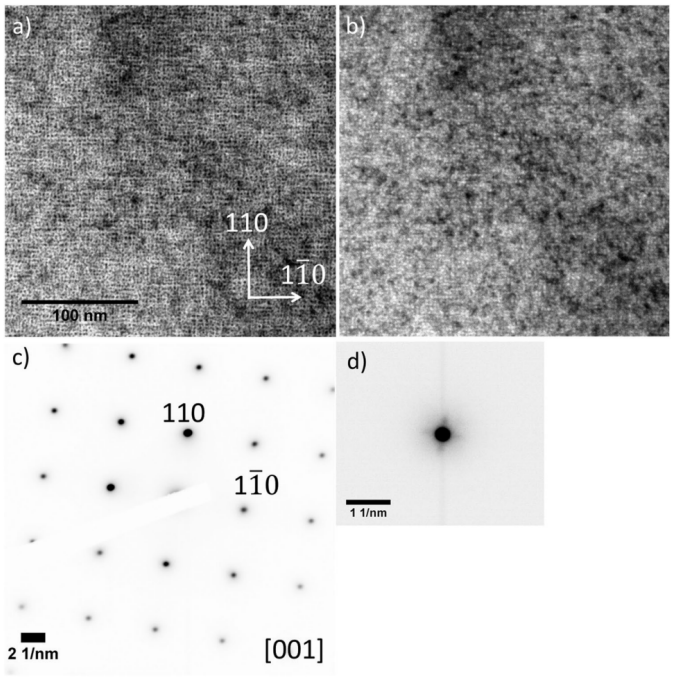

Figure 2.4: Bright-field Transmission Electron Microscope (TEM) images and diffraction patterns of a BCC helium bubble superlattice in BCC tungsten. (a) and (b) show over- and under-focused images of the bubble lattice; (c) is a selected area diffraction pattern (SADP); and (d) shows the diffraction pattern around the 000 spot. Gas bubbles are shown as white objects. This image is reused with permission and taken from Figure 2 of [70].

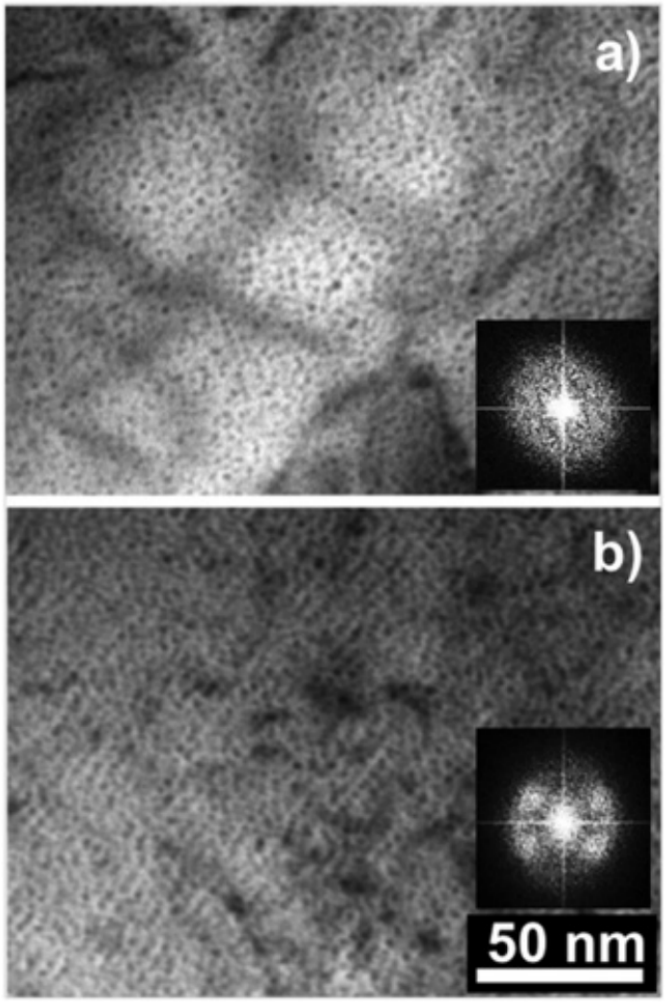

Figure 2.5: Bright-field Transmission Electron Microscope (TEM) images of an FCC helium bubble superlattice in FCC copper. (a) an amorphous array, and (b) an ordered lattice. Insets show corresponding Fast Fourier Transform (FFT) images. Gas bubbles are shown as black objects. This image is reused with permission and taken from Figure 1 of [131].

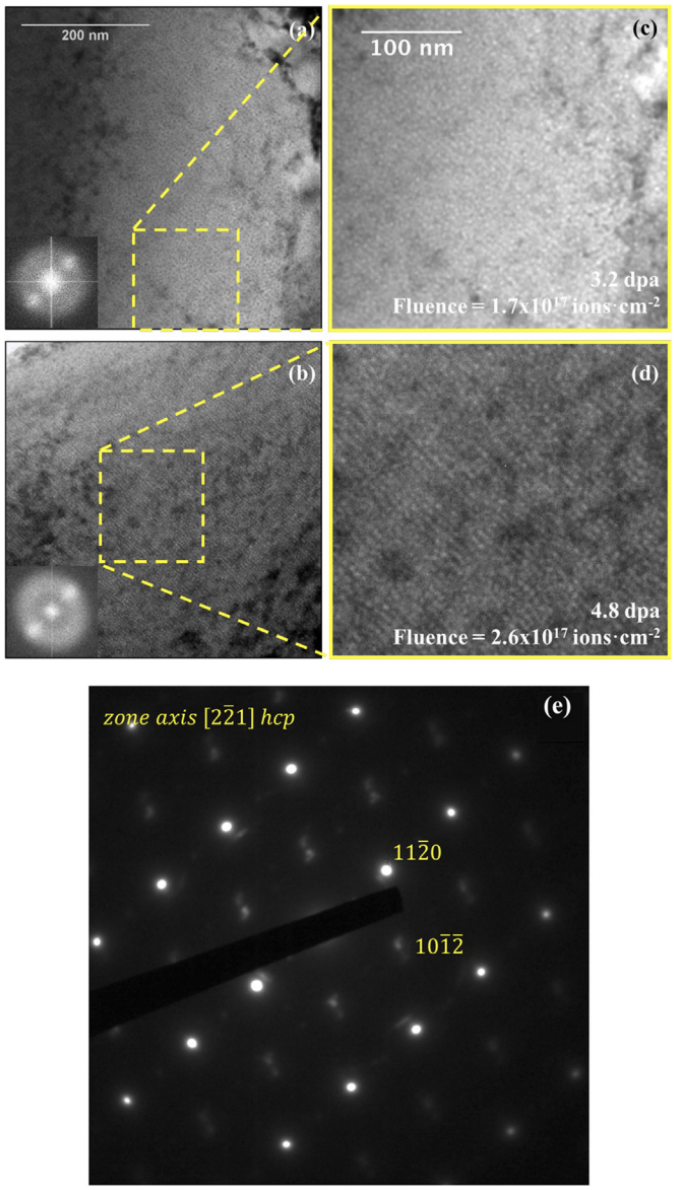

Figure 2.6: Bright-field Transmission Electron Microscope (TEM) images of helium bubble planar lattices in HCP zirconium. (a, c) and (b, d) show bubble arrangements at 3.2 adn 4.8 dpa respectively. Insets in (a) and (b) show Fast Fourier Transform (FFT) images confirming lattice periodicity. (e) is a selected area diffraction pattern (SADP) confirming the α-Zr phase. Gas bubbles appear as white objects. This image is reused with permission and taken from Figure 6 of [132].

2.2.2 Formation and Development

Similar to the void superlattices, gas bubble superlattices follow stages of development. The first four are the same as the void superlattices in that a random distribution of gas bubbles forms, the established gas bubbles begin to grow, the bubbles begin to self-order into local pockets of order, and the local pockets expand to form a long-range superlattice [71, 79]. There is a fifth stage for gas bubbles, where the gas bubbles continue to grow, and small pipe-like structures begin to emerge, connecting the gas bubbles [80].

Like void superlattices, gas bubbles typically form isomorphically with the host metal lattice, i.e. FCC in FCC metals, BCC in BCC metals, and rafts or planes of gas bubbles parallel to the basal plane in HCP metals. However, there are several notable exceptions. P. B. Johnson and D. J. Mazey created a BCC helium bubble superlattice in FCC iron [65], S. Van de Berghe et al. in 2008 [133], J. Gan et al. in 2010 and 2014 [75, 134], and D. Salvato et al. in 2018 [135] have all reported an FCC xenon gas bubble superlattice in U-7%Mo nuclear dispersion fuel, and C. Sun et al. reported a BCT gas bubble superlattice in molybdenum in 2018 [76] and in chromium in 2022 [74]. These results seriously challenge the previously held belief that gas bubble superlattices formed isometrically with the host metal lattice. However, Sun et al. reported that they believed their BCT superlattices resulted from slight lattice strain and would otherwise have been BCC.

The FCC xenon gas bubble superlattice is, however, unquestionable, having been validated by three separate teams. Interestingly, the xenon gas bubble superlattices observed also have the strongest ordering of all the observed gas bubble superlattices to date. D. Salvato et al. reported that the lattice initially formed on the grain boundaries and then proceeded into the interior of the grains upon increasing burnups [135]. Further analysis using low burnups suggested that the xenon gas bubble superlattice observed was, in fact, a well-structured void superlattice and became a xenon gas bubble superlattice once considerable amounts of xenon had been produced.

2.2.3 Temperature Window

The homologous temperature window of formation is lower than void superlattices; for gas bubble superlattices, it is $0.15T_m < T < 0.35T_m$ [16, 136]. The original gas bubble superlattice observed by S. L. Sass and B. L. Eyre was achieved at room temperature, which is $0.1T_m$ for molybdenum. However, further experiments with helium-implanted molybdenum determined that the lower bound of the temperature window was, in fact, $0.15T_m$. The helium gas bubble superlattice was believed to have formed due to heating from the ion beam [65].

The lower temperature bound of $0.15T_m$ was broken by A. M. Robinson et al. in 2017 [131]. Irradiating copper with low energy helium ions, a gas bubble superlattice was observed at 173, 299, and 272 K (-100 °C, room temperature, and 100 °C or $0.13T_m$, $0.22T_m$, and $0.27T_m$). This was also the first time a gas bubble superlattice was observed well below room temperature. Robinson et al. also showed that the gas bubble superlattice parameter was positively correlated with temperature. In contrast, the critical dose rate for ordering a gas bubble superlattice was negatively correlated with temperature.

Also in 2017, J. A. Harrison et al. [70] designed a series of experiments where they implanted helium gas bubbles into tungsten with different helium appm:dpa ratios whilst maintaining a constant dose, dose rate, and temperature. The helium appm:dpa parameter was calculated using Stopping and Range of Ions in Matter (SRIM). In helium ion irradiation, the injected helium gas and the damage created are typically done simultaneously with different ion energies, however, they showed it is possible to change this, and the resultant parameter, helium appm:dpa, can be manipulated, allowing experimentation with different helium appm:dpa ratios. They reported both the helium gas bubble diameter and the helium gas bubble superlattice lattice parameter were negatively correlated with the helium appm:dpa ratio and that the trends could be extrapolated to void superlattices formed in tungsten under neutron irradiation with 1.54 dpa irradiation at 1,023 K [137]; suggesting this could be proof that void and gas bubble superlattices are linked. They concluded that the dependence of a gas bubble superlattice on the helium appm:dpa ratio underlined the significance of the supply of

vacancies in determining the gas bubble lattice's physical characteristics.

In 2019, C. Sun and D. J. Sprouster et al. [71] reported that the temperature window for gas bubble superlattices can be manipulated by changing the helium appm:dpa ratio (calculated using SRIM similar to J. A. Harrison et al.) during their experiments with helium implanted molybdenum. Sun et al. reported that increasing the helium appm:dpa ratio caused both the lower and the upper bound of the temperature window to be shifted down and, additionally, the temperature window itself to broaden.

2.2.4 Diameter and Superlattice Lattice Parameter

The summary statistics for gas bubble diameters and gas bubble superlattice lattice parameters (a_L) are given in Table 2.8. Similar to a void superlattice, the ratio between the gas bubble superlattice lattice parameter and the gas bubble diameter is typically 2–4. The gas bubble superlattice bubble diameters, d, and the gas bubble superlattice lattice parameters, a_L, are smaller than void superlattices.

Metric	Structure	Mean (nm)	Min (nm)	25^{th} Pctl (nm)	Median (nm)	75^{th} Pctl (nm)	Max (nm)
Diameter	BCC	2.13	1.1	1.85	2.33	2.4	3
a_L	BCC	5.18	3.2	4.45	5.2	5.75	9.1
Diameter	FCC	2.33	1.23	1.8	2	2.4	3.9
a_L	FCC	7.83	3	5.5	7.7	11.5	12.5
Diameter	HCP	5.24	2.2	2.8	3	3	22.85
a_L	HCP	11.38	4.5	5.9	7.5	11.8	38.85

Table 2.8: Summary statistics for gas bubble diameters and superlattice lattice parameters (a_L) in BCC, FCC, and HCP metals.

2.2.5 Dependence on Irradiation Conditions

In 2018, Y. Gao et al. proposed a new theory based on thermodynamic-driven instability [138]. To validate this new theory, D. J. Sprouster et al., C. Sun et al., and E. Jossou et al. constructed a series of experiments to investigate the dependence of the gas bubble superlattice parameter on temperature, dose rate, and dose, with dose

rate being the helium ion flux and the dose being the helium ion fluence [71, 77, 139]. For the helium gas bubble superlattices reported in tungsten by D. J. Sprouster et al. and the helium gas bubble superlattices reported in molybdenum by C. Sun et al., they concluded that the gas bubble superlattice lattice parameter, a_L, was positively correlated with temperature, negatively correlated with dose rate, and would plateau over dose. These trends are similar to the trends observed in void superlattices in BCC metals [73, 121, 123, 124] and update the previous statement by P. B. Johnson and D. J. Mazey that the lattice parameter, a_L, for gas bubble superlattices, unlike void superlattices, had no dependence on temperature and dose rate [65]. This evidence further suggests a similarity between the formation and development of void and gas bubble superlattices.

2.2.6 Effect of Alloying

Regarding alloying, in 2019, R. W. Harrison et al. irradiated progressively more complex nickel alloys, implanting helium into pure nickel, NiFe, and FeCrNiCo [140]. This extended the literature for gas bubble superlattices in nickel and its alloys, which had previously only involved pure nickel, unlike void superlattices where nickel and Ni-X%Al alloys had been explored with 2, 4, 6, and 8% additions [117]. R. W. Harrison et al. reported that the gas bubble superlattice bubble diameter and lattice parameter were smaller as the nickel alloy became increasingly more complex than its pure metal, suggesting the cause was due to slow-moving diffusion.

2.2.7 Gas Bubble Superlattice Stability

In 2022, C. Sun et al. explored the stability of a gas bubble superlattice under different irradiation conditions, thermal annealing, and mechanical deformation [74]. C. Sun et al. irradiated a sample of chromium with krypton, which caused a void superlattice to form in the chromium target. Upon further krypton irradiation, they observed the shrinking and disappearance of the void superlattice and the formation of a krypton gas bubble superlattice. When they increased the krypton appm:dpa ratio, the rate of

shrinking increased in the void population; additionally, the population of pre-existing voids led to larger gas bubble superlattice bubble diameters and lattice parameters for the proceeding krypton gas bubble superlattice.

In 2018, J. Gan et al. explored thermal annealing in a helium gas bubble superlattice in molybdenum [141]. They reported that the gas bubble superlattice remained stable as the temperature was increased from 573 K up to 1,125 K (or $0.20T_m$ up to $0.39T_m$) and remained stable at a constant temperature of 1,125 K for 30 minutes. Performing a similar experiment in 2020, C. Sun et al. reported that when a helium gas bubble superlattice in molybdenum was raised from a temperature of 573 K up to a temperature of 1,273 K, it became unstable after 1 hour [142]. Additionally, helium gas bubble superlattices produced in molybdenum in the same way at a temperature of 573 K were found to disappear under further krypton irradiation at 2.5 dpa. C. Sun et al. performed complementary phase-field simulations of the experiment. The simulations showed that the inhomogeneous growth and coarsening of the helium gas bubbles caused the order-disorder transformation.

2.2.8 Summary of Experimental Results

Matrix	Structure	Projectile	Energy keV	Temp. K	T/T_m	Dose dpa	Dose Rate dpa/s	Fluence $10^{17}/cm^2$	Flux $10^{17}/cm^2 \cdot s$	Diameter nm	a_L nm	Reference	Notes
Au	FCC	He	160	280	0.21	—	—	10	—	2/70	8/105	[128]	
Co	PLANAR	Kr	80	300	0.17	—	—	0.15–0.25	—	4.5	4.5	[181]	
Cr	BCT	Kr	300	523	0.25	80	4.8	1	0.09	1.4	5.1	[74]	
Cr	BCC	He	40	298	0.14	—	—	3	—	2.4	5.1	[65]	
Cr (pre void)	BCC	Kr	200	523	0.25	80	4.8	1	0.09	2.2	5.6	[74]	
Cu	FCC	He	12	173	0.13	5.48	10	1.29	1.5	1.8	3	[131]	
Cu	FCC	He	12	299	0.22	2.09	10	0.49	1.5	2.1	3.3	[131]	
Cu	FCC	He	12	373	0.27	2.69	10	0.63	1.5	2.4	3.8	[131]	
Cu	FCC	He	25	173	0.13	5.48	10	2	1.5	1.48	5.4	[182]	
Cu	FCC	He	25	173	0.13	5.48	10	2	1.5	1.37	5.44	[182]	
Cu	FCC	He	25	173	0.13	5.48	10	10	1.5	1.23	5.75	[182]	
Cu	FCC	He	30	373	0.27	2.69	10	5	1.5	2.4	10	[183]	
Cu	FCC	H	16	300	0.22	—	—	130	—	2	12	[184]	
Cu	FCC	He	16	293.15	0.22	—	—	130	—	2	7.7	[184]	(a)
Cu	FCC	He	30	293.15	0.22	—	—	4	—	2	7.7	[80, 126, 127]	
Fe	BCC	He	†	300	0.17	—	—	†	—	†	†	[159, 185]	
Fe	BCC	He	50	298	0.16	—	—	3	—	2.5	6	[65]	
316 SS	FCC	He	30	298	0.17	—	—	4	—	2	6.5	[80, 126, 127]	
321 SS	FCC	He	30	300	0.17	—	—	4	—	2	6.4	[80, 126, 127]	
Mo	BCT	He	150	573	0.20	2.69	10	1.2	6.5	1.8	4.5/3.9	[76]	
Mo	BCC	Kr	300	673	0.23	105	10	0.45	0.38	1.8	5.2	[77]	
Mo	BCC	Kr	300	673	0.23	234	10	1	0.38	1.9	5.3	[77]	
Mo	BCC	Kr	300	773	0.27	59	10	0.25	0.38	2.1	5.4	[77]	
Mo	BCC	Kr	300	773	0.27	105	10	0.45	0.38	2.3	5.6	[77]	
Mo	BCC	Kr	300	773	0.27	234	10	1	0.38	2.5	5.7	[77]	
Mo	BCC	He	40	573	0.20	4	10	1.2	6.5	1.1	5.1	[71]	
Mo	BCC	He	40	573	0.20	4	10	1.2	6.5	1.3	5.2	[71]	
Mo	BCC	He	40	573	0.20	4	10	1.2	6.5	1.6	5.2	[71]	
Mo	BCC	He	40	423	0.15	4	10	1.2	6.5	1.2	3.2	[71]	
Mo	BCC	He	40	723	0.25	4	10	1.2	6.5	2.7	7.1	[71]	

Table 2.9: Experimental observations of gas bubble superlattices — Part 1. Table data collated from Table 2 of [62], Table 2 of [64], Table 3 of [66], and Tables 2 and 3 of [67]. The melting temperatures used to calculate the T/T_m ratio were: gold = 1,337.58 K [174], cobalt = 1,768 K [174], chromium = 2,130 K [174], copper = 1,356.6 K [174], iron = 1,808 K [174], 316 and 321 stainless steel = 1,783.15 K [171], and molybdenum = 2,896 K [174]. **Notes:** (a) Weak ordering, the lattice parameters were poorly defined. †: There were no details available in the source material. —: Intentionally left blank.

Matrix	Structure	Projectile	Energy keV	Temp. K	T/T_m	Dose dpa	Dose Rate dpa/s	Fluence $10^{17}/cm^2$	Flux $10^{17}/cm^2 \cdot s$	Diameter nm	a_L nm	Reference	Notes
Mo	BCC	He	36	973	0.34	—	—	2	—	2.4	5	[16, 65, 136]	(b)
Mo	BCC	Ne	100	823	0.28	—	—	1	—	3	5	[136]	
Mo	BCC	He	100	823	0.28	—	—	1	—	2.2	5.1	[136]	
Mo	BCC	He	40–60	673	0.23	—	—	8	—	2.2	6.2	[65]	
Mo	BCC	He	36	298	0.10	—	—	1	—	2.4	5.2	[16, 65, 136]	(b)
Mo	BCC	He	40	773	0.27	—	—	5	—	2.4	5.4	[16, 65, 136]	(b)
Mo	BCC	Ne	100	823.15	0.28	—	—	1	—	2.4	3.6	[136]	
Mo	BCC	He	36	293.15	0.10	—	—	1	—	2.4	3.7	[16, 136]	
Mo	BCC	He	25	523.15	0.18	—	—	4.5	—	2.4	3.2	[16, 136]	
Mo	BCC	He	36	573.15	0.20	—	—	2	—	2.4	3.4	[16, 136]	
Mo	BCC	He	40	573.15	0.20	—	—	2	—	2.4	3.5	[16, 136]	
Mo	BCC	He	36	673.15	0.23	—	—	2	—	2.4	5	[16, 136]	
Mo	BCC	He	60	673.15	0.23	—	—	2	—	2.4	4.5	[16, 136]	
Mo	BCC	He	40	673.15	0.23	—	—	5	—	2.4	3.6	[16, 136]	
Mo	BCC	He	36	773.15	0.27	—	—	2	—	2.4	3.6	[16, 136]	
Mo	BCC	He	40	773.15	0.27	—	—	5	—	2.4	3.8	[16, 136]	
Mo	no	Kr	300	673	0.23	35	10	0.15	0.38	0.9	7.1	[77]	
Mo	no	Kr	300	673	0.23	59	10	0.25	0.38	1.6	7.1	[77]	
Mo	no	Kr	300	773	0.27	35	10	0.15	0.38	1.8	5.3	[77]	
Mo	no	He	40	573	0.20	4	10	1.2	6.5	1	4.5/3.9	[71]	
Ni	FCC	He	30	298	0.17	2.69	10	1.5	6	2	8.7	[140]	
Ni	FCC	Kr	†	300	0.17	—	—	†	—	†	†	[159, 185]	
Ni	FCC	He	0.25–8	570	—	—	—	1	—	2	8.1	[186]	
Ni	FCC	He	30	293.15	0.17	—	—	4	—	2	6.6	[80, 126, 127]	
Ni	FCC	He	0.25–8	298	0.17	—	—	1	—	2	8.1	[186]	
NiFe	FCC	He	30	298	—	2.69	10	4	6	1.8	5.5	[140]	
FeCrNiCo	FCC	He	30	298	—	2.69	10	4	6	1.8	6	[140]	
Ta	BCC	He	30	573	0.17	—	—	5	—	2.3	6.4	[65]	
Ti	PLANAR	He	30	300	0.15	—	—	15	—	3	7.5	[80]	
Ti	PLANAR	Kr	100	300	0.15	—	—	0.16	—	3	5.6	[129]	
Ti	PLANAR	He	30	293.15	0.15	—	—	15	—	3	9	[80]	

Table 2.10: Experimental observations of gas bubble superlattices — Part 2. Table data collated from Table 2 of [62], Table 2 of [64], Table 3 of [66], and Tables 2 and 3 of [67]. The melting temperatures used to calculate the T/T_m ratio were: molybdenum = 2,896 K [174], nickel = 1,726 K [174], tantalum = 3,293 K [174], and titanium = 1,945 K [174]. **Notes:** (b) The lattice parameter has been converted from {110} interplanar to BCC. †: There were no details available in the source material. —: Intentionally left blank.

Matrix	Structure	Projectile	Energy keV	Temp. K	T/T_m	Dose dpa	Dose Rate dpa/s	Fluence $10^{17}/cm^2$	Flux $10^{17}/cm^2 \cdot s$	Diameter nm	a_L nm	Reference	Notes
U-7Mo	COHERENT	neutron	1	423	—	80	4.8	1	0.09	2	6–7	[133]	
U-7Mo	FCC	neutron	1	382	—	80	4.8	3.2	0.09	3.5	11.5	[135]	
U-7Mo	FCC	neutron	1	373–473	—	80	4.8	0.7	0.09	3.8	12.5	[135]	
U-7Mo	FCC	neutron	1	373–473	—	80	4.8	1.1	0.09	3.6	12	[135]	
U-7Mo	FCC	neutron	1	373–473	—	80	4.8	1.4	0.09	3.9	11.9	[135]	
U-7Mo	FCC	neutron	1	373–473	—	80	4.8	1.8	0.09	3.9	11.8	[135]	
U-7Mo	FCC	neutron	1	403	—	80	4.8	5.2	0.09	3.6	12.2	[75]	
V	FCC	He	30	323	0.15	—	—	5	—	1.5	3.9	[65]	
W	BCC	He	15	773	0.21	3	1	1.1	0.62	1.3	4.4	[140]	
W	BCC	He	30	773	0.21	3	1	0.7425	0.62	1.6	5.5	[140]	
W	BCC	He	60	773	0.21	3	1	0.15	0.62	1.6	7.9	[140]	
W	BCC	He	85	773	0.21	3	1	0.0375	0.62	1.8	9.1	[140]	
W	BCC	He	40	923	0.25	3	10	1	0.62	2.37	6.28	[139]	
W	BCC	He	40	773	0.21	3	10	1	0.62	1.44	4.92	[139]	
W	BCC	He	40	773	0.21	3	0.43	1	0.27	2.28	5.9	[139]	
W	BCC	He	40	773	0.21	3	0.43	2	0.27	2.33	5.8	[139]	
W	no	He	40	623	0.17	3	10	1	0.62	1.12	4.92	[139]	
W	no	He	40	773	0.21	3	0.43	0.6	0.27	1.81	4.92	[139]	
W	no	He	40	773	0.21	3	0.15	1	0.09	2.49	5.8	[139]	
W	BCC	He	50	773	0.21	—	—	1.5	—	2	6.2	[65]	
Zr	PLANAR	Kr	100	300	0.14	—	—	0.16	—	3	7.5	[130]	
alpha-Zr	BASAL	He	6	473	—	80	4.8	3.2	0.09	2.8	11.8	[132]	
alpha-Zr	BASAL	He	400	473	—	80	4.8	2	1.67	2.2	5.9	[187]	
alpha-Zr	BASAL	He	400	673	—	80	4.8	2	1.67	22.85	38.85	[187]	
beta-Zr	PLANAR	He	6	1,148	—	80	4.8	3.2	0.09	2.8	11.8	[132]	

Table 2.11: Experimental observations of gas bubble superlattices — Part 3. Table data collated from Table 2 of [62], Table 2 of [64], Table 3 of [66], and Tables 2 and 3 of [67]. The melting temperatures used to calculate the T/T_m ratio were: vanadium = 2,163 K [174], tungsten = 3,695 K [174], and zirconium = 2,128 K [174]. **Notes:** —: Intentionally left blank.

2.3 Theoretical and Simulation Studies

Since the initial observations of void and gas bubble superlattices, several mechanisms have been proposed to explain their formation and development [15, 16]. The original mechanisms included:

1. Elastic interactions between voids
2. Isomorphic decomposition
3. Anisotropic self-interstitial atom diffusion
4. Self-interstitial dislocation loop punching
5. Phase instability

These mechanisms have been summarised briefly in Section 1.4, and they have been thoroughly reviewed in the literature reviews of K. Krishan [62], J. H. Evans [63], and N. M. Ghoniem, D. Walgraef, and S. J. Zinkle [66]. Since 2001, these mechanisms have been explored and refined through experimentation, simulation, and theoretical studies. New thermodynamics-driven mechanisms have been proposed; Y. Gao et al. implemented a new take on the phase instability mechanism [138, 143, 144] and M. W. Noble et al. proposed a new mechanism entirely based on Turing instability [145]. A superlattice has two distinct features:

1. A characteristic length, i.e. the superlattice lattice parameter that quantifies the regular periodicity of the superlattice
2. The crystal structure, i.e. the observed patterning which presents itself as the superlattice develops

For a theory to successfully address the mechanism of superlattice formation, it needs to predict and explain the characteristic length and the crystal structure.
The proposed mechanisms can be divided broadly into three distinct groups, which are:

1. Thermodynamics based theories
2. Anisotropic self-interstitial atom diffusion-based theories

3. Instability based theories

Anisotropic self-interstitial atom diffusion-based theories focus on predicting the crystal structure of the pattern formation, i.e. whether the superlattice is BCC, FCC, etc. In contrast, the instability-based theories focus on predicting the characteristic length of the pattern formation, i.e. the superlattice lattice parameter. They are often coupled to achieve both and fully describe the evolution of a superlattice [67].

2.3.1 Thermodynamics Based Theories

Thermodynamics-based theories are based on arguments of elastic anisotropy. The motivation of the thermodynamics theories is the observation that superlattices typically mimic the crystal structure of the host metal lattice, i.e. BCC in BCC metals and FCC in FCC metals. Therefore, it is reasonable to assume that the formation and development of superlattices are driven by the thermodynamic elastic interactions between the voids or the gas bubbles which constitute the superlattice. The argument is fundamentally one of energy minimisation. The elastic moduli in some crystalline solids, along specific crystal orientations, can be anisotropic. Within a crystal lattice, the strain energy is dependent on the underlying crystal structure, and the introduction of voids or gas bubbles will change this compared to the un-defected crystal. Therefore, the ordering observed, i.e. the formation and development of a void or a gas bubble superlattice, is the minimisation of this strain energy, which results in equally spaced voids and gas bubbles within the superlattice.

The theory of elastic interactions between voids was first proposed by K. Malen and R. Bullough in 1971 [81], and was followed by A. M. Stoneham in the same year [146]. K. Malen and R. Bullough conjectured that the ordering of void lattices was because of the elastic cubic anisotropy of voids, with the elastic field generated by the surface tension at the surface of the voids. They argued that these fields would create energy minima, prompting voids to repel one another within the host metal lattice structure, causing the spacing of a periodic lattice. A. M. Stoneham, calculating this elastic interaction, reported that for the BCC crystal molybdenum, a BCC void superlattice with a superlattice lattice parameter to void radius ratio of $a_L/d_r = 3.1$ was the

most stable configuration. The problem, however, is that the predicted value of 3.1 is inconsistent with the experimental observations of void superlattices in molybdenum, which, on average, are approximately 11.3.

In 1983, E. Johnson and L. T. Chadderton, motivated by the formation of an anion void superlattice in CaF_2, proposed that the elastic interactions between voids in a void superlattice were analogous to the elastic interactions between precipitates in age-hardened alloys [147] and 2D phase-field modelling performed by H-C. Yu and W. Lu, in 2005 [148], showed that the elasticity of this nature drove the ordering of the voids in a void superlattice. There are two problems, however: 1) it is unclear whether H-C. Yu and W. Lu's phase-field model is applicable when extended from 2D to 3D, i.e. the ordering observed in 2D would be sustained in 3D, and 2) T. H. Ding et al. in 2005 [122] returned to CaF_2 and created a void superlattice using electron irradiation. They used calcium elemental mapping obtained from energy-filtered transmission electron microscopy and characterised the voids as cavities without calcium, suggesting that both the anion and the cation sublattice were damaged. Because E. Johnson and L. T. Chadderton assumed that the damage was purely radiolytic, that the void superlattice formed on the anion sublattice with anion vacancies and anion interstitials, and left the cation sublattice unaffected, this undermines the basis of their theory.

Criticism of the elastic interactions between voids in a void superlattice began with J. H. Evans in 1990 [63]. There are four main issues:

1. BCC tungsten is elastically isotropic [70, 108, 139]. It is rather difficult to have a formation mechanism based on elastic anisotropy and yet observe a void superlattice in an elastically isotropic material.

2. Stabilisation: the elastic interaction required to stabilise the voids in a void superlattice is much higher than the elastic interactions shown by molecular dynamics simulations [149].

3. Irradiation conditions: the characteristics of a void and gas bubble superlattice strongly depend on the irradiation conditions. The proposed mechanism of elastic interactions ignores this dependence.

4. Elastic interactions between voids and gas bubbles cannot explain the planar ordering observed in stage three of the superlattice development when the voids and gas bubbles begin to self-order into local pockets of order. This was further compounded by a detailed analysis performed by Y. Gao et al. in 2022 [150]. They studied the elastic anisotropy in cubic systems. They reported that elastic anisotropy can result in a superlattice with a simple cubic or an FCC structure but not for a BCC structure. This contradicts the many observed BCC void and gas bubble superlattices.

These difficulties mean the formation and development mechanism for void and gas bubble superlattices being caused by the elastic interactions between the voids or the gas bubbles which constitute the superlattice is unlikely.

2.3.2 Anisotropic Self-Interstitial Atom Diffusion-Based Theories

Anisotropic self-interstitial atom diffusion-based theories focus on predicting the characteristic structure of a superlattice, and it is the general consensus in the literature that anisotropic self-interstitial diffusion is the mechanism which selects the characteristic structure of superlattices due to its effect on changing the recombination rate of vacancies and self-interstitial atoms.

Originating with the work done by A. J. E. Foreman in their 1974 Harwell report [84], they proposed that ordering voids into a void superlattice is due to the anisotropic diffusion of self-interstitial atoms. There were two model variations; one was 1D and the other 2D — although, importantly, the 2D version is not an extension of the 1D version. The 1D version described the preferential migration and alignment along close-packed directions, and the 2D version described the preferential migration and alignment along close-packed planes.

1D Self-Interstitial Atom Diffusion

The argument in 1D was based on the flux of self-interstitial atoms that a void would receive if aligned along the self-interstitial atoms' diffusion paths. The voids which were aligned along these preferential self-interstitial atom paths would shield each other from the self-interstitial atoms and hence receive a smaller flux, allowing them to grow, compared to the voids which existed outside of this alignment, which would receive a higher self-interstitial atom flux, and hence shrink away. Because the diffusion paths of self-interstitial atoms are more likely the close-packed directions of the crystal structure, the voids which were able to grow did so along the close-packed directions. C. H. Woo and W. Frank investigated the effect of 1D self-interstitial atom diffusion on the evolution of voids under irradiation. To capture the fluxes received by the voids, they modelled the evolution of the voids using the Fokker-Planck equation. They found that voids existing in crowdion-supply-cylinders (CSC) received a smaller net flux of self-interstitial atoms and, therefore, a higher net flux of vacancies than those existing off of these cylinders, allowing them to grow [86, 151].

In 2009, S. Hu et al. investigated 1D self-interstitial atom diffusion using a phase-field model. They used a Cahn-Hilliard equation for the evolution of voids and coupled a 1D self-interstitial atom random walk. They reported that a random distribution of voids would self-order into a void superlattice when the mobility of the 1D self-interstitial atom was four orders of magnitude larger than the mobility of the vacancy [152]. They extended their phase-field model in 2016 from a 2D void superlattice to a 2D gas bubble superlattice by incorporating a concentration field for xenon gas; they also refined their model to include elastic interactions between the bubbles [153]. They reported that the characteristic structure of the gas bubble superlattice was dependent on the direction of the self-interstitial atom diffusion, not on the structure of the crystal lattice. When the 1D self-interstitial atom diffusion was along the $\langle 111 \rangle$ direction, an FCC gas bubble superlattice was produced, allowing the FCC xenon gas bubble superlattice in U-7Mo to be explained [75, 133, 135].

J. H. Evans criticised the 1D self-interstitial atom diffusion mechanism because it suggested the formation of 1D void alignment during superlattice formation rather

than the 2D planes of voids observed in experiments [79].

2D Self-Interstitial Atom Diffusion

The 1D version was adapted by C. H. Woo et al. in the late 1980's and early 1990's [86–89] to create a 2D version, although their model did require a specific crowdion configuration. J. H. Evans, at the same time [61, 63, 90–92] created their model of 2D self-interstitial atom diffusion. Similar to the 1D version, after carefully considering the vacancy and self-interstitial atom fluxes along close-packed planes, a void within one of these planes would experience a smaller flux of self-interstitial atoms than one existing off this plane. As such, the interconnection of these planes would create a void superlattice as the voids on the planes would grow, and the voids off of the planes would shrink. Exploring 2D self-interstitial atom diffusion with kinetic Monte Carlo simulations, they produced simple cubic, BCC, and FCC superlattice structures when this planar diffusion was present on symmetrical close-packed planes.

Y. Zhang et al. reported that 1D self-interstitial atom diffusion along a single close-packed direction produced 1D void alignment, but 1D self-interstitial atom diffusion along symmetric close-packed directions produced 2D planar void alignment along specific directions [144]. They confirmed their theoretical predictions with atomic kinetic Monte Carlo simulations, demonstrating the three-stage formation of a void superlattice: an initial random distribution transitioning into planar ordering along close-packed planes and finally into a 3D void superlattice. They concluded that 1D self-interstitial diffusion does not necessarily lead to 1D void alignment but changes which characteristic structure the superlattice is allowed to take. They demonstrated this by showing 1D self-interstitial atom diffusion along the $\langle 111 \rangle$ direction or 2D self-interstitial atom diffusion along the $\{110\}$ plane would result in a BCC lattice structure. Their results assumed the self-interstitial atom diffusion was much faster than the vacancy diffusion [154].

Extension to Self-Interstitial Atom Clusters

V. I. Dubinko et al. extended the idea of anisotropic self-interstitial atom diffusion to clusters to explain gas bubble superlattices. They proposed that over-pressurised gas bubbles would punch out 1D self-interstitial atom loops and that it was this repulsive interaction between bubbles that would cause them to order if the bubbles were aligned in the same loop punching directions [93]. For voids, they proposed the interaction mechanism was based on the elastically induced absorption of 1D self-interstitial dislocation loops from the matrix [155]. These extensions may help explain superlattice formation in metals with an FCC structure or within BCC iron where self-interstitial atoms do not diffuse anisotropically, the former being because of the crystal structure having two characteristic lengths and the latter being because BCC iron self-interstitial atoms form dumbbells, which diffuse in 3D.

2.3.3 Instability-Based Theories

Several theories have been proposed to explain the formation of superlattices based on the concept of instability. These instability-based theories focus on the idea that an initially uniform concentration field of vacancies becomes unstable when perturbed, leading to the emergence of concentration waves. High vacancy concentrations form at the periodic peaks of these concentration waves, creating the void superlattice structure with a lattice parameter, a_L, being related to the wavelength, q, of these concentration waves.

These models can be categorised into two groups based on whether they explicitly consider and account for a thermodynamic driving force: dynamic instability and thermodynamics-driven instability. The first group does not explicitly account for the thermodynamic driving force, whereas the second group does.

The two key differences between the dynamic and thermodynamics-driven instability models lie in their consideration of the dynamic evolution of defect clusters. In the first group, the dynamic instability category, the models require at least one type of defect cluster to induce the instability. In the second group, the thermodynamics-based

instability category, these models do not require this explicit consideration.

Dynamic Instability

Dynamic instability theories are based on the Bullough-Eyre-Krishan (BEK) rate equations derived by R. Bullough, B. L. Eyre, and K. Krishan in 1975 [97]. The BEK equations describe the evolution of vacancy and self-interstitial atom concentration fields through space and time, with the diffusion of the vacancies and the self-interstitial atoms governed by Fickian diffusion. In their most generalised form, the BEK rate equations are written as:

$$\begin{aligned} \frac{\partial c_v}{\partial t} &= D_v \nabla^2 c_v - K_r c_v c_i - S_v c_v + G_v \\ \frac{\partial c_i}{\partial t} &= D_i \nabla^2 c_i - K_r c_v c_i - S_i c_i + G_i \end{aligned} \tag{2.1}$$

where:

- c_v and c_i are the concentrations of vacancies and self-interstitial atoms, respectively;
- D_v and D_i are the diffusion coefficients of vacancies and self-interstitial atoms, respectively;
- K_r is the annihilation (or recombination) rate coefficient between vacancies and self-interstitial atoms;
- S_v and S_i are the sink loss terms representing the removal of defects to dislocations, voids, grain boundaries, etc. for vacancies and self-interstitial atoms, respectively;
- G_v and G_i are the source terms for vacancies and self-interstitial atoms, respectively.

To create instability, the rate equations for vacancies and self-interstitial atoms are often coupled with other rate equations describing the spatially dependent evolution of defect clusters, such as voids. Different theories based on dynamic instability differ in the causes of the instability and in choosing which defect clusters are coupled. For

example, in K. Krishan's 1982 paper, they focused on different defect-sink interactions causing the instability [95], in G. Martin's 1983 paper, they focussed on the mutual recombination of the vacancies and the self-interstitial atoms causing the instability [156], and in D. Walgraef et al.'s 1996 paper, they focussed on the contributions that vacancies and self-interstitial atoms have in driving void growth causing the instability [157].

To predict the characteristic length scale, i.e. the superlattice lattice parameter, a_L, a bifurcation analysis was performed by K. Krishan in the same 1982 paper [95]. Using their rate equations, which defined the evolution of the vacancy and the self-interstitial atom concentration fields, alongside the coupled rate equations defining the evolution of the defects, which included voids and vacancy loops, they demonstrated that the stable uniform concentration fields would become unstable when spatially perturbed, creating stable concentration waves within the system and that their wavelength could be extracted from the parameters used in the rate equations.

Between 1989 and 2003, D. Walgraef and N. M. Ghoniem proposed a collection of spatially dependent reaction–diffusion equations over a series of papers to model the evolution of a vacancy concentration, c_v, a self-interstitial atom concentration, c_i, the sessile interstitial loop density, ρ_I, the vacancy loop density, ρ_V, and the void sink density, ρ_C [157–159]. They performed a non-linear stability analysis of their system, and similar to K. Krishan [95] and G. Martin [156], they were able to demonstrate and predict the wavenumber of pattern formation. Through coupling, they introduced the anisotropic mobility of self-interstitial atoms, which allowed them to select the type of pattern formation, i.e. they could now predict the lattice parameter and the crystal structure. An issue, however, was the characteristic lengths that their model would predict were often larger than those from experimental observations. They believe this was due to the non-linear interactions in the post-bifurcation regime [66]. K. Krishan made a similar comment when they reviewed their own model [62], that whilst pattern formation was possible, and wavenumbers could be predicted, whether the pattern and the wavelength remained stable over time resulted from the non-linear interactions.

Thermodynamics-Driven Instability

Thermodynamics-driven instability models effectively couple the Cahn-Hilliard equations of thermodynamics-driven phase separation [85] with the BEK rate equations [97], which handle the reactions, such as the production of vacancies and self-interstitial atoms, their annihilation, or their loss to defect sinks. This coupling allows thermodynamic forces, such as free energy minimisation, to play a direct role in pattern selection, in contrast to the purely kinetic basis of the dynamic instability models. These reaction–diffusion systems are driven to separate into different phases by including a concentration-dependent free energy functional. The combination of reaction and diffusion can cause the uniform concentration fields to become unstable and separate into clusters, such as voids. Two new theories have been proposed for superlattice formation using this idea.

One such theory was developed by Y. Gao et al. and Y. Zhang et al. across a series of papers published between 2018 and 2020 [138, 143, 144]. Their model consisted of a Cahn-Hilliard equation for the evolution of the vacancy concentration field and a BEK rate equation for the evolution of the self-interstitial atom concentration. Additionally, the model included 1D self-interstitial atom diffusion. Their equations are:

$$\begin{aligned} \frac{\partial c_v}{\partial t} &= P(1-c_v) + \nabla \cdot M_v \nabla \left(\frac{\delta F}{\delta c_v} \right) - k_{iv} c_i c_v - k_{vs} D_v c_v \\ \frac{\partial c_i}{\partial t} &= P(1-c_v) + \nabla \cdot D_i \nabla c_i - k_{iv} c_i c_v - k_{is} D_i c_i \end{aligned} \tag{2.2}$$

where:

- c_v and c_i are the concentrations of the vacancies and the self-interstitial atoms, respectively;
- P is the defect production rate due to irradiation (also referred to as the dose rate);
- D_v and D_i are the diffusion coefficients of the vacancies and the self-interstitial atoms, respectively;
- $M_v = D_v/(K_B T)$ is the atomic mobility of the vacancies, related to the diffu-

sivity D_v and the temperature T;

- F is the total free energy of the system;
- $\frac{\delta F}{\delta c_v}$ is the variational derivative of the free energy, providing the chemical potential;
- $\nabla \cdot M_v \nabla \left(\frac{\delta F}{\delta c_v} \right)$ is the Cahn-Hilliard diffusion term for the vacancies, driven by chemical potential gradients;
- $\nabla \cdot D_i \nabla c_i$ is the Fickian diffusion of the self-interstitial atoms, driven by concentration gradients;
- k_{iv} is the annihilation (or recombination) rate coefficient between the vacancies and the self-interstitial atoms;
- k_{vs} and k_{is} are the sink rate coefficients for the vacancies and the self-interstitial atoms, respectively;
- $k_{vs} D_v c_v$ and $k_{is} D_i c_i$ represent the flux of defects absorbed at sinks such as voids, dislocations, or grain boundaries;

They concluded that whilst the instability was thermodynamically driven by vacancy supersaturation, the structure was kinetically driven by the anisotropic diffusion of self-interstitial atoms. By changing the directions of the anisotropic self-interstitial atom diffusion, they could simulate different superlattice structures. This directional control provided a mechanism for symmetry selection, offering a kinetic pathway for tuning the resulting lattice structures in simulations.

In 2020, M. W. Noble et al. [145] [1] proposed a new superlattice formation mechanism, [2] showing that void superlattice formation resulted from a Turing-like instability. Their model consisted of a pair of Cahn-Hilliard equations to describe the evolution of the vacancy and the self-interstitial atom concentration fields. Their equations were coupled through an annihilation term and included a creation term. Although referred to as a Turing instability, the mechanism emerges within a Cahn-Hilliard-type framework due to the difference in defect mobilities, rather than from phase

[1] The current author.
[2] The focus of this thesis.

separation alone. They showed that when the mobility of the self-interstitial atoms was significantly larger than the mobility of the vacancies, a population of uniformly sized, equally inter-distanced voids would emerge and self-order into a void superlattice instead of the more intuitive Ostwald ripening. The need for the self-interstitial atom mobility to be significantly larger than the vacancy mobility for the pattern formation to occur was consistent with the phase-field modelling performed by S. Hu and C. H. Henager in 2009 [152]. M. W. Noble et al. simulated their model using 2D phase-field simulations and found that the structure of the void superlattice produced was HCP, the equivalent in 3D being BCC. Their model, however, could not predict an FCC lattice structure, as their model only creates one characteristic length, and the FCC structure requires two. Their model, perhaps surprisingly, demonstrated HCP void superlattice formation without refinements, such as the anisotropic mobility of self-interstitial atoms. [3]

Despite differences in their underlying assumptions, both model types — dynamic instability and thermodynamics-driven instability — demonstrate that instabilities, whether driven by kinetics or thermodynamics, give rise to spatially ordered defect patterns. Together, these instability-based models offer complementary insights into the mechanisms behind void superlattice formation. Dynamic instability models emphasise the importance of defect kinetics and feedback mechanisms between defect populations, while thermodynamics-driven models highlight the role of free energy landscapes and mobility anisotropies. Although each category offers distinct advantages, they both reveal that the emergence of ordered structures requires a delicate balance between reaction rates, diffusion behaviours, and defect interactions.

[3] The demonstration that a Turing instability can be used as a new mechanism to model the formation and development of void superlattices in nuclear-irradiated materials garnered recognition from Philip Ball, who dedicated one of their Nature Materials columns to them [160].

2.4 Discussion of Void and Gas Bubble Superlattices

2.4.1 Necessary Conditions for Superlattice Formation

Through experimentation, it has been established that the formation of a superlattice is dependent on temperature, the appm:dpa ratio during irradiation, the dose, and the dose rate. Additionally, superlattices can be formed in a diverse range of materials with different crystalline structures and bonding natures through many irradiation sources. Complementary simulation and theoretical studies have also shown the importance of anisotropic diffusion of self-interstitial atoms. These factors can be distilled into two essential conditions.

1. Instability
2. Anisotropic mobility

The irradiation conditions provide an instability that perturbs an otherwise uniform defect concentration field, creating concentration waves of wavenumber q, which drives the characteristic length of the superlattice. The anisotropic mobility, whilst not a requirement for instability to occur, influences the superlattice ordering and allows the characteristic structure of the pattern formation to be selected.

The influence of the instability has been established through experimentation, but the influence of the anisotropic mobility of self-interstitial atoms and self-interstitial atom clusters, whilst shown through simulation and theoretical studies, remains challenging to test experimentally due to the timescales required. However, exploring and understanding the role of self-interstitial atoms and self-interstitial atom clusters may be the key to understanding superlattice formation in the FCC metals and BCC iron. Additionally, anisotropic mobility may be a path to tailor the superlattice itself. T. Suzudo et al. and N. Castin et al. have both suggested that 1D self-interstitial atom diffusion is affected by alloying [161, 162] and C. Sun et al. suggested that 1D self-interstitial atom diffusion is affected by strain, resulting in their observed BCT void and helium gas bubble superlattices in chromium and molybdenum respectively [74,

76]

Looking beyond metals and alloys, if the necessary conditions for superlattice formation are simply instability and an anisotropic mobility factor, then the studies of superlattice formation can be extended to other materials or length scales. These extensions not only help test the robustness of the theoretical models, they could potentially lead to materials with new functional properties.

Effect of the Irradiation Source

Because it is possible to create void and gas bubble superlattices using neutrons, ions, and electrons, it could be concluded that the irradiation source is irrelevant to superlattice formation; however, electron irradiation and ion/neutron irradiation create damage in very different ways: the damage cascade. Ion/neutron irradiation will create large amounts of damage in a small localised area, which can directly lead to the creation of large defects such as voids and clusters. Electron irradiation, however, will create damage as single vacancy-interstitial pairs.

The dynamic instability-based theories of K. Krishan, G. Martin, D. Walgraef, etc. [95, 156, 157] are based on the Bullough-Eyre-Krishan (BEK) rate equations, which require the direct generation of defects in order to induce their instability [97]. Under these theories, void superlattice formation should not be possible via electron irradiation, and yet, they have been created experimentally [122, 147, 163, 164]. Furthermore, in the second group of instability models, which are thermodynamically driven, there is no term for direct void generation, yet they still create an instability [138, 145]. This is shown further still with 3D atomic kinetic Monte Carlo simulations [138] and 3D phase-field simulations [143] demonstrating void superlattice formation with single vacancy-interstitial pair production.

Void superlattice formation through electron irradiation may have unknown additional factors driving their formation and development. The experimental setup of electron irradiation, perhaps. Damage creation in BCC metals requires the transition electron microscope to be operated at a considerably high voltage, coupled with the sample needing to be a thin foil in order to image; this could be setting up a strong surface sink

effect, which is affecting the diffusion properties of the vacancies and the self-interstitial atoms. Additionally, void superlattices formed through ion/neutron irradiation create voids as a direct result of the displacement cascade, which could act as nucleation sites for stable voids within the void superlattice. Therefore, void superlattices produced through ion/neutron irradiation may have a lower critical dose threshold for formation compared to the void superlattices produced through electron irradiation.

This represents a potential area for future experimental research: to explore the critical dose threshold of formation of a superlattice on the irradiation source. Because electron irradiation provides tighter control of the irradiation conditions, the defect dynamics described by the rate equations in the thermodynamics-based instability theories would be more accurate. Anisotropic self-interstitial atom mobility could be introduced through the choice of metal. Additionally, for the theoreticians and the modellers, atomic kinetic Monte Carlo simulations could be used to explore and estimate the irradiation conditions of such an experiment. Void superlattices created by electron irradiation may be the best method to prove the thermodynamics-based instability theories [67].

Thermal Stability of Superlattices

A key question to be answered in finding the mechanism of formation of a void and gas bubble superlattice is whether or not void and gas bubble superlattices are thermodynamically stable. Superlattice formation through anisotropic elastic interactions between voids and gas bubbles is unlikely and suggests a thermodynamic stabilisation mechanism doesn't exist. Additionally, there are energy considerations for gas bubbles and voids. Gas bubbles exert elastic strain on the metal lattice when they coalesce, as will their bubble pressure. The voids in a void superlattice are more uniform than random voids. They will, therefore, have a larger surface-to-volume ratio than coarsened voids, meaning the voids in a void superlattice are less energetically favourable. It seems, therefore, that void and gas bubble superlattices are not thermodynamically stable but are stabilised by reactions with crystalline defects such as vacancies, self-interstitial atoms, loops, etc. Given their apparent lack of thermodynamic stability,

the voids and gas bubbles in void and gas bubble superlattices should coarsen under thermal annealing. The thermal annealing of a krypton gas bubble superlattice in molybdenum by J. Gan et al. and C. Sun et al. [141, 142] demonstrated the thermal stability of gas bubble superlattices. This thermal stability may be due to the ordering of the gas bubbles slowing down the coarsening kinetics. Coarsening takes two forms. The first, Ostwald ripening, involves the growth of larger bubbles/voids at the expense of smaller bubbles/voids due to the imbalance between the flux of gas atoms/vacancies emitted from the surface and the flux of gas atoms/vacancies absorbed by the surface. The second, coalescence, is the migration and combination of two or more bubbles/voids. Therefore, in the case of Ostwald ripening, the fluxes between ordered voids and gas bubbles in a void or gas bubble superlattice are negligible because they are all uniform in size, meaning coarsening via Ostwald ripening is slowed. In the case of coalescence, large gas bubbles and voids migrate slower than smaller gas bubbles and voids; again, because they are of uniform size and distribution, the migration and, therefore, coalescence is slowed. For both cases, coarsening is slowed when the voids and gas bubbles are ordered in a void and gas bubble superlattice. C. Sun et al. demonstrated this using phase-field simulations; they reported that ordered gas bubbles in a gas bubble superlattice were more resistant to coarsening than a random distribution of gas bubbles in the same conditions [142].

Irradiation Stability of Superlattices

Unlike the thermodynamics-based theories and the anisotropic mobility-based theories, the instability-based theories — reviewed in Section 2.3.3 — are all dependent upon the irradiation conditions through the BEK rate equation (or the creation and the annihilation terms in the case of M. W. Noble et al.). Additionally, unlike the anisotropic mobility-based theories, the instability-based theories focus on predicting the characteristic length of the superlattice. As irradiation conditions vary, three things can be expected to happen:

1. In the case of continuous irradiation over time, the lattice would remain stable at the characteristic length of the system. As the number of defects introduced

into the system increases, their number will eventually be too large for the superlattice to remain, and the superlattice will collapse. This was demonstrated by D. Salvato et al., where they observed recrystallisation in continuously U-7%Mo [135]

2. In the case of a slight change to the irradiation conditions. Because the characteristic length is dependent upon the particular choices of temperature, rate of defect production, rate of defect recombination, etc., that quantify the irradiation conditions, changing the irradiation conditions will change the characteristic length of the system, and the superlattice should adapt and change its lattice parameter to reflect the new conditions.

3. In the case of a significant change to the irradiation conditions. The new characteristic length of the system will either be significantly different than the current characteristic length or a characteristic length isn't possible because the new irradiation conditions do not support a concentration wave. The superlattice lattice parameter should still adapt and transition to the new characteristic length in the former. C. Sun et al. demonstrated this using chromium irradiated with krypton ions. They reported that a pre-established void superlattice would collapse and re-form with a different characteristic length when the irradiation conditions were changed [74].

The Effect of the Initial Microstructure

The irradiation conditions are not the only variable that can be changed to influence the properties of a superlattice; there is also a dependency on the microstructure of the material. The vacancy and self-interstitial atom concentrations are critical for instability to occur. Material features such as dislocation loops, alloying elements, grain boundaries, and grain size will all affect these concentrations to some degree. These features act as sinks, absorbing the vacancies and the self-interstitial atoms diffusing within the material. If the sink strength is too high, then too many vacancies and self-interstitial atoms will be absorbed instead of interacting, inducing instability and creating concentration waves. If the sink strength is too low, then the recombination

rate between the vacancies and the self-interstitial atoms will be too high, and again, a superlattice will not be possible.

Grain boundaries are particularly interesting as they may facilitate nucleation sites for voids, hastening the formation of a void superlattice. D. Salvato reported this in their observations of xenon gas bubble superlattices in U-7%Mo [135], where the xenon gas bubble superlattice formed near the grain boundaries first and then progressed into the interior of the grain body.

Then, there are the unique and highly customisable microstructures that additively manufactured metallic materials can produce. P. C. Collins wrote a sound review on them in their paper "Microstructural Control of Additively Manufactured Metallic Materials" [165]. Defects such as porosity, balling, hot tears, and fish scaling are all possible depending on the processing parameters. It would be interesting to see how these structures would affect the formation and development of void and gas bubble superlattices.

Functional Properties of Superlattices

The study of void and gas bubble superlattices has generally been reserved for bulk structural metals and their alloys. This focus is understandable, given their relevance to fission and fusion reactor materials and the problems gas buildup in those materials can cause. But looking beyond these materials, if the necessary conditions for a void or gas bubble superlattice are simply an instability and an anisotropic mobility factor, then creating void and gas bubble superlattices in other materials may warrant pursuit. For example, ceramics such as CaF_2 and SrF_2 have been shown to support void superlattice formation under electron irradiation by L. T. Chadderton et al. [113] and T. H. Ding et al. [122]; and A. H. van Omen et al. achieved the ordering of oxide precipitates in oxygen implanted silicon [166]. Superlattices in these materials may lead to materials with new functional properties.

Similarity of Void and Gas Bubble Superlattices

Given all of the similarities between void and gas bubble superlattices, an important question arises: do they share a common formation mechanism? For example, fundamentally, void and gas bubble superlattices are both ordered cavities within a crystalline material; the latter, gas bubbles, are simply cavities filled with gas atoms. They both form via the same staged process of a random distribution transitioning into ordered planes and finally developing into a 3D superlattice. Their superlattice lattice parameters are both positively correlated with temperature, negatively correlated with dose rate, and will plateau with increasing dose. This is, therefore, an important question when designing materials for fission and fusion reactors. In fission reactors, xenon and krypton gas bubbles are formed by implanting fission gases, whereas in fusion reactors, helium gas bubbles are generated through transmutation reactions.

The answer probably depends on the initial conditions from which the void or gas bubble superlattice formed. When a crystalline material is irradiated, the concentration of vacancies will first increase linearly before plateauing at a high dose; however, the gas concentration will continue to increase linearly with the dose due to the conservation of mass. It probably depends, therefore, on when, within this balance, the process of superlattice formation begins: the vacancy-dominated regime or the gas-dominated regime.

Suppose the superlattice begins to form in the vacancy-dominated regime, i.e. before a significant amount of gas has been introduced into the system. In that case, the growth of both voids and gas bubbles is governed by the vacancy flux the voids and gas bubbles receive. Under these conditions, they probably form and develop via the same mechanism. However, inert gas atoms bond strongly with vacancies — as shown by the density functional theory (DFT) simulations performed by C. Jiang et al. in 2018 [167] — significantly reducing their ability to diffuse. Additionally, the object kinetic Monte Carlo simulations performed by C. Jiang et al. in 2021 [168] showed the thermal stability of voids was increased, along with their ability to nucleate small voids, when the voids had gas atoms inside of them. The combination of slow-moving gas atoms due to being tightly bound to vacancies and gas-filled vacancies facilitating

the nucleation of small voids suggests the superlattice lattice parameter will decrease with an increasing gas appm:dpa ratio. This could explain the results observed in BCC tungsten by R. W. Harrison et al. and D. J. Sprouster et al. in 2019 [139, 140]. Additionally, the analysis of the xenon gas bubble superlattice produced using low burnups by D. Salvato et al. in 2018 suggested this. The xenon gas bubble superlattice observed was, in fact, a well-structured void superlattice and became a xenon gas bubble superlattice once considerable amounts of xenon had been produced. If the superlattice begins to form in the gas-dominated regime, i.e. after a substantial amount of gas has been introduced into the system, then the nucleation and growth of gas bubbles is controlled by either self-interstitial atom emission, as shown by the molecular dynamics simulations of Y. Zhang et al. [169] of by self-interstitial atom loop punching, as shown by the molecular dynamics simulations of M. Jin et al. [170]. In this case, the gas bubble superlattice will form via the mechanism of over-pressurised gas bubbles punching out self-interstitial atom loops as proposed by V. I. Dubinko et al. [93]. In the scenario of superlattice formation in the gas-dominated regime, a gas bubble superlattice may form at lower temperatures when the vacancy diffusion is slower [67].

Chapter 3

Phase-Field Model Creation and Analytical Results

3.1 Introduction

In 1952, Alan Turing proposed a mechanism for pattern formation within a reaction–diffusion system [18]. They showed that a system with two or more concentrations, which could move freely and interact with one another, could support pattern formation if the difference in their diffusivities was significant enough; this mechanism was driven by the interactions between the typically smoothing diffusion and the non-linear reaction terms. This phenomenon of pattern formation in a reaction–diffusion system became known as a "Turing instability". Pattern formation in these systems occurs when an initial uniform state with no diffusion, called the base state, is perturbed in the presence of diffusion, resulting in the system evolving into a patterned and ordered state, with the periodicity of the pattern being driven by the largest positive eigenvalue of the solution of the base state.

Whilst rare, these systems have been shown to exist within liquid-chemical systems [188, 189], with the reason for their rarity being that the difference in diffusivities

is often not significant enough to satisfy the conditions for a Turing instability. In the solid state, however, the diffusivities of impurities and defects are governed by non-linear Arrhenius equations $D \propto \exp\left(-E_{mig}/k_B T\right)$ — where E_{mig} is the energy of the migration barrier of the species, and T is the temperature of the system. The migration energies of defects in solid-state materials are enormous, with vacancies typically having E_{mig} of several eV compared to less than one eV for interstitials [48]. This results in the diffusivity ratio between self-interstitial atoms and vacancies being orders of magnitude apart. The large ratios of diffusivities between defects in the solid-state could imply that a Turing instability is not only possible but is commonplace, unlike the rare observations in liquid-chemical systems.

In this chapter, I explore the hypothesis that the void superlattices observed in nuclear-irradiated materials result from a Turing-like instability. In Section 3.2, I derive a pair of coupled Cahn-Hilliard equations, Equation 3.6. In Section 3.3, I follow the derivation of M. Cross and H. Greenside [2] to perform a linear stability analysis on the pair of coupled Cahn-Hilliard partial differential equations describing the concentrations of the vacancies and the self-interstitial atoms. The equations are coupled by the annihilation term. I derive the determinant of the system, Equation 3.34, and the trace, Equation 3.33. In Section 3.4, I explore their behaviour for different diffusivity ratios and parameter choices, such as the base state values for the vacancies and the self-interstitial atoms, $\bar{v}$ and $\bar{s}$, respectively. In Section 3.5, having shown that a Turing-like instability is possible within this system, I show that the conditions to create one are not particularly restrictive and that a wide selection of values would satisfy the conditions.

3.2 Deriving the Cahn-Hilliard Equations

The equilibrium defect concentration, c_{eq}, for a crystalline material at a finite temperature, T, is proportional to its formation energy, E_f, by the relationship,

$$c_{eq} \propto \exp \frac{-E_f}{k_B T} \tag{3.1}$$

Non-equilibrium defect concentrations, c_{non-eq}, are formed under extreme, often externally driven conditions, such as neutron and ion irradiation. Void superlattices form during these extreme non-equilibrium conditions over days, weeks, and months depending on the irradiation conditions [66, 67, 153]. I hypothesise that a void superlattice is the result of a Turing-like instability driven by the extreme non-equilibrium conditions of irradiation creating non-equilibrium concentrations of vacancies and self-interstitial atoms, the annihilation of vacancies and self-interstitial atoms when they meet, and the significant difference in their mobilities.

Modelling the evolution of the vacancies and the self-interstitial atoms as a phase-field, I define two continuous concentration fields to describe the populations of vacancies and self-interstitial atoms, $v(\mathbf{x}, t)$ and $s(\mathbf{x}, t)$. I assume that vacancies and self-interstitial atoms are created and annihilated in pairs with no other sinks or biases; therefore, $v(\mathbf{x}, t)$ and $s(\mathbf{x}, t)$ are conserved variables.

To describe the evolution over space and time of conserved and continuous variables, I begin with the generic Cahn-Hilliard equation,

$$\frac{\partial c}{\partial t} = D\nabla^2 \left(\frac{\delta F[c]}{\delta c} \right) \tag{3.2}$$

where c is the concentration field, D is the diffusivity of the concentration variable, and $F[c]$ is some free energy functional driving the system with respect to the concentration field.

As the system evolves, I want to create and annihilate vacancies and self-interstitial atoms, so I need to add a term for a rate of creation, c, and a term for a rate of annihilation, $-a$. I want to couple the equations together. The creation of vacancies and self-interstitial atoms occurs in pairs and at a constant rate due to irradiation damage, so c will be a constant. But for the annihilation, this is dependent on a vacancy

and a self-interstitial atom meeting within the system. Hence, annihilation will be represented by $-asv$. Modifying the generic Cahn-Hilliard equation, Equation 3.2, to include these creation and annihilation terms for the vacancies and the self-interstitial atoms, and writing out the evolution equations for vacancies and self-interstitial atoms separately, I now have the following pair of modified Cahn-Hilliard equations coupled through annihilation,

$$\begin{aligned} \frac{\partial s}{\partial t} &= M_s \nabla^2 \left(\frac{\delta F\left[s,v\right]}{\delta s} \right) + c - asv \\ \frac{\partial v}{\partial t} &= M_v \nabla^2 \left(\frac{\delta F\left[s,v\right]}{\delta v} \right) + c - asv \end{aligned} \tag{3.3}$$

where v is the continuous and conserved vacancy concentration, s is the continuous and conserved self-interstitial atom concentration, M_v is the atomic mobility of the vacancies, M_s is the atomic mobility of the self-interstitial atoms, $F[s,v]$ is the free-energy functional driving the system, c is the uniform creation term, and $-asv$ is the annihilation term which couples the two equations together. The atomic mobility, M, is proportional to the diffusivity, D.

The free energy functional,

$$F = \int_V \left[v^2 \left(1-v\right)^2 + \frac{\gamma_v}{2} \left|\nabla v\right|^2 + s^2 \left(1-s\right)^2 + \frac{\gamma_s}{2} \left|\nabla s\right|^2 \right] dV \tag{3.4}$$

drives the system. The free energy functional takes the form of a double-well potential; it has minimum values when s and v are 0 or 1. These minima will encourage the formation of clusters and voids. γ_s and γ_v are the gradient energy coefficients for self-interstitial atoms and vacancies, respectively. They can be thought of as the interface width of the region separating the void and the cluster phases. The $\left|\nabla s\right|^2$ and $\left|\nabla v\right|^2$ terms penalise concentration gradients and try to drive the concentration field flat.

Substituting Equation 3.4 into Equations 3.3, I perform the differentiation as so; using v as the worked example:

$$
\begin{aligned}
\frac{\delta F[s,v]}{\delta v} &= \frac{\delta}{\delta v}\left(v^2(1-v)^2 + \frac{\gamma_v}{2}|\nabla v|^2 + s^2(1-s)^2 + \frac{\gamma_s}{2}|\nabla s|^2\right) \\
&= \frac{\delta}{\delta v}\left(v^2(1-v)^2\right) + \frac{\delta}{\delta v}\left(\frac{\gamma_v}{2}|\nabla v|^2\right) + \frac{\delta}{\delta v}\left(s^2(1-s)^2\right) + \frac{\delta}{\delta v}\left(\frac{\gamma_s}{2}|\nabla s|^2\right) \\
&= \frac{\delta}{\delta v}\left(v^2(1-v)^2\right) + \frac{\delta}{\delta v}\left(\frac{\gamma_v}{2}|\nabla v|^2\right) + \cancelto{0}{\frac{\delta}{\delta v}\left(s^2(1-s)^2\right)} + \cancelto{0}{\frac{\delta}{\delta v}\left(\frac{\gamma_s}{2}|\nabla s|^2\right)} \\
&= \frac{\delta}{\delta v}\left(v^2(1-v)^2\right) + \frac{\delta}{\delta v}\left(\frac{\gamma_v}{2}|\nabla v|^2\right) + 0 + 0 \\
&= \frac{\delta}{\delta v}\left(v^2(1-v)^2\right) - \gamma_v\nabla^2 v \\
&= \frac{\delta}{\delta v}\left(v^2\left(1-2v+v^2\right)\right) - \gamma_v\nabla^2 v \\
&= \frac{\delta}{\delta v}\left(v^4 - 2v^3 + v^2\right) - \gamma_v\nabla^2 v \\
&= \left(4v^3 - 6v^2 + 2v\right) - \gamma_v\nabla^2 v
\end{aligned}
\tag{3.5}
$$

with s following the same working. I can now explicitly express the pair of Cahn-Hilliard equations as:

$$
\begin{aligned}
\frac{\partial s}{\partial t} &= M_s\nabla^2\left[\left(4s^3 - 6s^2 + 2s\right) - \gamma_s\nabla^2 s\right] + c - asv \\
\frac{\partial v}{\partial t} &= M_v\nabla^2\left[\left(4v^3 - 6v^2 + 2v\right) - \gamma_v\nabla^2 v\right] + c - asv
\end{aligned}
\tag{3.6}
$$

I now present some critical notes regarding the explicitly stated Cahn-Hilliard equations in Equation 3.6.

Firstly, this is a nondimensionalised model: the mobility parameters for the vacancies and the self-interstitial atoms, M_v and M_s, the creation term, c, the coupling annihilation term, $-asv$, and the gradient energy coefficients, γ_s and γ_v; all have effective values, not physical values. This approximation is made because of the timescales over which void superlattices form; void superlattices form over days, weeks, and months depending on the irradiation conditions [66, 67, 153]. At this timescale, it is impossible to model the phenomenon with molecular dynamics, which can accomplish simulation times of milliseconds at most. Instead, the underlying atomic processes that these

effective values represent are the average values over the many realisations that would occur during the real-world experiment. For example, the annihilation term, $-asv$, is not a probability of recombination but an effective value to describe the proportion of vacancies and self-interstitial atoms which would be removed from the material if they recombined during the evolution of the model.

Secondly, Equations 3.6 will conserve — with the exception of the creation and the annihilation terms — the number of defects within the system as it evolves; this contrasts the coupled rate equation model explored by R. Bullough, B. Eyre, and K. Krishan [97], which involves only second-order spatial derivatives. The Cahn-Hilliard equations are coupled by the annihilation term; without this, the two concentrations in the system would decouple, and in doing so, the system would evolve via the standard coarsening behaviour of Ostwald ripening [48]. Put another way, the irradiation beam needs to be turned on for a Turing instability to exist and pattern formation to occur; this is a non-equilibrium phenomenon.

Finally, in the phase-field model, the vacancy and the self-interstitial atoms only interact with one another when they meet. This model is a modified reaction–diffusion model, not a Fokker-Planck diffusion model. This is an important distinction, as the former is a reaction–diffusion system, and the latter is a diffusion within a position-dependent potential system [152, 190].

3.3 Linear Stability Analysis

I now proceed to follow the derivation of M. Cross and H. Greenside [2] and perform a linear stability analysis on the coupled pair of Cahn-Hilliard partial differential equations; Equations 3.6.

The Cahn-Hilliard equations represent the reaction and diffusion of vacancies and self-interstitial atoms within an irradiated system and are presented in their explicit form (again, hence no tag) as

$$\frac{\partial s}{\partial t} = M_s \nabla^2 \left[\left(4s^3 - 6s^2 + 2s \right) - \gamma_s \nabla^2 s \right] + c - asv$$
$$\frac{\partial v}{\partial t} = M_v \nabla^2 \left[\left(4v^3 - 6v^2 + 2v \right) - \gamma_v \nabla^2 v \right] + c - asv$$

or more generally as:

$$\begin{aligned} \frac{\partial u_1}{\partial t} &= M_1 \nabla^2 u_1 + f_1(u_1, u_2) \\ \frac{\partial u_2}{\partial t} &= M_2 \nabla^2 u_2 + f_2(u_1, u_2) \end{aligned} \tag{3.7}$$

Writing them in their vector form, they look like this

$$\frac{\partial \mathbf{u}}{\partial t} = \mathbf{M} \nabla^2 \mathbf{u} + \mathbf{f}(\mathbf{u}) \tag{3.8}$$

with u_1 and u_2 representing the concentration fields — what would be s for self-interstitial atoms and v for vacancies, respectively — and $\mathbf{u}$ is the vector representation of this concentration field. $f_1(u_1, u_2)$ and $f_2(u_1, u_2)$ represent the non-linear functions of the coupled Cahn-Hilliard equations; these would be the creation, c, and the annihilation, $-asv$, terms respectively, $\mathbf{f}(\mathbf{u})$ is their vector representation. $f_1(u_1, u_2) = f_2(u_1, u_2)$ in the system of equations. Finally, M_1 and M_2 are the mobilities; they would be the self-interstitial atom mobility, M_s and the vacancy mobility M_v, respectively, and $\mathbf{M}$ represents their diagonal 2×2 mobility matrix:

$$\mathbf{M} = \begin{pmatrix} M_1 & 0 \\ 0 & M_2 \end{pmatrix} \tag{3.9}$$

I begin with the assumption that a stationary, uniform base state, $\mathbf{u_b} = (u_{1b}, u_{2b})$ exists and that it satisfies Equations 3.6 when the space and time derivatives are set to 0, leading to the general equations of:

$$\begin{aligned} f_1(u_{1b}, u_{2b}) &= 0 \\ f_2(u_{1b}, u_{2b}) &= 0 \end{aligned} \tag{3.10}$$

which means, using $u_2 = v$ as the worked example:

$$\begin{aligned} &\frac{\partial \bar{v}}{\partial t} = M_v \nabla^2 \left[\left(4\bar{v}^3 - 6\bar{v}^2 + 2\bar{v} \right) - \gamma_v \nabla^2 \bar{v} \right] + c - a\bar{s}\bar{v} \\ &\qquad \text{Differentials go to 0:} \\ &\frac{\partial \bar{v}}{\partial t} = M_v \nabla^2 \left[\left(4\bar{v}^3 - 6\bar{v}^2 + 2\bar{v} \right) - \gamma_v \nabla^2 \bar{v} \right] + c - a\bar{s}\bar{v} \\ &\qquad \text{After simplification:} \\ &0 = M_v \times 0 \times \left[\left(4\bar{v}^3 - 6\bar{v}^2 + 2\bar{v} \right) - \gamma_v \times 0 \times \bar{v} \right] + c - a\bar{s}\bar{v} \\ &0 = 0 + c - a\bar{s}\bar{v} \\ &0 = c - a\bar{s}\bar{v} \end{aligned} \tag{3.11}$$

where $\mathbf{u_b} = (u_{1b}, u_{2b}) = (\bar{s}, \bar{v})$ are the base states of the vacancies and the self-interstitial atoms, respectively. $u_1 = s$ would follow the same working, but it is a moot point here, as they both return the same result of $0 = c - a\bar{s}\bar{v}$.

Linearising about this base state, $\mathbf{u_b} = (u_{1b}, u_{2b}) = (\bar{s}, \bar{v})$, an arbitrary, infinitesimally small perturbation of the base state, of the form $\delta\mathbf{u}(t, x) = (\delta u_1(t, x), \delta u_2(t, x))$, evolves in time according to the linear equations with constant coefficients:

$$\begin{aligned} \frac{\partial u_1}{\partial t} &= M_1 \nabla^2 u_1 + a_{11}\delta u_1 + a_{12}\delta u_2 \\ \frac{\partial u_2}{\partial t} &= M_2 \nabla^2 u_2 + a_{21}\delta u_1 + a_{22}\delta u_2 \end{aligned} \tag{3.12}$$

where the constant coefficients in the linear equations, a_{ij}, are the 2×2 Jacobian matrix, $\mathbf{A} = \partial\mathbf{f}/\partial\mathbf{u}$, evaluated at the base state, $\mathbf{u_b} = (u_{1b}, u_{2b}) = (\bar{s}, \bar{v})$

$$a_{ij} = \left.\frac{\partial f_i}{\partial u_j}\right|_{\mathbf{u_b}} \tag{3.13}$$

and written in vector notation, they are:

$$\frac{\partial \delta \mathbf{u}}{\partial t} = \mathbf{M}\nabla^2 \delta \mathbf{u} + \mathbf{A}\delta \mathbf{u} \tag{3.14}$$

Because Equations 3.12 are linear, have constant coefficients, and have boundaries at infinity, i.e. the material is so large there is not a boundary edge with respect to the area where the void lattice would occur, I assume that the solutions have translational symmetry, i.e. are invariant to changes without rotation, and I look for solutions which satisfy applying an infinitesimally small perturbation in space and time, $\delta\mathbf{u}(t,x) = (\delta u_1(t,x), \delta u_2(t,x))$, of the form:

$$\delta \mathbf{u} = \delta \mathbf{u_q} \exp(\lambda t + i\mathbf{q}\cdot\mathbf{x}) \tag{3.15}$$

where $\delta\mathbf{u_q}$ is a constant eigenvector, λ is the eigenvalue, and $\mathbf{q} = |\mathbf{q}| = \left(q_x^2 + q_y^2\right)^{1/2}$ is the wavenumber in 2D.

A vital discussion item here is that the infinitesimally small perturbation vector components, $\delta\mathbf{u}$, must have the same dependence on space and time.

Substituting Equation 3.15 into Equation 3.14, realising the differentials, dividing through the exponentials in space and time from the substitution, and collecting the terms, I reduce to the following eigenvalue problem.

$$\frac{\partial \delta \mathbf{u}}{\partial t} = \mathbf{M}\nabla^2 \delta \mathbf{u} + \mathbf{A}\delta \mathbf{u}$$

Inserting the base state with the exponentials:

$$\frac{\partial \left(\delta \mathbf{u_q} \exp(\lambda t + i\mathbf{q}\cdot\mathbf{x})\right)}{\partial t} = \mathbf{M}\nabla^2 \left(\delta \mathbf{u_q} \exp(\lambda t + i\mathbf{q}\cdot\mathbf{x})\right) + \mathbf{A}\left(\delta \mathbf{u_q} \exp(\lambda t + i\mathbf{q}\cdot\mathbf{x})\right)$$

Performing differentiation:

$$\lambda \times \delta \mathbf{u_q} \exp(\lambda t + i\mathbf{q}\cdot\mathbf{x}) = \mathbf{M} \times i^2 \times q^2 \times \delta \mathbf{u_q} \exp(\lambda t + i\mathbf{q}\cdot\mathbf{x}) + \mathbf{A}\left(\delta \mathbf{u_q} \exp(\lambda t + i\mathbf{q}\cdot\mathbf{x})\right)$$

Dividing out the exponentials:

$$\lambda \delta \mathbf{u_q} = -\mathbf{M}q^2 \delta \mathbf{u_q} + \mathbf{A}\delta \mathbf{u_q}$$

Collecting terms:

$$\lambda \delta \mathbf{u_q} = \left(\mathbf{A} - \mathbf{M}q^2\right)\delta \mathbf{u_q}$$

Simplifying:

$$\lambda \delta \mathbf{u_q} = \mathbf{A_q}\delta \mathbf{u_q} \tag{3.16}$$

where

$$\mathbf{A_q} = \left(\mathbf{A} - \mathbf{M}q^2\right) = \begin{pmatrix} a_{11} - M_1 q^2 & a_{12} \\ a_{21} & a_{22} - M_2 q^2 \end{pmatrix} \tag{3.17}$$

with the values of a_{11}, a_{12}, a_{21}, and a_{22} being the values of the Jacobian matrix defined in Equation 3.13.

To derive $\lambda\delta\mathbf{u_q}$ in the system, I performed the following — using $u_1 = s$ as the worked example, and with $u_2 = v$ following the same working

Begin:

$\partial s/\partial t$

Inserting the base state with the exponentials:

$\partial \left(\bar{s} \exp(\lambda t + i\mathbf{q} \cdot \mathbf{x}) \right) / \partial t$

Performing differentiation:

$\lambda \times \bar{s} \exp(\lambda t + i\mathbf{q} \cdot \mathbf{x})$

Simplifying:

$\lambda \bar{s}$

(3.18)

To derive the elements of $\mathbf{A_q}$; and referring to the matrix elements as follows: [1]

$$\mathbf{A_q} = \begin{pmatrix} x_{11} & x_{12} \\ x_{21} & x_{22} \end{pmatrix} \tag{3.19}$$

then for x_{11}, and performing piecemeal, I begin with $\mathbf{M}\nabla^2 \left[\left(4s^3 - 6s^2 + 2s \right) - \gamma_s \nabla^2 s \right]$:

[1] using x to avoid confusion as I have already used a for the terms of the Jacobian matrix.

Begin:

$$\mathbf{M}\nabla^2\left[\left(4s^3 - 6s^2 + 2s\right) - \gamma_s\nabla^2 s\right]$$

Multiplying through by $\mathbf{M}\nabla^2$:

$$\mathbf{M}\nabla^2(4s^3 - 6s^2 + 2s) - \mathbf{M}\gamma_s\nabla^4 s$$

Inserting the base state with the exponentials:

$$\mathbf{M}\nabla^2(4\bar{s}^3 - 6\bar{s}^2 + 2\bar{s})\exp(\lambda t + i\mathbf{q}\cdot\mathbf{x}) - \mathbf{M}\gamma_s\nabla^4\bar{s}\exp(\lambda t + i\mathbf{q}\cdot\mathbf{x})$$

Performing differentiation:

$$\mathbf{M}\times i^2\cdot q^2\times(12\bar{s}^2 - 12\bar{s} + 2)\exp(\lambda t + i\mathbf{q}\cdot\mathbf{x}) - \mathbf{M}\gamma_s\times i^4\cdot q^4\times\exp(\lambda t + i\mathbf{q}\cdot\mathbf{x})$$

Collecting the terms:

$$-\mathbf{M}q^2(12\bar{s}^2 - 12\bar{s} + 2) - \mathbf{M}\gamma_s q^4$$

Simplifying:

$$-\mathbf{M}((12\bar{s}^2 - 12\bar{s} + 2)q^2 + \gamma_s q^4) \tag{3.20}$$

and for $c - asv$:

Begin:

$$c - asv$$

Inserting the base state with the exponentials:

$$c - a\bar{s}\bar{v}\exp(\lambda t + i\mathbf{q}\cdot\mathbf{x})\exp(\lambda t + i\mathbf{q}\cdot\mathbf{x}) \tag{3.21}$$

Performing differentiation and simplifying:

$$-a\bar{v}$$

and putting it all together

$$x_{11} = -M_s \left(q^2 \left(12\bar{s}^2 - 12\bar{s} + 2 \right) + \gamma_s q^4 \right) - a\bar{v} \tag{3.22}$$

For x_{12}, I am differentiating the self-interstitial atom equation with respect to the vacancy concentration, so it is a simple reduction as only the coupled annihilation term, $-asv$, has any v fields. I will still perform it for completeness and do so piecemeal for readability. Beginning with $\mathbf{M}\nabla^2 \left[\left(4s^3 - 6s^2 + 2s \right) - \gamma_s \nabla^2 s \right]$:

Begin:

$\mathbf{M}\nabla^2 \left[\left(4s^3 - 6s^2 + 2s \right) - \gamma_s \nabla^2 s \right]$

Multiplying through by $\mathbf{M}\nabla^2$:

$\mathbf{M}\nabla^2 (4s^3 - 6s^2 + 2s) - \mathbf{M}\gamma_s \nabla^4 s$

Inserting the base state with the exponentials:

$\mathbf{M}\nabla^2 (4\bar{s}^3 - 6\bar{s}^2 + 2\bar{s}) \exp(\lambda t + i\mathbf{q} \cdot \mathbf{x}) - \mathbf{M}\gamma_s \nabla^4 \bar{s} \exp(\lambda t + i\mathbf{q} \cdot \mathbf{x})$

Performing differentiation and simplifying:

0

(3.23)

and for $c - asv$:

Begin:

$c - asv$

Inserting the base state with the exponentials:

$c - a\bar{s}\bar{v} \exp(\lambda t + i\mathbf{q} \cdot \mathbf{x}) \exp(\lambda t + i\mathbf{q} \cdot \mathbf{x})$

Performing differentiation and simplifying:

$-a\bar{s}$

(3.24)

and putting it all together:

$$x_{12} = -a\bar{s} \tag{3.25}$$

Performing a similar working for elements x_{21} and x_{22}, the final $\mathbf{A_q}$ matrix for the Cahn-Hilliard system is:

$$\mathbf{A_q} = \begin{pmatrix} -M_s\left(q^2\left(12\bar{s}^2 - 12\bar{s} + 2\right) + \gamma_s q^4\right) - a\bar{v} & -a\bar{s} \\ -a\bar{v} & -M_v\left(q^2\left(12\bar{v}^2 - 12\bar{v} + 2\right) + \gamma_v q^4\right) - a\bar{s} \end{pmatrix} \tag{3.26}$$

and defining g_s and g_v as:

$$\begin{aligned} g_s &= 12\bar{s}^2 - 12\bar{s} + 2 \\ g_v &= 12\bar{v}^2 - 12\bar{v} + 2 \end{aligned} \tag{3.27}$$

I can improve readability. The matrix $\mathbf{A_q}$ can therefore be more compactly written as:

$$\mathbf{A_q} = \begin{pmatrix} -M_s\left(q^2 g_s + \gamma_s q^4\right) - a\bar{v} & -a\bar{s} \\ -a\bar{v} & -M_v\left(q^2 g_v + \gamma_v q^4\right) - a\bar{s} \end{pmatrix} \tag{3.28}$$

The eigenvalue equation, (derived in Equation 3.16):

$$\lambda\delta\mathbf{u_q} = \mathbf{A_q}\delta\mathbf{u_q} \tag{3.29}$$

shows that the eigenvalue, λ and the eigenvector, $\delta\mathbf{u_q}$, will form an eigenvalue–eigenvector pair of the 2×2 matrix $\mathbf{A_q}$, shown in Equation 3.28 and that there exists a single eigenvalue problem for each value of the wavenumber $\mathbf{q}$. Generally, an

eigenvalue problem like Equation 3.29 will have two linearly independent eigenvectors, $\delta\mathbf{u_{1q}}, \delta\mathbf{u_{2q}}$ with the corresponding eigenvalues being $\lambda_{1q}, \lambda_{2q}$, where 1 and 2 are in reference to s and v — the concentration fields of the self-interstitial atoms and the vacancies respectively. Solutions of these eigenvalue–eigenvector pairs take the form of:

$$[c_{1q}\delta\mathbf{u_{1q}}\exp(\lambda_{1q}t) + c_{2q}\delta\mathbf{u_{2q}}\exp(\lambda_{2q}t)]\exp(iqx) \tag{3.30}$$

where c_{1q} and c_{2q} are complex constants.

Equation 3.30 will decay if the real part for both eigenvalues is negative. The infinitesimally small perturbation, $\delta\mathbf{u}(t,x) = (\delta u_1(t,x), \delta u_2(t,x))$ is a superposition over all wavenumbers, q. Therefore, the uniform base state, $\mathbf{u_b} = (u_{1b}, u_{2b}) = (\bar{v}, \bar{s})$, is stable if both eigenvalues, λ_{1q} and λ_{2q} have negative real parts for all wavenumbers, q.

The characteristic polynomial for the matrix, $\mathbf{A_q}$, in Equation 3.28 is written as:

$$0 = det(\mathbf{A_q} - \lambda_q\mathbf{I}) = \lambda_q^2 - tr(\mathbf{A_q})\lambda_q + det(\mathbf{A_q}) \tag{3.31}$$

where $det(\mathbf{A_q})$ is the determinent of the matrix $\mathbf{A_q}$ and $tr(\mathbf{A_q})$ is the trace of the matrix $\mathbf{A_q}$.

The two eigenvalues are the roots of the characteristic polynomial equation, which, for a quadratic equation, can be calculated using the following:

$$\lambda_q = \frac{tr(\mathbf{A_q}) \pm \sqrt{(tr(\mathbf{A_q}))^2 - 4det(\mathbf{A_q})}}{2} \tag{3.32}$$

On inspection of Equation 3.31 a simple criterion for the real parts of both eigenvalues being negative, and therefore the system being stable, is the $tr(\mathbf{A_q}) < 0$ and the $det(\mathbf{A_q}) > 0$.

A Turing instability arises within a system when a base state is stable in the absence

of diffusion, i.e. $M_s = 0$ and $M_v = 0$; but becomes unstable when it experiences a perturbation of a particular wavenumber, q. The growing solution then leads to periodic patterns with the wavenumber, q, of the perturbation. In the system, when $q = 0$, the eigenvalues will be either $\lambda_{iq} = 0$ or $\lambda_{iq} = -a\,(\bar{s} + \bar{v})$, so for all base states, no unstable pattern-forming mode, $(\lambda_{iq} > 0)$, is possible without diffusion.

When diffusion is re-introduced, i.e. when M_s and M_v take non-zero positive values, one or both eigenvalues become non-zero, i.e. $(\lambda_{iq} > 0)$, when either the $tr(\mathbf{A_q}) > 0$ and $(tr(\mathbf{A_q}))^2 - 4det(\mathbf{A_q}) > 0$, this is condition 1, or when the $tr(\mathbf{A_q}) < 0$ and the $det(\mathbf{A_q}) < 0$, this is condition 2.

The trace of a matrix is calculated by taking the sum of the main diagonal. So for $\mathbf{A_q}$, in Equation 3.28 I can calculate the $tr(\mathbf{A_q})$ by:

$$
\begin{aligned}
\mathbf{A_q} &= \begin{pmatrix} -M_s\left(q^2 g_s + \gamma_s q^4\right) - a\bar{v} & -a\bar{s} \\ -a\bar{v} & -M_v\left(q^2 g_v + \gamma_v q^4\right) - a\bar{s} \end{pmatrix} \\
tr(\mathbf{A_q}) &= x_{11} + x_{22} \\
tr(\mathbf{A_q}) &= [-M_s(q^2 g_s + \gamma_s q^4) - a\bar{v}] + [-M_v(q^2 g_v + \gamma_v q^4) - a\bar{s}] \\
tr(\mathbf{A_q}) &= -M_s\gamma_s q^4 - M_v\gamma_v q^4 \\
&\quad - M_s g_s q^2 - M_v g_v q^2 \\
&\quad - a\bar{v} - a\bar{s} \\
tr(\mathbf{A_q}) &= -(M_s\gamma_s + M_v\gamma_v)q^4 \\
&\quad - (M_s g_s + M_v g_v)q^2 \\
&\quad - (\bar{v} + \bar{s})a
\end{aligned}
\tag{3.33}
$$

which is always negative in the system. This means that condition 1 is not possible, and one of the logic criteria for condition 2 is always satisfied. Therefore, for the Turing instability to be present in the system, it is sufficient that only $det(\mathbf{A_q}) < 0$.

The determinant of a matrix is calculated by taking the product of the main diagonal and subtracting the product of the off-diagonal. So for $\mathbf{A_q}$, in Equation 3.28, I can calculate the $det(\mathbf{A_q})$ by:

$$\mathbf{A_q} = \begin{pmatrix} -M_s\left(q^2 g_s + \gamma_s q^4\right) - a\bar{v} & -a\bar{s} \\ -a\bar{v} & -M_v\left(q^2 g_v + \gamma_v q^4\right) - a\bar{s} \end{pmatrix}$$

$$\begin{aligned} det(\mathbf{A_q}) &= x_{11} \times x_{22} - x_{12} \times x_{21} \\ det(\mathbf{A_q}) &= [-M_s(q^2 g_s + \gamma_s q^4) - a\bar{v}] \times [-M_v(q^2 g_v + \gamma_v q^4) - a\bar{s}] - [-a\bar{s}] \times [-a\bar{v}] \\ det(\mathbf{A_q}) &= M_v M_s q^8 \\ &\quad + M_v M_s \left(g_s + g_v\right) q^6 \\ &\quad + \left[M_v M_s g_s g_v + a\left(M_v\bar{v} + M_s\bar{s}\right)\right] q^4 \\ &\quad + a\left(M_v\bar{v}g_v + M_s\bar{s}g_s\right) q^2 \end{aligned} \tag{3.34}$$

which is a 4th-order polynomial in q^2.

To better understand the system's stability properties, particularly the behaviour characterised by the eigenvalues λ_{1q} and λ_{2q}, it is useful to examine the $tr(\mathbf{A_q})$–$det(\mathbf{A_q})$ plane visually; this is done in Figure 3.1. The boundary between regions is defined by the parabola $det(\mathbf{A_q}) = \frac{1}{4}\left(tr(\mathbf{A_q})\right)^2$, which divides the plane into two main areas. Above this parabola, the eigenvalues are complex, while below it, they remain real. Stability is ensured when both eigenvalues have negative real parts, corresponding to the shaded region.

Instability can arise when crossing certain boundaries in this plane. A *stationary instability* occurs when the trajectory crosses the negative $tr(\mathbf{A_q})$ axis, where $tr(\mathbf{A_q}) < 0$ and $det(\mathbf{A_q}) < 0$. Conversely, an *oscillatory instability* occurs when crossing the positive $det(\mathbf{A_q})$ axis, where $tr(\mathbf{A_q}) > 0$ and $det(\mathbf{A_q}) > 0$. These transitions define different instability mechanisms in the system.

Figure 3.1 was created in Whimsical and recreates Figure 1 from M. Cross and H. Greenside [2], illustrating how determinant and trace influence the stability of $\mathbf{A_q}$.

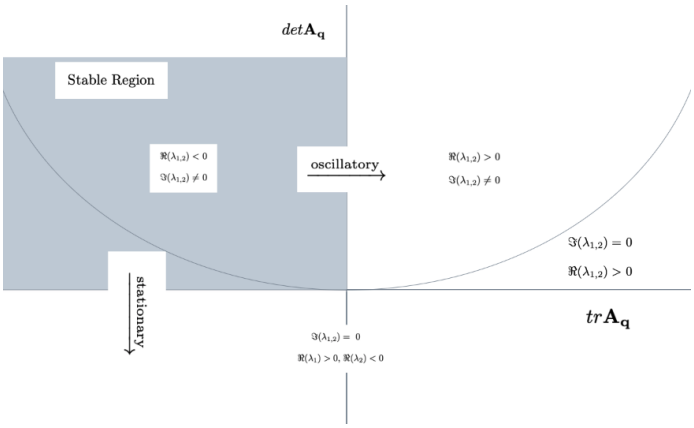

Figure 3.1: A visualisation of the $tr(\mathbf{A_q})$–$det(\mathbf{A_q})$ plane, illustrating the different regions characterised by the two eigenvalues, λ_{1q} and λ_{2q}. The parabola — shown schematically and not to scale — corresponds to $det(\mathbf{A_q}) = \frac{1}{4}\left(tr(\mathbf{A_q})\right)^2$, dividing the plane into two distinct regions. Above the parabola, the eigenvalues are complex, while below it, they are real. The shaded region represents the stable domain, where both eigenvalues have negative real parts. Instability arises when transitioning out of this region: a *stationary instability* occurs when crossing the negative $tr(\mathbf{A_q})$ axis, where $tr(\mathbf{A_q}) < 0$ and $det(\mathbf{A_q}) < 0$, whereas an *oscillatory instability* occurs when crossing the positive $det(\mathbf{A_q})$ axis, where $tr(\mathbf{A_q}) > 0$ and $det(\mathbf{A_q}) > 0$. This figure was created using Whimsical and is a recreation of Figure 1 from M. Cross and H. Greenside [2].

3.4 Determinant Investigation and Results

The determinant of the matrix $\mathbf{A_q}$, $det(\mathbf{A_q})$, is a 4th order polynomial in q^2; it is therefore possible to solve it numerically through different choices of parameters. The parameter space of $0 \leq q \leq 2\pi$, $M_v = 1$, $M_s/M_v = \{1, 2, 3, 4, 5, 10, 50, 100, 500, 1\,000, 5\,000, 10\,000\}$, $0 \leq s \leq 0.5$, $0 \leq v \leq 0.5$, and $a = 0.5$, can be searched through with the Python code documented in Appendix A.1. This builds a DataFrame like Table 3.1, where `condition_1` is: $tr(\mathbf{A_q}) > 0$ and $\left(tr(\mathbf{A_q})\right)^2 - 4det(\mathbf{A_q}) > 0$ and `condition_2` is: $tr(\mathbf{A_q}) < 0$ and $det(\mathbf{A_q}) < 0$.

M_s	M_v	s	v	q	a	$det(\mathbf{A_q})$	$tr(\mathbf{A_q})$	Condition 1	Condition 2
1	1	0.00	0.00	0.0	0.5	0.0	−0.000	False	False
1	1	0.01	0.00	0.0	0.5	0.0	−0.005	False	False
1	1	0.02	0.00	0.0	0.5	0.0	−0.010	False	False
1	1	0.03	0.00	0.0	0.5	0.0	−0.015	False	False
1	1	0.04	0.00	0.0	0.5	0.0	−0.020	False	False

Table 3.1: DataFrame `.head()` of the parameter search for Turing instability conditions.

Examining the percentage of `condition_1` and `condition_2` that are `True` across the entire parameter space reveals that multiple parameter combinations of q, M_s, M_v, s, v, and a satisfy `condition_2`, indicating the presence of a Turing instability (see Table 3.2). In contrast, `condition_1` never occurs, as the trace $tr(\mathbf{A_q})$ remains negative throughout the system.

M_s/M_v	Perc. `condition_1`	Perc. `condition_2`
1	0.00%	9.70%
2	0.00%	8.95%
3	0.00%	8.15%
4	0.00%	7.41%
5	0.00%	6.74%
10	0.00%	5.12%
50	0.00%	3.23%
100	0.00%	2.82%
500	0.00%	2.33%
1 000	0.00%	2.22%
5 000	0.00%	2.08%
10 000	0.00%	2.05%

Table 3.2: Percentage of the parameter space supporting a Turing instability.

3.4.1 Visualising the Parameter Space

Figures 3.2 and 3.3 visualise the results of the numerical parameter search. The Python code used to create the 3D and 2D plots is available in Appendices A.3 and A.2 respectively.

The evolution of the sub-plots in Figures 3.2 and 3.3 show that as M_s/M_v increases,

the unstable region undergoes structural changes. For lower values ($M_s/M_v \leq 10$), the instability region occupies a broad section of the parameter space. However, for larger values ($M_s/M_v \geq 50$), the instability region shifts and becomes more constrained.

Figure 3.2: 3D Scatter Plots of Instability Regions

Figure 3.2 visualises the parameter search in three-dimensional space, where:

- The **x-axis** represents v (ranging from 0 to 0.5).
- The **y-axis** represents s (ranging from 0 to 0.5).
- The **z-axis** represents q (ranging from 0 to 2π).

Each subplot corresponds to a different mobility ratio, M_s/M_v, varying across a range of values $\{1, 2, 3, 4, 5, 10, 50, 100, 500, 1\,000, 5\,000, 10\,000\}$. The blue points represent parameter combinations where the Turing instability condition (`condition_2`) is satisfied. As M_s/M_v increases, a clear structural shift in the unstable region is observed, with the instability region appearing to expand in some parameter directions while contracting in others.

Figure 3.3: 2D Projection of Instability Regions

To enhance interpretability, Figure 3.3 provides a 2D projection of the 3D parameter space by overlaying the values of q onto the v–s plane:

- The **x-axis** represents v (ranging from 0 to 0.5).
- The **y-axis** represents s (ranging from 0 to 0.5).
- Each blue dot indicates a parameter combination where at least one q value satisfies the Turing instability condition.

This visualisation allows for a clearer identification of the regions where instability is most likely to occur. The density of blue points in certain areas suggests that multiple values of q contribute to the instability for specific parameter choices. The denser the marks on the scatterplot, i.e. the more q values which are overlaid on top of one another, means more q values satisfy `condition_2` for a given value of v and s in that projection.

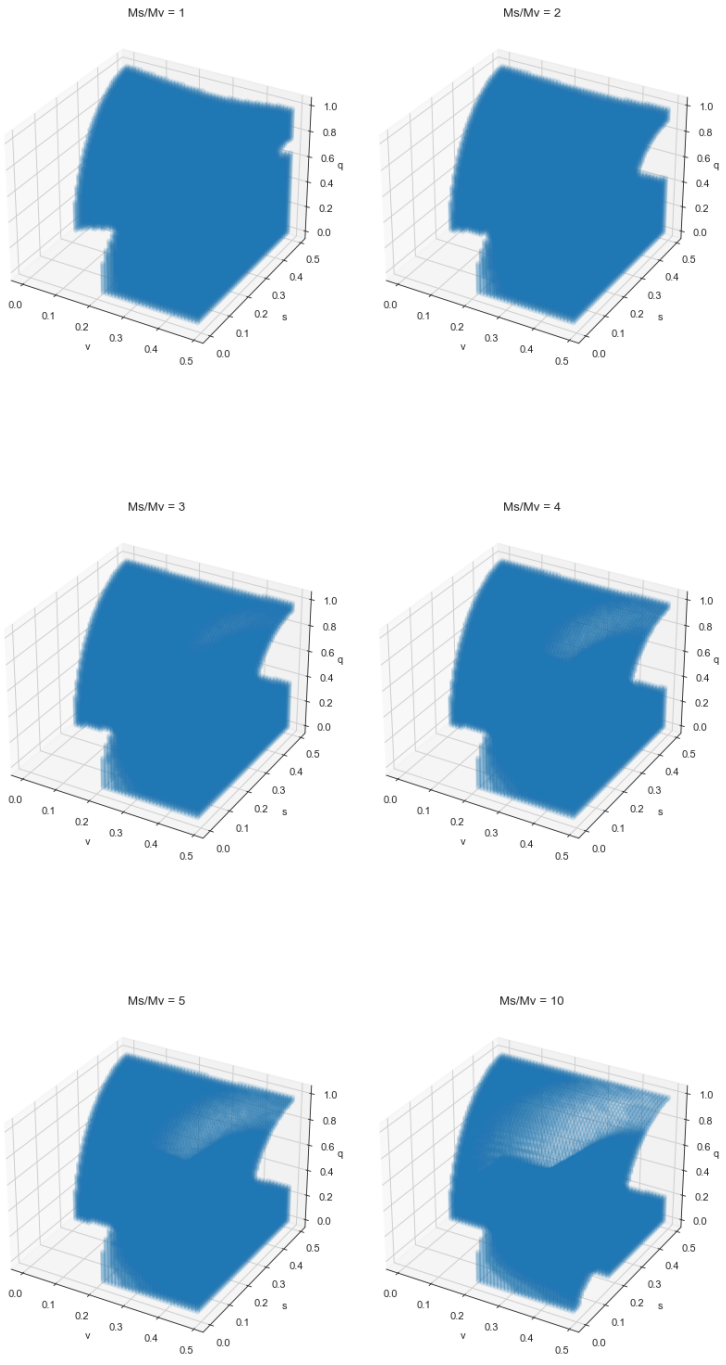
Ms/Mv = 1
Ms/Mv = 2
Ms/Mv = 3
Ms/Mv = 4
Ms/Mv = 5
Ms/Mv = 10
q
v
s

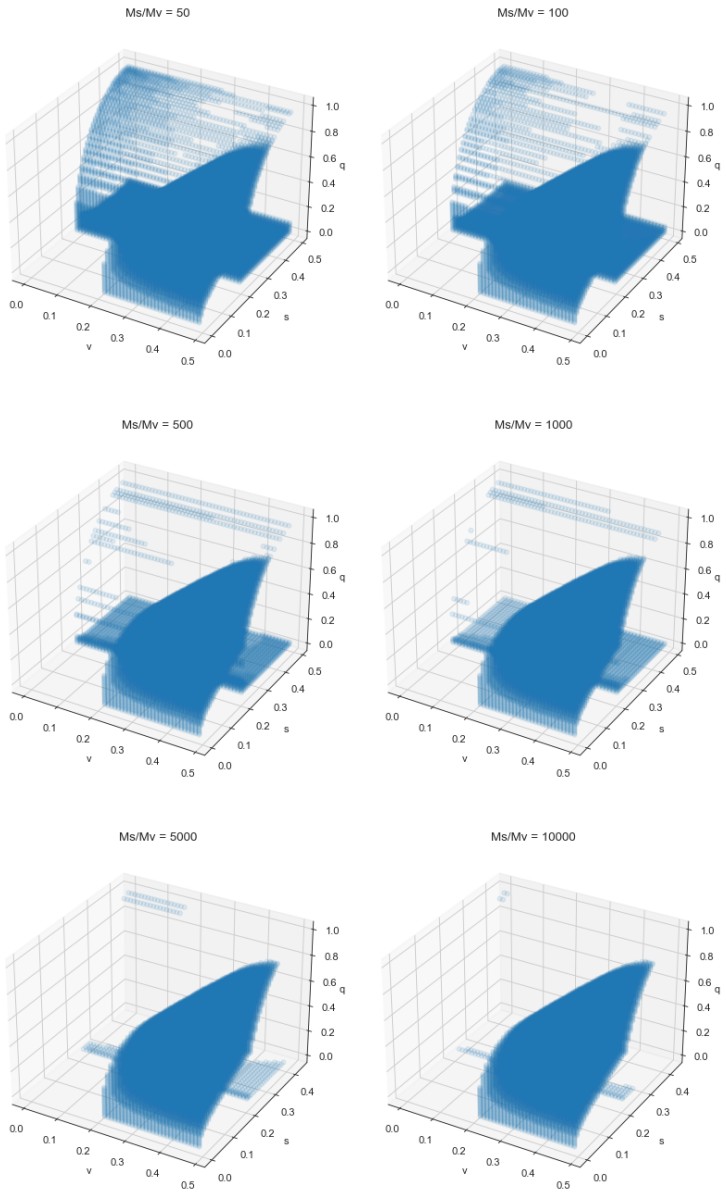

Figure 3.2: 3D Scatter Plots visualising the parameter search for the second Turing instability condition. x-axis is v in the range $0 \leq v \leq 0.5$, y-axis is s in the range $0 \leq s \leq 0.5$. z-axis is q in the range $0 \leq q \leq 2\pi$. $M_s/M_v = \{1, 2, 3, 4, 5, 10, 50, 100, 500, 1\,000, 5\,000, 10\,000\}$ plots are separated into individual sub-figures. The annihilation term was constant for all plots, $a = 0.5$

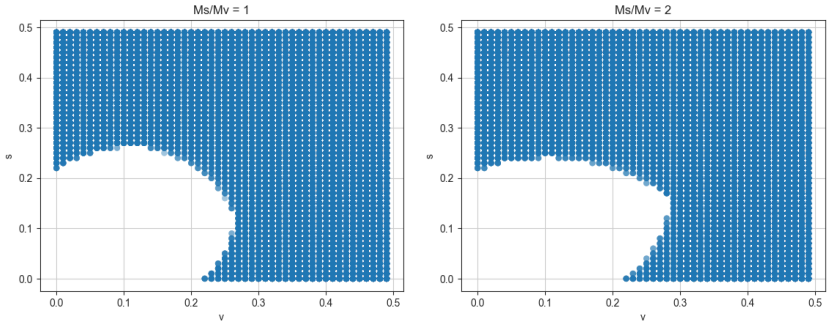
Ms/Mv = 1
Ms/Mv = 2
s
v
0.0
0.1
0.2
0.3
0.4
0.5

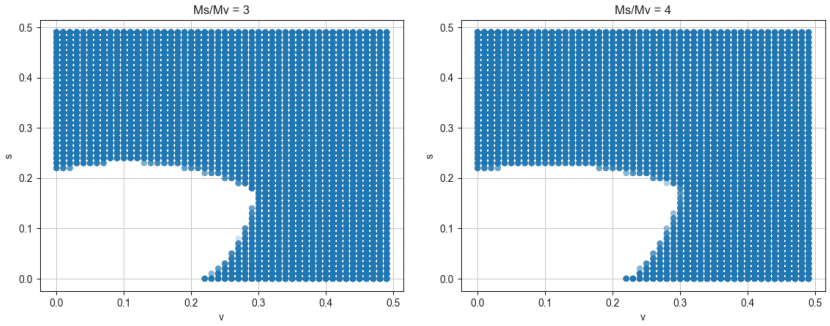
Ms/Mv = 3
Ms/Mv = 4
s
v
0.0
0.1
0.2
0.3
0.4
0.5

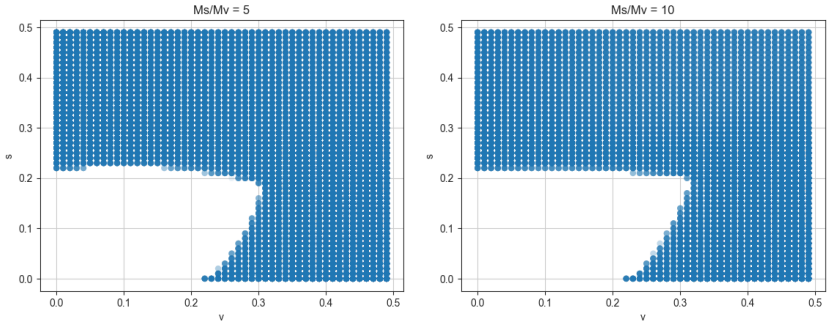
Ms/Mv = 5
Ms/Mv = 10
s
v
0.0
0.1
0.2
0.3
0.4
0.5

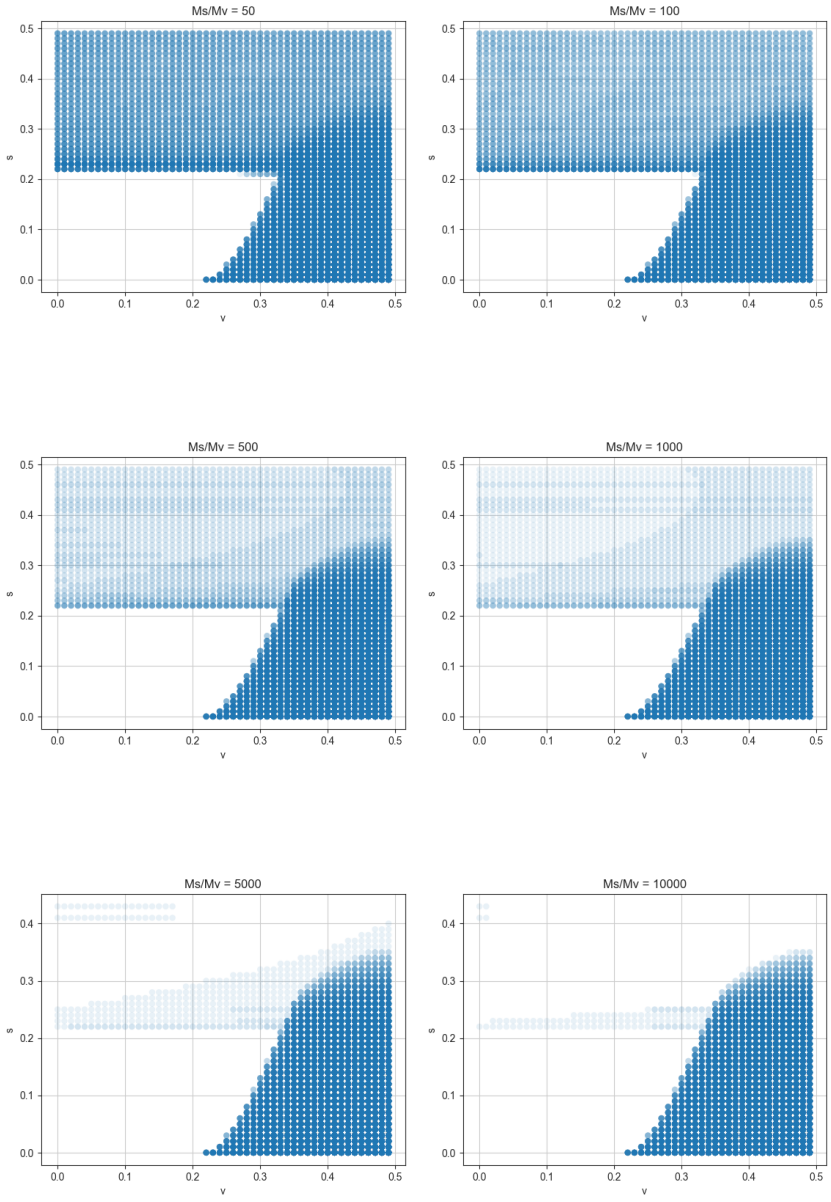

Figure 3.3: 2D Scatter Plots visualising the parameter search for the second Turing instability condition. x-axis is v in the range $0 \leq v \leq 0.5$, y-axis is s in the range $0 \leq s \leq 0.5$. q was varied in the range $0 \leq q \leq 2\pi$. $M_s/M_v = \{1, 2, 3, 4, 5, 10, 50, 100, 500, 1\,000, 5\,000, 10\,000\}$ plots are separated into individual sub-figures. The annihilation term was constant for all plots, $a = 0.5$

3.4.2 Plotting $det(\mathbf{A_q})$ vs Q

During a cascade, the self-interstitial atoms diffuse away much faster than the vacancies, represented by $M_s \gg M_v$. This typically leads to a "halo" of self-interstitial atoms surrounding a high-density vacancy region [48]. This behaviour can be represented by setting $\bar{v} = 0.25$ and $\bar{s} = 0.01$. As can be seen in the 2D and 3D scatter plots of Figures 3.3 and 3.2, this choice of $\bar{v}$ and $\bar{s}$ has the possibility of leading to a Turing instability. Created using the Python code in Appendix A.4, and having changed the units of the x-axis to be q^2 rather than q ($Q \equiv q^2$) to represent a 4th order polynomial rather than an 8th order polynomial, Figure 3.4 shows the $det(\mathbf{A_q})$ vs Q for mobility ratios, $M_s/M_v = \{1,\ 2,\ 3,\ 4,\ 5,\ 10,\ 50,\ 100,\ 500,\ 1\,000,\ 5\,000,\ 10\,000\}$.

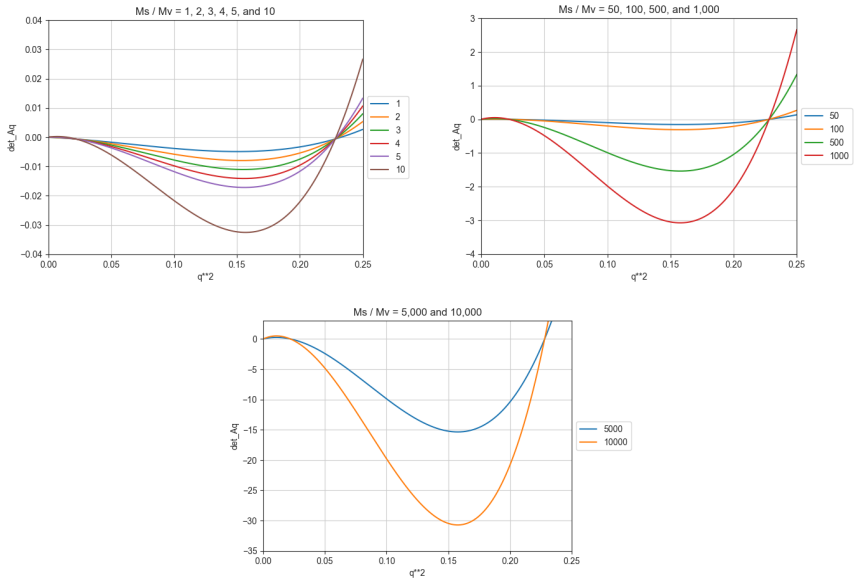

Figure 3.4: Plots of $det(\mathbf{A_q})$ vs Q for varying choices of M_s/M_v.

The plots in Figure 3.4 show that as the mobility ratio M_s/M_v increases, the magnitude of $det(\mathbf{A_q})$ increases, deepening the instability.

From inspection of the determinant, $det(\mathbf{A_q})$, in Equation 3.34, and its visualisation in Figure 3.4, I will make a few observations about its behaviour in relation to the system.

Firstly, the wavenumber, q, is inverse to real space, so as $q \to 0$ and $det(\mathbf{A_q}) \to 0$, this

corresponds to the complete decomposition of the system into void and un-defected crystal phases at large distances. This is also seen in the $det(\mathbf{A_q})$ passing through $q = 0$. This reflects the conservation of the vacancies and the self-interstitial atoms within the system; at vast distances, the vacancies and the self-interstitial atoms would completely decompose into a single void and an un-defected crystal. This would be the realisation of the standard coarsening behaviour of Ostwald ripening. This would be expected without the creation term, c, and the annihilation term, $-asv$.

Secondly, $q > 2\pi$ is also not physically interesting since it corresponds to a wavelength of patterns less than the interface width.

3.4.3 Plotting the eigenvalue of $\mathbf{A_q}$ vs Q

Using the Python code in Appendix A.5, the maximum eigenvalue of $\mathbf{A_q}$ for $0 \leq Q \leq 2\pi$ can be found given the parameters $M_s/M_v = \{1, 2, 3, 4, 5, 10, 50, 100, 500, 1\,000, 5\,000, 10\,000\}$, $s = 0.01$, $v = 0.25$, and $a = 0.5$. The results are plotted in Figure 3.5.

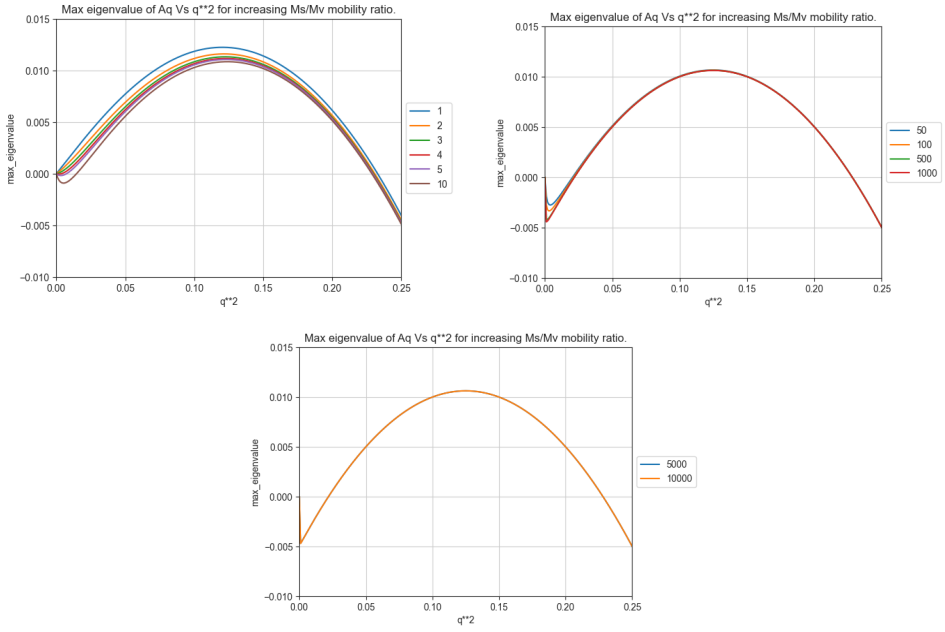

Figure 3.5: Max eigenvalue of $\mathbf{A_q}$ vs Q for varying choices of M_s/M_v.

Inspecting the plots in Figure 3.5, the maximum, most unstable eigenvalue occurs at the turning point of the line, which in Figure 3.5 occurs at approximately $Q \approx 0.125$. Because $Q \equiv q^2$, this means a wavenumber of approximately $q \approx 0.35$ — for this choice of parameters.

3.4.4 Periodicity

The periodicity of the pattern, Λ, can be calculated using Equation 3.35:

$$\Lambda = \frac{2\pi}{\left(Q/\sqrt{2}\right)} \tag{3.35}$$

where Q is the largest root of $\frac{d\left(det(\mathbf{A_q})\right)}{dQ} = 0$, which for $Q \approx 0.125$, corresponds to a pattern period of $\Lambda \approx 25.13$.

Because the interface width was set to be $\gamma_s = \gamma_v = 1$, the pattern period of the lattice is approximately 25 times the interface width of the phase-field model. Suppose I assume that the simulation's interface width is four crystal lattice spacings of a real-world material. This corresponds to a period pattern of about 100 crystal lattice spacings of a real-world material. The interface width is an effective value chosen to appropriately balance the bulk and interface terms in the free energy equation, Equation 3.4. These numbers do not necessarily need to correspond precisely to the size of the physical interface at the void surface in this nondimensionalised and minimalistic model, however, a periodic pattern of approximately 100 crystal lattice spacings of the underlying crystal lattice is consistent with experimentally observed void superlattices [66, 67].

The $M_s = M_v = 1$ system has a positive eigenvalue across the entire range of wavenumbers, which would create a negative $det(\mathbf{A_q})$, including $q = 0$. This means the system is unstable to complete decomposition rather than the finite band of wavenumbers characteristic of a Turing instability.

3.5 Descartes's Rule of Signs

$\bar{v} = 0.25$ and $\bar{s} = 0.01$ were chosen as reasonable examples, but inspecting the 3D and 2D regions in Figures 3.2 and 3.3, it can be seen that the instability regions are not particularly restrictive. This can be shown using Descartes's rule of signs [2] which is a fundamental algebraic tool for analysing the real roots of polynomial equations by counting the sign changes in the coefficients of a polynomial to provide valuable insights into the number of positive and negative real roots. I can use Descartes's rule of signs to investigate the roots because Equation 3.34 is a 4th-order polynomial in Q. Descartes's rule of signs states that a 4th-order polynomial equation has two positive roots — and hence looks like the plot of the $det(\mathbf{A_q})$ in Figure 3.4 — when two conditions are met: the discriminant is positive, and there are two sign changes between two successive terms in the polynomial. In the 4th-order polynomial equation, Equation 3.34, the first coefficient is always positive, meaning the first term is always positive; this means that the last coefficient, and therefore the last term, must also be positive. The coefficients of either the second or the third terms must be negative to make either of the second or the third terms negative and, therefore, create the two sign changes required.

The discriminant of a 4th-order polynomial equation:

$$ax^4 + bx^3 + cx^2 + dx^1 + e = 0 \tag{3.36}$$

is given by [192]:

[2] Developed by the French philosopher and mathematician René Descartes in their work "La Géométri" in 1637 [191].

$$\begin{aligned} discriminant = {} & 256a^3e^3 - 192a^2bde^2 - 128a^2c^2e^2 + 144a^2cd^2e \\ & - 27a^2d^4 + 144ab^2ce^2 - 6ab^2d^2e - 80abc^2de \\ & - 18abcd^3 + 16ac^4e - 4ac^3d^2 - 27b^4e^2 \\ & + 18b^3cde - 4b^3d^3 - 4b^2c^3e + b^2c^2d^2 \end{aligned} \tag{3.37}$$

where a, b, c, d, and e are the first through fifth coefficients.

Using the Python code in Appendix A.6, the parameter space of $M_v = 1$, $0 \leq M_s \leq 5$, $v = 0.01$, $s = 0.25$, $a = 0.5$, and $0 \leq q \leq 2\pi$ was searched through to calculate the discriminant of the $det(\mathbf{A_q})$, the sign changes of the four terms, and the number of sign changes within the four terms. This builds a DataFrame like Table 3.3.

M_v	M_s	v	s	a	q	Discriminant	Changes	# Changes
1	0.001	0.25	0.01	0.5	0.1	7.636373e-33	$(+,+,+,-)$	1
1	0.001	0.25	0.01	0.5	0.2	3.127859e-29	$(+,+,+,-)$	1
1	0.001	0.25	0.01	0.5	0.3	4.058282e-27	$(+,+,+,-)$	1
1	0.001	0.25	0.01	0.5	0.4	1.281171e-25	$(+,+,+,-)$	1
1	0.001	0.25	0.01	0.5	0.5	1.864349e-24	$(+,+,+,-)$	1

Table 3.3: DataFrame `.head()` of the parameter search for Descartes's Rule of Signs.

For the parameter values of $\bar{s} = 0.01$ and $\bar{v} = 0.25$, the last term in the determinant equation, Equation 3.34 becomes positive, i.e. the sign flip occurs in either the second or the third term, and Descartes's rule of signs can be satisfied when $M_s/M_v > 3.322$. For mobility ratios $M_s/M_v < 3.322$, as $q \to 0$, the determinant decreases and eventually becomes negative. This means the sub-threshold system, unlike the post-threshold system, is unstable to complete decomposition and will evolve in the standard way via Ostwald ripening.

3.6 Chapter Discussion

Alan Turing proposed a mechanism in which pattern formation arises in reaction–diffusion systems when a competition exists between the smoothing effect of diffusion and the amplifying effect of non-linear reaction terms. This occurs when the concentration species exhibit sufficiently different diffusivities. Under irradiation, similar conditions can arise in a solid-state system due to irradiation-driven deviations from equilibrium and the stark differences in the mobilities of vacancies and self-interstitial atoms. Based on this, I hypothesised that a void superlattice could form as a result of an instability driven purely by differences in defect mobilities and Cahn–Hilliard-type diffusion, without the need for external periodic drivers or additional complexity in defect kinetics such as advection terms describing driving forces (the elastic interactions between established voids or the anisotropic mobility of the self-interstitial atoms). The only necessary condition would be a disparity in defect mobilities.

This study builds upon classical reaction–diffusion models, yet differs in key ways. The model is not a Fokker-Planck diffusion system, which is sometimes used to describe defect migration in spatially varying potential fields such as elastic energy landscapes, nor is it based on externally imposed concentration gradients or directionality. Instead, the pattern formation is an emergent phenomenon driven by the intrinsic properties of the diffusion of the vacancy and self-interstitial atom defects, coupled only through a simple annihilation term. This fundamental distinction underpins the core claim of this work: instabilities and self-organising patterns can arise in irradiated materials purely due to diffusion differences, without the need for complex external forces or additional kinetic effects.

3.6.1 Key Theoretical Findings

In Section 3.2, I developed a nondimensionalised phase-field model based on a coupled pair of Cahn-Hilliard equations (Equations 3.6). This approach represents a significant simplification of the more commonly used rate-equation models, such as the Bullough-Eyre-Krishan (BEK) rate equations [97]. In the BEK model, the defect kinetics are

typically described by a system of coupled equations incorporating Fickian diffusion, defect production and annihilation, and explicit sink interactions. However, a key finding in this study is that pattern formation is possible even when these terms are simplified to their most basic forms, and, in the absence of additional terms such as sink interactions.

The simplification arises due to two key modifications:

1. The Cahn-Hilliard equations extend the standard Fickian diffusion used in BEK models by introducing a fourth-order diffusion term, allowing for spatial inhomogeneity to be dynamically preserved rather than homogenised.
2. The interaction between vacancies and self-interstitials is captured only through a simple annihilation term, $-asv$, rather than a more complex set of interaction terms.

Despite these simplifications, the system still exhibits a well-defined instability that drives pattern formation. This demonstrates that superlattice formation does not depend on the full complexity of defect kinetics but can instead emerge from mobility differences and conservative diffusion alone.

This minimal framework contrasts not only with traditional rate-theory models like the BEK rate equations but also with hybrid approaches such as those by Y. Gao et al. and Y. Zhang et al. [138, 143, 144]. Their model couples a Cahn-Hilliard equation for vacancies with a Fickian diffusion equation for self-interstitial atoms and incorporates anisotropic mobility to select lattice symmetry. By contrast, the present model uses Cahn-Hilliard dynamics for both species, isotropic diffusion, and minimal reaction terms. The results that follow in Chapter 5 show that such simplification is sufficient to capture both instability and pattern formation.

3.6.2 Stability Analysis and Conditions for Pattern Formation

In Section 3.3, I applied a linear stability analysis following the derivation of M. Cross and H. Greenside [2] to identify the necessary conditions for a Turing instability. By

linearising the system around a homogeneous base state $\bar{s}(\mathbf{x}, t)$ and $\bar{v}(\mathbf{x}, t)$ (Equation 3.11), I determined the form of perturbations that could grow over time. This led to the construction of the stability matrix $\mathbf{A_q}$ (Equation 3.28) and the derivation of its trace and determinant (Equations 3.33 and 3.34).

Through inspection of the $tr(\mathbf{A_q})$–$det(\mathbf{A_q})$ plane visualised in Figure 3.1, and Equations 3.33 and 3.34, because the $tr(\mathbf{A_q})$ is always negative for my model, a sufficient condition for instability is that $det(\mathbf{A_q}) < 0$.

3.6.3 Parameter Space Exploration and Implications

Section 3.4 extends this theoretical analysis by numerically evaluating the determinant across a broad parameter space. I investigated how the stability conditions varied with parameters M_v, M_s, v, s, a, and q, showing that Turing instabilities can emerge under specific conditions. The 3D and 2D visualisations in Figures 3.2 and 3.3 illustrate how the instability region evolves as the mobility ratio M_s/M_v changes.

Furthermore, in Section 3.5, I applied Descartes' Rule of Signs to analyse the determinant $det(\mathbf{A_q})$, which is a fourth-order polynomial in q^2. This revealed the number of possible positive real roots, indicating the number of unstable wavenumbers that could grow over time. Along with evaluating the polynomial discriminant, I determined that the threshold mobility ratio required to drive pattern formation is $M_s/M_v = 3.322$. This provides a concrete predictive criterion for when Turing instabilities should occur in an irradiated material.

3.6.4 Broader Implications and Next Steps

The identification of a Turing instability as a potential mechanism for void superlattice formation is significant. It suggests that complex spatial ordering in irradiated materials may emerge not due to external driving fields or imposed directionality of the concentration gradients, but comes intrinsically from defect diffusion dynamics. If validated, this provides a new theoretical framework for understanding self-assembled patterns in radiation damage systems.

However, a key limitation of the current approach is that the linear stability analysis only predicts the onset of instability. It does not determine the long-term evolution of the defect structures. While the results suggest that an instability should drive pattern formation, they do not reveal whether the patterns remain stable, undergo coarsening, or break down into a different steady-state structure.

To address this, it is necessary to move beyond the linear analysis and numerically integrate the full set of governing equations over time. This will allow for an exploration of the non-linear post-bifurcation regime, where the long-term behaviour of the system emerges.

3.6.5 Transition to MOOSE Simulations

To perform this next stage of investigation, I will use the Multiphysics Object-Oriented Simulation Environment (MOOSE), an open source finite element framework designed for solving complex coupled partial differential equations. MOOSE provides a robust framework for time-dependent simulations, including the implicit backward Euler method, which is particularly well-suited for stiff systems like the Cahn-Hilliard equations. By implementing the phase-field model in MOOSE, I will be able to:

1. Track the evolution of the defect concentrations over time.
2. Determine whether a stable superlattice forms or if coarsening effects disrupt the pattern.
3. Investigate the non-linear interactions that shape the final steady-state structure.

This transition marks the next step in the study, enabling validation of whether the predicted instabilities can evolve into experimentally consistent superlattice structures over time.

Chapter 4

MOOSE Implementation and Simulation Setup

4.1 Introduction

The formation and evolution of void superlattices in reaction–diffusion systems presents a complex challenge due to the non-linear phase separation dynamics of vacancies and self-intertitial atoms and the large differences between their mobilities. In Chapter 3, a theoretical framework was developed using coupled Cahn-Hilliard partial differential equations (PDE) to model this behaviour, and a linear stability analysis was conducted to predict the conditions under which void superlattices would emerge. The analysis, detailed in Sections 3.3, 3.4, and 3.5, established a critical mobility ratio threshold of $M_s/M_v = 3.322$ and a predicted superlattice periodicity of 25.13 units for the parameter values of $M_s = 1\,000$, $M_v = 1$, $\gamma_s = \gamma_v = 1$, $\bar{s} = 0.01$, $\bar{v} = 0.125$, $a = 0.5$, and $c = 0.00125$. The theoretical approach followed the methodology outlined in *Pattern Formation and Dynamics in Nonequilibrium Systems* by M. Cross and H. Greenside [2].

However, as raised by K. Krishan [62], linear stability analysis provides insight only

into the onset of instability, leaving the post-bifurcation regime unexplored, where non-linearity becomes dominant. In this regime, voids must not only form but also persist, coarsen, and self-organise into an ordered void superlattice. A significant challenge in modeling this behaviour lies in the drastically different time and space scales required for the two separate behaviours the coupled Cahn-Hilliard model is capturing. The equations are stiff, 4th-order partial differential equations made more complex with the associated constant creation and concentration-dependent annihilation terms. The nature of the Cahn-Hilliard equation is to capture both a rapid phase separation on a tiny spatial scale and a gradual coarsening on a large spatial scale, the former driving the fast-changing thin interface between the phases and the latter causing the gradual bulk phase separation [193, 194]. Combined, the Cahn-Hilliard equation has historically been complicated to model.

To address these challenges, simulations were performed using the Multiphysics Object-Oriented Simulation Environment (MOOSE) [98, 100–102]. MOOSE is an open source finite element modelling framework capable of massive parallelisation and great flexibility with its ability to swap in and combine many different numerical methods and pieces of physics. MOOSE was used to numerically solve the coupled pair of Cahn-Hilliard partial differential equations using the implicit method of backward Euler time integration via the second-order backward differentiation scheme. The second-order scheme was used because the Cahn-Hilliard equation is a fourth-order partial differential equation and can't be solved with standard first-order elements. The backward Euler time integration method produces linear and non-linear equations at each time step. The underlying solver of MOOSE is PETSc [195, 196]. MOOSE has implemented three methods via PETSc to handle the solving of these non-linear equations: the Newton–Raphson method (Newton's method), the Jacobian Free Newton Krylov method (JFNK), or the preconditioned JFNK method [197]. The Newton method was selected to solve the non-linear partial differential equations. For the linear equations required to invert the Jacobian matrix, the methods chosen were the Additive Schwartz Method (ASM) and Lower-Upper (LU) decomposition, as was recommended in the MOOSE documentation [197].

Simulations were initially conducted in a 2D domain with periodic boundary conditions. 3D simulations are possible as the instability driven by the maximum eigenvalue depends only on the wavenumber $|\mathbf{q}|$, which is dimensionally independent, however 3D simulations present significant computational overhead.

The simulations were run on a Google Cloud Platform (GCP) `n2-standard-128` virtual machine. This machine type has 128 vCPU (64 cores) and 512 GB memory. The time taken for the simulations to complete depended on the complexity of the simulation being run, but for 2D, generally scaled linearly, with the key driver being the size of the simulation domain. 50×50 domain simulations completed in approximately 10–20 minutes, 100×100 in approximately an hour, 200×200 in approximately 3–5 hours, 300×300 in approximately a day, and 400×400 in approximately 3–5 days.

This chapter serves as a step-by-step guide to the MOOSE implementation, ensuring reproducibility, and providing context for the simulation results and quantitative analyses presented in Chapter 5.

4.2 Phase-Field Simulations with MOOSE

4.2.1 Environment Setup and Installing MOOSE

GCP Environment

I ran the simulations on a GCP virtual machine (VM). The machine was configured using the GCP console via the user interface (UI) as follows:

Region and zone: The region was set to `europe-west3 (Frankfurt)` and the zone was set to `europe-west3-c`.

Machine configuration: A standard `n2-standard-128` machine was selected. It comes with 128 vCPU (64 core) and 512 GB memory.

Image: The operating system was `Ubuntu` and the version was `Ubuntu 20.04 LTS`.

Disk: A balanced persistent disk of `1 000 GB` was selected.

To tunnel into the VM, the following `gcloud` command was used:

```
gcloud compute ssh --zone "europe-west3-c" "mwn-moose" ...
... --tunnel-through-iap --project "matt-world"
```

`conda` MOOSE Environment

To set up MOOSE on the VM, I followed the documentation on the `https://mooseframework.inl.gov/getting_started/installation/conda.html` website [198].

MOOSE uses `conda` and `mambaforge` to manage the package library of its applications. In Linux, `mambaforge` can be installed with the following command:

```
curl -L -O https://github.com/conda-forge/miniforge/releases/ ...
... /latest/download/Mambaforge-Linux-x86_64.sh

bash Mambaforge-Linux-x86_64.sh -b -p ~/mambaforge3
```

Once installed in the home directory of the VM, I exported the system path, initialised `mamba`, and closed the terminal:

```
export PATH=$HOME/mambaforge3/bin:$PATHCopy

mamba init

exit

exit
```

Upon logging back into the VM — and assuming it was successful — the new prompt was pre-fixed with `(base)`:

```
(base) mwn-moose:~$
```

Finally, to access the INL `conda` package library, I added the INL public channel to the `conda` config file:

```
conda config --add channels https://conda.software.inl.gov/public
```

Install and `git clone` MOOSE

To install MOOSE, I used `conda` to create a new application environment and install the package libraries necessary for application development. Once completed, I activated the new MOOSE environment; this changed the terminal prompt from a pre-fixed `(base)` to a pre-fixed `(moose)`.

```
mamba create -n moose moose-dev

mamba activate moose
```

MOOSE is an open source software hosted on GitHub; the codebase is available here: `https://github.com/idaholab/moose`. I created a new directory called `projects` to house the MOOSE application, used `git clone` to download a copy of the MOOSE codebase into that directory, navigated to that new `moose` directory, and changed to the `master` branch:

```
mkdir projects

cd ~/projects/

git clone https://github.com/idaholab/moose.git

cd ~/projects/moose/

git checkout master
```

To build and test the MOOSE installation, I navigated to the `projects/moose/test` directory, performed a `make -j 10` — where the number given to the `-jobs` flag is the number of parallel processes one wishes to perform — and then executed the `run_tests` bash script:

```
cd ~/projects/moose/test/

make -j 10

./run_tests -j 10
```

Creating a New Application

To set up a new application for my phase-field modelling, I followed the documentation on the `https://mooseframework.inl.gov/getting_started/new_users.html` website [199].

Creating a new application is handled by the bash script `./moose/scripts/stork.sh`. To avoid path errors, it is advised to execute the `./projects/moose/scripts/stork.sh` bash script from within the parent `/projects/` directory, not the child `/moose/` directory.

```
cd ~/projects/

./moose/scripts/stork.sh void_lattices
```

I added the MOOSE physics modules of interest to the new application by selecting `yes` against the appropriate line item in the `/projects/void_lattices/Makefile` using `nano`. For ease, I selected `yes` to `ALL_MODULES`:

```
################################### MODULES
# To use certain physics included with MOOSE, set variables below to
# yes as needed. Or set ALL_MODULES to yes to turn on everything (overrides
# other set variables).

ALL_MODULES              := yes

CHEMICAL_REACTIONS       := no
CONTACT                  := no
ELECTROMAGNETICS         := no
EXTERNAL_PETSC_SOLVER    := no
FLUID_PROPERTIES         := no
FSI                      := no
FUNCTIONAL_EXPANSION_TOOLS := no
GEOCHEMISTRY             := no
HEAT_CONDUCTION          := no
LEVEL_SET                := no
MISC                     := no
NAVIER_STOKES            := no
OPTIMIZATION             := no
PERIDYNAMICS             := no
PHASE_FIELD              := no
POROUS_FLOW              := no
RAY_TRACING              := no
REACTOR                  := no
RDG                      := no
RICHARDS                 := no
STOCHASTIC_TOOLS         := no
THERMAL_HYDRAULICS       := no
TENSOR_MECHANICS         := no
XFEM                     := no

include $(MOOSE_DIR)/modules/modules.mk
#####################################
```

I compiled and tested the new `void_lattices` application in the same way I compiled and tested the `moose` application:

```
cd ~/projects/void_lattices/

make -j 10

./run_tests -j 10
```

4.2.2 Defining the Configuration File

With MOOSE installed, the new application created, and both being compiled, the next step was to make the config file that will define the MOOSE simulation to be run. In the following sections, I will describe each block within the config file.

Mesh

The `Mesh` module handles defining the simulation box. The `GeneratedMeshGenerator` class is the built-in MOOSE mesh generator; it allows a square simulation box to be created. The `nx` and `ny` parameters define the number of elements in the x and y directions, respectively. The `xmax` and `ymax` parameters define the points on the grid in the x and y directions, respectively. The below code example represents a 200×200 domain box discretised into a 400×400 grid of points. The `dim` parameter is the dimensions of the simulation; I have selected `2` because the simulation box I wanted to create is a 2D square [200, 201].

```
[Mesh]
  [./Square]
    type = GeneratedMeshGenerator
    nx = 400
    ny = 400
    xmax = 200
    ymax = 200
    dim = 2
  [../]
[]
```

BCs

The `BCs` system defines the boundary conditions of the simulation box. The `./Periodic` system is used for periodic boundary conditions; this loops around the left and right boundaries and the top and bottom boundaries, respectively, creating a quasi-infinite domain. The `./all` method is a catch-all for all variables tracked within the simulation box. The `./auto_direction` parameter explicitly sets the `x` and `y` axes of the simulation [202, 203].

```
[BCs]
  [./Periodic]
    [./all]
      auto_direction = 'x y'
    [../]
  [../]
[]
```

Modules

The `Modules` system is community-developed; they allow the type of finite element simulation to be defined. They encapsulate commonly re-used code pieces to define the kernels, boundary conditions, etc. [204] I have chosen a conserved variable

phase-field module by selecting the `[./PhaseField] [./Conserved]`, this uses the `ConservedAction` class [205, 206].

The variables of s and v are defined in `./s` and `./v` blocks, where the `s` and `v` parameters are the concentrations of self-interstitial atoms and vacancies, respectively.

The `solve_type` parameter defines the method of solving the coupled pair of Cahn-Hilliard partial differential equations. I have used `forward_split`, which adds the time derivative of the conserved variable `s` corresponding to $\frac{\partial s}{\partial t}$ [207], and the derivative of the free energy with respect to the coupled variable, which corresponds to $\frac{\partial F}{\partial v}$ [208]. The two Cahn-Hilliard equations are discretised using first-order elements by splitting the 4th-order equations into two 2nd-order equations, as described by L. Zhang et al. [209]. This is the purpose of `forward_split`. The `./v` block will pair the opposite for the vacancies.

The `free_energy` parameter is the variable name of the free energy function defined in the free energy material. This is referenced as `F`, and it is defined later in the `Materials` code block under `./fbulk`. The `kappa` parameter is the gradient energy coefficient used in the phase-field model; it is referenced here and is defined later in the `Materials` code block under `./constants`. The `mobility` parameter is the mobility of the concentration variables used in the phase-field model, one for self-interstitial atoms, `Ms`, and another for vacancies `Mv`; they are referenced here and defined later in the `Materials` code block under `./constants`. The `coupled_variables` parameter is the coupled concentration variable used in the phase-field model. This allows `s` to be coupled to `v` and vice-versa; they are referenced here and defined later in the `Materials` code block under `./gen_mask`.

```
[Modules]
  [./PhaseField]
    [./Conserved]
      [./s]
        solve_type = forward_split
        free_energy = F
        kappa = kappa
        mobility = Ms
        coupled_variables = v
      [../]
      [./v]
        solve_type = forward_split
        free_energy = F
        kappa = kappa
        mobility = Mv
        coupled_variables = s
      [../]
    [../]
  [../]
[]
```

`ICs`

The `ICs` system handles the initial conditions of the simulation box. The `./v_IC` and `./s_IC` code blocks handle the vacancies and the self-interstitial atoms, respectively. I use the `RandomIC` class to define a random uniform distribution in the $0.2475 \leq v \leq 0.2525$ and $0.0099 \leq s \leq 0.0101$ ranges, which corresponds to the base states of $\bar{v} = 0.25 \pm 1\%$ and $\bar{s} = 0.01 \pm 1\%$. The `seed` parameter allows for reproducibility by fixing the random seed of the `RandomIC` class [210, 211].

```
[ICs]
  [./v_IC]
    type = RandomIC
    seed = 123
    max = 0.2525
    min = 0.2475
    variable = v
  [../]
  [./s_IC]
    type = RandomIC
    seed = 69
    max = 0.0101
    min = 0.0099
    variable = s
  [../]
[]
```

A second input block was developed for experiments 5, 6, and 7 to create a pre-existing void population. It uses the `MultiSmoothCircleIC` class. The `variable` parameter defines the variable that will be created as a pre-existing population of smooth, randomly distributed circles. The `invalue` and `outvalue` parameters are the values of the variable inside and outside of the generated circles, respectively. When randomly placed in the simulation box, the `bubspac` parameter is the minimum center-to-center distance between the circles. The `numbub` parameter is the number of circles to be placed. The `radius` parameter is the radius of the circles to be placed. The `int_width` parameter is the interface width between the inside and outside of the circle, i.e., the boundary between the void and the rest of the domain. The `rand_seed` parameter is the random seed of the `MultiSmoothCircleIC` class; setting this allows for reproducibility. The `radius_variation` parameter is used to establish a percentage variation of the circle radius; for example, if I wanted to change the radii of the circles to be $\pm 20\%$, then I would state `radius_variation = 0.2`. The `radius_variation_type` parameter defines the type of the random distribution used when randomising the circle radii [212].

The two blocks `[ICs] [./v_IC]` and `[ICs] [./s_IC]`, control the initial conditions of the vacancies and the self-interstitial atoms, respectively. Working together, they create a pre-existing vacancy population and self-interstitial atom circles. By setting the same value of the **`rand_seed`** parameter for each block but differing the **`invalue`** and **`outvalue`** values, the pre-existing random distribution of voids will be mirrored by a pre-existing random distribution of self-interstitial atom "holes".

```
[ICs]
  [./v_IC]
    type = MultiSmoothCircleIC
    variable = v
    invalue = 1.0
    outvalue = 0.034
    bubspac = 15.0
    numbub = 35
    radius = 5.9
    int_width = 1.0
    rand_seed = 111
    radius_variation = 0
    radius_variation_type = normal
  [../]
  [./s_IC]
    type = MultiSmoothCircleIC
    variable = s
    invalue = 0.00688
    outvalue = 0.00692
    bubspac = 15.0
    numbub = 35
    radius = 5.9
    int_width = 1.0
    rand_seed = 111
    radius_variation = 0
    radius_variation_type = normal
  [../]
[]
```

`Materials`

The `Materials` system allows the simulation's space-varying variables — what MOOSE calls "properties" — to be defined on-demand. The properties can be accessed and used by other code blocks in the simulation, such as `Kernels` to define the physics applied to a variable, `PostProcessors` to create metrics of the variables at a given timestep, or other `Materials` themselves via self-referencing. Additionally, the properties are designed to be directly coupled to the simulation variables, allowing the actual non-linear behaviour of the phase-field model to be captured [213].

The `./constants` code block defines the fixed value parameters via the `GenericConstantMaterial` class. The interface width, γ, is represented by `kappa` and set to 1. The mobilities of the self-interstitial atoms and vacancies, M_s and M_v, are represented by `Ms` and `Mv`, respectively. In this example, $M_s = 1\,000$ and $M_v = 1$. The annihilation rate, a, is represented by `a` and $a = -0.5$ [214].

The annihilation rate a coupling to the self-interstitial atom concentration, s and the vacancy concentration, v, is handled by the `./annihilation_for_s` and `./annihilation_for_v` code-blocks, respectively. The `DerivativeParsedMaterial` class allows for symbolic differentiation of the formula passed as the `expression` parameter. The `material_property_names` parameter will enable me to specify the material property to be acted upon by the given code block. The `coupled_variables` parameter sets what the material property being acted upon is coupled to. The `property_name` parameter is the name of the new property created; this is the referenceable variable by other systems [215].

The simple double-well free energy potential which drives the separation of the system into voids and areas of high self-interstitial atom concentration, $F = v^2\left(1-v\right)^2 + s^2\left(1-s\right)^2$, is defined in `./f_bulk`.

The `./creation_mask` code block represents the vacancy-only portion of F. It is coupled with the creation term defined in `[Kernels] [./s_creation]` and `[Kernels] [./v_creation]`.

```
[Materials]
  [./constants]
    type = GenericConstantMaterial
    prop_names = 'kappa Ms Mv a'
    prop_values = '1 1000 1 -0.5'
  [../]
  [./annihilation_for_s]
    type = DerivativeParsedMaterial
    material_property_names = 'a'
    coupled_variables = v
    property_name = av
    expression = 'a * v'
  [../]
  [./annihilation_for_v]
    type = DerivativeParsedMaterial
    material_property_names = 'a'
    coupled_variables = s
    property_name = as
    expression = 'a * s'
  [../]
  [./f_bulk]
    type = DerivativeParsedMaterial
    property_name = F
    expression = 's^2 * (1 - s)^2 + v^2 * (1 - v)^2'
    coupled_variables = 's v'
  [../]
  [./creation_mask]
    type = DerivativeParsedMaterial
    property_name = creation_mask
    expression = '(1 - v)^2'
    coupled_variables = 'v'
  [../]
[]
```

Kernels

The `Kernels` system handles the individual pieces of physics the spatial variables follow during the evolution of the simulation [216].

The creation rate of the self-interstitial atoms and the vacancies, c, is handled by the `./s_creation` and `./v_creation` code blocks, respectively. I used the `MaskedBodyForce` kernel, which implements a source term. It is limited to the `variable` and the `coupled_variables` parameters to which it is applied and the material property `creation_mask` via the `mask` parameter. The mask is defined in `[Materials] [./creation_mask]` — note that `[Materials] [./creation_mask] [property_name]` = `[Kernels] [./s_creation] [mask]` = `[Kernels] [./v_creation] [mask]`. The self-interstitial atom and vacancy concentrations' creation rate, c, was set to 0.00125 [217].

The annihilation rate of the self-interstitial atoms and the vacancies, $-asv$, is handled by the `./s_recombination` and `./v_recombination` code blocks, respectively. I used the `MatReaction` class here. It is similar to the `MaskedBodyForce` class in that it can be thought of as adding a source term (a negative source term in this case, as I am using it for annihilation). Still, the difference is, unlike the `MaskedBodyForce` class, `MatReaction` is not modified by a material mask. The `variable` parameter is the name of the variable the class operates on. The `args` parameter is the name of the variable that the class depends upon. The `mob_name` parameter defines the reaction rate used by the `MatReaction` class. The `mob_name = as` and `mob_name = av` parameters are defined in `[Materials] [./annihilation_for_v] [property_name]` and `[Materials] [./annihilation_for_s] [property_name]`, respectively. The anhilation rate is set to -0.5 in `[Materials] [./constants] [prop_names]` [218].

```
[Kernels]
  [./s_creation]
    type = MaskedBodyForce
    value = 1.25e-3
    variable = s
    mask = creation_mask
    coupled_variables = v
  [../]
  [./v_creation]
    type = MaskedBodyForce
    value = 1.25e-3
    variable = v
    mask = creation_mask
    coupled_variables = s
  [../]
  [./s_recombination]
    type = MatReaction
    variable = s
    args = v
    mob_name = av
  [../]
  [./v_recombination]
    type = MatReaction
    variable = v
    args = s
    mob_name = as
  [../]
[]
```

`Preconditioning` and `Executioner`

The `Executioner` system works alongside the `Preconditioning` system; together, they handle how the phase-field simulation will be numerically solved and how it will evolve by allowing the user to specify and configure different solving methods. The `Preconditioning` system allows the user to precisely define the preconditioning matrix used in the numerical solve and any manipulations that might be required to

said matrix for their given method(s) [196, 219].

PETSc — which stands for "Portable, Extensible Toolkit for Scientific Computation" — is the underlying numerical solver used by MOOSE; it was chosen because of its wide range of implemented linear and non-linear equation solvers. Its parameters can be configured via `petsc_options_iname` and `petsc_options_value` [195, 196].

The `Executioner` system uses the `Transient` class, the standard MOOSE executioner [220]. It will perform a single non-linear solve of the chosen `solve_type` (`NEWTON` in my case) and the chosen `scheme` (`bdf2` in my case) for each timestep of the simulation. It provides the ability to customise the solver further through the parameter values, the `./TimeStepper` system [221], and the `./Predictor` system [222].

The `NEWTON` system will use Newton's method [223] to solve the system of non-linear equations [197]. It requires a full Jacobian matrix, so I have explicitly stated this in the `Preconditioning` system. I have chosen `SMP`, which stands for "single matrix preconditioner"; SMP is the standard MOOSE preconditioner. SMP will build the preconditioning Jacobian matrix with the off-diagonal parts. By setting the `full` parameter to `true`, the complete set of couplings between all matrix variables will be created, i.e. the full off-diagonal Jacobian matrix will be produced as the Newton method requires. This is more concise than setting the parts individually [224]. The `scheme` specifies the type of time integration that the Newton method will use; here, `bdf2` is used. It stands for second-order backward differentiation, a standard method for numerically integrating stiff partial differential equations [225].

The `./TimeStepper` system handles the run time and the time steps of the `Transient` class. It was configured to run to an `end_time` of 50 000 [221]. To handle the stiff partial differential equations, MOOSE has a `IterationAdaptiveDT` class; this allows the time step to be increased or decreased based on the ability to converge the solution after a specified number of iterations, the `optimal_iterations` parameter. Initially, the time step `dt` parameter is set to be 0.1, and the solution will iterate 9 times to find a converged solution. If a solution can be found within these iterations, then the timestep will grow by 10%, this is the `growth_factor` parameter; if it cannot converge the system in that number of iterations, then the timestep will be reduced by 50%, this

is the `cutback_factor` parameter. The decision of the `IterationAdaptiveDT` class to increase or decrease the time step is governed by both the total number of the linear and non-linear iterations, which are the `l_max_its` and `nl_max_its` parameters, respectively. Here, I have adopted a general approach and only specified an `optimal_iterations` parameter. Because I have not set a value for the `iteration_window` parameter — the `iteration_window` parameter being the range over which the time step is kept constant — then I have set the `linear_iteration_ratio` parameter to be a large number as per the documentation [226]. These were all standard choices based on the MOOSE phase-field model examples in their documentation.

The PETSc parameters were configured with the parameters of the `petsc_options_iname` and `petsc_options_value`. The scaling of the system variables was configured with the `automatic_scaling` and `compute_scaling_once` parameters. The non-linear parameters of the solver were configured with `nl_rel_tol`, `nl_abs_tol`, and `nl_max_its`. The linear parameters of the solver were configured with `l_tol` and `l_max_its` [220].

The `petsc_options_iname` and `petsc_options_value` parameters allow the type of PETSc solver(s) to be chosen and configured.

The `automatic_scaling` parameter allows the variables to be scaled; this assists with convergence. It is used alongside the `compute_scaling_once` parameter. By setting `compute_scaling_once = false`, the scaling factor calculation will be performed at the beginning of each simulation time step.

The `nl_max_its` parameter is the maximum number of iterations that the non-linear solve is allowed to take, i.e. the number of attempts at solving the non-linear equations which are allowed before MOOSE will abandon that particular non-linear solve attempt, cut the timestep by the `cutback_factor`, and attempt the non-linear equation solve again. The `nl_rel_tol` parameter defines the relative tolerance allowed when solving the non-linear equations; this is the orders of magnitude the residual needs to be reduced before MOOSE will treat a particular solution as converged. The `nl_abs_tol` parameter is the absolute tolerance of the non-linear variables' value. It is similar to `nl_max_its`, but instead of abandoning the solve and trying again with

a smaller timestep when the value falls below this value, it will treat the solution as converged. This is useful at the end of the simulation as the system approaches a steady state and there is little change between the timesteps.

The `l_max_its` parameter is the maximum number of iterations that the linear solve is allowed to take, i.e. the number of linear iterations which are allowed before MOOSE believes the Jacobian inversion approximation is good enough, stops, and proceeds to solve the next non-linear iteration. The `l_tol` parameter, the linear variables' tolerance, is the number of orders of magnitude the residual for inverting the Jacobian matrix has to decrease from its initial value before MOOSE considers the solve converged.

The `petsc_options_iname` and `petsc_options_value` parameters implement the Additive Schwartz Method (ASM) via `-pc_type` and Lower-Upper decomposition (LU) via `-sub_pc_type`. LU is more accurate but computationally demanding and does not scale well with the number of processors. In contrast, ASM, whilst a good approach for most models, is the only approach that works well for phase-field simulations which use Cahn-Hilliard partial differential equations. These choices were selected after reading the MOOSE documentation detailing the solving of phase-field models [197].

The values of the `l_tol`, `l_max_its`, `nl_rel_tol`, `nl_abs_tol`, and `nl_max_its` parameters were chosen after trial and error. Together, they fine-tune the numerical solvers' ability to converge.

The `./Predictor` system implements the `SimplePredictor` class. It allows the system to make better predictions by using the solution to the system at the previous timestep as the initial guess for the non-linear solve of the proceeding time step. The `scale` parameter allows the user to scale this previous solution by the value given; here, I have selected 1 to use the last solution exactly as the initial guess for the proceeding non-linear iteration [222, 227].

```
[Executioner]
  type = Transient
  scheme = bdf2
  solve_type = NEWTON
  end_time = 50000
  [./TimeStepper]
    type = IterationAdaptiveDT
    dt = 0.1
    optimal_iterations = 9
    growth_factor = 1.1
    cutback_factor = 0.5
    linear_iteration_ratio = 1000
  [../]
  petsc_options_iname = '-pc_type -sub_pc_type -pc_asm_overlap'

  petsc_options_value = 'asm lu 2'
  l_tol = 1e-4
  l_max_its = 250
  nl_rel_tol = 1e-8
  nl_abs_tol = 1e-9
  nl_max_its = 12
  automatic_scaling = true
  compute_scaling_once = false
  [./Predictor]
    type = SimplePredictor
    scale = 1.0
  [../]
[]
```

```
[Preconditioning]
  [./SMP]
    type = SMP
    full = true
  [../]
[]
```

`Postprocessors` and `VectorPostprocessors`

The `Postprocessors` system allows single scalar metrics to be calculated and retrieved from the simulation as it evolves [228]. The `VectorPostprocessors` works similarly but can output multiple metrics as a vector [229].

The `TimestepSize` class in the `./dt` code block will return the timestep size, dt, of the solution [230].

The `FeatureFloodCount` class in the `./num_voids` code block will return the total number of voids in the simulation. It does this by tracking connected element regions in the simulation for the defined `variable` within a given `threshold`. In this case, `variable = v` is the vacancy concentration, and the threshold definition is `threshold = 0.5`. This means if a high vacancy region of elements ($v > 0.5$) is surrounded by a series of low vacancy elements ($v < 0.5$), then the boundary will be the connected series of elements which bridge that transition. Inside this boundary, elements with a high vacancy concentration will be counted as a void. By setting `compute_var_to_feature_map = true`, a map of these voids and their positions will be accessible [231]. For ease of visualisation, see Figure 4.1 reproduced with permission from [232].

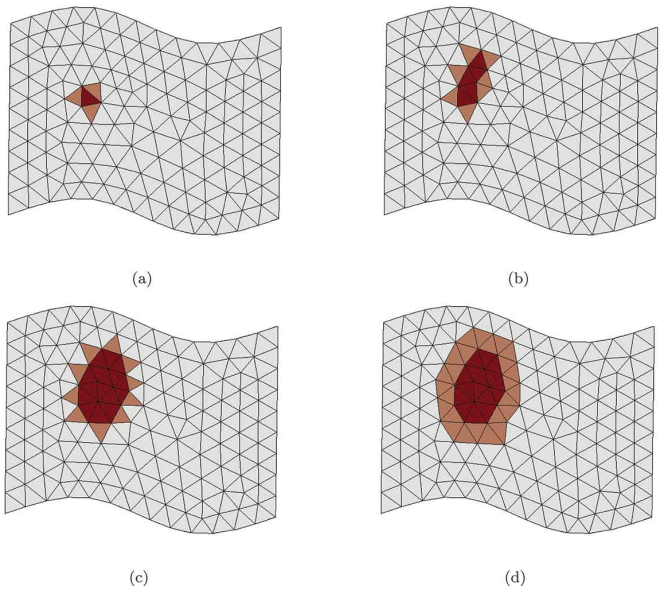

Figure 4.1: A visualisation of the `FeatureFloodCount` class performing a classification of a single feature (dark red) from the rest of the material (grey) with the associated boundary (light red). (a) demonstrates the initial identification of the feature, or the "seed element" and the surrounding "halo elements" which share a boundary. (b) and (c) show the identified feature area increasing through its intermediary stages until all elements of the surrounding halo satisfy the threshold value. (d) Finally, the halo is filled in, and the feature is considered to have been identified. Reproduced with permission from [232]

The `VolumePostprocessor` class in the `./mesh_volume` code block will compute the volume of the simulation. The timing of this calculation is controlled by the `execute_on` parameter. Here, I have set the value to `'true'`, meaning that the volume of the simulation is calculated at the start of the simulation and is not re-calculated again [233].

The `FeatureVolumeFraction` class in the `./porosity` code block will calculate the porosity of the voids, i.e., the total volume of voids in the simulation divided by the system's total volume. It does this by taking both the `[Postprocessors] [./mesh_volume]` and the `[VectorPostprocessors] [./void_volumes]` metrics as an input [234].

The `ElementAverageValue` class in the `[Postprocessors] [./average_v_conc]` and

the `[Postprocessors][./average_s_conc]` code blocks will calculate the average concentration of the `variable = v` and `variable = s` respectively; this is used in experiments 5, 6, and 7 to understand the initial vacancy and initial self-interstitial atom concentrations when using pre-existing voids as the initial conditions rather than a random uniform distribution [235].

The `FeatureVolumeVectorPostprocessor` class in the `[VectorPostprocessors][./void_volumes]` code block will work with the `FeatureFloodCount` class in the `[./num_voids]` code block to calculate the number of voids in the simulation; however, unlike the scalar metric of the `[./num_voids]` code block, the `[./void_volumes]` code block will return a vector of their positions [229, 236].

```
[Postprocessors]
  [./dt]
    type = TimestepSize
  [../]
  [./num_voids]
    type = FeatureFloodCount
    variable = v
    threshold = 0.5
    compute_var_to_feature_map = true
  [../]
  [./mesh_volume]
    type = VolumePostprocessor
    execute_on = 'initial'
  [../]
  [./porosity]
    type = FeatureVolumeFraction
    feature_volumes = void_volumes
    mesh_volume = mesh_volume
  [../]
  [./average_v_conc]
       type = ElementAverageValue
    variable = v
  [../]
  [./average_s_conc]
       type = ElementAverageValue
    variable = s
  [../]
[]
```

```
[VectorPostprocessors]
  [./void_volumes]
    type = FeatureVolumeVectorPostprocessor
    flood_counter = num_voids
    output_centroids = true
  [../]
[]
```

`Outputs`

The `Outputs` system allows the results and metrics generated by the simulation to be saved [237].

The `Exodus` class in the `./exodus_file` code block enables saving the simulation as an EXODUS file. The path it will be saved to is specified by the `file_base` parameter [238].

The `CSV` class in the `./csv_file` code block enables the saving of a series of CSV files representative of the timesteps of the simulation. The path to which the CSV files are saved is specified by the `file_base` parameter. MOOSE will save a single output CSV named (`output.csv`), which has the output values of the `Postprocessors` and the `VectorPostprocessors` systems as individual rows. These are the metrics for each timestep of the simulation. These are also printed as outputs in the terminal window. Additionally, there is a CSV file for each of the timesteps (e.g. `output_void_volumes_0008.csv`) where the number in the file name is the timestep the CSV file has data for. These CSV files record the feature map of each void in the simulation; it has the centroid coordinates and the volumes of the voids among other columns of data [239].

Setting the `print_linear_residuals` and the `print_nonlinear_residuals` parameters to `false` will stop the table of the linear and non-linear residuals, respectively, from being printed to the terminal window. These were set to `true` whilst designing the simulation and fine-tuning the parameters of the `Executioner` system [240].

Setting the `perf_graph` parameter to `false` will stop the final performance log from

being printed to the terminal window [240].

```
[Outputs]
  print_linear_residuals = false
  print_nonlinear_residuals = false
  perf_graph = false
  [./exodus_file]
    type = Exodus
    file_base = output-files/appropiate_run_name/exodus_file/output
  [../]
  [./csv_file]
    type = CSV
    file_base = output-files/appropiate_run_name/csv_files/output
  [../]
[]
```

4.2.3 Running MOOSE

The command below was run from the application directory: `/projects/void_lattices/` to execute the MOOSE phase-field simulation using a specified config file. MOOSE supports parallelisation to increase performance and reduce run time via the `mpich` library [241, 242]. To invoke parallelisation, prefix the moose execution command with `mpiexec`. [1]

The MOOSE config files for random initial conditions and pre-existing voids can be found in Appendix B.1 and B.2, respectively.

```
cd ~/projects/void_lattices/

mpiexec -n 127 ./void_lattices-opt -i input-files/void-lattice.i
```

[1] When parallelising, it is best practice to use $n - 1$ CPU cores, where n is the maximum number of CPU cores on the machine.

Chapter 5

MOOSE Simulation Results and Analysis

5.1 Introduction

Chapter 4 outlined the implementation of the MOOSE framework for simulating the evolution of void superlattices in a reaction–diffusion system, building on the theoretical predictions established in Chapter 3. This chapter presents the results of the MOOSE simulation experiments which were designed to validate those predictions and assess the robustness of void superlattice formation and stability under varying conditions.

The primary goal of these simulations is to investigate the formation and stability of void superlattices across different input parameters and initial conditions. By systematically varying the mobility ratio, domain size, and initial conditions (comparing random perturbations against pre-existing void distributions) Experiments 1–7 examined how these factors influence void pattern formation, evolution, and long-term stability. The experiments provide insight into both the conditions necessary for void superlattice formation and the robustness of my model.

In addition, this chapter also examines the relationship between my model and the standard Cahn-Hilliard equation. Experiment 8 specifically explores the conditions under which the reaction terms in the coupled equations can be eliminated or approximated, revealing how the traditional coarsening behaviour of phase-separating systems relates to the ordered pattern formation observed in the simulations.

5.1.1 Experiments Performed

With the GCP virtual machine created, the MOOSE framework set up, and the MOOSE configuration files defined, the next step was to run the simulations and analyse the results for different experimental motivations.

Experiment 1

Experiment 1 served as a foundational test to determine whether a void superlattice would form as the system evolved from a slightly perturbed random distribution. The parameters were derived from the linear stability analysis in Section 3.4, ensuring conditions conducive to a potential Turing instability.

A single simulation was run using $M_s = 1\,000$, $M_v = 1$, $\gamma_s = \gamma_v = 1$, $\bar{s} = 0.01$, $\bar{v} = 0.25$, $a = -0.5$, and $c = 0.00125$. The system was initialised with uniform random perturbations around the base states and evolved on a 200×200 domain (discretised into a 400×400 grid with periodic boundary conditions) until $t = 50\,000$. The simulation took approximately 4 hours to complete.

Experiment 2

Experiment 2 investigated how varying the mobility ratio M_s/M_v influenced the formation and evolution of a void superlattice. Simulations were run across the range $M_s/M_v = \{1,\ 10,\ 100,\ 1\,000,\ 10\,000\}$, with all other parameters held constant from Experiment 1. Each simulation was run until $t = 50\,000$ and took approximately 3–5 hours to complete per simulation, depending on the mobility ratio.

Experiment 3

Experiment 3 explored the threshold for void superlattice formation by scanning the mobility ratios $M_s/M_v = \{1, 2, 4, 5, 10\}$ to identify the transition point between continuous coarsening and ordered self-assembly. These values were selected to validate the theoretical threshold of $M_s/M_v = 3.322$ predicted in Section 3.5. All other simulation settings were consistent with Experiment 1. Each simulation was run until $t = 50\,000$ and took approximately 3 hours to complete per simulation.

Experiment 4

Experiment 4 investigated the influence of domain size on pattern formation by systematically varying the simulation domain: 50×50, 100×100, 200×200, 300×300, and 400×400. Each domain was discretised using two elements per unit length. Parameters and initial conditions matched those in Experiment 1. Simulation time scaled strongly with domain size: the smallest case (50×50) completed in approximately 15 minutes, while the largest domain (400×400) took approxiamtely 4 days.

Experiment 5

Experiment 5 examined whether a predefined randomly distributed population of voids would self-assemble into a void superlattice. The system was initialised with 65 randomly positioned voids of radius 5.9 units, based on the final state from Experiment 1. Void placement was controlled to avoid overlap, and the s field was initialised with corresponding "holes" using the same random seed. The simulation was run until $t = 50\,000$ and took approximately 3 hours to complete.

Experiment 6

Experiment 6 extended Experiment 5 by systematically varying the initial void size while keeping the void count fixed. The `radius_variation` parameter introduced controlled fluctuations of $\pm 0\%$, $\pm 20\%$, $\pm 40\%$, $\pm 60\%$, and $\pm 80\%$ in void radius. All other parameters matched Experiment 5. The simulations were run until until $t =$

50 000 and took approximately 3–5 hours to complete per simulation, depending on the initial void size.

Experiment 7

Experiment 7 extended Experiment 5 by systematically varying the initial void count while keeping the void size fixed. The `numbub` parameter was adjusted to initialise 35, 50, 65, 80, or 95 voids. All other parameters matched Experiment 5. The simulations were run until until $t = 50\,000$ and took approximately 3–5 hours to complete per simulation, depending on the initial void count.

Experiment 8

Experiment 8 examined the relationship between the reaction–diffusion model developed in this work and the standard Cahn-Hilliard model, assessing whether the latter could be recovered under specific limiting cases.

To explore this connection, the creation and annihilation terms (c and a) were set to zero, decoupling the vacancy and self-interstitial atom equations. The resulting stability matrix $\mathbf{A_q}$, derived in Section 5.6.2, reduced to the standard coarsening condition in the limit $q^2 \to 0$, characteristic of phase-separation dynamics. However, assuming an infinitely large self-interstitial atom mobility ($M_s \to \infty$) led to a coupled ordinary differential equation (ODE) and partial differential equation (PDE) system, with self-interstitial atoms reaching a steady-state distribution.

Two limiting cases were simulated:

- ODE w/ Coupled PDE: The self-interstitial concentration followed an ODE, interacting with the average vacancy concentration.
- Single PDE w/ Constant s: The steady-state value of s was substituted into the vacancy equation, yielding a PDE with an additional reaction term.

Both models were simulated using the same domain, discretisation, boundary conditions, and parameter choices as in Experiment 1. Despite their simplified equations, the results, shown in Figure 5.30, confirmed the emergence of void superlattice forma-

tion. The simulations were run until $t = 50\,000$ and took approximately 1–4 hours to complete per simulation, depending on the model.

5.1.2 Data Captured from the Simulations

The outputs of MOOSE were a folder containing CSV files and a folder containing the EXODUS file of the simulation.

CSV Files

The CSV folder contained two types of CSV files. The first was a single output file of the name `output.csv` and additionally multiple CSV files, one for each of the time steps of the simulation, named like so: `output_void_volumes_0668.csv` where the number references the appropriate time step of that simulation. The `output.csv` rows represented one simulation timestep, an example `.tail()` is shown in Table 5.1.

time	avg_s_conc	avg_v_conc	dt	mesh_volume	num_voids	porosity
48 567.62	0.0087	0.2077	463.050	90 000	149	0.18259
49 030.67	0.0087	0.2077	463.050	90 000	149	0.18257
49 493.72	0.0087	0.2077	463.050	90 000	149	0.18251
49 956.77	0.0087	0.2077	463.050	90 000	149	0.18252
50 000	0.0087	0.2077	43.223	90 000	149	0.18252

Table 5.1: Example `.tail()` of the `output.csv` file for experiment 5.

The individual time step files captured information on each of the voids present in the simulation at that timestep. Not all columns were of interest in the analysis later. An example reduced `.head()` is shown in Table 5.2.

centroid_x	centroid_y	feature_volumes
95.7235	26.54127	110.1163
121.4245	238.9802	114.5629
194.3587	171.3739	127.8554
225.8884	224.7045	106.3874
255.5233	178.9712	138.3810

Table 5.2: Reduced example `.head()` of the `output_void_volumes_0668.csv` file for the $M_s/M_v = 1\,000$ and 300×300 MOOSE simulation.

EXODUS Files and ParaView

In addition to multiple CSV files, MOOSE can export an EXODUS file of the simulation.

First proposed in 1988, EXODUS is a binary file format with the extension `.e`. It is designed to store simulation data for finite element analyses. It enables the reconstruction of finite element meshes, elemental results, and time-dependent simulation data. It facilitates post-processing and visualisation [243, 244].

ParaView, an open source scientific visualisation tool, is used to process and replay EXODUS files, allowing for detailed analysis of the simulated void evolution. It provides a graphical interface for visualising field data, contour maps, and vector fields, supporting in-depth exploration of the system's behaviour. ParaView can be downloaded from the official website: `https://www.paraview.org/` [245].

ParaView Colour Legend

The same double-well free energy is used across Experiments 1–8. This model has a maximum at 1 and a minimum at 0, where a value of 1 corresponds to complete saturation of the vacancy concentration (i.e., a void), and a value of 0 represents the complete absence of vacancies (i.e., a self-interstitial atom cluster).

To improve readability, an enlarged version of the colour legend is provided here in Figure 5.1 as it might be too small for the reader to interpret next to the simulation results.

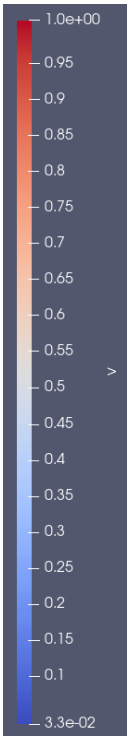

Figure 5.1: ParaView colour legend for Experiments 1–8 simulation results.

5.1.3 Data Analysis Performed

Fast Fourier Transform Analysis

To quantify the emergence of periodic ordering in the void structures, a Fast Fourier Transform (FFT) was applied to the visualised simulation data. FFTs identify dominant spatial frequencies and provide an objective measure of ordering within the void lattice. The analysis was performed using Python; the associated code is provided in Appendix C.1.

For each experiment:

- FFTs were computed on the spatial distribution of voids at multiple time steps.
- The evolution of spectral peaks was tracked to assess the emergence of hexagonal close-packed ordering.
- Progressive sharpening of the FFT peaks was used as an indicator of increasing structural coherence.

Statistical Analysis

The simulation data was extracted and analysed from the MOOSE-generated EXODUS and CSV output files using Python scripts (Appendix C.2). The following metrics were calculated to quantify void evolution and structural self-organisation over time:

- Total number of voids.
- Average void radius.
- Spread of void radii.
- Median nearest-neighbour distance between voids.

To accurately capture the nearest neighbour distances, void centroids were extracted using the `output_centroids` flag in the `[VectorPostprocessors] [./void_volumes]` MOOSE configuration block. However, due to limitations in handling periodic boundary conditions, post-processing corrections were applied. Specifically, voids that disappeared were excluded from centroid tracking, and median values were used instead of averages to mitigate the impact of outliers [236].

5.2 Experiments 1, 2, and 3: Mobility-Driven Void Superlattice Formation

5.2.1 Experiment 1: Formation of a Void Superlattice from a Random Distribution

Experiment 1:

Experiment Objective

Experiment 1 was designed to establish whether a void superlattice would emerge from an initially random distribution of vacancies and self-interstitial atoms. This experiment served as a foundational test to validate the theoretical predictions made in the linear stability analysis. By running a single simulation with fixed parameters, the goal was to determine whether the system would transition from a disordered state into a periodic arrangement of voids over time. If successful, this would confirm that, under specific conditions, the system naturally evolves towards self-assembled void structures rather than undergoing unstructured coarsening.

Experiment 1:

Simulation Setup and Parameters

The simulation domain was defined as a 200×200 unit system, discretised into a 400×400 grid to ensure sufficient numerical resolution. Periodic boundary conditions were applied to remove edge effects, ensuring that the system could evolve as if it were an infinite domain.

The parameters and initial conditions were chosen based on the linear instability analysis, ensuring that conditions were suitable for potential void pattern formation.

- **Domain size**: 200×200 units

- **Grid resolution**: 400×400
- **Boundary conditions**: Periodic
- **Mobility values**: $M_s = 1\,000$, $M_v = 1$
- **Mean concentrations**: $\bar{v} = 0.25$, $\bar{s} = 0.01$
- **Surface energy terms**: $\gamma_s = \gamma_v = 1$
- **Reaction coefficients**: $a = -0.5$, $c = 0.00125$

The initial conditions of vacancies and self-interstitial atoms within the simulation were implemented as a uniform random perturbation around the mean concentrations, specifically $\bar{v} = 0.25 \pm 1\%$ and $\bar{s} = 0.01 \pm 1\%$. This introduced small fluctuations in the system, allowing for natural instability-driven pattern formation.

The simulation was run until $t = 50\,000$, requiring a total of 540 time steps to reach this final state. This took approximately 4 hours to complete on the GCP `n2-standard-128` virtual machine. The timestamps shown are approximate for ease of reading; the exact timestamps from the simulation are shown in Table 5.3.

Written Time	Exact Simulation Time (t)
$t = 0$	0
$t \approx 500$	538.408
$t \approx 750$	754.393
$t \approx 1\,000$	1 015.52
$t \approx 2\,500$	2 514.51
$t \approx 5\,000$	5 028.07
$t \approx 10\,000$	10 020.8
$t \approx 20\,000$	20 099.1
$t = 50\,000$	50 000

Table 5.3: Timestamp map for Experiment 1.

Experiment 1:

Simulation Results and Analysis

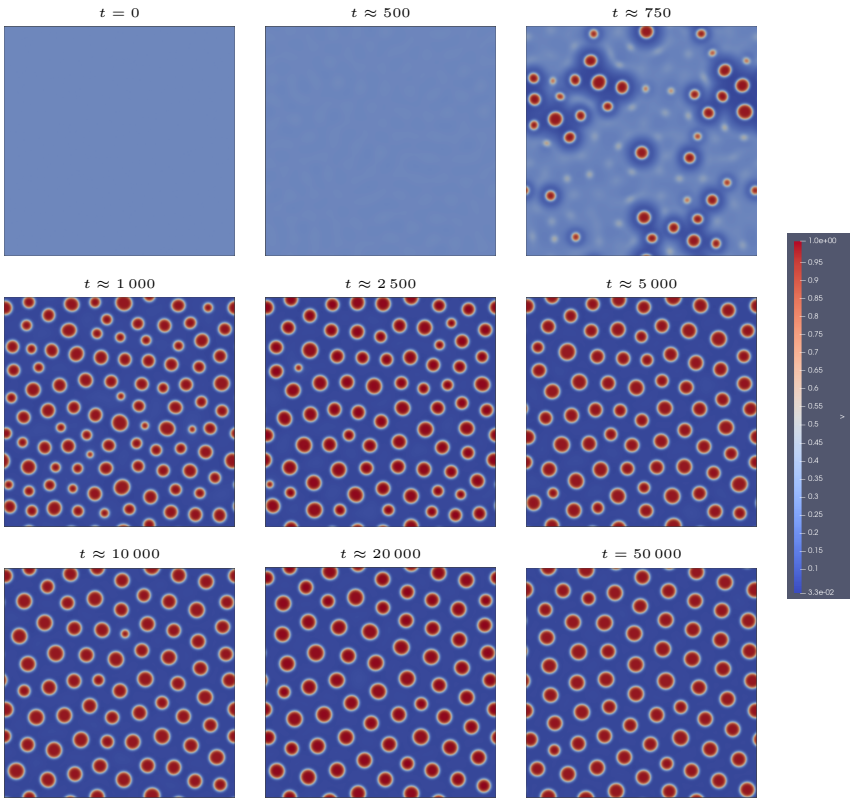

Figure 5.2: MOOSE simulation results for Experiment 1, demonstrating the formation and evolution of a void superlattice from an initially random distribution. The ParaView colour legend is shown to the right.

The simulation results for Experiment 1, presented in Figure 5.2, illustrate the evolution of void structures over time under conditions where the system begins from a random distribution of vacancies and self-interstitial atoms. The objective of this experiment was to assess whether a void superlattice would spontaneously emerge from an initially homogeneous state and stabilise into a periodic structure.

At $t = 0$, the system starts with a uniform random perturbation around the base-state concentrations, specifically $\bar{v} = 0.25 \pm 1\%$ and $\bar{s} = 0.01 \pm 1\%$. As the simulation

progresses, phase separation occurs, leading to the formation of localised vacancy-rich regions. By $t \approx 750$, small voids have nucleated and begun to grow through diffusion-driven interactions.

By $t \approx 1\,000$, voids have coarsened significantly, and a structured arrangement begins to emerge. Smaller voids either shrink and disappear or migrate towards larger stable voids, which continue growing. The growth of the voids however reaches a plateau and a uniform size begins to emerge. By $t \approx 10\,000$, voids have self-organised into a periodic configuration, exhibiting an early-stage hexagonal close-packed arrangement. At later times, $t \approx 20\,000$ to $t = 50\,000$, the system reaches a steady state, with voids stabilising in size and forming a well-ordered superlattice. The final configuration confirms that void self-assembly is an intrinsic outcome of the reaction–diffusion dynamics governing the system.

Overall, Experiment 1 demonstrates that void superlattice formation is a natural consequence of the system's phase separation dynamics. The results confirm that, given the appropriate parameter conditions, the system will self-organise into a stable and predictable periodic structure in the absence of external driving forces.

5.2.2 Experiment 2: Influence of M_s/M_v Ratios on Void Superlattice Stability

Experiment 2:

Experiment Objective

Experiment 2 examined how increasing the mobility ratio M_s/M_v influenced void superlattice formation by systematically varying it across a broad range of values. Building upon the results of Experiment 1, which demonstrated successful void ordering at $M_s/M_v = 1\,000$, this experiment explored whether further increases in mobility enhanced structural organisation or led to a saturation effect, as well as how the system behaved at lower ratios.

To achieve this, the mobility ratio was varied across five values: $M_s/M_v = \{1,\ 10,$

100, 1 000, 10 000}. All other parameters remained fixed from Experiment 1 to ensure comparability. Each simulation was run until $t = 50,000$, with time steps ranging from 518 to 920, depending on the mobility ratio, taking approximately 3–5 hours per simulation.

The results, shown in Figure 5.3, indicate that void ordering strengthens with increasing M_s/M_v, with a hexagonal close-packed arrangement emerging for $M_s/M_v \geq 10$, while no void ordering occurred at $M_s/M_v = 1$. However, beyond $M_s/M_v = 100$, no significant additional refinement in ordering was observed, suggesting a saturation point.

Experiment 2:

Simulation Setup and Parameters

The simulation setup for Experiment 2 was consistent with Experiment 1 to ensure direct comparability. The domain size, discretisation, boundary conditions, and initial perturbations remained unchanged:

- **Domain size**: 200×200 units
- **Grid resolution**: 400×400
- **Boundary conditions**: Periodic
- **Mean concentrations**: $\bar{v} = 0.25$, $\bar{s} = 0.01$
- **Surface energy terms**: $\gamma_s = \gamma_v = 1$
- **Reaction coefficients**: $a = -0.5$, $c = 0.00125$
- **Initial conditions**: Uniform random perturbation, $\bar{v} = 0.25 \pm 1\%$, $\bar{s} = 0.01 \pm 1\%$

The mobility ratio M_s/M_v was systematically varied across five values:

- $M_s/M_v = 1$
- $M_s/M_v = 10$
- $M_s/M_v = 100$
- $M_s/M_v = 1\,000$

- $M_s/M_v = 10\,000$

Each simulation was run until $t = 50\,000$, requiring 518 to 920 time steps depending on the mobility ratio used. The exact number of time steps for each mobility ratio is shown in Table 5.4.

Mobility Ratio M_s/M_v	Number of Time Steps
1	609
10	518
100	520
1 000	540
10 000	920

Table 5.4: Number of time steps required for different mobility ratios in Experiment 2.

The simulations were run on a Google Cloud Platform `n2-standard-128` virtual machine (128 vCPUs, 512 GB RAM). The simulations took approximately 3–5 hours to complete per simulation, depending on the mobility ratio.

ParaView was used to visualise the simulation results at key timestamps. The approximate written times and the exact timestamps recorded in the simulation are shown in Table 5.5.

Written Time	Exact Simulation Time (t)				
	$M_s = 1$	$M_s = 10$	$M_s = 100$	$M_s = 1\,000$	$M_s = 10\,000$
$t \approx 650$	652.37	657.179	657.179	654.65	654.621
$t \approx 750$	752.585	755.996	751.653	753.838	753.421
$t \approx 1\,000$	1 016.83	1 020.21	1 009.14	1 026.1	1 009.52
$t \approx 5\,000$	5 007.79	5 017.65	5 004.02	5 057.58	5 017.38
$t \approx 10\,000$	10 022.8	10 009.4	10 026.6	10 104.4	10 011.5
$t = 50\,000$	50 000	50 000	50 000	50 000	50 000

Table 5.5: Timestamp map for Experiment 2.

Experiment 2:

Simulation Results and Analysis

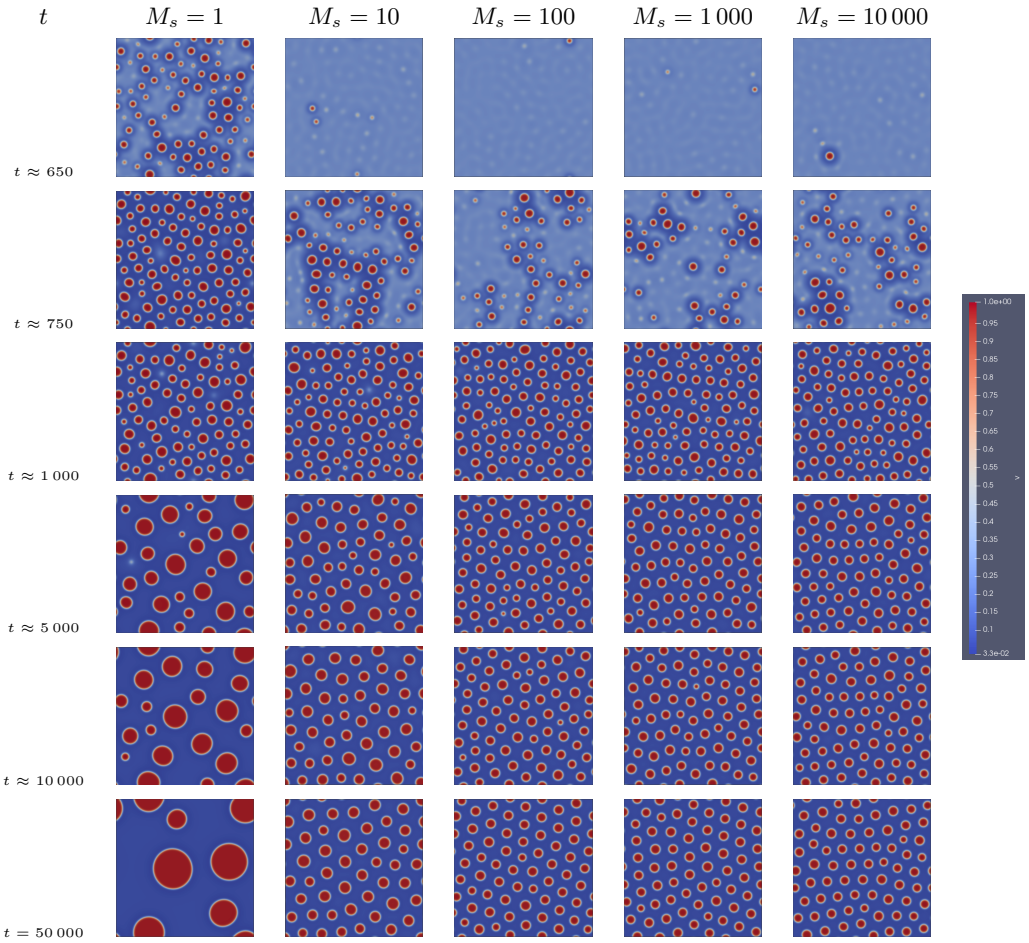

Figure 5.3: MOOSE simulation results for Experiment 2, which explored the influence of the M_s/M_v ratio on void superlattice stability. The ParaView colour legend is shown to the right.

The evolution of the system for different values of the mobility ratio M_s/M_v is visualised in Figure 5.3. At the initial stage ($t \approx 650$), all cases exhibit a nearly uniform distribution with minor fluctuations. As the simulation progresses, the impact of increasing M_s/M_v on void formation and ordering becomes apparent.

For $M_s/M_v = 1$, void evolution follows the classical Ostwald ripening process, where larger voids grow at the expense of smaller ones. No long-range ordering emerges, and coarsening continues throughout the simulation. By contrast, for $M_s/M_v = 10$, voids stabilise earlier, and some degree of periodicity is visible by $t \approx 5\,000$, although the arrangement is not fully developed.

A significant shift occurs at $M_s/M_v = \{100,\ 1\,000,\ 10\,000\}$. In these cases, voids quickly stabilise into a hexagonal close-packed configuration, with a more uniform void size distribution and a consistent spacing between voids. By $t \approx 10\,000$, further coarsening is minimal, and the superlattice structure remains stable. The final configurations for $M_s/M_v \geq 100$ are nearly indistinguishable, suggesting that once a sufficiently high mobility ratio is reached, further increases do not lead to additional refinement in ordering.

These results confirm that increasing the mobility ratio enhances void ordering, transitioning from continuous coarsening at low M_s/M_v to rapid stabilisation at high values. However, beyond $M_s/M_v = 100$, no further improvement in ordering is observed, indicating a saturation point where the system reaches its optimal structured configuration. This finding reinforces the hypothesis that the mobility ratio plays a critical role in void superlattice formation, with a well-defined threshold beyond which additional increases yield no further structural benefits.

5.2.3 Experiment 3: Investigating the Threshold for Void Superlattice Formation

Experiment 3:

Experiment Objective

Experiment 3 investigated the critical mobility ratio M_s/M_v required for void superlattice formation. While Experiment 1 established that a void superlattice emerges at $M_s/M_v = 1\,000$, and Experiment 2 demonstrated how ordering strength evolves with increasing mobility ratio, Experiment 3 focused on identifying the precise transition

threshold between unstructured coarsening and periodic void ordering.

To achieve this, the mobility ratio was systematically varied across $M_s/M_v = \{1, 2, 4, 5, 10\}$ to determine whether there exists a critical value at which voids transition from Ostwald ripening to self-organised pattern formation. This range was chosen to validate the theoretical threshold of $M_s/M_v = 3.322$, as predicted in Section 3.5. All other parameters remained fixed from Experiment 1 to ensure comparability.

The results, presented in Figure 5.4, reveal a clear transition. For $M_s/M_v \leq 2$, voids exhibit continuous coarsening, leading to unstructured growth characteristic of Ostwald ripening. In contrast, for $M_s/M_v \geq 4$, voids stabilise and begin self-organising into a periodic configuration, albeit with weaker ordering than observed in Experiment 2 at higher mobility ratios.

Experiment 3:

Simulation Setup and Parameters

The simulation setup for Experiment 3 was consistent with Experiment 1 to ensure direct comparability. The domain size, discretisation, boundary conditions, and initial perturbations were unchanged:

- **Domain size**: 200×200 units
- **Grid resolution**: 400×400
- **Boundary conditions**: Periodic
- **Mean concentrations**: $\bar{v} = 0.25$, $\bar{s} = 0.01$
- **Surface energy terms**: $\gamma_s = \gamma_v = 1$
- **Reaction coefficients**: $a = -0.5$, $c = 0.00125$
- **Initial conditions**: Uniform random perturbation, $\bar{v} = 0.25 \pm 1\%$, $\bar{s} = 0.01 \pm 1\%$

The mobility ratio M_s/M_v was systematically varied across five values:

- $M_s/M_v = 1$
- $M_s/M_v = 2$
- $M_s/M_v = 4$

- $M_s/M_v = 5$
- $M_s/M_v = 10$

Each simulation was run until $t = 50\,000$, requiring 518 to 723 time steps depending on the mobility ratio used. The exact number of timesteps for each mobility ratio is show in Table 5.6.

Mobility Ratio M_s/M_v	Number of Time Steps
1	609
2	723
4	720
5	599
10	518

Table 5.6: Number of time steps required for different mobility ratios in Experiment 3.

The simulations were run on a Google Cloud Platform `n2-standard-128` virtual machine (128 vCPUs, 512 GB RAM). The simulations took approximately 3 hours to complete per simulation.

ParaView was used to visualise the simulation results at key timestamps. The approximate written times and the exact timestamps recorded in the simulation are shown in Table 5.7.

Written Time	Exact Simulation Time (t)				
	$M_s = 1$	$M_s = 2$	$M_s = 4$	$M_s = 5$	$M_s = 10$
$t \approx 650$	652.37	653.91	662.178	656.991	657.179
$t \approx 750$	752.585	760.144	755.189	752.55	755.996
$t \approx 1\,000$	1 016.83	1 006.76	1 014.58	1 015.97	1 020.21
$t \approx 5\,000$	5 007.79	5 001.28	5 020.13	5 023.07	5 017.65
$t \approx 10\,000$	10 022.8	10 000.6	10 009.1	10 018.2	10 009.4
$t = 50\,000$	50 000	50 000	50 000	50 000	50 000

Table 5.7: Timestamp map for Experiment 3.

Experiment 3:

Simulation Results and Analysis

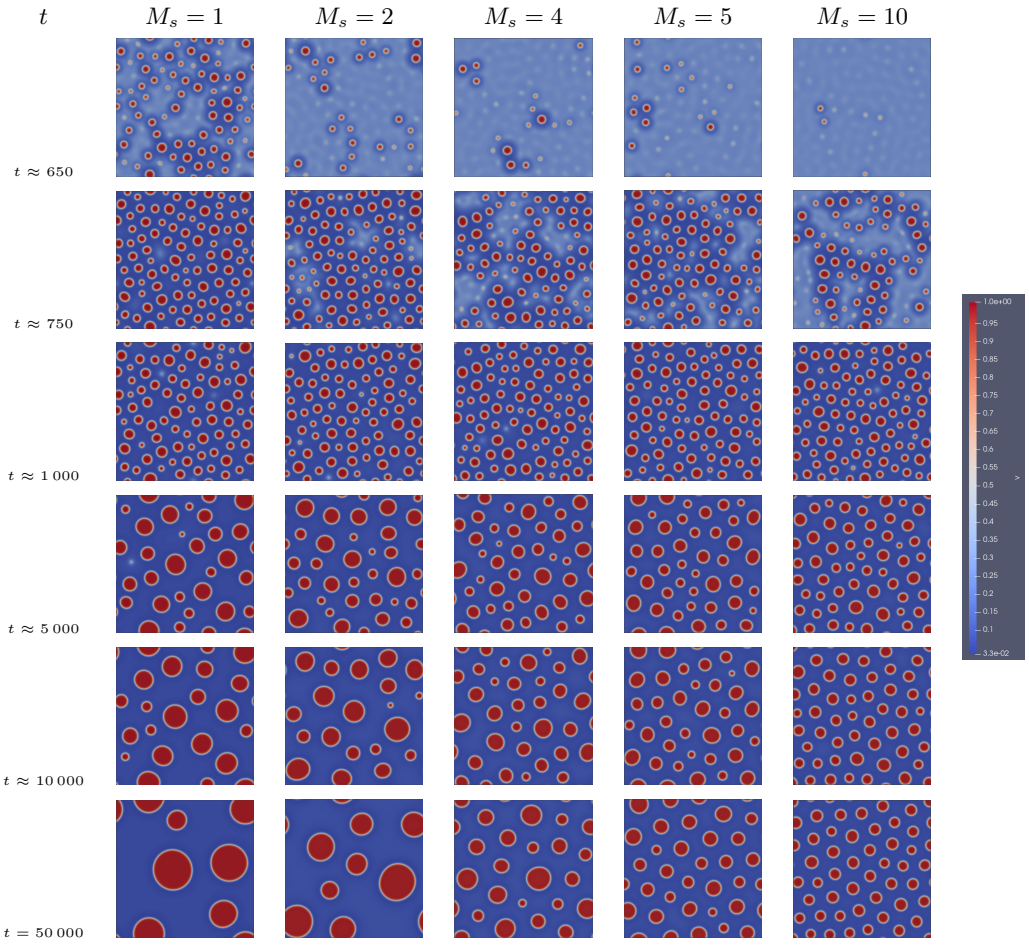

Figure 5.4: MOOSE simulation results for Experiment 3, which explored the threshold for void superlattice formation and development. The ParaView colour legend is shown to the right.

The simulation results for Experiment 3, displayed in Figure 5.4, illustrate the evolution of void structures over time for different values of the mobility ratio M_s/M_v. Initially, the system begins with a randomly distributed perturbation for all M_s/M_v cases. As the simulation progresses, voids nucleate and grow, but their long-term

behaviour depends significantly on the mobility ratio.

For $M_s/M_v = 1$ and $M_s/M_v = 2$, voids continue to coarsen throughout the simulation. Larger voids grow at the expense of smaller ones, leading to a disordered distribution that persists over time. This behaviour is characteristic of classical Ostwald ripening, where no long-range ordering emerges, and voids remain dynamically evolving without stabilisation.

In contrast, for $M_s/M_v = 4, 5, 10$, a transition towards void superlattice formation is observed, but the degree of ordering varies. At $M_s/M_v = 4$, only weak signs of periodicity appear, with voids beginning to stabilise in size but lacking a well-defined superlattice structure. At $M_s/M_v = 5$, ordering becomes more apparent, though some irregularities remain, and full hexagonal close-packing has not yet emerged at $t = 50\,000$. It is only at $M_s/M_v = 10$ that a well-developed superlattice is clearly visible, with voids reaching a stable, periodic configuration. These results indicate that while the theoretical threshold $M_s/M_v = 3.322$ marks the onset of pattern formation, achieving a fully developed void superlattice requires higher mobility ratios, with robust ordering observed primarily at $M_s/M_v = 10$.

These results provide direct evidence of a transition threshold near the theoretically predicted $M_s/M_v = 3.322$. Below this value, the system evolves via continuous coarsening; above it, voids stabilise into an ordered structure.

5.2.4 Experiments 1, 2, and 3: Fast Fourier Transform Analysis

Experiments 1 and 2:

Fast Fourier Transform Analysis

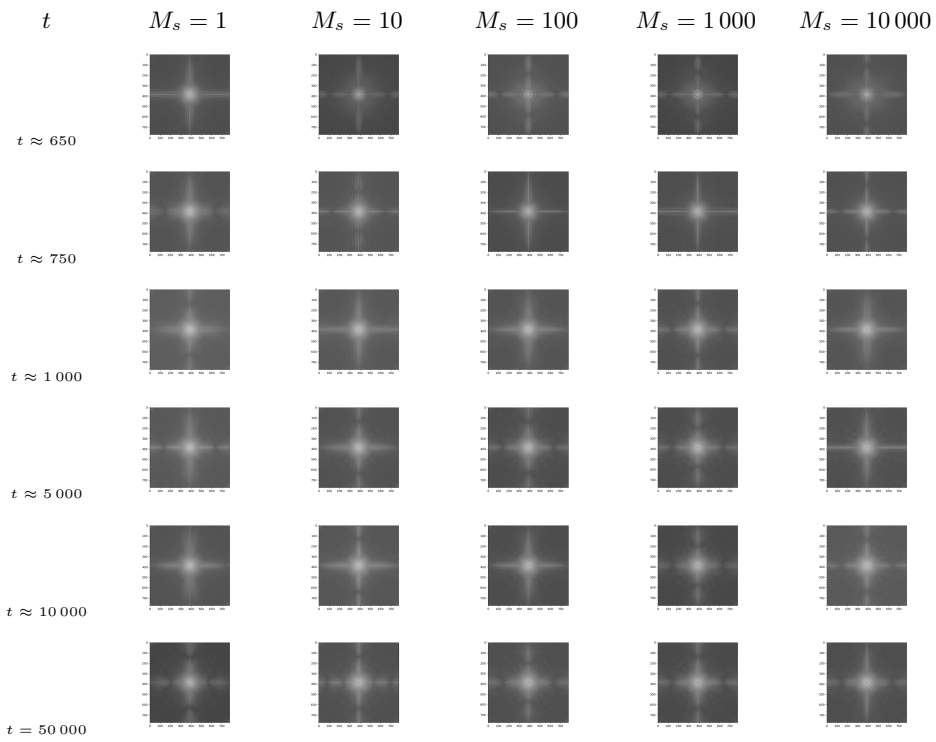

Figure 5.5: Fast Fourier Transform analysis of MOOSE simulation results for Experiments 1 and 2.

The Fast Fourier Transform (FFT) analysis, presented in Figure 5.5, provides a quantitative measure of void ordering across different mobility ratios over time. These results correspond directly to the simulation images in Figure 5.3, allowing for an objective assessment of periodicity in Experiments 1 and 2.

At early times ($t \approx 650$), all cases exhibit diffuse FFT spectra, confirming the absence of long-range order in the initial conditions. This aligns with the visual results, where

voids are randomly distributed without a discernible periodic structure.

For $M_s/M_v = 1$, the FFT spectra remain diffuse throughout the simulation, indicating continued unstructured coarsening. This is consistent with the observed Ostwald ripening behaviour, where voids grow at the expense of smaller ones but do not stabilise into an ordered arrangement.

In contrast, for $M_s/M_v = 10$, frequency peaks begin to emerge around $t \approx 5\,000$, reflecting the onset of void ordering. However, these peaks remain relatively weak, mirroring the simulation results where periodicity is visible but not fully developed.

A pronounced transition occurs for $M_s/M_v = 100$, $1\,000$, and $10\,000$. In these cases, well-defined spectral peaks emerge by $t \approx 5\,000$ and sharpen significantly by $t \approx 10\,000$, confirming the formation of a hexagonal close-packed void superlattice. At $t = 50\,000$, the FFT spectra for $M_s/M_v \geq 100$ reach maximum sharpness, indicating that further increases in mobility ratio do not enhance the periodicity beyond this threshold.

These results validate the simulation observations, demonstrating that increasing the mobility ratio facilitates rapid superlattice formation. The FFT analysis quantitatively confirms the transition from continuous coarsening at low M_s/M_v to stabilised periodic ordering at high values, with a saturation point beyond $M_s/M_v = 100$, where further increases yield no additional structuring effects.

Experiment 3:

Fast Fourier Transform Analysis

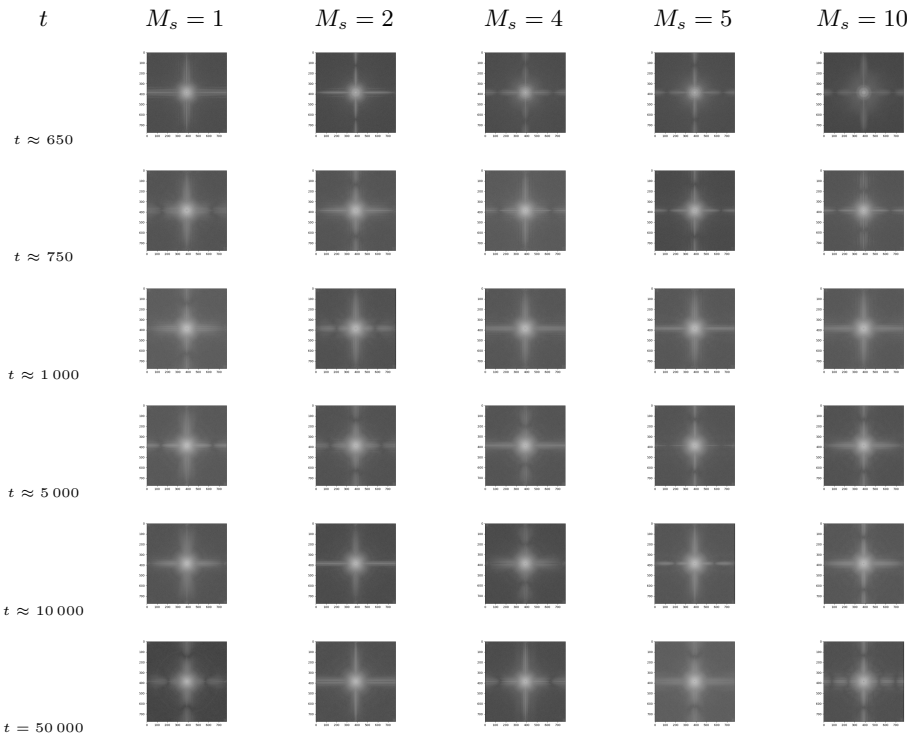

Figure 5.6: Fast Fourier Transform analysis of MOOSE simulation results for Experiment 3.

The Fast Fourier Transform (FFT) analysis in Figure 5.6 provides a quantitative assessment of periodic ordering in the system for different values of the mobility ratio M_s/M_v. These results correspond directly to the simulation images in Figure 5.4, with the FFT capturing the emergence of periodic structuring over time in Experiment 3. At early times ($t \approx 650$), all cases exhibit a diffuse FFT spectrum, confirming the absence of long-range periodicity. This aligns with the simulation results, where voids are initially distributed randomly without any visible ordering as they begin to nucleate. For $M_s/M_v = 1$ and $M_s/M_v = 2$, the FFT spectra remain diffuse throughout the simulation, indicating persistent disorder. No distinct frequency peaks emerge, mirroring

the visual results in Figure 5.4, where voids continue to coarsen in an unstructured manner without stabilisation via Ostwald ripening.

In contrast, for $M_s/M_v \geq 4$, a transition toward periodic ordering is observed, though the degree of regularity varies. At $M_s/M_v = 4$, weak peaks appear in the FFT spectrum, suggesting the initial emergence of periodicity, though the void structure remains inconsistent. At $M_s/M_v = 5$, these peaks become more defined, reflecting increased ordering, though some irregularities remain.

It is only at $M_s/M_v = 10$ that the FFT spectrum exhibits sharply defined peaks, confirming a highly regular periodic structure. This aligns with the simulation images in Figure 5.4, where a well-formed hexagonal close-packed arrangement is visible, with voids reaching a stable and predictable configuration.

Overall, the FFT analysis validates the visual observations, demonstrating that a transition toward superlattice formation occurs for $M_s/M_v \geq 4$, though full periodic ordering is only achieved at $M_s/M_v = 10$. These findings reinforce the presence of a critical mobility ratio threshold, beyond which voids self-organise into a robust and stable superlattice.

5.2.5 Experiments 1, 2, and 3: Statistical Analysis

Number of Voids Over Time

The evolution of the number of voids across Experiments 1, 2, and 3 — Figure 5.7 — provides a clear distinction between systems that undergo void coarsening via Ostwald ripening and those that exhibit self-assembly into a void superlattice.

Experiment 1:

Formation of a Void Superlattice from a Random Distribution

For $M_s/M_v = 1\,000$, the number of voids initially increases sharply due to phase separation, peaking at approximately 97 voids around $t \approx 750$ to $t \approx 1\,000$ as small voids nucleate. Following this peak, the system undergoes a rapid coarsening phase, where smaller voids shrink and disappear or merge into larger more stable voids. This process continues until the void count stabilises at approximately 66 voids by $t = 50\,000$, indicating that the system has reached dynamic equilibrium, with minimal further void elimination or nucleation. The plateau in the void count suggests that the system has successfully self-assembled into a stable periodic void superlattice rather than undergoing unrestricted coarsening.

Experiment 2:

Influence of M_s/M_v Ratios on Void Superlattice Stability

When exploring a range of mobility ratios ($M_s/M_v = \{1, 10, 100, 1\,000, 10\,000\}$), clear trends emerge:

- For $M_s/M_v = 1$, voids exhibit continuous coarsening, following Ostwald ripening, where larger voids grow at the expense of smaller ones, and no stable configuration is reached.
- For $M_s/M_v = 10$, the void count stabilises early, indicating that a hexagonal close-packed void superlattice begins to form, though the ordering is weaker compared to higher mobility ratios.
- For $M_s/M_v = \{100, 1\,000, 10\,000\}$, the void count evolution is nearly identi-

cal, suggesting that ordering reaches a saturation point beyond $M_s/M_v = 10$, reinforcing the idea that a sufficiently high mobility difference promotes self-assembly into a stable periodic void superlattice.

Experiment 3:

Investigating the Threshold for Void Superlattice Formation

For mobility ratios near the predicted linear stability threshold of $M_s/M_v = 3.322$, the system exhibits a clear transition between Ostwald ripening self-assembly into a void superlattice:

- For $M_s/M_v = \{1, 2\}$, voids undergo continuous coarsening with no signs of stabilisation, indicating that the system remains unstable to complete decomposition. The number of voids continuously decreases, showing no tendency towards self-assembly.
- For $M_s/M_v = \{4, 5, 10\}$, the void count stabilises after an initial decrease, confirming the formation of a self-assembled superlattice. This aligns with the theoretical prediction that a threshold exists near $M_s/M_v = 3.322$, beyond which voids stop coarsening indefinitely and instead reach a stable ordered configuration.

A log-log plot of void count evolution highlights this transition:

- For $M_s/M_v \geq 4$, the void count plateaus, indicating self-assembly.
- For $M_s/M_v \leq 2$, void elimination continues indefinitely, confirming unbounded coarsening.

Conclusion

The number of voids provides clear evidence of a critical mobility ratio threshold governing the transition from Ostwald ripening to void superlattice formation:

- Low mobility ratios ($M_s/M_v = \{1, 2\}$): Void count decreases continuously, showing unbounded coarsening and no signs of stabilisation, characteristic of Ostwald ripening.

- Intermediate mobility ratios ($M_s/M_v = \{4, 5, 10\}$): The void count stabilises, indicating a transition to weak ordering and the onset of self-assembly.
- High mobility ratios ($M_s/M_v \geq 100$): Void count plateaus early, confirming the formation of a well-ordered hexagonal close-packed superlattice.

These results conclusively establish a threshold at $M_s/M_v \approx 3.322$, beyond which voids transition from continuous coarsening to self-limited superlattice formations.

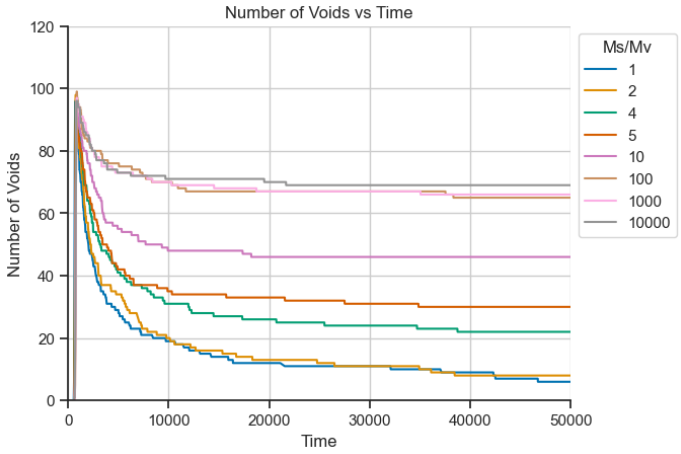

(a) Regular plot

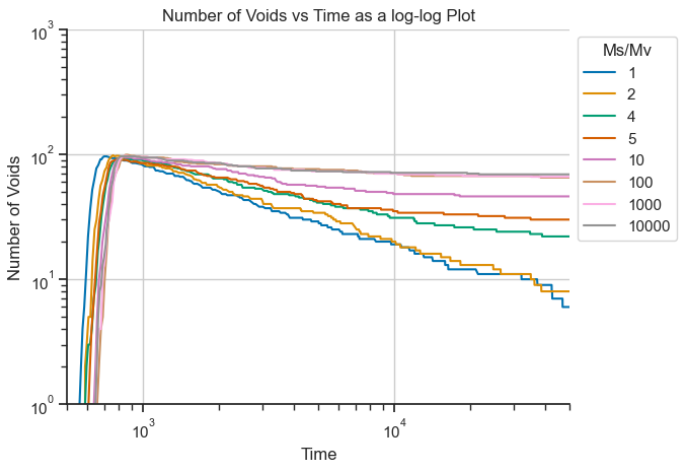

(b) Log-log plot

Figure 5.7: Number of voids over time for Experiments 1, 2, and 3 shown as (a) a regular plot and (b) a log-log plot.

Average Void Radius Over Time

The evolution of the average void radius across Experiments 1, 2, and 3 — Figure 5.8 — further reinforces the distinction between systems that undergo continuous void coarsening via Ostwald ripening and those that transition into a stable void superlattice.

Experiment 1:

Formation of a Void Superlattice from a Random Distribution

For $M_s/M_v = 1\,000$, the average void radius initially exhibits a sharp increase as voids nucleate and grow via phase separation, coinciding with the peak in the number of voids at $t \approx 750$ to $t \approx 1\,000$. As smaller voids shrink and merge into larger ones, the system undergoes a rapid coarsening phase, causing a steep rise in the void radius. This growth rate slows significantly between $t \approx 1\,000$ and $t \approx 10\,000$ as the system approaches equilibrium. By $t \approx 20\,000$, the average void radius stabilises at approximately 6 units, confirming that further coarsening effects have ceased. The steady-state behaviour suggests that the voids have reached a characteristic equilibrium size within the superlattice, reinforcing the emergence of a self-organised periodic void superlattice structure.

Experiment 2:

Influence of M_s/M_v Ratios on Void Superlattice Stability

The impact of the mobility ratio on void growth follows a systematic trend, highlighting distinct transitions between coarsening regimes:

- For $M_s/M_v = 1$, void evolution follows classical Ostwald ripening, where larger voids grow at the expense of smaller ones. The void radius continues to increase throughout the simulation, with no clear sign of stabilisation. The stepwise, nonlinear growth pattern suggests intermittent void merging events, characteristic of unstructured coarsening dynamics.
- For $M_s/M_v = 10$, void growth stabilises earlier, and some degree of periodicity is observed, though ordering remains weak. This indicates that void interactions are beginning to promote self-assembly but are not yet dominant.

- For $M_s/M_v = \{100,\ 1\,000,\ 10\,000\}$, voids rapidly stabilise, reaching a well-defined equilibrium size. The system self-organises into a periodic superlattice, with minimal further coarsening beyond $t \approx 10\,000$. The near-identical final configurations for $M_s/M_v \geq 100$ suggest a saturation point, where additional increases in mobility ratio do not significantly refine void ordering.

These results confirm that increasing the mobility ratio enhances void ordering, transitioning from continuous coarsening at low M_s/M_v to rapid stabilisation at high values. However, beyond $M_s/M_v = 100$, no further improvement in ordering is observed, indicating a saturation point where the system reaches its optimal structured configuration.

Experiment 3:

Investigating the Threshold for Void Superlattice Formation

For mobility ratios near the predicted linear stability threshold of $M_s/M_v = 3.322$, the system exhibits a clear transition between unbounded Ostwald ripening and void superlattice formation:

- For $M_s/M_v = \{1, 2\}$, void growth remains unbounded, showing no sign of stabilisation. The non-linear sawtooth pattern in average void radius reflects intermittent void coalescence events.
- For $M_s/M_v = \{4, 5, 10\}$, the average void radius stabilises after an initial increase, confirming that voids reach an equilibrium size. This stabilisation marks the onset of a periodic void superlattice, where void growth is no longer dominated by random coarsening but instead by self-organisation into a structured pattern.

The saturation of void size at higher mobility ratios supports the hypothesis that sufficiently high M_s/M_v values facilitate void ordering and prevent indefinite coarsening. This result reinforces the presence of a critical mobility ratio threshold ($M_s/M_v \approx 3.322$), beyond which the system transitions from unbounded Ostwald ripening to the formation of a stable periodic void superlattice.

Conclusion

The average void radius evolution further confirms that mobility ratio controls void growth behaviour:

- For $M_s/M_v = \{1, 2\}$: The void radius increases indefinitely, with no stable size emerging, reflecting unbounded Ostwald ripening.
- For $M_s/M_v = \{4, 5, 10\}$: Voids begin to stabilise, showing early signs of self-limiting growth.
- For $M_s/M_v \geq 100$: The void radius converges to a characteristic equilibrium size of approximately 6 units, reinforcing the emergence of a stable superlattice.

These findings confirm sufficiently high mobility ratios halt void coarsening, enforcing a self-organised, periodic void superlattice structure.

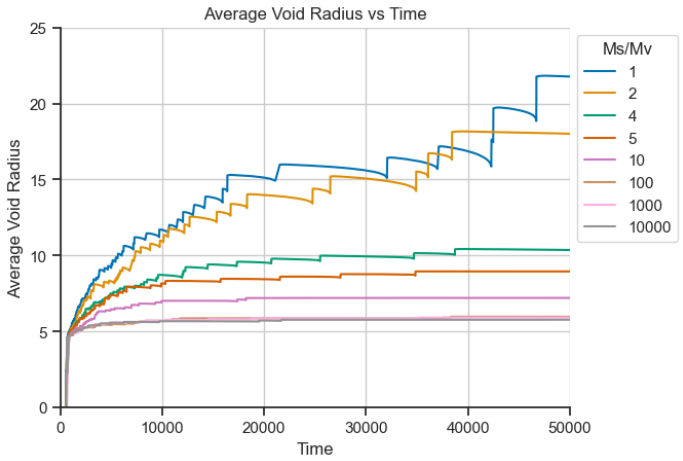

(a) Regular plot

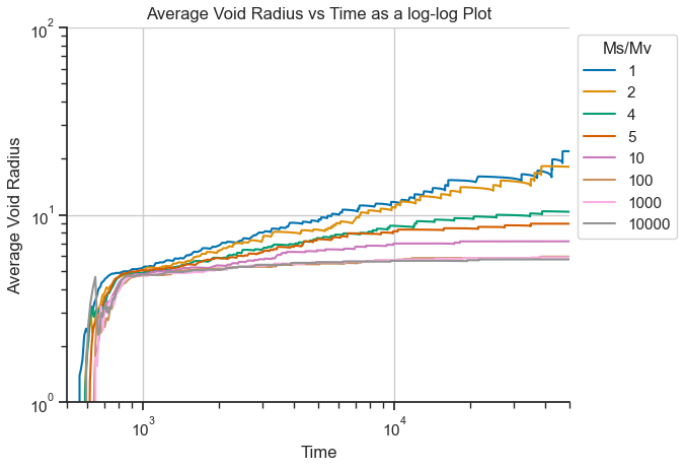

(b) Log-log plot

Figure 5.8: Average void radius over time for Experiments 1, 2, and 3 shown as (a) a regular plot and (b) a log-log plot.

Spread of Void Radius Over Time

The evolution of the spread of void radius across Experiments 1, 2, and 3 — Figure 5.9 — provides key insights into the uniformity of void sizes and the extent of void coarsening in different mobility ratio regimes.

Experiment 1:

Formation of a Void Superlattice from a Random Distribution

For $M_s/M_v = 1\,000$, the spread in void radius initially exhibits a high degree of variability, reflecting the early-stage nucleation and coarsening dynamics. At early times, $t \approx 750$ to $t \approx 1\,000$, voids form with a wide range of sizes, leading to significant fluctuations in the spread. As smaller voids shrink and disappear while larger voids stabilise, the spread decreases rapidly. By $t \approx 10\,000$, the spread has significantly reduced, and after $t \approx 20\,000$, it stabilises at a near-zero value. The minor periodic fluctuations at later times suggest that residual adjustments in void sizes continue, but overall, the system has reached a state where voids have a characteristic and uniform size. This behaviour confirms that voids in the system self-assemble into a well-ordered superlattice with minimal size variation.

Experiment 2:

Influence of M_s/M_v Ratios on Void Superlattice Stability

The spread in void radius exhibits a clear dependence on the mobility ratio, highlighting distinct transitions between Ostwald ripening and void superlattice formation:

- For $M_s/M_v = 1$, the spread remains high and fluctuates throughout the simulation, indicating persistent variations in void size. This behaviour is characteristic of Ostwald ripening, where some voids continue to grow while others shrink and disappear, leading to a broad size distribution.
- For $M_s/M_v = 10$, the spread decreases significantly compared to the $M_s/M_v = 1$ case, suggesting that voids begin to stabilise in size. However, fluctuations persist, indicating that ordering is not yet fully developed.
- For $M_s/M_v = \{100,\ 1\,000,\ 10\,000\}$, the spread reaches consistently low values, confirming that voids attain a uniform equilibrium size. This reinforces the

transition from a coarsening-dominated system to one where voids self-assemble into a periodic superlattice with minimal size variation.

The near-identical behaviour of the spread for $M_s/M_v \geq 100$ suggests a saturation effect, where additional increases in mobility ratio do not lead to further refinement in void size uniformity. These results confirm that the mobility ratio plays a central role in determining the degree of void size uniformity, with higher ratios promoting a well-defined and stable superlattice structure.

Experiment 3:

Investigating the Threshold for Void Superlattice Formation

For mobility ratios near the predicted linear stability threshold of $M_s/M_v = 3.322$, the spread of void radius highlights the transition between unbounded coarsening and the emergence of a stable void superlattice:

- For $M_s/M_v = \{1, 2\}$, sharp spikes in the spread correspond to void merging events, indicating sustained coarsening and a lack of stabilisation. The persistent fluctuations suggest that voids continue to grow at the expense of smaller voids, characteristic of Ostwald ripening.
- For $M_s/M_v = \{4, 5\}$, the spread decreases gradually at later times, suggesting a weak trend toward ordering. This aligns with the stability threshold near $M_s/M_v = 3.322$, where void interactions start to impose structural constraints.
- For $M_s/M_v = 10$, the spread remains consistently low throughout the simulation, confirming that voids reach a uniform equilibrium size with minimal merging events. This behaviour confirms that sufficiently high mobility ratios facilitate void ordering and prevent continuous size fluctuations.

These results reinforce the conclusion that the transition from unbounded Ostwald ripening to self-assembly occurs at a critical mobility ratio of approximately $M_s/M_v = 3.322$. For mobility ratios exceeding this threshold, voids reach a well-defined equilibrium size with minimal spread, supporting the emergence of a stable periodic superlattice.

Conclusion

The spread in void radius provides a direct measure of void size uniformity and the transition from disordered coarsening to ordered self-assembly:

- For $M_s/M_v = \{1, 2\}$: The spread remains high and erratic, dominated by frequent void merging and size fluctuations typical of Ostwald ripening.
- For $M_s/M_v = \{4, 5, 10\}$: The spread gradually decreases, showing the early stages of void size uniformity.
- For $M_s/M_v \geq 100$: The spread stabilises at low values, confirming that voids have attained a uniform equilibrium size within a periodic superlattice.

These results reinforce that void self-assembly imposes structural constraints, leading to consistent void sizes and a well-ordered spatial arrangement beyond the critical mobility threshold.

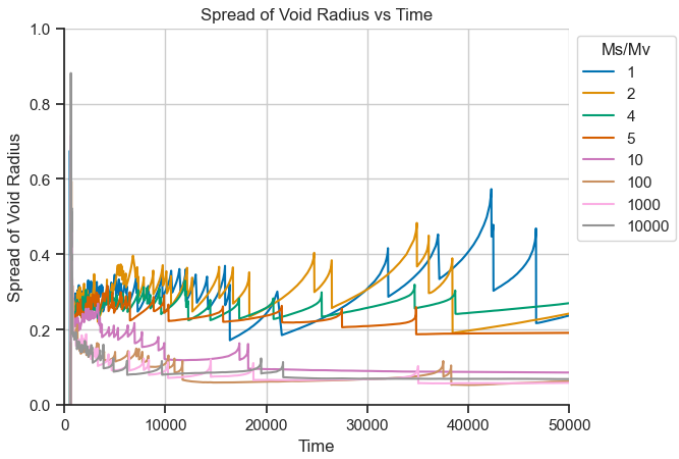

(a) Regular plot

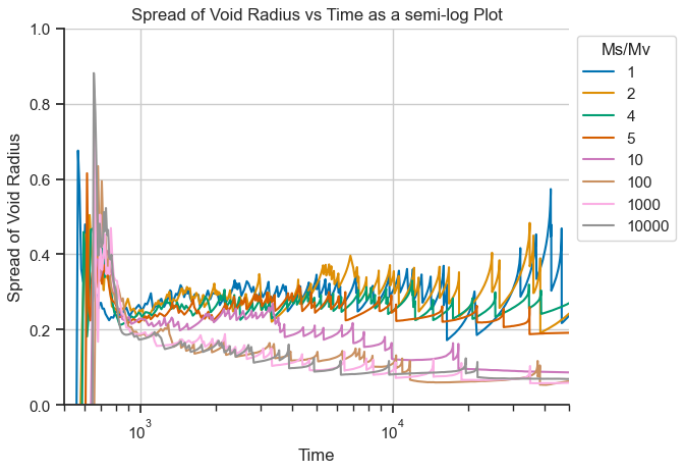

(b) Semi-log plot

Figure 5.9: Spread of void radius over time for Experiments 1, 2, and 3 shown as (a) a regular plot and (b) a semi-log plot.

Median Void Nearest Neighbour Distance Over Time

The median nearest neighbour distance provides a quantitative measure of void spatial organisation, highlighting the transition from random coarsening to self-assembly into a periodic void superlattice. The evolution of nearest neighbour distances across Experiments 1, 2, and 3 — Figure 5.10 — captures the effect of increasing mobility ratio on void spacing regularity.

Experiment 1:

Formation of a Void Superlattice from a Random Distribution

For $M_s/M_v = 1\,000$, the median nearest neighbour distance initially increases as voids nucleate and coarsen. This rapid growth phase continues until $t \approx 10\,000$, where voids begin to stabilise in size and spacing. By $t \approx 20\,000$, the nearest neighbour distance converges to a steady value, indicating that the voids have self-organised into a stable periodic lattice.

The final equilibrium distance of approximately 24.53 units confirms the emergence of long-range order, consistent with a hexagonal close-packed superlattice. The absence of large fluctuations in spacing at late times further supports the conclusion that voids have settled into a periodic structure.

Experiment 2:

Influence of M_s/M_v Ratios on Void Superlattice Stability

The impact of the mobility ratio on void spacing follows a systematic trend:

- For $M_s/M_v = 1$: Nearest neighbour distances remain highly variable, with no sign of convergence. Voids undergo continuous merging and growth, never reaching a stable configuration, as expected from unbounded Ostwald ripening.
- For $M_s/M_v = 10$: The median nearest neighbour distance stabilises earlier compared to lower ratios, but ordering remains weak.
- For $M_s/M_v = \{100, 1\,000, 10\,000\}$: Void spacing rapidly stabilises, reaching an equilibrium distance that remains consistent throughout the remainder of the simulation. These cases exhibit virtually identical ordering behaviour, reinforcing that once the mobility ratio exceeds a threshold, further increases do not

significantly refine void positioning.

These results confirm that increasing the mobility ratio promotes void self-assembly, leading to the emergence of regular void spacing and long-range order.

Experiment 3:

Investigating the Threshold for Void Superlattice Formation

For mobility ratios near the predicted linear stability threshold of $M_s/M_v = 3.322$, a sharp transition in void spacing behaviour is observed:

- For $M_s/M_v = \{1, 2\}$: The nearest neighbour distance continues to grow, consistent with continuous void merging and random coarsening.
- For $M_s/M_v = \{4, 5, 10\}$: The nearest neighbour distance gradually stabilises, indicating the early stages of self-assembly.
- For $M_s/M_v \geq 100$: Void spacing stabilises rapidly, forming a highly ordered superlattice, where the nearest neighbour distance remains fixed at equilibrium values.

These results reinforce the presence of a critical threshold at $M_s/M_v \approx 3.322$, beyond which voids stop coarsening indefinitely and instead settle into a periodic structure.

Conclusion

The evolution of nearest neighbour distance confirms the mobility ratio as the governing parameter for void ordering:

- For $M_s/M_v = 1, 2$: No stabilisation is observed — voids merge and grow continuously, preventing long-range order.
- For $M_s/M_v = 4, 5, 10$: Void spacing begins to stabilise, but full ordering remains incomplete.
- For $M_s/M_v \geq 100$: The nearest neighbour distance rapidly converges, confirming that voids self-assemble into a stable periodic void superlattice.

These findings directly support the hypothesis that a Turing instability drives void self-assembly in nuclear-irradiated materials. The transition from random void coars-

ening to an ordered void lattice occurs once M_s/M_v exceeds a well-defined threshold, reinforcing the role of mobility contrast in void pattern formation.

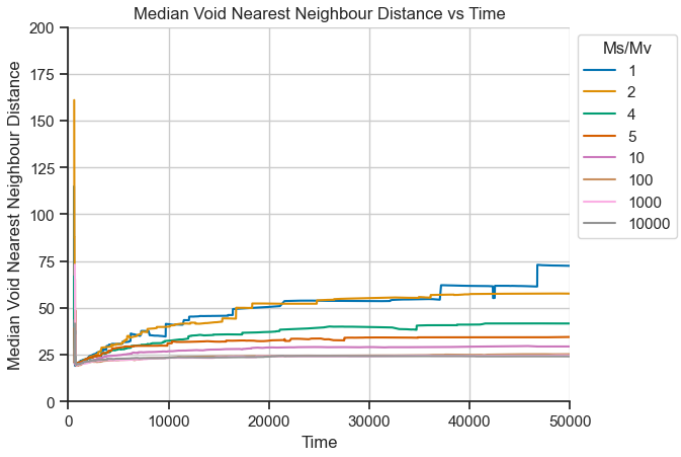

(a) Regular plot

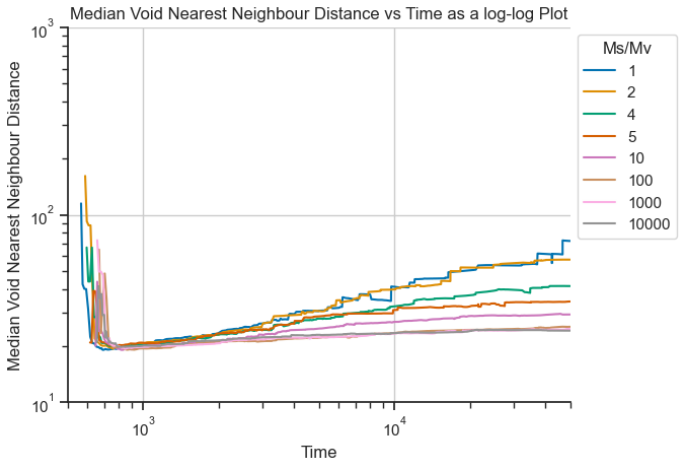

(b) Log-log plot

Figure 5.10: Median void nearest neighbour distance over time for Experiments 1, 2, and 3 shown as (a) a regular plot and (b) a log-log plot.

5.2.6 Experiments 1, 2, and 3: Conclusions

Objective

These experiments investigated the formation, stability, and threshold conditions for void superlattice structures in a reaction–diffusion system. The key focus was understanding how mobility ratios influence void self-assembly, transitioning from continuous Ostwald ripening to stable periodic ordering.

Experiment 1:

Formation of a Void Superlattice from a Random Distribution

Goal

To determine whether a void superlattice spontaneously emerges from an initially random distribution of vacancies and self-interstitials.

Findings

- At $M_s/M_v = 1\,000$, voids initially form via phase separation and subsequently self-organise into a periodic superlattice.
- Early-stage void growth is characterised by diffusion-driven interactions, with voids growing, merging, and coarsening.
- By $t \approx 10\,000$, a well-ordered hexagonal close-packed structure emerges.
- The final state at $t = 50\,000$ confirms that void self-assembly is an intrinsic property of the system under the given conditions.

Conclusion

The experiment validates theoretical predictions that, under appropriate conditions, voids naturally transition from random distributions to stable superlattices rather than undergoing unrestricted coarsening.

Experiment 2:

Influence of M_s/M_v Ratios on Void Superlattice Stability

Goal

To explore how variations in the mobility ratio M_s/M_v affect void ordering and stability.

Findings

- Five mobility ratios were tested: $M_s/M_v = 1,\ 10,\ 100,\ 1\,000,\ 10\,000$.
- At $M_s/M_v = 1$, voids undergo continuous coarsening (Ostwald ripening), showing no long-range order.
- At $M_s/M_v = 10$, voids begin stabilising, but ordering remains weak..
- At $M_s/M_v \geq 100$, voids rapidly self-organise into a stable superlattice, with spacing and size remaining consistent.
- Increasing M_s/M_v beyond 100 does not significantly enhance ordering, suggesting a saturation threshold where further increases in the mobility ratio yield diminishing structural benefits.

Conclusion

Void ordering strengthens with increasing M_s/M_v, but once a sufficiently high threshold is reached ($M_s/M_v \geq 100$), no additional structural refinement occurs.

Experiment 3:

Investigating the Threshold for Void Superlattice Formation

Goal

To determine the critical mobility ratio at which the system transitions from unstructured coarsening to self-organised void patterning.

Findings

- Five mobility ratios were tested: $M_s/M_v = 1,\ 2,\ 4,\ 5,\ 10$

- At $M_s/M_v \leq 2$, voids exhibit continuous Ostwald ripening, with persistent coarsening and no stable arrangement.
- At $M_s/M_v = 4$, early signs of self-organisation emerge, though ordering is weak.
- At $M_s/M_v = \{5, 10\}$, a periodic superlattice starts forming, but full ordering is only achieved at higher ratios
- These results confirm the theoretical threshold of $M_s/M_v \approx 3.322$, where voids transition from unstructured coarsening to a stable periodic arrangement

Conclusion

A critical mobility ratio threshold exists ($M_s/M_v \approx 3.322$) beyond which voids stop undergoing unbounded coarsening and begin self-organising into a structured superlattice.

Overall Conclusions

1. Void superlattice formation is a natural outcome of reaction–diffusion dynamics.
2. Mobility ratio is the key driver of this transition, with M_s/M_v controlling void stability, ordering, and size uniformity.
3. A threshold exists at $M_s/M_v \approx 3.322$, beyond which the system self-organises rather than undergoing continuous coarsening
4. For $M_s/M_v \geq 100$, void ordering saturates, meaning further increases in mobility ratio do not refine the pattern further
5. These findings reinforce the hypothesis that a Turing-like instability governs void superlattice formation in irradiated materials.

This series of experiments provides direct evidence that self-assembled void superlattices emerge from reaction–diffusion interactions, with the mobility ratio acting as the primary control parameter.

5.3 Experiment 4: The Role of Domain Size in Void Superlattice Self-Assembly

5.3.1 Experiment 4: Experiment Recap

Experiment 4 extended the analysis of void superlattice formation by examining the role of domain size in the pattern formation process. While Experiments 1, 2, and 3 focused on the impact of mobility ratio, Experiment 4 sought to determine whether domain size imposed constraints or introduced artefacts that could affect void self-assembly.

A key question was whether increasing or decreasing the system size would alter the fundamental ordering behaviour by enabling new long-range interactions or introducing potential boundary effects present in smaller domains. By systematically varying the domain size while keeping all other parameters constant, Experiment 4 aimed to establish whether void superlattice formation is an intrinsic, scale-independent property of the system.

5.3.2 Experiment 4: Simulation Setup and Parameters

The simulation setup for Experiment 4 was designed to maintain consistency with Experiments 1, 2, and 3 while introducing a systematic variation in domain size. To ensure direct comparability, all parameters except for the domain size remained unchanged:

- **Mobility values**: $M_s = 1\,000$, $M_v = 1$
- **Surface energy terms**: $\gamma_s = \gamma_v = 1$
- **Mean concentrations**: $\bar{v} = 0.25$, $\bar{s} = 0.01$

- **Reaction coefficients**: $a = -0.5$, $c = 0.00125$
- **Initial conditions**: Uniform random perturbation, $\bar{v} = 0.25 \pm 1\%$ and $\bar{s} = 0.01 \pm 1\%$
- **Boundary conditions**: Periodic

The domain size was systematically varied across five cases:

- 50×50 units (grid resolution: 100×100)
- 100×100 units (grid resolution: 200×200)
- 200×200 units (grid resolution: 400×400)
- 300×300 units (grid resolution: 600×600)
- 400×400 units (grid resolution: 800×800)

Each simulation was run until $t = 50\,000$ to allow the system to reach steady state. The number of required time steps varied depending on domain size, they are recorded in Table 5.8.

Domain Size	Number of Time Steps
50×50	272
100×100	412
200×200	540
300×300	668
400×400	811

Table 5.8: Number of time steps required for different domain sizes in Experiment 4.

The simulations were run on a Google Cloud Platform `n2-standard-128` virtual machine (128 vCPUs, 512 GB RAM). The completion times of the simulations scaled with the domain size as seen in Table 5.9.

Domain Size	Approximate Completion Time
50×50	10–20 minutes
100×100	1 hour
200×200	3–5 hours
300×300	1 day
400×400	3–5 days

Table 5.9: Approximate simulation completion times for different domain sizes on a GCP `n2-standard-128` virtual machine for Experiment 4.

ParaView was used to visualise the simulation results at key timestamps. The approximate written times and the exact timestamps recorded in the simulation outputs are shown in Table 5.10.

Written Time	Exact Simulation Time (t)				
	50×50	100×100	200×200	300×300	400×400
$t \approx 650$	671.173	654.65	657.179	651.683	654.621
$t \approx 750$	761.658	753.838	754.393	752.752	755.927
$t \approx 1\,000$	1 002.64	1 026.1	1 015.52	1 004.61	1 000.85
$t \approx 5\,000$	5 132.31	5 057.58	5 028.07	5 028.81	5 011.57
$t \approx 10\,000$	10 162.6	10 104.4	10 020.8	10 027.1	10 037.4
$t = 50\,000$	50 000	50 000	50 000	50 000	50 000

Table 5.10: Timestamp map for Experiment 4.

5.3.3 Experiment 4:

Simulation Results and Analysis

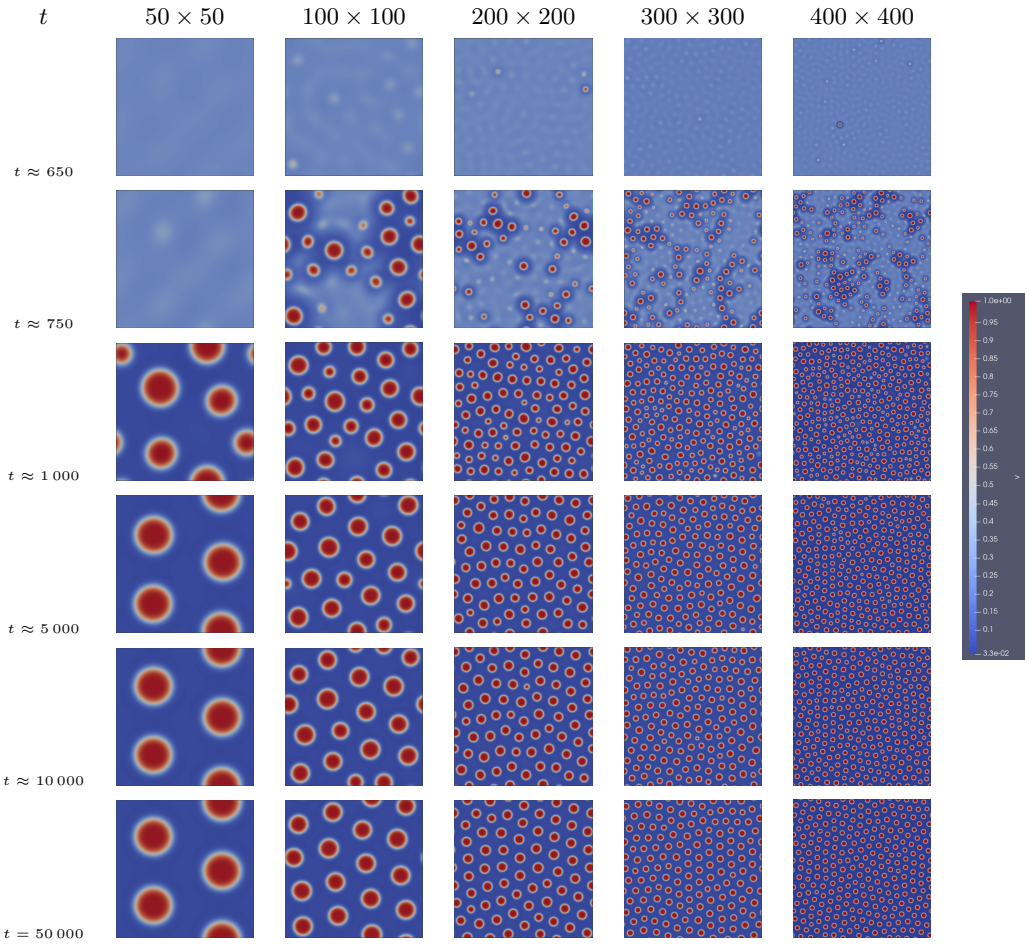

Figure 5.11: MOOSE simulation results for Experiment 4, which explored the role of the domain size in void superlattice self-assembly. The ParaView colour legend is shown to the right.

The simulation results for Experiment 4, shown in Figure 5.11, examine the influence of domain size on void superlattice formation. Building on Experiments 1–3, this experiment assesses whether the observed self-assembly process is an intrinsic property of the system or an artefact of finite domain effects.

Across all domain sizes, voids nucleate, grow, and self-organise into a hexagonal superlattice, following the same evolution pathway. Smaller domains appear as a "zoomed-in" version of larger ones, capturing fewer voids but maintaining the same characteristic spacing and patterning. The smallest domain (50×50) exhibits some spatial constraints, but beyond 100×100, the self-assembled structure remains consistent, confirming that finite-size effects are negligible at sufficiently large scales.

These results demonstrate that void superlattice formation is robust and independent of domain size, provided the domain is large enough to accommodate multiple void spacings. The model exhibits scale invariance, reinforcing that the observed self-assembly behaviour is an intrinsic property of the system rather than an artefact of simulation constraints.

5.3.4 Experiment 4: Fast Fourier Transform Analysis

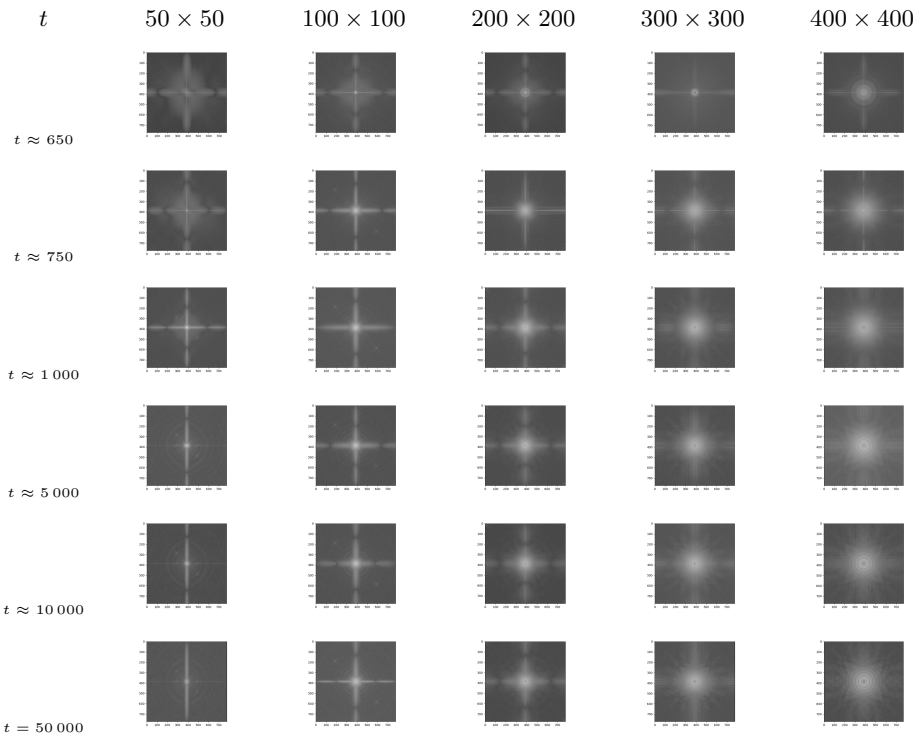

Figure 5.12: Fast Fourier Transform analysis of MOOSE simulation results for Experiment 4.

The Fast Fourier Transform (FFT) analysis, shown in Figure 5.12, provides a quantitative measure of the periodicity and structural ordering of the void superlattice across different domain sizes. These results correspond directly to the simulation images in Figure 5.11, capturing the transition from an initially disordered state to a well-defined periodic structure.

At early times ($t \approx 650$), the FFT spectra remain diffuse across all domain sizes, confirming the absence of long-range periodicity. This aligns with the simulation results, where voids have not yet fully nucleated or organised.

By $t \approx 750$, void formation begins, but the FFT spectra remain diffuse, indicating

that periodicity has yet to emerge. At $t \approx 1\,000$, faint peaks start to develop, particularly in larger domains (100×100 and above), marking the early stages of structural organisation.

By $t \approx 5\,000$, the FFT spectra exhibit sharper peaks, reflecting increased void ordering. The transition is more apparent in the 300×300 and 400×400 domains, where a clearer periodic pattern emerges. The smallest domain (50×50) also develops periodic features, but its constrained size limits long-range order, and no further improvement is observed beyond this point.

At $t \approx 10\,000$, well-defined sixfold symmetric peaks appear in all sufficiently large domains, confirming the formation of a hexagonal close-packed void superlattice. The 300×300 and 400×400 domains exhibit the strongest and most consistent spectral peaks, benefiting from a larger dataset reducing the noise.

At the final simulation time ($t = 50\,000$), the FFT spectra remain stable across all domains except the smallest, reinforcing that the system has reached a steady-state configuration. The peak intensity and positions are consistent across the larger domains, demonstrating that void self-assembly follows a scale-invariant process, provided the system is large enough to support multiple void spacings.

These results confirm that void superlattice formation is a robust and intrinsic property of the system, unaffected by domain size beyond a critical threshold. The FFT analysis quantitatively validates the visual observations, showing that periodic ordering emerges naturally and stabilises, with larger domains providing the clearest representation of the superlattice structure.

5.3.5 Experiment 4: Statistical Analysis

Number of Voids Over Time

Figure 5.13 shows the number of voids over time for five domain sizes, ranging from 50×50 to 400×400. Despite the change in absolute void count, all cases followed the same qualitative trajectory: an initial increase during void nucleation, a sharp decline during coarsening, and eventual stabilisation as the system approached a steady-state superlattice configuration.

The 50×50 domain displayed minor deviations in timing due to spatial constraints, with slightly delayed nucleation. However, beyond this, all other domain sizes evolved identically. The final void count scaled linearly with domain size, preserving void density across systems and confirming that void elimination dynamics are unaffected by scale. These results affirm that void self-assembly is intrinsically domain size invariant.

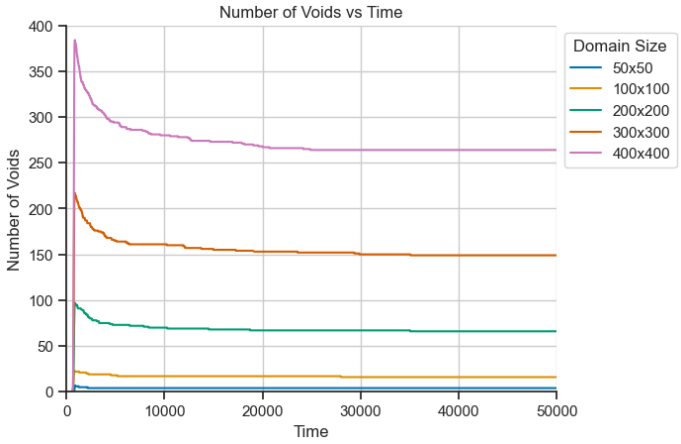

(a) Regular plot

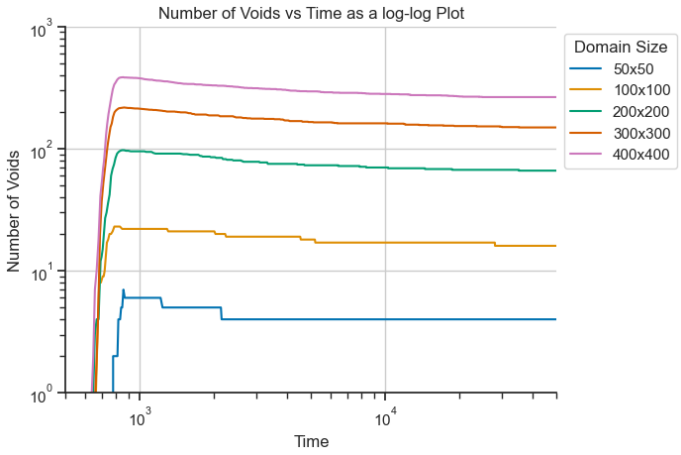

(b) Log-log plot

Figure 5.13: Number of voids over time for Experiment 4 shown as (a) a regular plot and (b) a log-log plot.

Average Void Radius Over Time

As shown in Figure 5.14, the average void radius increased across all domain sizes following the onset of coarsening. Initially, voids grew rapidly due to nucleation and the elimination of smaller neighbours, with growth slowing after $t \approx 10\,000$ as the system approached equilibrium.

Final average void radii were virtually identical across domains, confirming that void size is dictated by the reaction–diffusion dynamics rather than spatial scale. Larger domains simply hosted more voids; they did not affect individual void growth trajectories. This confirms that the self-assembly process imposes a characteristic equilibrium void size, independent of the simulated system's domain size.

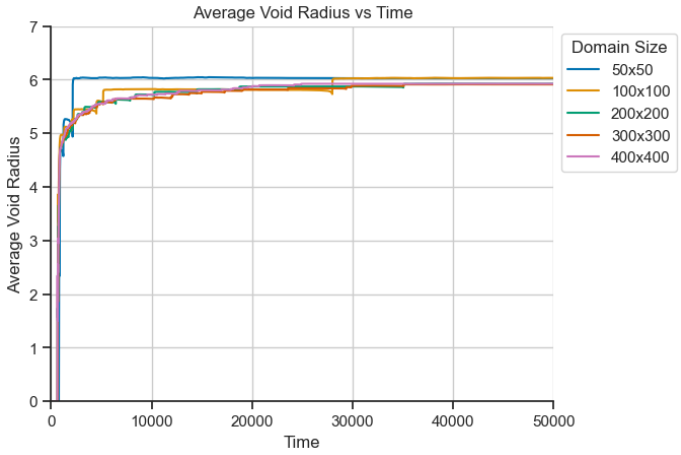

(a) Regular plot

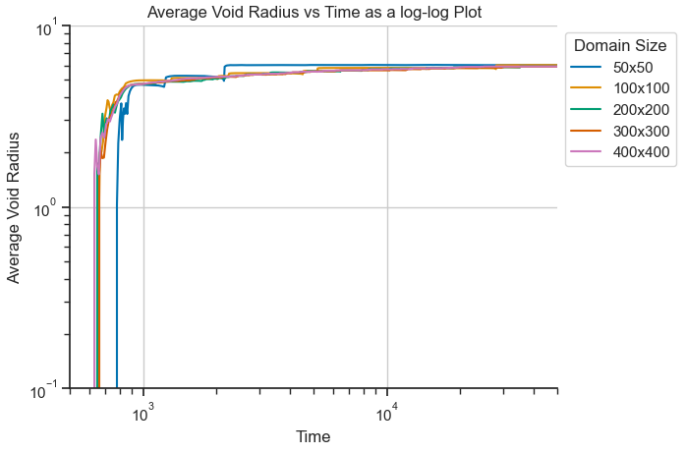

(b) Log-log plot

Figure 5.14: Average void radius over time for Experiment 4 shown as (a) a regular plot and (b) a log-log plot.

Spread of Void Radius Over Time

Figure 5.15 presents the spread in void radius as a function of time. All systems showed a marked early decline in spread as merging eliminated smaller voids and the population became more uniform in size. This stabilisation process occurred consistently across domain sizes.

The 50×50 domain exhibited a markedly sharper convergence, with the spread in void radius dropping by nearly two orders of magnitude below the larger domains. This reflects the reduced number of voids and diminished statistical variance, but reinforces that void size uniformity is a robust and emergent feature of the self-assembly process across all scales.

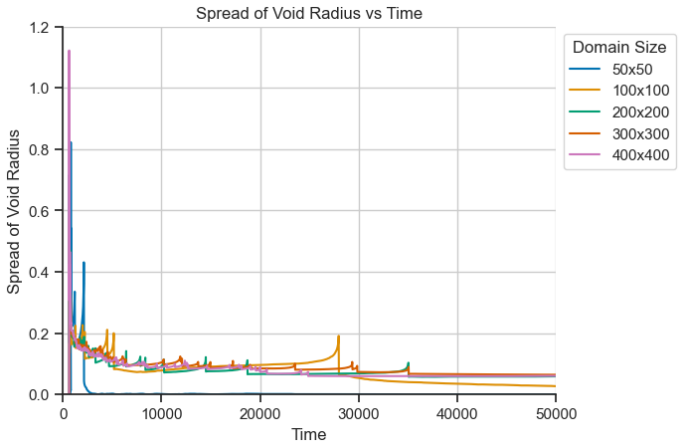

(a) Regular plot

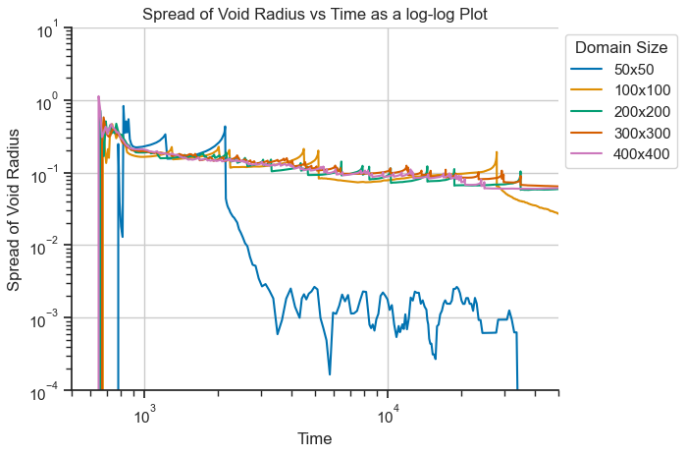

(b) Semi-log plot

Figure 5.15: Spread of void radius over time for Experiment 4 shown as (a) a regular plot and (b) a semi-log plot.

Median Nearest-Neighbour Distance Over Time

The evolution of median nearest-neighbour distance is shown in Figure 5.16. In all cases, spacing decreased as the system transitioned from a disordered, randomised initial distribution to an ordered superlattice. The final equilibrium distance stabilised at approximately 25 units, matching the analytically predicted spacing $\Lambda \approx 25.13$. Crucially, this convergence was invariant to domain size. Larger systems contained more voids but preserved the same characteristic spacing. These results further confirm that void self-assembly is governed by the underlying energy landscape of the model, not by the simulated system's domain size.

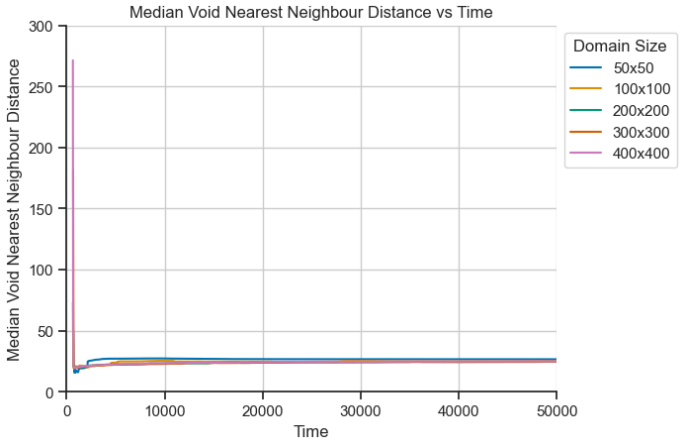

(a) Regular plot

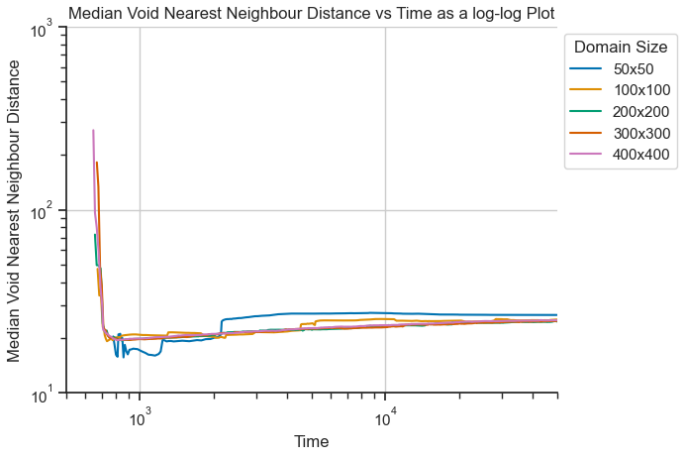

(b) Log-log plot

Figure 5.16: Median void nearest neighbour distance over time for Experiment 4 shown as (a) a regular plot and (b) a log-log plot.

5.3.6 Experiment 4: Conclusions

Objective

Experiment 4 examined the role of domain size on void superlattice formation to determine whether finite-size effects impact self-assembly. Unlike Experiments 1–3, which focused on mobility ratio, this study systematically varied the domain size while keeping all other parameters constant. The goal was to assess whether void pattern formation is an intrinsic, scale-independent property of the system.

Findings

- Five domain sizes were tested: 50×50, 100×100, 200×200, 300×300, and 400×400.
- Across all domain sizes, voids nucleate, coarsen, and self-organise into a hexagonal close-packed void superlattice following the same evolution pathway.
- Smaller domains appear as "zoomed-in" versions of larger ones, containing fewer voids but maintaining identical characteristic spacing and patterning.
- Key structural metrics, including the number of voids, average void radius, spread of void radius, and median nearest-neighbour distance were independent of domain size.
- Fast Fourier Transform analysis confirmed that periodic ordering emerges at the same rate and stabilises identically across sufficiently large domains.

Comparison with Experiments 1–3

- Experiments 1–3 established that mobility ratio is the primary driver of void superlattice formation. Experiment 4 reinforces these findings by showing that this process remains robust across different system sizes.
- Whereas Experiments 1–3 identified a mobility ratio threshold ($M_s/M_v \approx 3.322$) for self-assembly, Experiment 4 confirms that once voids begin ordering, domain

size has no effect on their final configuration.

- The findings from Experiment 4 support the hypothesis that void superlattices are a natural, emergent phenomenon in reaction–diffusion systems rather than an artefact of simulation constraints.

Overall Conclusions

Experiment 4 demonstrates that void superlattice formation is an intrinsic and scale-invariant property of the system:

1. Void self-assembly follows the same fundamental process regardless of domain size.
2. Structural properties, including void size, spacing, and ordering remain consistent across all domains.
3. Finite-size effects are negligible beyond a critical threshold (100×100), confirming that the observed self-assembly behaviour is the proper behaviour of the system.

Overall, Experiment 4 provides compelling evidence that void superlattice formation is an intrinsic property of the system, governed by reaction–diffusion dynamics rather than domain constraints. These findings reinforce the robustness of self-assembled void structures and confirm their scale-invariance in my reaction–diffusion framework.

5.4 Experiments 5 and 6: Influence of Initial Void Conditions on Superlattice Self-Assembly

5.4.1 Experiment 5: Self-Assembly of a Pre-Existing Void Population

Experiment 5:

Experiment Objective

Experiment 5 investigated whether a randomly distributed population of pre-existing voids would self-organise into a periodic superlattice over time. Unlike previous experiments that began with randomly distributed point defects, this setup directly initialised voids to assess their migration, coalescence, and potential stabilisation into an ordered structure.

To achieve this, 65 voids were randomly placed based on the final $t = 50\,000$ state of Experiment 1. Each void had an average radius of 5.9 and a minimum spacing of 15 units to prevent overlap. The corresponding self-interstitial atom concentration was adjusted to match the void locations. The objective was to assess whether these voids evolved into a stable, periodic arrangement through migration and interactions.

Experiment 5:

Simulation Setup and Parameters

To ensure comparability with previous experiments, the simulation setup followed the same parameter selection while modifying the initial condition to introduce pre-existing voids. The simulation domain and numerical discretisation remained consistent:

- **Domain size**: 200×200 units
- **Grid resolution**: 400×400

- **Boundary conditions**: Periodic
- **Mobility values**: $M_s = 1\,000$, $M_v = 1$
- **Surface energy terms**: $\gamma_s = \gamma_v = 1$
- **Reaction coefficients**: $a = -0.5$, $c = 0.00125$

The initial void and self-interstitial atom structure was generated using the `MultiSmoothCircleIC` class, the parameters are shown in Table 5.11.

	`[./v_IC]`	`[./s_IC]`
`variable`	v	s
`invalue`	1.0	0.0068
`outvalue`	0.034	0.00692
`bubspac`	15.0	15.0
`numbub`	65	65
`radius`	5.9	5.9
`int_width`	1.0	1.0
`rand_seed`	111	111
`radius_variation`	0	0
`radius_variation_type`	`normal`	`normal`

Table 5.11: Table of `MultiSmoothCircleIC` parameter values for Experiment 5.

The initial concentration of vacancies and self-interstitial atoms were calculated by the MOOSE post-processor `ElementAverageValue` to be $\bar{v} = 0.205$ and $\bar{s} = 0.007$ respectively.

Each simulation was run until $t = 50\,000$, requiring 288 time steps to reach a final steady state. The simulation was run on a Google Cloud Platform `n2-standard-128` virtual machine (128 vCPUs, 512 GB RAM). The simulation took approximately 3 hours to complete.

ParaView was used to visualise the simulation results at key timestamps. The approximate written times and the exact timestamps recorded in the simulation outputs are shown in Table 5.12.

Written Time	Exact Simulation Time (t)
$t = 0$	0
$t \approx 500$	538.408
$t \approx 750$	751.301
$t \approx 1\,000$	1 000.61
$t \approx 2\,500$	2 521.47
$t \approx 5\,000$	5 184.05
$t \approx 10\,000$	10 132
$t \approx 20\,000$	20 219.9
$t = 50\,000$	50 000

Table 5.12: Timestamp map for MOOSE Experiment 5.

Experiment 5:

Simulation Results and Analysis

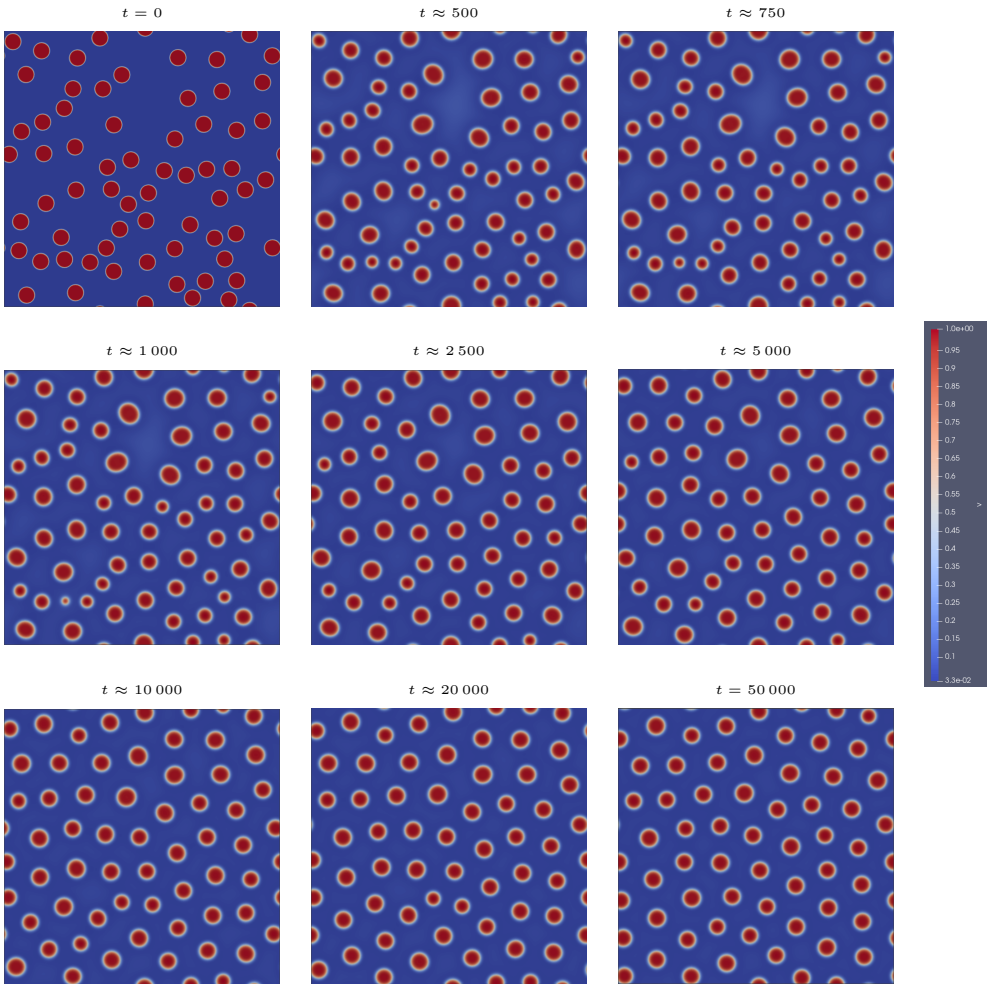

Figure 5.17: MOOSE simulation results for Experiment 5 demonstrating the evolution of a void superlattice from an initially random distribution of pre-existing voids. The ParaView colour legend is shown to the right.

The simulation results for Experiment 5 (Figure 5.17) illustrate the evolution of a pre-existing void population. Unlike previous experiments, where voids emerged from a uniform random distribution of vacancies and self-interstitial atoms, this experiment

began with a predefined set of randomly positioned voids and examined whether they would self-organise into a superlattice.

At $t = 0$, the voids are randomly positioned without any apparent periodic structure. By $t \approx 500$, diffusion-driven interactions cause voids to shift, initiating early-stage reorganisation. This movement continues through $t \approx 750$ to $t \approx 1\,000$, with voids merging or dissolving as they migrate toward more stable configurations.

By $t \approx 2\,500$, voids increasingly move into preferred locations, with early indications of local ordering. However, the overall structure remains undefined, and a well-defined lattice has yet to emerge. Around $t \approx 5\,000$, the reorganisation intensifies, with voids clustering into a more structured arrangement, though some continued movement and disorder persists. By $t \approx 10\,000$, a recognisable hexagonal close-packed pattern has formed, marking the transition to a stable superlattice.

At later times ($t \approx 20\,000$ to $t = 50\,000$), the system reaches a steady state, with only minor adjustments as voids fully stabilise into a periodic superlattice. The final configuration closely matches the structures observed in Experiments 1–4, confirming that void self-assembly is an intrinsic process. Voids not initially aligned with lattice sites either migrate to stable positions or disappear, reinforcing the idea that the hexagonal superlattice represents the system's natural equilibrium state.

These results demonstrate that self-assembly is robust and independent of the initial void configuration. Even when starting from a predefined void population, the system naturally evolves toward the same ordered structure, driven by diffusion and coarsening dynamics.

5.4.2 Experiment 6: Effect of Initial Void Size Variability

Experiment 6:

Experiment Objective

Experiment 6 extended the investigation of pre-existing void populations by examining the impact of initial void size variations on the self-assembly process. While

Experiment 5 assessed whether randomly positioned voids evolved into a periodic superlattice, this experiment systematically varied the initial void radii to determine whether size heterogeneity influenced structural stability or final void configuration. To achieve this, the `radius_variation` parameter in the `MultiSmoothCircleIC` class was adjusted to introduce controlled variations of ±0%, ±20%, ±40%, ±60%, and ±80% in initial void size. The goal was to assess whether voids of different initial radii converged to a uniform equilibrium state or if variations persisted throughout the simulation.

Experiment 6:

Simulation Setup and Parameters

To maintain consistency with Experiment 5, the simulation parameters remained unchanged except for the controlled variation in void size:

- **Domain size**: 200×200 units
- **Grid resolution**: 400×400
- **Boundary conditions**: Periodic
- **Mobility values**: $M_s = 1\,000$, $M_v = 1$
- **Surface energy terms**: $\gamma_s = \gamma_v = 1$
- **Reaction coefficients**: $a = -0.5$, $c = 0.00125$

The initial void distribution was generated using the `MultiSmoothCircleIC` class with a fixed number of voids (65) while varying the `radius_variation` parameter. The initial average concentrations of vacancies ($\bar{v}$) and self-interstitial atoms ($\bar{s}$) were computed using the MOOSE `ElementAverageValue` post-processor. The results are shown in Table 5.13.

Radius Variation	$\bar{v}$	$\bar{s}$
±0%	0.2059	0.006936
±20%	0.2049	0.006936
±40%	0.2051	0.006936
±60%	0.2119	0.006933
±80%	0.2073	0.006935

Table 5.13: Initial concentrations of $\bar{v}$ and $\bar{s}$ for Experiment 6.

Each simulation was run until $t = 50\,000$, requiring 275 to 294 time steps depending on the mobility ratio used. The exact number of timesteps for each radius variation is shown in Table 5.14.

Radius Variation	Number of Time Steps
±0%	288
±20%	294
±40%	275
±60%	275
±80%	275

Table 5.14: Number of time steps required for different void radii in Experiment 6.

The simulations were run on a Google Cloud Platform `n2-standard-128` virtual machine (128 vCPUs, 512 GB RAM). The simulations took approximately 3–5 hours to complete per simulation, depending on the initial void size.

ParaView was used to visualise the simulation results at key timestamps. The approximate written times and the exact timestamps recorded in the simulation outputs are shown in Table 5.15.

Written Time	Exact Simulation Time (t)				
	±0%	±20%	±40%	±60%	±80%
$t = 0$	0	0	0	0	0
$t \approx 500$	538.408	538.408	538.408	578.085	506.856
$t \approx 1\,000$	1 000.61	1 020.96	1 040.7	1 006.98	1 030.08
$t \approx 5\,000$	5 184.05	5 084.25	5 222.65	5 008.84	5 002.89
$t \approx 10\,000$	10 132	10 058.8	10 012.5	10 254	10 244.1
$t = 50\,000$	50 000	50 000	50 000	50 000	50 000

Table 5.15: Timestamp map for MOOSE Experiment 6.

Experiment 6:

Simulation Results and Analysis

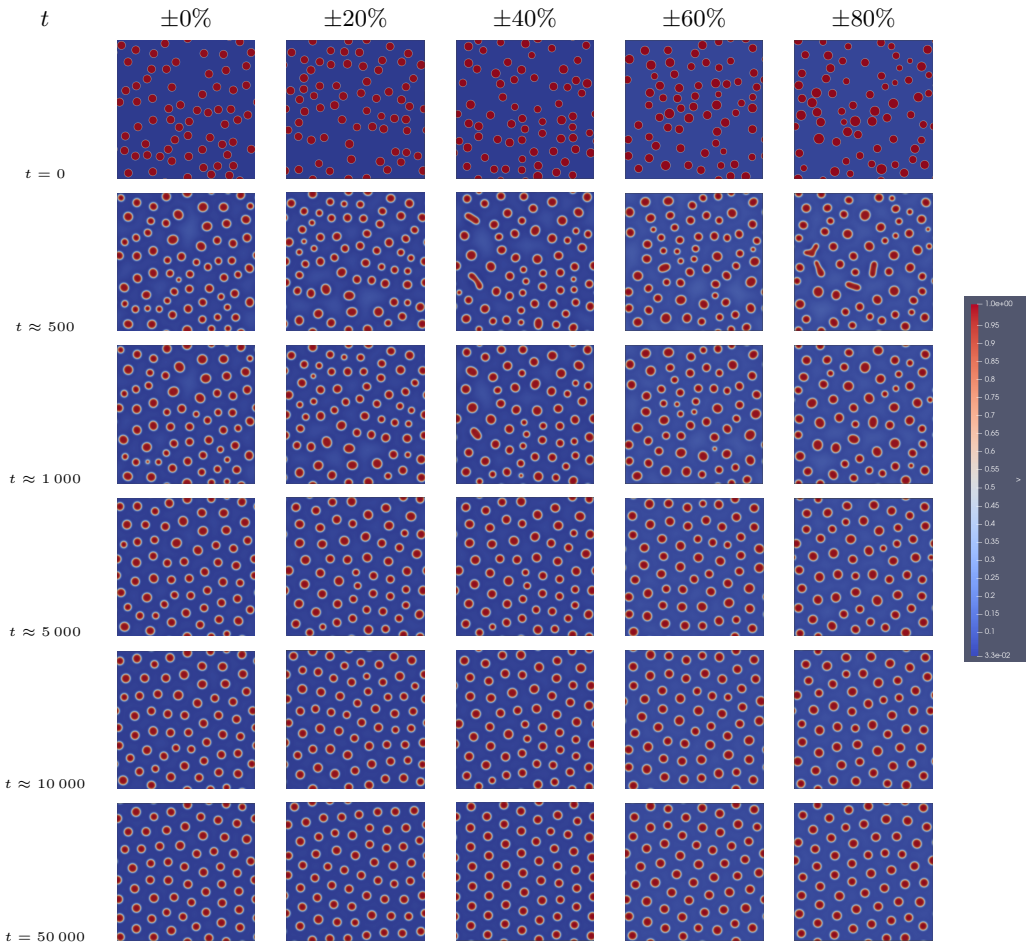

Figure 5.18: MOOSE simulation results for Experiment 6, which explored the influence of the initial void size of a random distribution of pre-existing voids on void superlattice formation and development. The ParaView colour legend is shown to the right.

The simulation results for Experiment 6, shown in Figure 5.18, demonstrate the influence of initial void size variations on superlattice formation. While void radii were varied by ±0%, ±20%, ±40%, ±60%, and ±80%, the overall self-assembly dynamics remained consistent across all cases.

At early times ($t \approx 500$ to $t \approx 1\,000$), voids began migrating and adjusting in size through reaction–diffusion interactions. Simulations with $\pm 0\%$ and $\pm 20\%$ variation exhibited relatively smooth reorganisation, while larger initial size variations ($\pm 40\%$ to $\pm 80\%$) introduced greater dynamism, with more merging and coarsening observed. Voids in the highest variation cases ($\pm 60\%$ and $\pm 80\%$) underwent significant reshuffling, leading to larger voids consuming smaller ones.

By $t \approx 5\,000$ to $t \approx 10\,000$, the influence of initial size variation had largely diminished. Voids continued to migrate and coarsen, with all cases converging towards a periodic structure. However, simulations with higher initial variation resulted in slightly fewer, more widely spaced voids due to increased early-stage merging.

At $t = 50\,000$, all cases formed a well-ordered hexagonal superlattice, confirming that self-assembly is robust against initial void size heterogeneity.

These results reinforce that void superlattice formation is an emergent property of reaction–diffusion dynamics, independent of precise initial conditions. Larger initial size variations led to more dynamic early evolution but did not prevent the system from converging to the same final ordered state.

5.4.3 Experiments 5 and 6: Fast Fourier Transform Analysis

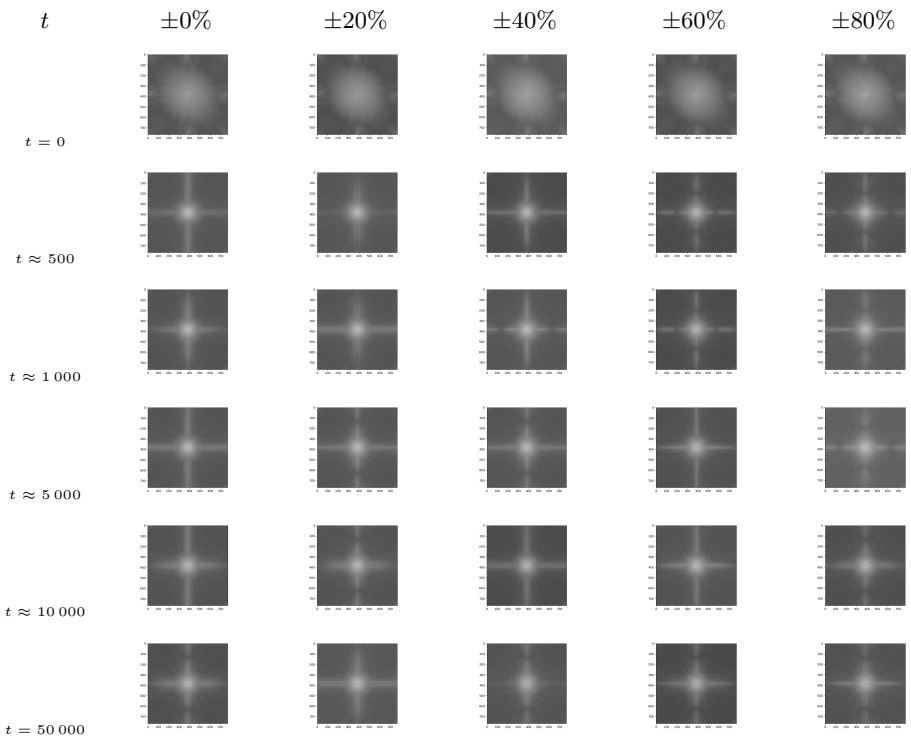

Figure 5.19: Fast Fourier Transform analysis of MOOSE simulation results for Experiments 5 and 6.

The Fast Fourier Transform (FFT) analysis provides a quantitative measure of periodic ordering in systems where voids initially follow a random distribution.

Experiment 5 investigates whether a system starting with a pre-existing but randomly distributed void population can transition into an ordered superlattice, while Experiment 6 extends this by introducing variability in the initial void radii to assess its impact on the self-assembly process.

The results of both experiments directly correspond to the simulation images shown in Figure 5.18, which captures the transition from an initially disordered state to a well-defined periodic arrangement. Experiment 5 represents the ±0% case of Experiment

6, serving as the baseline scenario without initial size variation.

Experiment 5:

Self-Assembly of a Pre-Existing Void Population

The FFT analysis of Experiment 5, shown in Figure 5.19 as the ±0% case of Experiment 6, examines whether a randomly distributed void population, without additional constraints on size, can evolve into a structured superlattice.

At $t = 0$, the FFT spectra exhibit a diffuse intensity distribution, confirming the absence of long-range periodicity. This aligns with the simulation images, where voids are randomly positioned with no apparent structure.

Between $t \approx 500$ and $t \approx 1\,000$, void movement and early-stage merging occur, but the FFT spectra remain largely diffuse. Voids migrate, merge, or dissolve, and no clear periodicity emerges, reflecting the continued dynamic rearrangement of the system.

By $t \approx 5\,000$, weak frequency peaks begin to appear, marking the onset of structural organisation. The voids start settling into more stable positions, and a periodic pattern begins forming.

At $t \approx 10\,000$, strong peaks emerge in the FFT spectra, confirming the formation of a hexagonal close-packed arrangement. The periodicity is now well-defined, though minor irregularities persist as voids continue refining their positioning.

By $t = 50\,000$, the FFT spectra remain stable, with sharp peaks indicating that the void system has fully self-organised into a void superlattice. The final state confirms that pre-existing void populations naturally transition into a structured periodic arrangement.

Experiment 6:

Effect of Initial Void Size Variability

The FFT analysis of Experiment 6, shown in Figure 5.19, extends Experiment 5 by introducing variations in initial void radii to determine whether size heterogeneity affects void self-assembly. Five levels of size variation were tested: ±0%, ±20%, ±40%, ±60%, and ±80%.

At early times ($t \approx 500$ to $t \approx 1\,000$), all size variation cases exhibit diffuse FFT spectra, confirming the absence of long-range periodicity. The system remains highly dynamic, with voids undergoing movement, coarsening, and merging. Larger initial size variations ($\pm 40\%$ to $\pm 80\%$) lead to slightly broader spectra, reflecting greater early-stage adjustments.

By $t \approx 5\,000$, weak peaks emerge across all cases, indicating the onset of structural ordering. Minor differences appear in cases with higher initial size variations due to more pronounced coarsening, merging, and dissolving, but the underlying pattern formation remains consistent.

At $t \approx 10\,000$, well-defined sixfold symmetry develops in the FFT spectra for all cases, confirming that voids have arranged into a periodic hexagonal structure. While larger initial size variations cause some residual size-dependent adjustments, the global ordering is unchanged.

By $t = 50\,000$, the FFT spectra exhibit sharp, stable sixfold peaks across all cases, demonstrating that void self-assembly follows an identical trajectory regardless of initial size heterogeneity. Although larger variations lead to more initial adjustments, the final structure remains fully periodic and invariant to the initial radii.

These results confirm that void superlattice formation is entirely independent of initial void size distribution. While increased variation affects early-stage dynamics, it does not influence the final ordering. The FFT analysis quantitatively demonstrates that the process of void self-assembly is robust, leading to a stable periodic structure regardless of initial void size.

5.4.4 Experiments 5 and 6: Statistical Analysis

Number of Voids Over Time

The evolution of the number of voids across Experiments 5 and 6 — Figure 5.20 — demonstrates that void self-assembly follows an almost identical process across all void radius variation cases, independent of initial void placement and size heterogeneity.

Experiment 5:

Self-Assembly of a Pre-Existing Void Population

For Experiment 5, where pre-existing voids were randomly distributed with no radius variation, the number of voids initially decreased due to dissolving or merging. Their random distribution makes some voids closer together, making it energetically favourable for certain voids to dissolve away or merge during the early stages.
Following this initial reduction, the system undergoes a period of reorganisation and coarsening, leading to further void elimination. By $t = 50\,000$, the number of voids stabilises at 62, confirming that a steady-state configuration has been reached.

Experiment 6:

Effect of Initial Void Size Variability

Introducing initial void size variability does not significantly alter the overall behaviour of void count evolution. Across all size variation levels ($\pm 0\%$, $\pm 20\%$, $\pm 40\%$, $\pm 60\%$, and $\pm 80\%$), the number of voids follows the same general trend as in Experiment 5. However, a subtle trend emerges where larger initial size variations result in slightly fewer final voids.

- Higher initial size variation increases the likelihood of smaller voids dissolving or merging early on, leading to a marginally lower void count.
- By $t \approx 5\,000$, the number of voids across all cases begins stabilising, and by $t = 50\,000$, the final void count falls within the range 57–62, confirming that any early differences due to size variation do not affect the long-term equilibrium state.

Conclusion

The number of voids over time confirms that void superlattice formation is largely independent of initial void size distribution. While larger size variations lead to slightly lower final void counts due to increased early-stage merging and dissolving, the overall self-assembly process remains unchanged. The final number of voids is remarkably consistent across all cases, reinforcing that diffusion-driven interactions, rather than initial conditions, dictate the steady-state configuration.

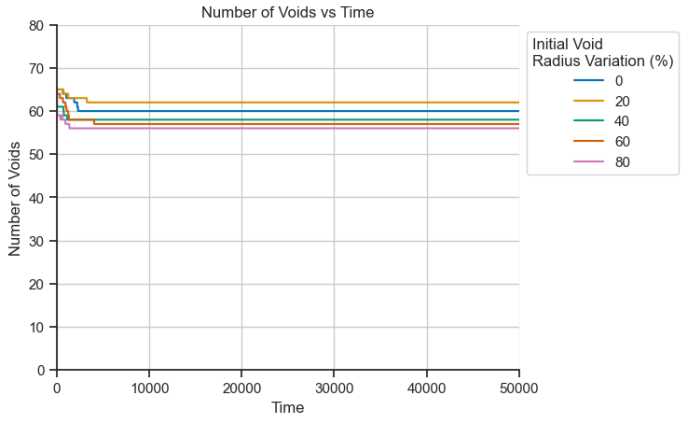

(a) Regular plot

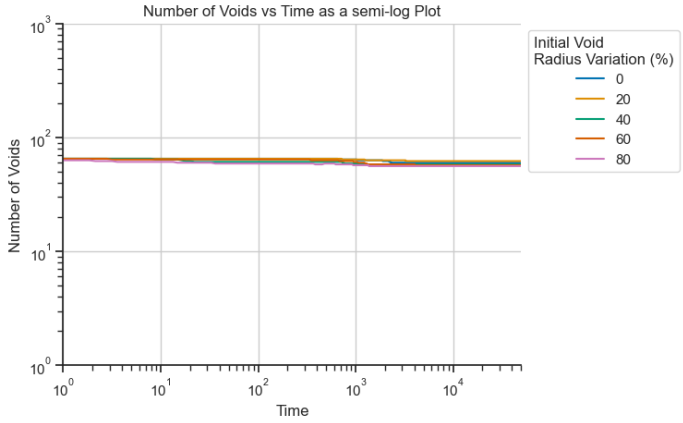

(b) Log-log plot

Figure 5.20: Number of voids over time for Experiments 5 and 6 shown as (a) a regular plot and (b) a log-log plot.

Average Void Radius Over Time

The evolution of the average void radius across Experiments 5 and 6 — Figure 5.21 — demonstrates that voids grow and stabilise to a characteristic equilibrium size, regardless of initial void distribution or size heterogeneity.

Experiment 5:

Self-Assembly of a Pre-Existing Void Population

For Experiment 5, the average void radius initially increases as voids coarsen and merge. This growth continues until $t \approx 1\,000$, after which smaller voids are eliminated or merged into larger ones. By $t \approx 10\,000$, the growth rate slows, and voids reach a stable characteristic size, which remains unchanged until the end of the simulation at $t = 50\,000$.

Experiment 6:

Effect of Initial Void Size Variability

The introduction of size heterogeneity slightly affects early void growth but does not meaningfully change the final void radius.

- Higher initial variations ($\pm 40\%$ to $\pm 80\%$) lead to a broader range of void sizes in the early stages, but as voids merge and coarsen, this variation diminishes.
- By $t \approx 10\,000$, the average void radius converges across all cases, indicating that self-assembly enforces a characteristic void size regardless of initial size heterogeneity.

At $t = 50\,000$, all cases exhibit nearly identical void radii, confirming that the final equilibrium size is an intrinsic property of the system.

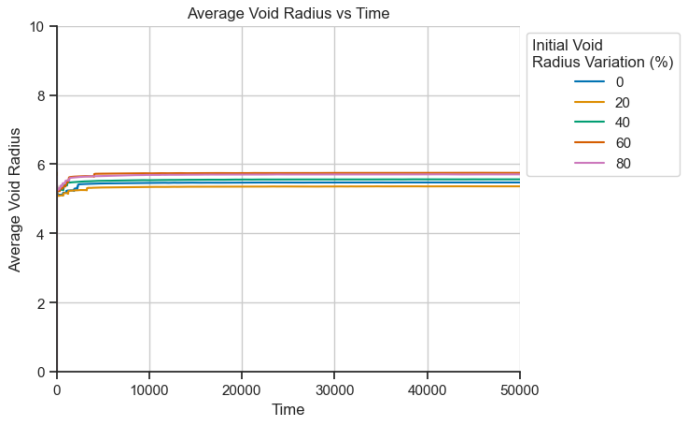

(a) Regular plot

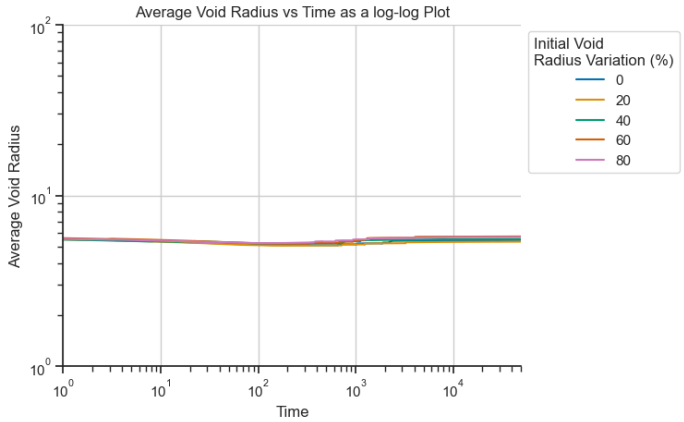

(b) Log-log plot

Figure 5.21: Average void radius over time for Experiments 5 and 6 shown as (a) a regular plot and (b) a log-log plot.

Spread of Void Radius Over Time

The evolution of the spread of void radius across Experiments 5 and 6 — Figure 5.22 — highlights how void sizes become more uniform as self-assembly progresses. While the spread decreases in all cases, larger initial void size variations result in more erratic behaviour during the early stages due to increased coarsening, merging, and dissolution.

Experiment 5:

Self-Assembly of a Pre-Existing Void Population

For Experiment 5, the spread in void radius initially fluctuates as voids undergo shrinking, coarsening, and merging. These interactions lead to rapid changes in void size, introducing short-lived spikes in the spread. As voids stabilise into preferred configurations, the spread decreases rapidly. By $t \approx 10\,000$, the spread has significantly reduced, confirming that void sizes are converging towards a uniform equilibrium state. From this point onward, the spread remains stable with minimal variation.

Experiment 6:

Effect of Initial Void Size Variability

Larger initial void size variations introduce more pronounced fluctuations in the early stages due to increased void shrinking, coarsening and merging. Higher variation cases ($\pm 40\%$ to $\pm 80\%$) exhibit larger spikes in the spread as smaller voids shrink or merge into larger ones, momentarily increasing the variability in void sizes.

- Early-stage fluctuations are more erratic in cases with larger initial variations, reflecting the higher degree of void redistribution.
- Despite these differences, all cases exhibit the same overall trend, with the spread decreasing over time.
- By $t \approx 10\,000$, the spread values in all cases begin to converge, and at $t = 50\,000$, the final spread values are nearly identical.

Conclusion

The spread in void radius confirms that self-assembly leads to a uniform void structure, regardless of initial size variation. While larger variations introduce fluctuations due to more extensive shrinking, merging, and coarsening, the long-term behaviour remains unchanged. All cases follow the same overall trend, where the spread decreases smoothly over time, demonstrating that the self-assembly process naturally eliminates initial size differences.

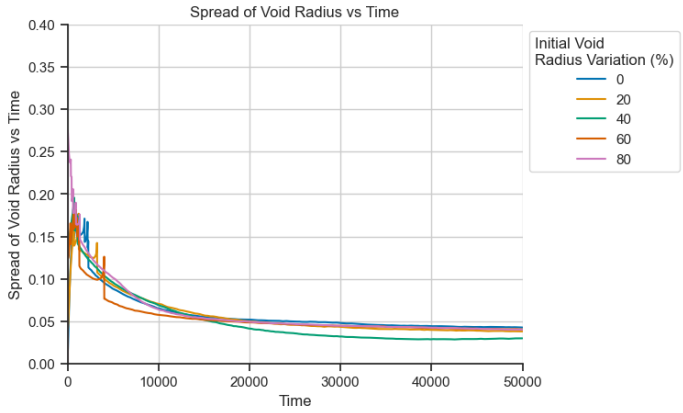

(a) Regular plot

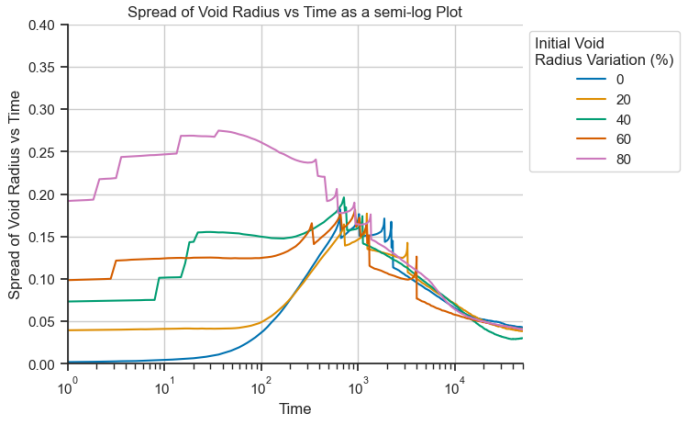

(b) Semi-log plot

Figure 5.22: Spread of void radius over time for Experiments 5 and 6 shown as (a) a regular plot and (b) a semi-log plot.

Median Void Nearest Neighbour Distance Over Time

The evolution of the median nearest neighbour distance across Experiments 5 and 6 — Figure 5.23 — provides insight into how voids rearrange and stabilise into a periodic structure. While void spacing is initially dynamic, it rapidly converges to a stable value, confirming the emergence of a void superlattice.

Experiment 5:

Self-Assembly of a Pre-Existing Void Population

For Experiment 5, the initial distribution of voids is random, leading to a wide range of nearest neighbour distances at $t = 0$. As voids migrate, merge, and coarsen, the spacing between them fluctuates, reflecting the ongoing reorganisation.

- During the first $t \approx 500$ to $t \approx 1\,000$, rapid void migration, merging, and coarsening cause sharp fluctuations in nearest neighbour distances.
- By $t \approx 5\,000$, voids begin settling into more stable locations, and fluctuations in spacing diminish.
- By $t \approx 10\,000$, the nearest neighbour distance stabilises, confirming the formation of a periodic structure.

At $t = 50\,000$, the void spacing remains unchanged, reinforcing that the system has reached its equilibrium state.

Experiment 6:

Effect of Initial Void Size Variability

Introducing initial void size variation does not significantly alter the evolution of nearest neighbour distances.

- Larger initial radius variations ($\pm 40\%$ to $\pm 80\%$) introduce minor deviations in early-stage void spacing due to increased coarsening and merging.
- By $t \approx 10\,000$, all cases stabilise at a median spacing between 25 and 27 units.
- At $t = 50\,000$, void spacing is nearly identical across all cases, confirming that self-assembly enforces a characteristic periodic arrangement.

Despite minor early-stage differences, all cases follow the same overall trend, demonstrating that void self-assembly is independent of initial size heterogeneity.

Conclusion

The median nearest neighbour distance confirms that voids naturally organise into a periodic lattice, regardless of initial void size variation. While early-stage fluctuations are more pronounced in cases with greater initial heterogeneity, the final spacing remains invariant. The system consistently converges to the same stable periodic structure, reinforcing that void self-assembly follows an intrinsic ordering principle.

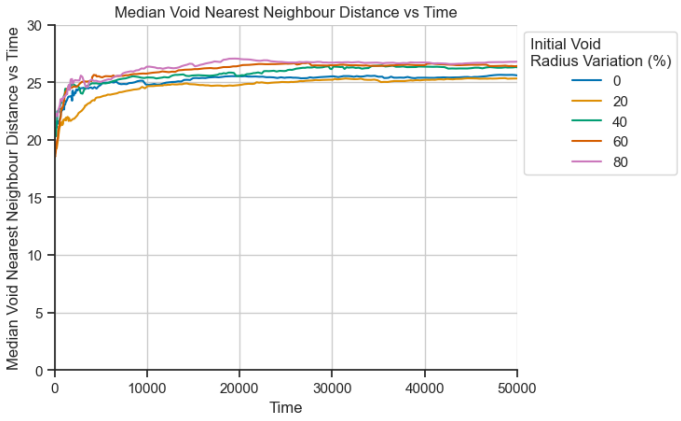

(a) Regular plot

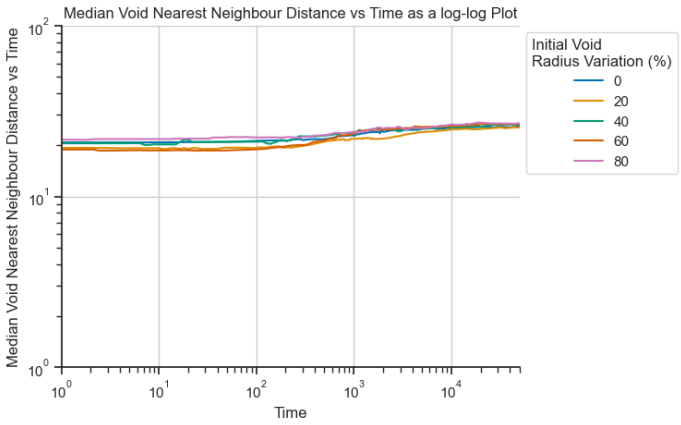

(b) Log-log plot

Figure 5.23: Median void nearest neighbour distance over time for Experiments 5 and 6 shown as (a) a regular plot and (b) a log-log plot.

5.4.5 Experiments 5 and 6: Conclusions

Objective

Experiments 5 and 6 investigated the robustness of void superlattice formation from a pre-existing and randomly distributed void population. Experiment 5 examined whether pre-existing voids, randomly placed within the simulation domain, could self-assemble into a periodic superlattice over time. Experiment 6 extended this analysis by introducing controlled variations in initial void radii, assessing whether size heterogeneity influenced the self-assembly process. The key focus was determining whether void ordering was an intrinsic property of the system, independent of initial conditions.

Experiment 5: Self-Assembly of a Pre-Existing Void Population

Goal

To determine whether a system initialised with a pre-existing, randomly distributed void population would evolve into a periodic superlattice through void migration, coarsening, and self-assembly.

Findings

- At $t = 0$, voids are randomly distributed with no discernible periodicity, as confirmed by diffuse FFT spectra and irregular nearest-neighbour distances.
- Between $t \approx 500$ and $t \approx 1\,000$, void migration and early-stage coarsening begin, but void spacing remains irregular.
- By $t \approx 5\,000$, weak frequency peaks emerge in the FFT spectra, indicating the onset of structural ordering.
- At $t \approx 10\,000$, a well-defined sixfold symmetric pattern appears in the FFT spectra, confirming that voids have settled into a periodic arrangement.
- At $t = 50\,000$, the system has fully self-organised into a stable hexagonal void superlattice, with voids maintaining a uniform size and spacing.

Conclusion

The results demonstrate that self-assembly into a periodic void superlattice is an intrinsic property of the system, independent of whether voids emerge spontaneously (as in previous experiments) or are introduced as an initial condition. Even when initialised with a pre-existing void population, the system naturally evolves towards a structured arrangement through diffusion-driven interactions and void coarsening.

Experiment 6:

Effect of Initial Void Size Variability

Goal

To assess whether variations in the initial radii of a randomly distributed void population affect void self-assembly and the stability of the final superlattice structure.

Findings

- Five levels of initial void size variability were tested: $\pm 0\%$, $\pm 20\%$, $\pm 40\%$, $\pm 60\%$, and $\pm 80\%$.
- At early times ($t \approx 500$ to $t \approx 1\,000$), voids undergo migration and coarsening, with larger variations displaying more pronounced size adjustments.
- By $t \approx 5\,000$, weak periodicity begins emerging across all cases, though void merging is more frequent at higher size variations.
- At $t \approx 10\,000$, all cases exhibit sixfold symmetric FFT peaks, confirming that self-assembly into a periodic structure is underway.
- At $t = 50\,000$, the final superlattice is identical across all cases, with voids achieving a uniform equilibrium size and spacing, regardless of initial size heterogeneity.

Conclusion

The final void arrangement remains invariant to initial void size variations, confirming that superlattice formation is independent of early-stage size heterogeneity. While larger variations introduce more dynamic early-stage behaviour, all cases ultimately

converge to the same periodic structure. This suggests that void self-assembly is governed by diffusion-driven interactions rather than the specifics of initial void size.

Overall Conclusions

1. Void self-assembly is a robust and intrinsic process, occurring regardless of whether voids form spontaneously or are pre-existing.
2. Initial void placement does not affect the final superlattice structure. Even when starting from a random void population, the system naturally evolves towards a periodic arrangement.
3. Initial void size heterogeneity has no impact on the long-term evolution of the superlattice. Larger initial size variations lead to more dynamic early-stage behaviour, but all cases converge to the same final state.
4. The formation of a periodic void superlattice is a fundamental outcome of reaction–diffusion dynamics, confirming that self-assembly is an emergent property of the system.
5. These findings reinforce the hypothesis that void pattern formation in irradiated materials is driven by diffusion-driven interactions, independent of specific initial conditions.

Experiments 5 and 6 provide direct evidence that void superlattice formation is not dependent on initial conditions such as void position or size. The system consistently transitions from a disordered state to an ordered periodic arrangement, validating that self-assembly is an intrinsic property of the system.

5.5 Experiment 7: Influence of Initial Void Number on Superlattice Formation

5.5.1 Experiment 7: Experiment Objective

Experiment 7 extended the investigation into void self-assembly by systematically varying the initial number of voids while keeping all other parameters constant. This experiment aimed to determine whether the final void count stabilises at a characteristic value regardless of the initial number of voids and whether self-assembly dynamics remain robust across different initial void populations.

While Experiment 5 demonstrated that a randomly positioned void population evolves into a periodic superlattice and Experiment 6 confirmed that self-assembly is resilient to initial void size variations, Experiment 7 examined how the number of initial voids influences the final steady-state configuration. The primary objective was to assess whether voids undergo elimination, migration, merging, and coarsening in a manner that leads to a consistent final void count and characteristic spacing.

5.5.2 Experiment 7: Simulation Setup and Parameters

To ensure comparability with Experiments 5 and 6, the simulation setup remained unchanged except for the initial void number:

- **Domain size**: 200×200 units
- **Grid resolution**: 400×400
- **Boundary conditions**: Periodic
- **Mobility values**: $M_s = 1\,000$, $M_v = 1$
- **Surface energy terms**: $\gamma_s = \gamma_v = 1$

- **Reaction coefficients**: $a = -0.5$, $c = 0.00125$

The initial void distribution was generated using the `MultiSmoothCircleIC` class, with the number of voids systematically varied while keeping all other parameters fixed:

- 35 voids
- 50 voids
- 65 voids
- 80 voids
- 95 voids

To maintain consistency, the initial average vacancy concentration ($\bar{v}$) and self-interstitial concentration ($\bar{s}$) were computed using the MOOSE `ElementAverageValue` post-processor. The results are shown in Table 5.16.

Number of Voids	$\bar{v}$	$\bar{s}$
35	0.1266	0.006977
50	0.1663	0.006956
65	0.2059	0.006936
80	0.2456	0.006915
95	0.2852	0.006895

Table 5.16: Initial concentrations of $\bar{v}$ and $\bar{s}$ for different void counts in Experiment 7.

Each simulation was run until $t = 50\,000$, with the required time steps varying based on the initial void count. The exact number of time steps for each void count is shown in Table 5.17.

Number of Voids	Number of Time Steps
35	352
50	282
65	288
80	345
95	510

Table 5.17: Number of time steps required for different initial void counts in Experiment 7.

The simulations were run on a Google Cloud Platform `n2-standard-128` virtual machine (128 vCPUs, 512 GB RAM). The simulations took approximately 3–5 hours to complete per simulation, depending on the initial void count.

ParaView was used to visualise the simulation results at key timestamps. The approximate written times and exact timestamps recorded in the simulation are shown in Table 5.18.

Written Time	Exact Simulation Time (t)				
	35	50	65	80	95
$t = 0$	0	0	0	0	0
$t \approx 500$	538.408	538.408	538.408	538.408	538.408
$t \approx 1\,000$	1 022.16	1 050.15	1 000.61	1 009.39	1 002.77
$t \approx 5\,000$	5 057.23	5 025.1	5 184.05	5 106.35	5 005.37
$t \approx 10\,000$	10 113.4	10 146.1	10 132	10 077.8	10 025.3
$t = 50\,000$	50 000	50 000	50 000	50 000	50 000

Table 5.18: Timestamp map for Experiment 7.

5.5.3 Experiment 7:

Simulation Results and Analysis

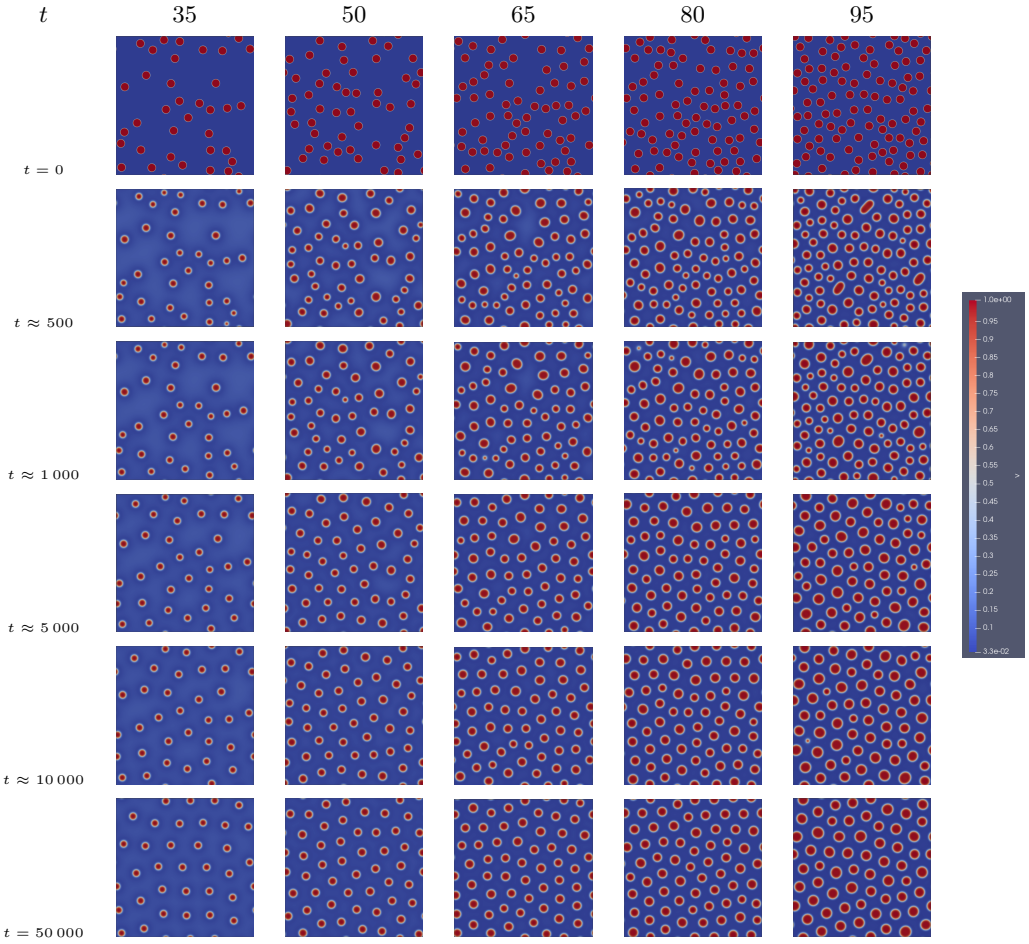

Figure 5.24: MOOSE simulation results for Experiment 7, which explored the influence of the initial void number on void superlattice formation and development. The ParaView colour legend is shown to the right.

The simulation results for Experiment 7, shown in Figure 5.24, examine the influence of initial void number on superlattice formation. Five cases were considered, with 35, 50, 65, 80, and 95 pre-existing voids randomly placed at $t = 0$. Higher initial void counts resulted in denser void distributions, while lower counts led to larger initial

spacing.

At $t \approx 500$ to $t \approx 1\,000$, voids began migrating due to diffusion-driven interactions. In cases with 80 and 95 initial voids, closely packed voids started to shrink or merge, while in the 35 and 50 void cases, voids remained stable and moved with minimal coarsening.

By $t \approx 5\,000$, voids in all cases had begun to cluster into more ordered configurations, though clear periodicity had yet to emerge. The 50- and 65-void cases exhibited the most structured void arrangements at this stage, while the 35-void case showed the weakest local ordering due to large inter-void distances. The 80- and 95-void cases remained highly dynamic, with continued merging and redistribution delaying the emergence of a clear pattern.

At $t \approx 10\,000$, all systems exhibited clearer signs of hexagonal ordering. The 50- and 65-void cases had largely stabilised into well-defined periodic patterns, with voids uniformly spaced in a near-hexagonal arrangement. In contrast, the 80- and 95-void cases continued to be more disordered due to ongoing rebalancing from their initially dense configurations. The 35-void case improved marginally but still lagged in achieving long-range periodicity.

At $t = 50\,000$, all cases had stabilised into a hexagonal close-packed arrangement, though the degree of ordering varied. The 50- and 65-void cases retained the strongest periodic structure, while the 80- and 95-void cases exhibited larger voids in a denser configuration. The 35-void case remained the weakest, with a more diffuse pattern and less pronounced long-range hexagonal order due to the larger inter-void distances and smaller voids.

These results confirm that void self-assembly follows a self-regulating process. Regardless of the initial void number, the system dynamically adjusts through coarsening and spatial reorganisation to reach a consistent final state. However, at very low initial void counts, the weaker hexagonal alignment suggests that there is a lower void threshold below which superlattice formation is incomplete.

5.5.4 Experiment 7:

Fast Fourier Transform Analysis

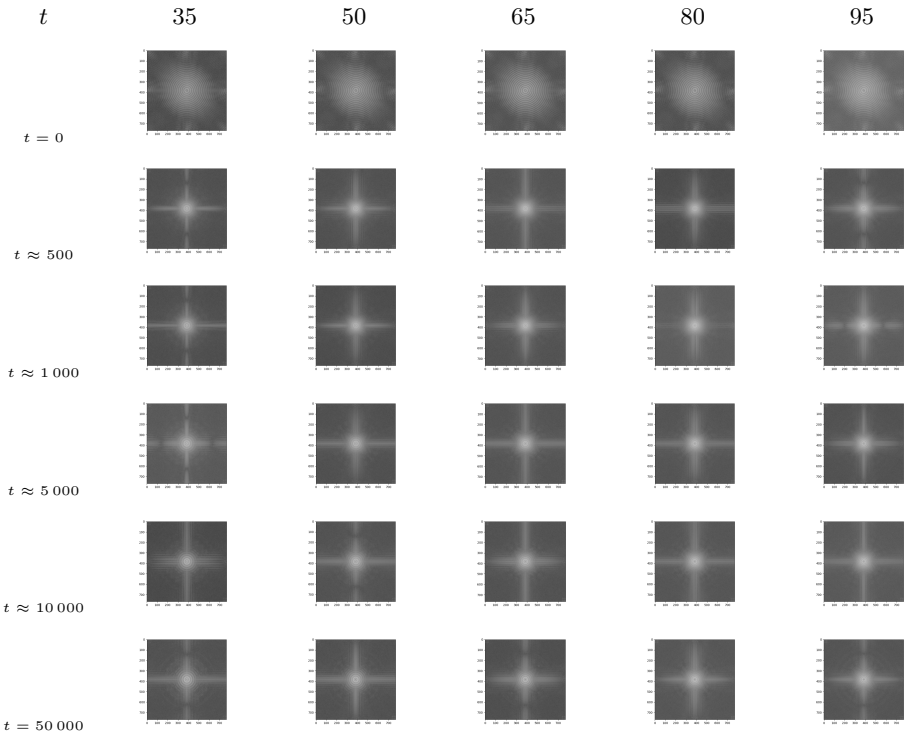

Figure 5.25: Fast Fourier Transform analysis of MOOSE simulation results for Experiment 7.

The Fast Fourier Transform (FFT) analysis, shown in Figure 5.25, provides a quantitative measure of periodic ordering across different initial void numbers. These results correspond directly to the simulation images in Figure 5.24, capturing the transition from an initially random void distribution to a stable hexagonal superlattice.

At $t = 0$, the FFT spectra for all cases exhibit diffuse intensity distributions, confirming the absence of long-range periodicity. This aligns with the initial conditions, where voids are randomly positioned without an underlying structured arrangement. Cases with higher initial void counts (80 and 95) exhibit broader spectral intensity, reflecting their increased void density and irregular spacing.

Between $t \approx 500$ to $t \approx 1\,000$, the FFT spectra remain largely diffuse, with no significant frequency peaks, indicating that voids are still in the early stages of migration, merging, and coarsening. At this stage, the system remains highly dynamic, with voids adjusting their positions without forming a discernible periodic structure.

By $t \approx 5\,000$, weak spectral peaks begin to emerge, indicating the initial stages of periodic ordering. The 50- and 65-void cases exhibit the most distinct peaks at this stage, suggesting that their moderate initial spacing facilitates earlier self-assembly. The 80- and 95-void cases remain slightly weaker, as the high void density leads to prolonged coarsening and void elimination. The 35-void case, however, shows the weakest periodic signature, likely due to the low void count and larger inter-void distances delaying the emergence of strong ordering.

At $t \approx 10\,000$, the FFT spectra display increasingly well-defined sixfold symmetric peaks, indicating the emergence of a hexagonal close-packed arrangement. However, periodicity remains weaker in the 35-void case, where the larger void spacing slows the development of a strong frequency signal. The 50- and 65-void cases exhibit the sharpest and most well-defined peaks. In contrast, the 80- and 95-void cases show broader, less intense peaks, reflecting the effects of higher void density and prolonged coarsening.

By $t = 50\,000$, the FFT spectra have stabilised, confirming that long-range periodicity emerges across all cases. The 35-void case remains the weakest, with lower spectral intensity due to the larger inter-void distances. The 50- and 65-void cases maintain the strongest periodic signatures, while the 80- and 95-void cases exhibit slightly broader peaks, suggesting that higher initial void densities introduce minor delays in achieving optimal hexagonal alignment. Despite these differences, all cases converge to the same fundamental periodic structure, reinforcing the robustness of the self-assembly process. These results quantitatively validate the simulation findings, demonstrating that void superlattice formation is largely independent of initial void count. While lower void counts lead to weaker final intensity due to increased spacing and higher initial void counts introduce delays in ordering due to void competition, the FFT analysis confirms that all cases ultimately stabilise into a periodic hexagonal superlattice.

5.5.5 Experiment 7: Statistical Analysis

Number of Voids Over Time

The number of voids over time for different initial void counts is shown in Figure 5.26. For the 35- and 50-void cases, the number of voids remained effectively constant throughout the simulation. These systems did not contain enough voids to initiate merging or elimination processes, and thus, each void persisted over time. In contrast, the 65-, 80-, and 95-void cases exhibited a distinct early-stage decline in void count before plateauing. This reflects coarsening and merging processes in which closely packed voids merge or dissolve due to high local density. The rate of void reduction scaled with the initial number: the 95-void case exhibited the sharpest decline, followed by 80, then 65. These differences can be attributed to increased void proximity at higher densities, which increases the likelihood of void interaction. The results indicate that if the initial void number is too low, the configuration remains stable, whereas excess voids are systematically reduced as the system converges into a steady-state configuration.

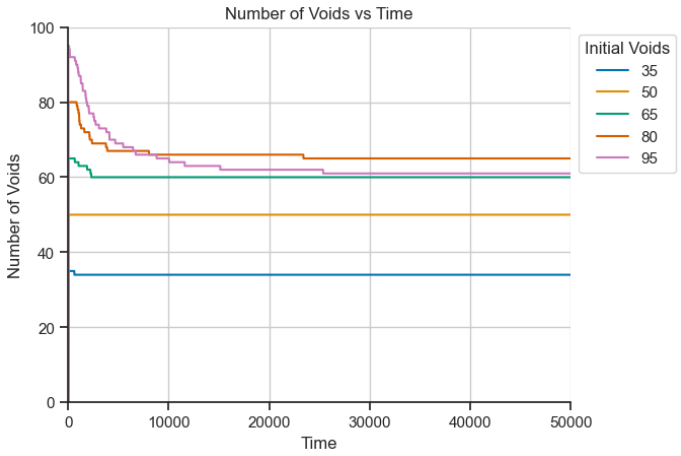

(a) Regular plot

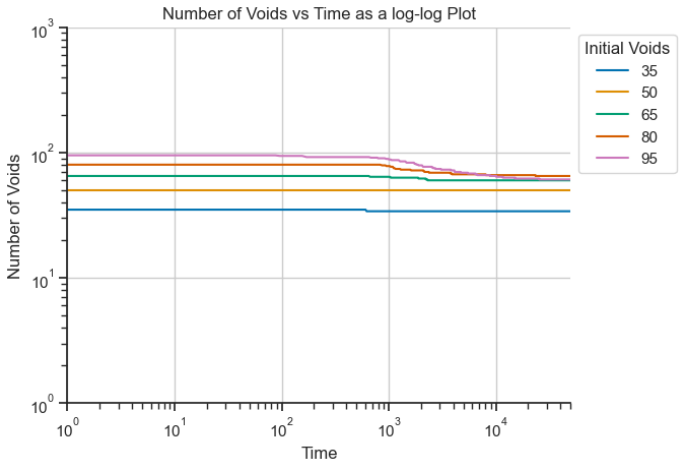

(b) Log-log plot

Figure 5.26: Number of voids over time for MOOSE Experiment 7 shown as (a) a regular plot and (b) a log-log plot.

Average Void Radius Over Time

Figure 5.27 presents the evolution of the average void radius across the five initial configurations. In the 65-, 80-, and 95-void cases, voids grew over time, with the 95-void case experiencing the most pronounced increase. This is a consequence of merging: as the number of voids decreases, the remaining voids absorb material and expand. The 35- and 50-void cases, by contrast, exhibited a decrease in void radius, followed by a plateau. In these cases, the voids were initially oversized relative to their environment and slightly shrank to reach a stable equilibrium. The final average void radius positively correlates with the number of initial voids. This suggests that the self-assembly process dynamically balances void number and void size to achieve stability.

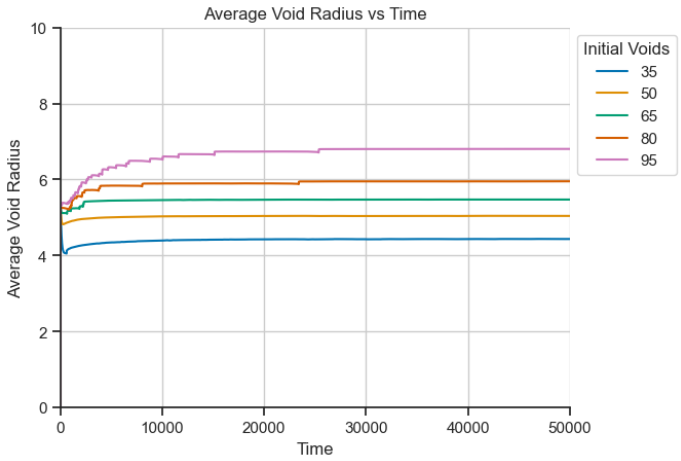

(a) Regular plot

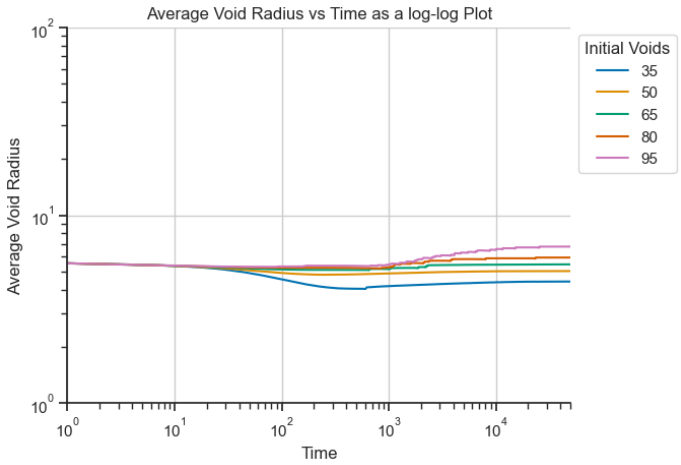

(b) Log-log plot

Figure 5.27: Average void radius over time for MOOSE Experiment 7 shown as (a) a regular plot and (b) a log-log plot.

Spread of Void Radius Over Time

The evolution of the void radius spread is shown in Figure 5.28. For all cases, the spread of the void radius rose as the voids coarsened. Following their peak, for the 35-, 50-, and 65-void systems, the spread steadily declined over time, indicating that the voids became more uniform in size. This uniformity is characteristic of a convergence towards a stable void superlattice. The 80- and 95-void systems, whilst they also decreased and converged, displayed frequent spikes in the spread at early and late-stage time points. These spikes correspond to void mergers or elimination events. Although these systems eventually stabilised, the fluctuations reveal a longer and more dynamic coarsening period due to higher initial densities. The results highlight that the system is capable of restoring uniformity even when initially overloaded with voids.

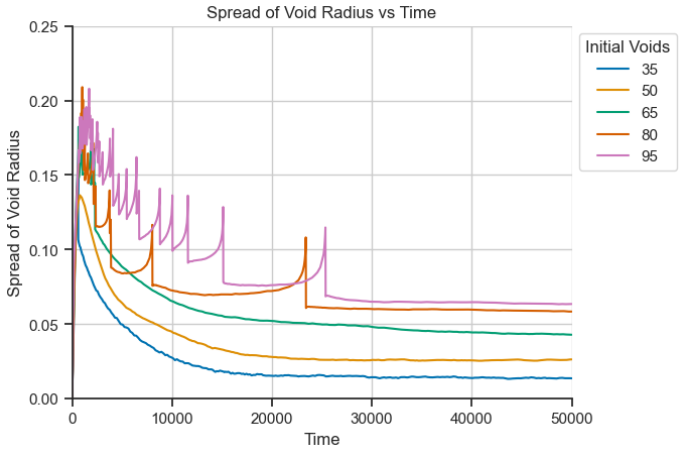

(a) Regular plot

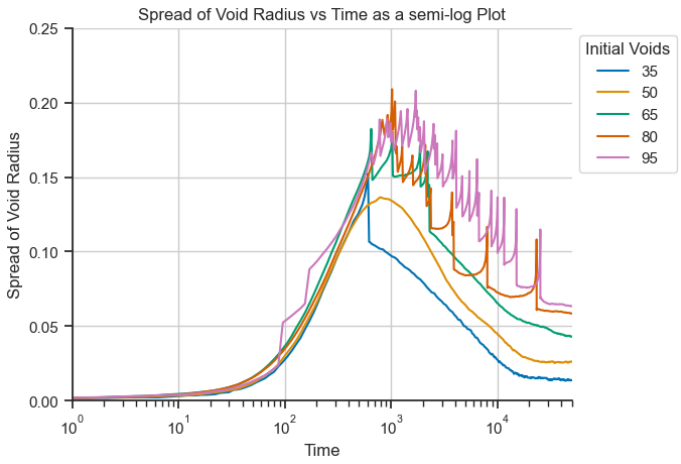

(b) Semi-log plot

Figure 5.28: Spread of void radius over time for MOOSE Experiment 7 shown as (a) a regular plot and (b) a semi-log plot.

Median Nearest-Neighbour Distance Over Time

Figure 5.29 shows the evolution of the median nearest-neighbour distance for each case. As voids were randomly distributed at $t = 0$, all systems began with a range of spacing values. Over time, each case exhibited a gradual increase and stabilisation of the median spacing, consistent with the transition toward an ordered void superlattice. The 65-, 80-, and 95-void cases converged to approximately the same final distance of 25 units, suggesting a characteristic equilibrium spacing governed by the system dynamics. In contrast, the 35- and 50-void cases plateaued at higher spacing values, reflecting the greater median distance between voids in sparser configurations. These results confirm that the self-assembly process enforces a consistent void spacing in sufficiently dense systems, while sparser systems stabilise with proportionally larger inter-void distances.

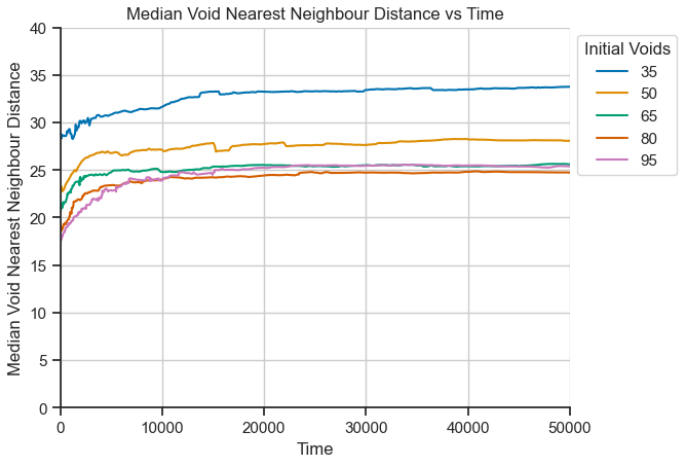

(a) Regular plot

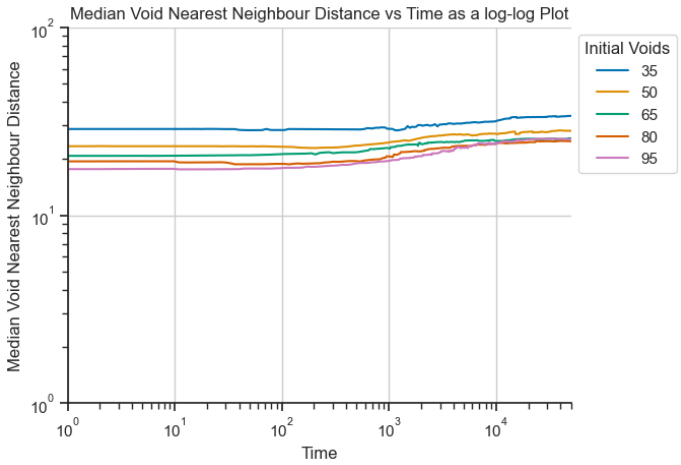

(b) Log-log plot

Figure 5.29: Median void nearest neighbour distance over time for MOOSE Experiment 7 shown as (a) a regular plot and (b) a log-log plot.

5.5.6 Experiment 7: Conclusions

Objective

Experiment 7 investigated the influence of initial void number on the evolution and stability of void superlattice formation. By systematically varying the number of randomly positioned pre-existing voids, the experiment assessed whether the final void configuration was sensitive to initial void density and whether the self-assembly process would adapt to under- or over-populated systems.

Findings

Simulation results revealed that all cases converged toward a hexagonal superlattice structure, though the rate and strength of ordering varied. The 50- and 65-void systems exhibited the strongest and most consistent self-assembly. Systems with too few voids (35) showed weaker periodicity due to large inter-void spacing, while systems with too many voids (80 and 95) experienced prolonged coarsening and void merging before stabilising.

FFT analysis confirmed that long-range periodicity emerged in all cases by $t = 50\,000$, with stronger frequency peaks observed in the 50- and 65-void systems. The 35-void case showed the weakest ordering, and the 80- and 95-void cases developed broader spectral peaks due to continued void evolution within the system.

Statistical analysis showed that:

- The number of voids remained constant in low-void cases and decreased in high-void cases due to merging.
- The final void radius scaled with initial void number, that fewer voids led to smaller radii, and excess voids merged into larger ones.
- Void size distributions converged over time, with higher initial densities exhibiting longer coarsening periods.
- Median nearest-neighbour distances stabilised around 25 units for denser sys-

tems, while sparser systems plateaued at higher values.

Conclusion

Experiment 7 demonstrates that the void self-assembly process is self-regulating and robust to variations in initial void number. While the initial configuration influences the dynamics and strength of ordering, all systems ultimately converge toward a periodic structure. However, there exists a practical lower threshold below which long-range order is diminished and an upper threshold above which excess voids are eliminated. These findings reinforce that void superlattice formation is an emergent, adaptive feature of the underlying reaction–diffusion system.

5.6 Experiment 8: Relationship to the Standard Cahn-Hilliard Equation

5.6.1 Experiment 8: Experiment Objective

Experiment 8 investigated the connection between the reaction–diffusion model developed in this work and the standard Cahn-Hilliard equation, examining whether the latter could be recovered under specific limiting cases. This experiment aimed to determine how void superlattice formation is affected when the reaction terms are removed or simplified, and whether the model transitions to classical phase-separation dynamics.

To explore this relationship, the creation and annihilation terms (c and a) were set to zero, effectively decoupling the vacancy and self-interstitial atom equations. Additionally, a second limiting case was considered where the self-interstitial atom mobility was assumed to be infinitely large ($M_s \to \infty$), leading to a steady-state distribution of self-interstitials and a modified governing equation for vacancies.

The following two reduced formulations were examined:

- **ODE w/ Coupled PDE**: The self-interstitial concentration followed an ordinary differential equation (ODE), interacting with the average vacancy concentration.
- **Single PDE w/ Constant** s: The steady-state value of s was substituted into the vacancy equation, yielding a single PDE with an additional reaction term.

By simulating these cases under identical conditions to Experiment 1, this experiment assessed whether self-assembly dynamics persisted in these simplified forms and whether void superlattice formation remained a characteristic outcome.

5.6.2 Experiment 8: Experiment Theory

In Section 3.4, I explored the determinant, $det(\mathbf{A_q})$, and showed that the predicted periodicity of a void superlattice, Λ, was approximately 25.13. And in Section 3.5, I used Descartes's rule of signs to explore the discriminant, and showed that the threshold for void superlattice formation, for the parameters $M_v = 1$, $\gamma_s = \gamma_v = 1$, $\bar{s} = 0.01$, $\bar{v} = 0.25$, $c = 0.00125$, and $a = -0.5$, was a ratio of $M_s/M_v = 3.322$. This was simulated in Experiment 1, and the results were shown in Section 5.2.1. When the $M_s/M_v < 3.322$, the last coefficient of the $det(\mathbf{A_q})$, Equation 3.34, is negative, and $det(\mathbf{A_q})$ has only one positive root. This means that when $det(\mathbf{A_q}) \to 0$, remembering that q is inverse to real space, the system, at infinitely large distances, will be unstable to complete decomposition. In Section 5.2.3, my third experiment explored the threshold for void superlattice formation and development, and for all $M_s/M_v < 3.322$ simulations, no pattern formation occurred, and the system evolved with the standard coarsening behaviour of Ostwald ripening. For $M_s/M_v > 3.322$, pattern formation did occur, and the system self-ordered itself into a stable void superlattice. Exploring this idea further, it is possible to recover the standard Cahn-Hilliard model from Equation 3.6 by setting the value of the creation term, c, and the value of the annihilation term, a, to 0 like so:

$$\frac{\partial s}{\partial t} = M_s \nabla^2 \left[\left(4s^3 - 6s^2 + 2s\right) - \gamma_s \nabla^2 s \right] + c - asv$$
$$\frac{\partial v}{\partial t} = M_v \nabla^2 \left[\left(4v^3 - 6v^2 + 2v\right) - \gamma_v \nabla^2 v \right] + c - asv$$

$$\begin{aligned} \frac{\partial s}{\partial t} &= M_s \nabla^2 \left[\left(4s^3 - 6s^2 + 2s\right) - \gamma_s \nabla^2 s \right] + \cancelto{0}{c} - \cancelto{0}{asv} \\ \frac{\partial v}{\partial t} &= M_v \nabla^2 \left[\left(4v^3 - 6v^2 + 2v\right) - \gamma_v \nabla^2 v \right] + \cancelto{0}{c} - \cancelto{0}{asv} \end{aligned} \tag{5.1}$$

$$\frac{\partial s}{\partial t} = M_s \nabla^2 \left[\left(4s^3 - 6s^2 + 2s\right) - \gamma_s \nabla^2 s \right]$$
$$\frac{\partial v}{\partial t} = M_v \nabla^2 \left[\left(4v^3 - 6v^2 + 2v\right) - \gamma_v \nabla^2 v \right]$$

which will have its own eigenvalue equation for each of the now decoupled self-interstitial atom and vacancy concentrations:

$$\lambda \delta \mathbf{u_q} = \mathbf{A_q} \delta \mathbf{u_q} \tag{5.2}$$

but, the matrix $\mathbf{A_q}$ will now be

$$\mathbf{A_q} = \begin{pmatrix} -M_s \left(q^2(12s^2 - 12s + 2) + \gamma_s q^4\right) & 0 \\ 0 & -M_v \left(q^2(12v^2 - 12v + 2) + \gamma_v q^4\right) \end{pmatrix} \tag{5.3}$$

which is approximately:

$$\mathbf{A_q} = \begin{pmatrix} -M_s(q^2(12s^2 - 12s + 2)) & 0 \\ 0 & -M_v(q^2(12v^2 - 12v + 2)) \end{pmatrix} \tag{5.4}$$

in the limit that $q^2 \to 0$, the coarsening condition is simply $(12s^2 - 12s + 2) < 0$ and

$(12v^2 - 12v + 2) < 0$.

As $M_s \to \infty$, i.e. the self-interstitial atoms have migrated away instantaneously. The self-interstitial atom concentration field, s, can no longer support gradients, and the gradient terms will tend to 0. The vacancy and the self-interstitial atom equations will still be coupled, but the standard Cahn-Hilliard equation for the evolution of the vacancies is not recovered. I derive this here:

$$\begin{aligned}
\frac{\partial s}{\partial t} &= M_s \nabla^2 \left[\left(4s^3 - 6s^2 + 2s\right) - \gamma_s \nabla^2 s \right] + c - asv \\
\frac{\partial v}{\partial t} &= M_v \nabla^2 \left[\left(4v^3 - 6v^2 + 2v\right) - \gamma_v \nabla^2 v \right] + c - asv
\end{aligned}$$

$$\begin{aligned}
\frac{\partial s}{\partial t} &= M_s \cancelto{0}{\nabla^2} \left[\left(4s^3 - 6s^2 + 2s\right) - \gamma_s \cancelto{0}{\nabla^2 s} \right] + c - asv \\
\frac{\partial v}{\partial t} &= M_v \nabla^2 \left[\left(4v^3 - 6v^2 + 2v\right) - \gamma_v \nabla^2 v \right] + c - asv
\end{aligned} \tag{5.5}$$

$$\begin{aligned}
\frac{\partial s}{\partial t} &= c - as\bar{v} \\
\frac{\partial v}{\partial t} &= M_v \nabla^2 \left[\left(4v^3 - 6v^2 + 2v\right) - \gamma_v \nabla^2 v \right] + c - asv
\end{aligned}$$

I have used the average value for the vacancy concentration, $\bar{v}$, in the self-interstitial atom partial differential equation. The idea here is that the vacancy concentration, v, will still have non-zero gradients; only the self-interstitial atom concentration, s, cannot support gradients. $\partial s/\partial t$ will therefore interact with the average concentration of vacancies, $\bar{v}$, in the system.

I can explain this behaviour with further analysis. Assuming that the self-interstitial atom concentration rapidly achieved a steady state, and in the ODE w/ Coupled PDE system — Equation 5.5 — this is precisely what happened. I can solve Equation 5.5 for the steady-state value of s:

$$
\begin{aligned}
\frac{\partial s}{\partial t} &= c - as\bar{v} \\
\frac{\partial \overset{0}{\cancel{s}}}{\partial t} &= c - as\bar{v} \\
0 &= c - as\bar{v} \\
c &= as\bar{v} \\
s &= \frac{c}{a\bar{v}}
\end{aligned}
\tag{5.6}
$$

and substituting it into the $\partial v/\partial t$ partial differential equation like so:

$$
\begin{aligned}
\frac{\partial v}{\partial t} &= M_v \nabla^2 \left[\left(4v^3 - 6v^2 + 2v \right) - \gamma_v \nabla^2 v \right] + c - asv \\
\frac{\partial v}{\partial t} &= M_v \nabla^2 \left[\left(4v^3 - 6v^2 + 2v \right) - \gamma_v \nabla^2 v \right] + c - a \left(\frac{c}{a\bar{v}} \right) v \\
\frac{\partial v}{\partial t} &= M_v \nabla^2 \left[\left(4v^3 - 6v^2 + 2v \right) - \gamma_v \nabla^2 v \right] + c \left(1 - \frac{v}{\bar{v}} \right)
\end{aligned}
\tag{5.7}
$$

I can represent the system as a single PDE, referred to as the "Single PDE w/ Constant s" equation below.

In the case of the single PDE with constant s — Equation 5.7 — I can see that the standard Cahn-Hilliard equation is also not recovered for the vacancy concentration. This is a Cahn-Hilliard equation with an additional reaction term capable of pattern formation under the correct conditions. In this limit, the modified Cahn-Hilliard model is analogous to the Ohta-Kawasaki model [246, 247].

5.6.3 Experiment 8:

Simulation Setup and Parameters

To ensure comparability with Experiment 1, the simulation parameters remained unchanged:

- **Domain size**: 200×200 units
- **Grid resolution**: 400×400

- **Boundary conditions**: Periodic
- **Surface energy terms**: $\gamma_s = \gamma_v = 1$
- **Reaction coefficients**: $a = -0.5$, $c = 0.00125$

The experiment investigated three different model reductions:

- **Coupled PDE**: The original reaction–diffusion model with no simplifications — Experiment 1.
- **ODE w/ Coupled PDE**: The self-interstitial concentration evolved according to an ordinary differential equation (ODE).
- **Single PDE w/ Constant** s: The steady-state self-interstitial concentration was substituted into the vacancy equation, yielding a single PDE with an additional reaction term.

Each case was simulated with the following parameter choices:

ODE w/ Coupled PDE

- **Mobility values**: $M_s = 1\,000$, $M_v = 1$
- **Surface energy terms**: $\gamma_s = \gamma_v = 1$
- **Self-interstitial concentration**: $s = 0.01$
- **Mean vacancy concentration**: $\bar{v} = 0.25 \pm 1\%$
- **Reaction coefficients**: $c = 0.00125$, $a = -0.5$

Single PDE w/ Constant s

- **Mobility value**: $M_v = 1$
- **Surface energy terms**: $\gamma_s = \gamma_v = 1$
- **Self-interstitial concentration**: $s = c/av$
- **Mean vacancy concentration**: $\bar{v} = 0.25 \pm 1\%$
- **Reaction coefficients**: $c = 0.00125$, $a = -0.5$

The initial concentrations of vacancies ($\bar{v}$) and self-interstitial atoms ($\bar{s}$) were computed using the MOOSE `ElementAverageValue` post-processor. The results are shown in Table 5.19.

Case	$\bar{v}$	$\bar{s}$
Coupled PDE	0.24999	0.01000
ODE w/ Coupled PDE	0.24999	0.01013
Single PDE w/ Constant s	0.25000	0.00999

Table 5.19: Initial concentrations of $\bar{s}$ and $\bar{v}$ for Experiment 8.

Each simulation was run until $t = 50\,000$, with the required time steps varying based on the model. The results are shown in Table 5.20.

Case	Number of Time Steps
Coupled PDE	540
ODE w/ Coupled PDE	662
Single PDE w/ Constant s	580

Table 5.20: Number of time steps required for different model reductions in Experiment 8.

The simulations were run on a Google Cloud Platform `n2-standard-128` virtual machine (128 vCPUs, 512 GB RAM). Completion times for the ODE w/ Coupled PDE and Single PDE w/ Constant s models were noticeably faster than the Coupled PDE model, taking approximately 1–2 hours to complete compared to the Coupled PDE model's 4 hours.

ParaView was used to visualise the simulation results at key timestamps. The approximate written times and the exact timestamps recorded in the simulation outputs are shown in Table 5.21.

Written Time	Exact Simulation Time (t)		
	Coupled PDE	ODE w/ Coupled PDE	Single PDE w/ Constant s
$t \approx 500$	—	501.3	505.5
$t \approx 650$	657.179	654.9	652.7
$t \approx 750$	754.393	750.9	755.1
$t \approx 1\,000$	1 015.52	1 000.5	1 011.1
$t \approx 5\,000$	5 028.07	5 032.5	5 055.9
$t \approx 10\,000$	10 020.8	10 050.1	10 009.5
$t = 50\,000$	50 000	50 000	50 000

Table 5.21: Timestamp map for Experiment 8.

5.6.4 Experiment 8:

Simulation Results and Analysis

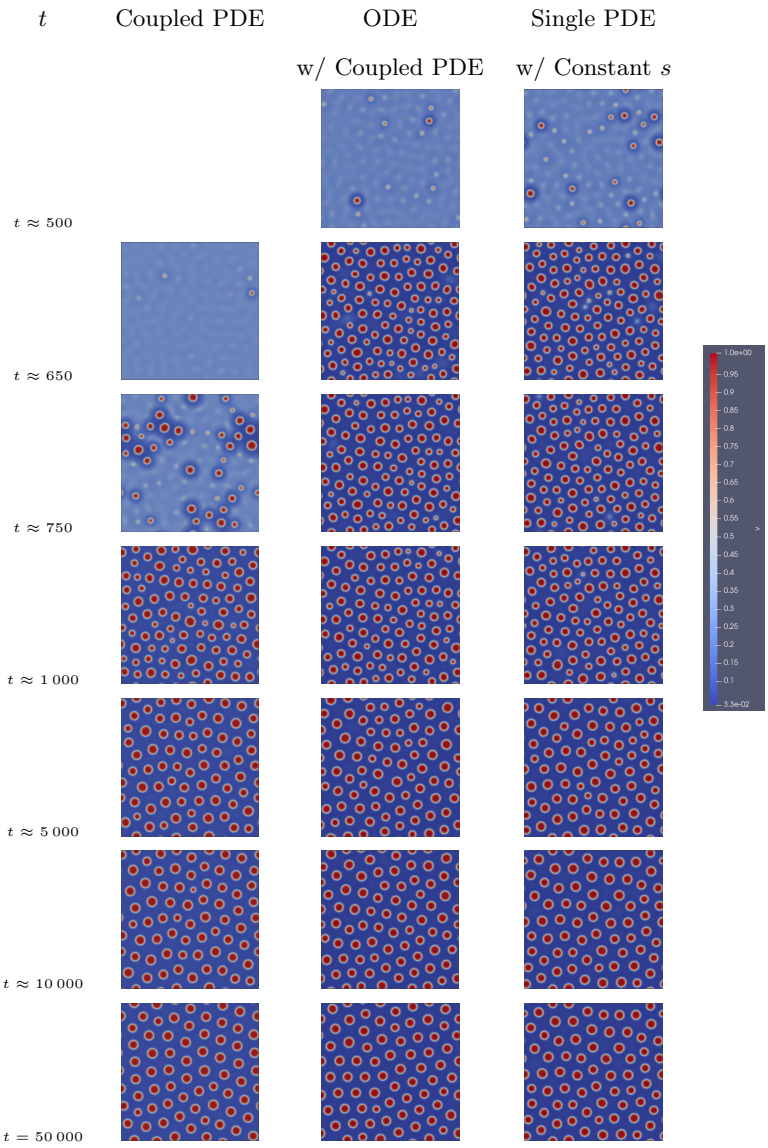

Figure 5.30: MOOSE simulation results for Experiment 8, which explored the relationship of my model to the standard Cahn-Hilliard equation. The ParaView colour legend is shown to the right.

The simulation results for Experiment 8, shown in Figure 5.30, explore the relation-

ship between the reaction–diffusion model developed in this work and the standard Cahn-Hilliard equation. Three cases were considered: the fully coupled PDE system (Coupled PDE), a hybrid model where the self-interstitial atom concentration evolved according to an ODE (ODE w/ Coupled PDE), and a further simplified model where the steady-state self-interstitial atom concentration was substituted into the vacancy PDE (Single PDE w/ Constant s).

At early times ($t \approx 500$ to $t \approx 1\,000$), all models exhibited initial phase separation and void nucleation, but their early evolution differed. The Coupled PDE case developed voids more gradually, while the ODE w/ Coupled PDE and Single PDE w/ Constant s cases exhibited faster void formation due to the simplified treatment of the self-interstitial atom concentration field.

By $t \approx 5\,000$ to $t \approx 10\,000$, all models had transitioned to a more structured arrangement. Despite differences in their governing equations, voids in all cases migrated, coarsened, and began forming a periodic structure. The Single PDE w/ Constant s case showed slightly more pronounced void growth and ordering, suggesting that reducing the dynamics of the self-interstitial atom concentration field accelerates pattern formation.

At $t = 50\,000$, all models reached a steady-state hexagonal superlattice, confirming that void self-assembly is a robust feature of the system. While the full Coupled PDE model provided the most detailed description of the process, the reduced models still captured the essential pattern formation behaviour.

These results demonstrate that void superlattice formation persists across different formulations of the model, reinforcing that self-assembly is an intrinsic outcome of the reaction–diffusion dynamics rather than a feature specific to the fully coupled system. Even in limiting cases where self-interstitial evolution is simplified, periodic structuring emerges, highlighting the robustness of the mechanism governing void formation.

5.6.5 Experiment 8:

Fast Fourier Transform Analysis

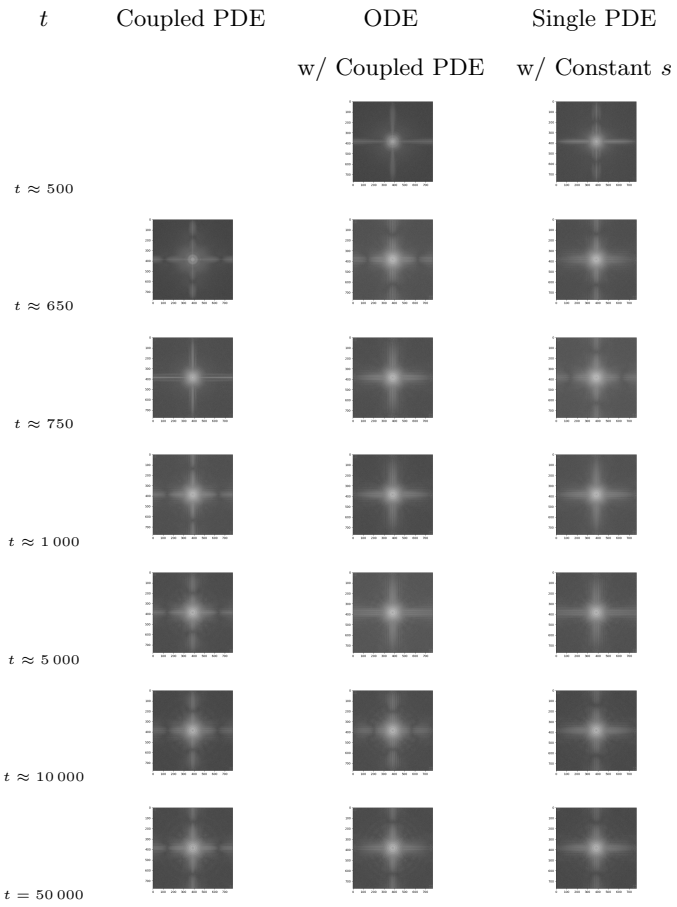

Figure 5.31: Fast Fourier Transform analysis of MOOSE simulation results for Experiment 8.

The Fast Fourier Transform (FFT) analysis, shown in Figure 5.31, provides a quantitative measure of periodic ordering across the three model formulations examined in Experiment 8. These results correspond directly to the simulation images in Figure 5.30, capturing the differences in early-stage evolution and the eventual convergence of all models to a well-defined hexagonal superlattice.

At early times ($t \approx 500$), the FFT spectra for the ODE w/ Coupled PDE and Single

PDE w/ Constant s cases already exhibit weak frequency peaks, reflecting their faster void formation dynamics. This aligns with the simulation results, where voids nucleate and begin coarsening earlier in these models due to the simplified treatment of the self-interstitial atom concentration. In contrast, the fully Coupled PDE case remains more diffuse, indicating a delayed onset of ordering, with significant void nucleation only becoming apparent by $t \approx 750$.

Between $t \approx 750$ and $t \approx 1\,000$, the FFT spectra for the ODE w/ Coupled PDE and Single PDE w/ Constant s cases show increasing peak definition, mirroring the early-stage ordering seen in the Coupled PDE case between $t \approx 1\,000$ and $t \approx 5\,000$. This suggests that the ordering process in the reduced models progresses at an accelerated rate, achieving structural coherence more quickly than the fully coupled system.

By $t \approx 10\,000$, the FFT spectra for all three models exhibit well-defined peaks, confirming that the weak periodicity observed earlier has intensified into a more structured arrangement.

At $t = 50\,000$, the FFT spectra for all cases display strong, well-defined sixfold symmetric peaks, confirming that a stable periodic structure has been reached. The Coupled PDE case exhibits slightly sharper peak definition, indicating marginally stronger hexagonal alignment compared to the reduced models. However, the differences are minor, and all three models converge to the same characteristic superlattice structure. These results quantitatively validate the simulation findings, demonstrating that void self-assembly is robust across different model formulations. While the reduced models exhibit faster initial ordering, and the fully Coupled PDE model shows slightly stronger final hexagonal alignment, the FFT analysis confirms that all cases ultimately stabilise into the same periodic superlattice. This reinforces the conclusion that self-assembly is an intrinsic property of the system, emerging consistently regardless of the specific treatment of the self-interstitial atom concentration field.

5.6.6 Experiment 8: Statistical Analysis

Number of Voids Over Time

Figure 5.32 shows the evolution of void count over time for the three formulations considered in Experiment 8. All models — Coupled PDE, ODE w/ Coupled PDE, and Single PDE w/ Constant s — following nucleation, exhibited a rapid initial reduction in void number, followed by a gradual plateau. This behaviour is characteristic of early-stage coarsening via void merging or elimination, followed by long-range ordering into a steady-state void superlattice.

While the overall trend is conserved across models, subtle differences emerge in timescales. The full Coupled PDE system exhibited slower coarsening dynamics, taking longer to reach its plateau. In contrast, both reduced models achieved steady-state void counts more quickly. This acceleration is consistent with the simplification of the self-interstitial atom concentration field, which removes gradient-driven coupling and allows faster relaxation.

The log-log plot in Figure 5.32 (b) confirms that all three systems approach similar asymptotic behaviour, reinforcing that the void count converges toward a consistent final state despite differences in early evolution. These results highlight that void elimination and equilibrium saturation are preserved features of the model, regardless of whether the full coupled dynamics are retained.

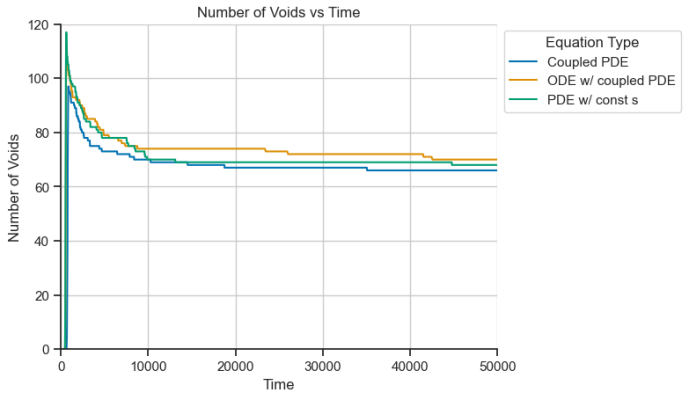

(a) Regular plot

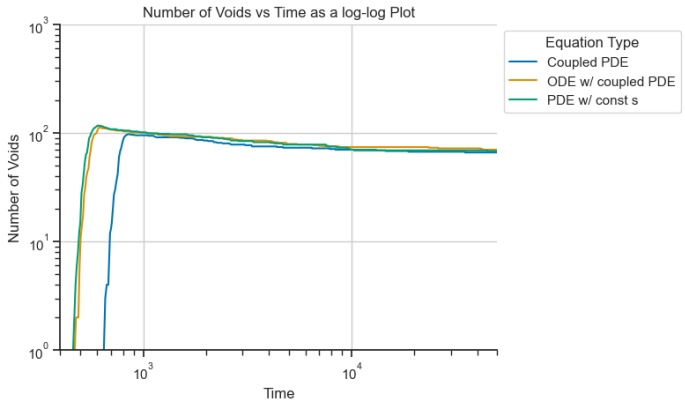

(b) Log-log plot

Figure 5.32: Number of voids over time for MOOSE Experiment 8 shown as (a) a regular plot and (b) a log-log plot.

Average Void Radius Over Time

The evolution of the average void radius is presented in Figure 5.33. All models display identical qualitative behaviour: a sharp increase in void radius during the early stages, followed by a smooth plateau as void growth slows. This growth phase corresponds to the coarsening process, during which smaller voids are eliminated and larger voids absorb material.

Notably, the final average void radius is nearly identical across all three model variants, with only minor discrepancies. The Coupled PDE model results in a slightly larger equilibrium void size, likely due to the additional degrees of freedom introduced by fully resolving the dynamics of the self-interstitial atom field. Nevertheless, the similarity in trends across all cases confirms that void growth is insensitive to the specific treatment of the s field.

These findings support the conclusion that average void size is governed by the overarching self-organisation mechanism rather than the presence or absence of reaction coupling or PDE complexity. The fact that the reduced models replicate this behaviour underscores the robustness of void radius evolution across formulations.

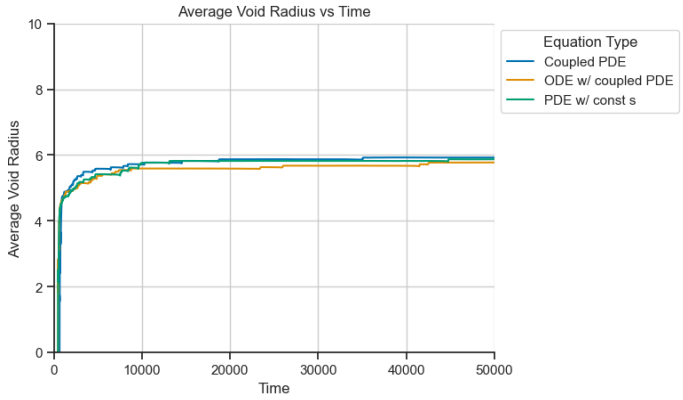

(a) Regular plot

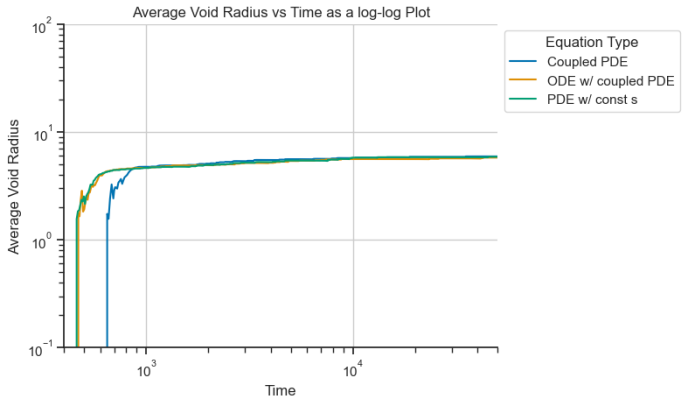

(b) Log-log plot

Figure 5.33: Average void radius over time for MOOSE Experiment 8 shown as (a) a regular plot and (b) a log-log plot.

Spread of Void Radius Over Time

Figure 5.34 displays the spread in void radius over time. All models exhibit an early decline in spread, reflecting the homogenisation of void sizes as the system self-assembles. This narrowing of the radius distribution signals the transition toward a stable, hexagonal close-packed void superlattice.

Superimposed on this trend are transient spikes in the spread, which correspond to void merging events. There is no meaningful difference in this behaviour across all three models.

All three models ultimately converge to the same narrow and stable distribution, indicating that void size uniformity is a robust feature of the self-assembly process. The presence of small fluctuations regardless of model complexity demonstrates the dynamic nature of coarsening but does not lead to divergence in final behaviour. These results confirm that the evolution of void size variability is fundamentally preserved across all formulations, with no significant deviation introduced by simplifying the treatment of the self-interstitial atom field.

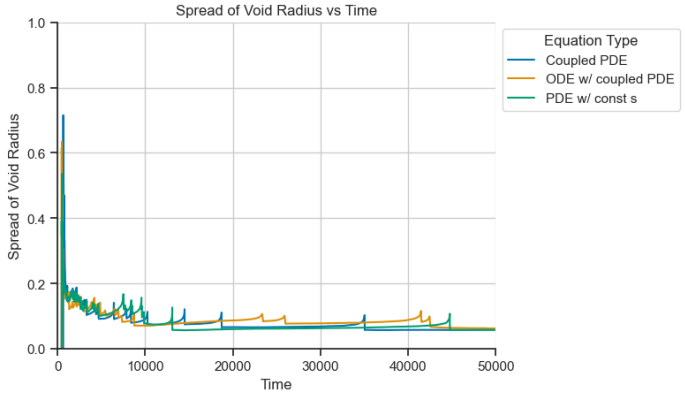

(a) Regular plot

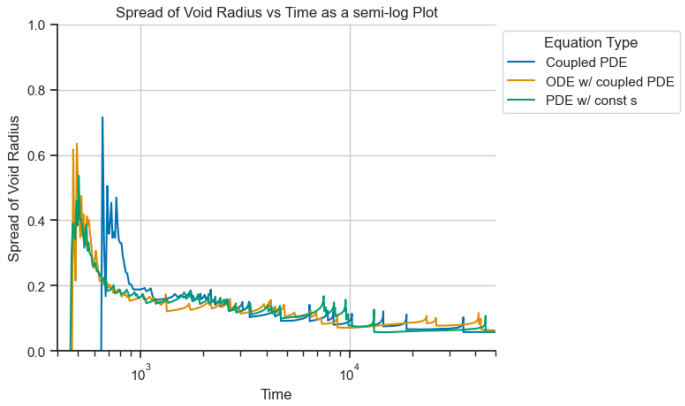

(b) Semi-log plot

Figure 5.34: Spread of void radius over time for MOOSE Experiment 8 shown as (a) a regular plot and (b) a semi-log plot.

Median Nearest-Neighbour Distance Over Time

The evolution of the median nearest-neighbour distance between voids is shown in Figure 5.35. All models show a sharp decrease in median nearest neighbour distance, followed by a plateau, converging towards a final spacing of approximately 25 units.

At early times, voids begin to nucleate at multiple locations. This leads to a wide distribution of spacing values, with the median distance initially high. As nucleation saturates and new void formation slows, existing voids begin to interact, merge, and self-organise, causing the median spacing to decrease and eventually stabilise.

All models converge to the same final distance of approximately 25 units, matching the analytically predicted superlattice spacing $\Lambda \approx 25.13$ from Section 3.4. This convergence occurs even in the simplified formulations, indicating that the emergence of an ordered void superlattice is governed by the fundamental length scale inherent in the system's free-energy functional, not the full complexity of the governing equations.

These results demonstrate that the process of void ordering is resilient across all model reductions. Whether the dynamics of the self-interstitial atom field are fully resolved or replaced by steady-state assumptions, the system robustly evolves toward the same equilibrium spacing.

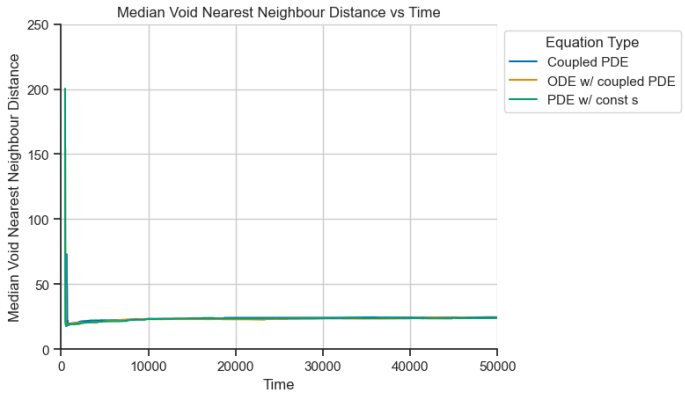

(a) Regular plot

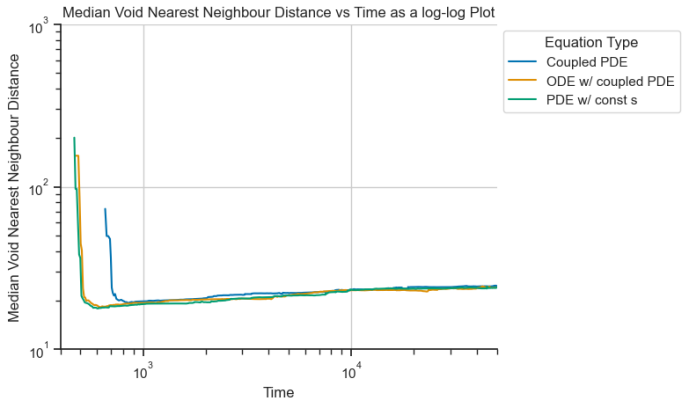

(b) Log-log plot

Figure 5.35: Median void nearest neighbour distance over time for MOOSE Experiment 8 shown as (a) a regular plot and (b) a log-log plot.

5.6.7 Experiment 8: Conclusions

Objective

Experiment 8 investigated whether void superlattice formation remains a robust and intrinsic feature of the system when the reaction–diffusion model is simplified. Specifically, it tested whether the standard Cahn-Hilliard equation could be recovered under limiting assumptions, and whether self-assembly persists in the absence of full coupling between the vacancy and self-interstitial atom concentration fields.

Findings

Simulation results showed that all model variants, i.e. the full Coupled PDE, the ODE w/ Coupled PDE, and the Single PDE w/ Constant s, exhibited the same qualitative behaviours: void nucleation, growth, coarsening, stabilisation, and eventual self-organisation into a hexagonal close-packed void superlattice.

FFT analysis confirmed that long-range periodicity emerged in all three cases by $t = 50\,000$, with clear sixfold symmetry observed in the frequency domain. The reduced models exhibited faster early ordering, while the Coupled PDE system produced slightly stronger final alignment.

Statistical analysis revealed consistent trends across all models:

- The number of voids increased rapidly due to nucleation and then steadily declined during early-stage coarsening and merging; eventually plateauing at the same final value in all three cases.
- The average void radius increased as smaller voids were eliminated, converging to nearly identical final sizes across models.
- The spread in void radius narrowed over time, with all models stabilising to the same uniform distribution.
- Median nearest-neighbour distances initially decreased during void formation and coarsening, then stabilised at approximately 25 units — consistent with the

predicted superlattice spacing $\Lambda \approx 25.13$.

Conclusion

Experiment 8 demonstrates that void superlattice formation is a resilient and intrinsic outcome of the system, persisting even when the reaction–diffusion model is significantly simplified. While the full Coupled PDE model captures the richest dynamics, the reduced models — despite omitting gradients in the self-interstitial atom field or replacing it with a steady-state value — still reproduce all key features of self-assembly. These findings confirm that the emergence of a void superlattice is not an artefact of model complexity but a consequence of the underlying free-energy landscape. Even in analytical limits approaching the standard Cahn-Hilliard form, the system retains its capacity for pattern formation. The reaction terms and coupling mechanisms, though not strictly necessary for superlattice formation, modulate the timescale and ordering dynamics. Ultimately, this reinforces the interpretation that self-assembly is an emergent feature of the governing equations' structure and energy minimisation principles.

5.7 Chapter Discussion

5.7.1 Core Findings from Simulation Experiments

The eight simulation experiments performed in this chapter collectively establish that void superlattice formation is a robust, intrinsic feature of the reaction–diffusion model developed in this work. These findings provide strong computational support for the hypothesis that a Turing-like instability underlies the emergence of ordered void patterns in irradiated materials, with pattern formation governed primarily by the difference in mobilities between the vacancies and self-interstitial atom species.

Experiments 1–3 identified the fundamental role of the mobility ratio M_s/M_v in controlling void self-assembly. Below a critical threshold ($M_s/M_v \leq 2$), systems exhibited classical Ostwald ripening with continuous coarsening and no long-range order. As

the mobility ratio increased, voids began to stabilise, and by $M_s/M_v \geq 10$, periodic superlattices consistently emerged. This transition was quantitatively consistent with linear stability predictions derived in Chapter 3, which identified a bifurcation threshold at $M_s/M_v \approx 3.322$. Beyond $M_s/M_v \approx 100$, ordering behaviour saturated, and further increases in mobility ratio yielded no additional structural refinement.

Experiment 4 demonstrated that void pattern formation is scale-invariant and insensitive to domain size beyond finite-size limits. Structural features, including void number, radius, and nearest neighbour distance remained unchanged across domains from 50×50 to 400×400, confirming that superlattice formation is not a boundary artefact but an intrinsic feature of the system dynamics.

Experiments 5–7 explored the influence of changing the initial conditions by beginning with pre-existing voids. The experiments varied the void size, and the total number. In all cases, the system self-organised into the same final structure: a hexagonal close-packed void superlattice with spacing $\Lambda \approx 25$. While initial conditions influenced early coarsening dynamics and the rate of ordering, they had no impact on the equilibrium configuration. Notably, Experiment 7 revealed a range of initial void densities (50–65 voids) that yielded optimal ordering, indicating a degree of self-regulation within the system and suggesting that long-range patterning emerges from internal constraints rather than external control.

Finally, Experiment 8 tested the robustness of pattern formation under systematic model simplification. Even when coupling between species was reduced or removed, and the system approached the standard Cahn-Hilliard form, all variants continued to exhibit void nucleation, coarsening, and superlattice formation. This confirmed that the emergence of periodic structure is not an artefact of model complexity or PDE coupling, but a fundamental outcome of the system's free-energy landscape and diffusion dynamics.

Taken together, these simulations demonstrate that void superlattices are not the product of fine-tuned initial states or extrinsic model features, but a natural and emergent consequence of the differences in mobilities and the conservative, non-linear diffusion dynamics encoded in the governing equations. Across all experiments, the

system converged to a stable periodic state characterised by a consistent wavelength, sixfold symmetry, and uniform void size — hallmarks of a diffusion-driven Turing-like instability.

5.7.2 Comparison to Prior Models and Literature

The simulation results presented in this chapter offer strong support for the hypothesis that void superlattice formation can emerge from a purely thermodynamically-driven instability mechanism, without the need for external symmetry selection or anisotropic transport mechanisms. This sets the present work apart from several major classes of models in the literature and offers new insights into the necessary ingredients for pattern formation in irradiated materials.

Comparison to Dynamic Instability Models (BEK Framework)

Traditional dynamic instability models, such as those based on the Bullough-Eyre-Krishan (BEK) framework [95, 97, 156, 157], describe vacancy and self-interstitial atom concentrations using Fickian diffusion and couple them through annihilation terms and sink dynamics. Instabilities in these models are typically introduced via feedback with additional defect populations (e.g., voids, vacancy loops, dislocations, etc.), and symmetry selection is often achieved through anisotropic SIA diffusion or directional sink terms.

While these models successfully demonstrate the theoretical possibility of pattern-forming instabilities, they often require fine-tuning, introduce additional equations for defect clusters, and exhibit discrepancies between predicted and observed length scales. In particular, N. M. Ghoniem and D. Walgraef noted that their models tended to over-predict lattice parameters compared to experimental systems [66]. The sensitivity of these models to post-bifurcation dynamics complicates their predictive power.

By contrast, the model presented here eliminates the need for such coupling mechanisms and external fields. Simulations show that self-assembly occurs spontaneously from random initial conditions and persists even when simplified (Experiment 8), suggesting that additional complexity is not required to achieve patterning. The emer-

gence of a well-defined superlattice driven solely by mobility contrast and conservative non-linear diffusion represents a significant conceptual simplification of dynamic instability theories.

Comparison to Hybrid Thermodynamic–Kinetic Models (Gao and Zhang)

More recent thermodynamics-driven models by Y. Gao et al. and Y. Zhang et al. [138, 144] adopt a hybrid structure: a Cahn-Hilliard equation for vacancies is coupled to a Fickian diffusion equation for self-interstitials, with both reaction and sink terms included i.e. a BEK rate equation. Crucially, their models incorporate anisotropic diffusion of self-interstitial atoms to enable crystal symmetry selection (e.g., BCC or FCC). This anisotropy is assumed to reflect crystallographic channeling or strain-assisted diffusion, and it is used as the mechanism for pattern orientation control.

While these models successfully replicate a wide range of void lattice symmetries, they rely on explicit directional bias. In contrast, the present model generates long-range order without any anisotropic transport. Experiments 1–8 show that hexagonal close-packed ordering emerges robustly under isotropic conditions, governed solely by the mobility ratio M_s/M_v and the free energy landscape. Even when gradient terms for the self-interstitial atom field are removed (Experiment 8), ordering persists, suggesting that directional control is not necessary for superlattice formation, though it may be important for orientation selection.

Thus, the findings challenge the assumption that anisotropic diffusion is a necessary ingredient for void patterning. The emergence of a single characteristic length scale (e.g., $\Lambda \approx 25$) is sufficient to produce hexagonal order in two dimensions, consistent with the simplest Turing-like patterning mechanisms.

Conceptual Novelty and Broader Implications

The model developed here represents a new class of conservative reaction–diffusion systems in which two conserved fields, each governed by fourth-order non-linear diffusion, are coupled only through physically motivated reaction terms (creation and

annihilation). Despite its minimal structure:

- It reproduces hexagonal ordering and void superlattice formation under purely isotropic conditions;
- It predicts a consistent periodicity that aligns with experimental observations;
- It generalises the concept of Turing instabilities to conserved-field systems, contrasting with classical models that rely on non-conserved activator-inhibitor dynamics.

This framework bridges prior dynamic and thermodynamic theories while removing the need for imposed sinks, defect clusters, or directional biases. It suggests that the essential mechanism for void ordering lies in the instability of the uniform state under mobility contrast, and that this is sufficient to produce long-range order through energy minimisation alone.

More broadly, the results have implications beyond voids: the same underlying instability may govern pattern formation in other systems involving conserved defect species, such as gas bubbles and other pattern formation phenomena in materials science. Future extensions incorporating elastic fields, anisotropic mobility, or gas pressure effects could enable a more unified treatment of defect ordering across different irradiated material systems.

5.7.3 Implications for Anisotropic Diffusion Debate

A longstanding assumption in the void superlattice literature is that anisotropic diffusion of self-interstitial atoms is required for superlattice formation and, in particular, for selecting its crystal structure. This hypothesis, originating with the work of A. J. E. Foreman [84] and later expanded by C. H. Woo et al. and J. H. Evans [63, 86], holds that self-interstitial atoms preferentially migrate along specific crystallographic directions or planes, biasing the net recombination rate between vacancies and self-interstitial atoms in a way that favours growth only in aligned voids. The result is a directional selection mechanism that explains the emergence of one-dimensional or planar ordering and ultimately determines whether a BCC, FCC, etc. lattice forms.

However, the results presented in this work provide a counterexample to the necessity of this mechanism. In all eight experiments, voids self-assembled into a periodic, hexagonally ordered arrangement under purely isotropic diffusion conditions, without any imposed directional bias or anisotropic transport. Even in Experiment 8, where the self-interstitial atom field was held constant and decoupled from the vacancy gradients, the same self-assembled pattern emerged. This confirms that anisotropic diffusion is not required to initiate or sustain void superlattice formation.

Instead, the ordering observed here is governed by a Turing-like instability driven by non-linear, isotropic, fourth-order diffusion. The free-energy functional, which contains a double-well potential, selects a single characteristic wavelength that sets the pattern's periodicity, $\Lambda \approx 25$. This single-wavelength mechanism is sufficient to drive spontaneous symmetry breaking and long-range ordering. The resulting arrangement in 2D is a hexagonal close-packed (HCP) lattice, which corresponds to a body-centred cubic (BCC) structure when extended into three dimensions.

This finding resonates with the phase-field simulations of S. Hu et al. [152, 153], who similarly demonstrated HCP and BCC ordering under simplified models of SIA diffusion. However, the present model goes further by showing that no anisotropic transport is required at all. The emergence of BCC-like structures can be explained solely by the presence of a single dominant mode in the unstable wavenumber spectrum.

Moreover, this raises a natural extension: in systems where two unstable wavelengths are present e.g., through a more complex free energy landscape where both wells of the double-well potential dip below the axis, it may be possible to generate superlattice structures with two characteristic length scales, such as FCC. In that context, anisotropic diffusion would no longer be the only route to symmetry selection; instead, the free-energy landscape itself would control both periodicity and pattern type.

This repositions anisotropic diffusion not as a necessary condition for superlattice formation, but as a modulating factor that influences the orientation and complexity of the resulting structure. The minimal, isotropic model presented here establishes a new baseline: that pattern formation and self-assembly can arise from conservative, non-linear diffusion alone, with crystal structure emerging from the interaction between

the free energy and the conserved field dynamics.

These findings challenge the traditional consensus that directional anisotropy in self-interstitial atom diffusion is essential for void superlattice formation. Instead, they demonstrate that a thermodynamically-driven instability with isotropic dynamics can fully explain both the emergence and periodicity of void superlattices, at least in systems characterised by a single unstable length scale. This opens the door to alternative pattern selection mechanisms based on multi-wavelength free-energy functionals, offering a richer and more flexible framework for understanding defect ordering in irradiated materials.

5.7.4 Model Robustness and Minimality

A central aim of this work was to establish the minimal set of ingredients required for void superlattice formation in irradiated materials. The results from Experiment 8 provide compelling evidence that the phenomenon is robust to major simplifications of the governing equations. Specifically, when the full coupled PDE system was reduced to (i) a coupled ODE–PDE system and (ii) a single vacancy PDE with a constant self-interstitial atom concentration, the system still reproduced all essential behaviours: void nucleation, coarsening, and self-organisation into a hexagonal superlattice.

This outcome demonstrates that the pattern-forming instability is not an artefact of complex coupling or high-dimensional phase-field dynamics. Rather, it emerges from the intrinsic structure of the vacancy equation and its nonlinear reaction–diffusion characteristics. Even in the limiting case where self-interstitial atoms are effectively removed from the spatial dynamics (i.e. replaced by a constant s field), the system retains its capacity for spontaneous pattern formation. This suggests that the mechanism responsible for ordering lies within the interplay of non-linear diffusion and thermodynamic instability in a single conserved field, as in the classical Ohta–Kawasaki framework [247].

These findings position the model as a minimal, physically motivated platform for studying void patterning. By removing unnecessary complexity, the reduced formulations clarify which features are essential and which are modulatory. For instance,

the annihilation coupling term modulates the timescale and alignment strength but is not strictly necessary for lattice formation. Similarly, the full spatial dynamics of the self-interstitial atom field accelerate early ordering but do not affect the final structure. In this way, the reduced models in Experiment 8 provide a hierarchy of minimal descriptions, each preserving the core phenomenology while abstracting different levels of physical detail. This not only strengthens confidence in the generality of the results but also lays a foundation for developing analytical approximations and faster computational models based on the same underlying instability mechanism.

5.7.5 Limitations and Future Questions

While the present model successfully captures the emergence of void superlattices via a thermodynamically-driven Turing-like instability, several limitations remain. These reflect both idealisations in the current formulation and simplifications necessary for computational runtimes. Addressing these limitations opens important avenues for future research.

First, the model currently produces only one characteristic length scale, set by a single minimum in the free-energy landscape. This naturally leads to hexagonal ordering in 2D and body-centred cubic (BCC) symmetry in 3D. However, face-centred cubic (FCC) superlattices, observed experimentally in void superlattice systems, require the coexistence of two competing length scales. The present double-well free energy cannot support this, as only one of the wells lies in the physical concentration range. Modifying the free energy to stabilise two physical minima would enable the exploration of FCC structures within a purely isotropic framework.

Second, the model omits anisotropic diffusion, long thought to be essential for symmetry selection. While the current results challenge this assumption by showing that ordering can arise without directional bias, anisotropic mobility remains an important factor in real materials. Incorporating anisotropic diffusion tensors would allow investigation of how directional effects compete or cooperate with thermodynamic instabilities in selecting pattern symmetry and orientation.

Third, elastic interactions and crystallographic effects are not currently included. In

practice, void growth and migration are influenced by stress fields, dislocation networks, and crystallographic orientation. These factors can reshape diffusion pathways, introduce additional instability modes, or act as symmetry-breaking fields. Extending the model to include elastic energy contributions and orientation-dependent mobility would improve its realism and align it more closely with experimental observations.

Fourth, the model is formulated in two dimensions. While this enables systematic parameter studies and visualisation of void organisation, void superlattices are inherently three-dimensional structures. Simulations in 3D are needed to confirm whether the same instability produces BCC patterns and to explore how pattern selection depends on dimensionality.

Finally, the current model assumes constant material parameters. In irradiated environments, these properties evolve over time with temperature, dose rate, and damage accumulation. Incorporating time-dependent mobilities, source terms, or environmental effects would allow simulations to probe dynamic responses such as superlattice dissolution, reformation, or hysteresis.

Collectively, these limitations point toward a broader research agenda. By building on the minimal, robust framework established here, future work can progressively reintroduce physical complexity such as directional diffusion, elastic fields, time-varying parameters, etc. while preserving the core insights into the mechanisms driving void superlattice formation.

5.8 Conclusion

This chapter has demonstrated, through extensive numerical simulations using the MOOSE framework, that void superlattice formation is a robust, emergent phenomenon in a coupled reaction–diffusion system of vacancies and self-interstitial atoms. Across all eight experiments, ranging from tests of mobility ratios, domain sizes, and initial conditions to analytical reductions of the governing equations, the same self-assembly behaviour consistently emerged under appropriate conditions.

The reaction–diffusion model developed in this work supports spontaneous pattern

formation from the initial conditions of a random distribution of vacancies and self-interstitial atoms or a pre-existing collection of voids. Provided the mobility ratio, M_s/M_v, exceeds the bifurcation threshold , the system reliably transitions from disordered phase separation to the formation of a hexagonal close-packed void superlattice. This process is driven entirely by diffusion and energetic minimisation, without the need for any imposed lattice geometry, anisotropic mobilities, or external elastic interactions or advection-driven effects.

The consistent convergence of all reduced models toward the same final void spacing $\Lambda \approx 25.13$ confirms that void self-assembly is not an artefact of model complexity. Even under limiting cases that approach the standard Cahn-Hilliard form, the essential pattern formation behaviour is preserved, reinforcing the view that the phenomenon is dictated by the underlying free-energy landscape and linear instability mechanisms.

5.8.1 Key Takeaways:

- Void superlattice formation is an intrinsic property of the reaction–diffusion model developed in Chapter 3, requiring only mobility contrast and diffusion to emerge.
- A mobility threshold exists at $M_s/M_v \approx 3.322$, consistent with linear stability predictions. Below this threshold, systems undergo Ostwald ripening; above it, voids self-organise into ordered lattices.
- The final superlattice spacing $\Lambda \approx 25.13$ is consistent across all cases — regardless of domain size, initial condition (random or pre-existing), or model reduction; highlighting a fundamental length scale set by the system's energetic landscape.
- Initial conditions influence transient dynamics but not the final state. Systems with pre-existing voids, varying void sizes, or different initial void numbers all converge to the same hexagonal ordering.
- Reduced models preserve pattern formation, even in analytical limits approaching the standard Cahn-Hilliard form. The presence of reaction terms and cou-

pling modifies the dynamics but not the outcome.

- Self-assembly is diffusion-driven and emergent, with no imposed lattice structure or external driving forces. This aligns closely with experimental observations of void ordering under irradiation [66, 67].
- The model captures key features of experimental systems, including void migration, merging, lattice locking, and spacing selection; offering a minimal and predictive framework for studying defect self-organisation.

These results provide strong computational support for the hypothesis that Turing-like instabilities underlie void superlattice formation in irradiated materials. The findings not only validate the theoretical framework introduced in earlier chapters but also establish a simulation platform that can be extended in future work to incorporate more realistic physics, such as anisotropic diffusion, elastic interactions, or gas bubble formation.

Chapter 6

Conclusions and Future Work

6.1 Conclusions

This thesis has introduced and validated a new phase-field model for void superlattice formation in irradiated materials, grounded in a fully conservative, thermodynamically driven reaction-diffusion framework. The model consists of two coupled Cahn-Hilliard equations describing the evolution of vacancy and self-interstitial atom concentrations. Unlike previous approaches that rely on anisotropic mobility, external sink terms, or external forces such as the elastic interactions between voids, this formulation demonstrates that a Turing-like instability can arise purely from non-linear, isotropic diffusion and the difference in mobilities between two conserved defect species.

Through a combination of linear stability analysis and eight simulation experiments, the model was shown to robustly produce hexagonally ordered void superlattices with a single emergent length scale. These patterns consistently emerged across varying initial conditions, domain sizes, and model reductions, which included simplified variants approaching the standard Cahn-Hilliard form.

These findings provide a counterexample to the longstanding assumption in the void superlattice literature that anisotropic diffusion of self-interstitial atoms is necessary for both the formation and lattice selection of ordered defect patterns. While anisotropic diffusion mechanisms remain important in many materials contexts, this work shows that long-range order can arise under isotropic conditions, provided the difference in mobilities exceeds a critical threshold. Anisotropy is therefore not a prerequisite for pattern formation in all cases.

Moreover, the results suggest that lattice selection — traditionally attributed to anisotropic diffusion — may instead be achievable by reshaping the free energy equation. The current model, driven by a single physically meaningful well, naturally selects a single characteristic length scale, favouring HCP-type ordering in 2D and BCC-type ordering in 3D. However, modifying the free energy to include two physically meaningful wells could introduce multiple driving wavelengths, enabling the thermodynamic stabilisation of more complex structures, such as FCC superlattices which require two length scales. This would offer a fully isotropic, diffusion-driven pathway for lattice selection, providing a conceptual alternative to anisotropic mobility and broadening the theoretical framework for pattern formation in irradiated materials.

Together, these contributions establish a minimal, extensible framework that captures the fundamental components for void superlattice formation. The model not only generalises classical Turing instabilities to systems of conserved fields, but also offers a predictive tool for exploring defect self-organisation across a wider class of irradiated and non-equilibrium materials systems.

6.1.1 Key Contributions

- Introduced a fully conservative, thermodynamically driven reaction-diffusion model for defect patterning;
- Identified that a critical mobility ratio is required for instability onset and pattern formation;
- Demonstrated robust pattern formation under isotropic diffusion, without

anisotropic diffusion, external sinks, or external forces such as elastic interaction effects;

- Validated the mechanism through eight simulation experiments, confirming resilience to initial conditions, finite-size effects, and model simplifications;
- Generalised classical Turing theory by extending it to coupled, conserved-field systems with fourth-order diffusion.

6.2 Future Work

Building on this foundation, several directions emerge to expand the model's physical realism, quantitative predictiveness, and experimental relevance:

6.2.1 Physical Parameterisation

The current model has been developed and explored using non-dimensionalised parameters designed to capture the essential features of defect-driven pattern formation. This approach enables general insights into the role of differences in mobilities, reaction rates, and non-linear diffusion, but it limits direct comparison with specific materials or experimental systems.

To enhance the model's predictive capability and experimental relevance, future work should incorporate physically relevant parameters drawn from molecular dynamics, kinetic Monte Carlo, or experimental measurements. Key quantities such as defect diffusivities, vacancy and self-interstitial generation rates under irradiation, and interface energies could be used to constrain the phase-field mobility terms, source/sink strengths, and gradient energy coefficients. Such parameterisation would allow the simulation outputs, such as void spacing, growth rates, and ordering timescales, to be interpreted in dimensional units (e.g., nanometres, seconds, etc.), enabling direct comparison with observations in irradiated metals or alloys.

This process may also reveal material-specific stability windows for void superlattices: ranges of temperature, dose rate, and composition where the conditions for instability are satisfied. These insights would support the use of the model as a screening tool for

identifying materials likely to exhibit ordered defect structures, and could guide the design of irradiation experiments aimed at tuning superlattice properties. Ultimately, embedding the model within a physically grounded parameter space would bridge the gap between conceptual theory and engineering application, advancing its utility for real-world materials design under irradiation.

6.2.2 Enabling FCC Void Superlattices

Anisotropic Diffusion

FCC ordering in simulation models is most commonly attributed to anisotropic self-interstitial diffusion along crystallographic directions. Embedding a direction-dependent mobility tensor into the current framework would extend its fidelity, enabling lattice selection through the inclusion of kinetics. This anisotropy would introduce secondary length scales and bias recombination, potentially stabilising FCC lattices within the existing single-well free energy structure. Such an extension would link directly to other anisotropic transport inclusion models while preserving my model's thermodynamic foundations of a coupled pair of Cahn-Hilliard equations.

Energy Landscape Engineering

Alternatively, FCC ordering could potentially be achieved from a modified free energy equation that supports two physically accessible concentration wells. This would allow two distinct driving wavelengths to coexist, generating interference patterns favouring FCC symmetry — even with isotropic diffusion. By tuning the energy landscape rather than the kinetics, this approach enables symmetry selection through thermodynamic design, offering a conceptually distinct route to complex ordering. It challenges the prevailing view that anisotropic diffusion is essential for FCC formation and broadens the theoretical paradigm for irradiated defect patterning.

6.2.3 Extending the Model to Three Dimensions

While the present model captures void self-organisation effectively in two dimensions, full characterisation of void superlattice symmetry requires extension to three dimensions. In 2D, the system reliably produces hexagonal ordering, consistent with a hexagonal close-packed (HCP) arrangement. This structure aligns with the in-plane projections of a body-centred cubic (BCC) lattice, where HCP planes are stacked in an ABAB configuration. As such, the current results are strongly indicative of BCC-type superlattice formation when extrapolated to 3D.

However, face-centred cubic (FCC) ordering corresponds to an ABC stacking of hexagonal planes and cannot be realised or verified within a two-dimensional framework. Even if the model were modified — via anisotropic diffusion or a redesigned free energy — to support the necessary conditions for FCC formation (i.e., multiple characteristic wavelengths or directional bias), the symmetry of the resulting superlattice could not be unambiguously identified without simulating the full three-dimensional structure.

This introduces a significant computational challenge. The simulations presented in this thesis were conducted on a standard `n2-standard-128` machine with 128 vCPU (64 core) and 512 GB memory. Using this machine, the 200×200 domain simulations typically required 3–5 hours to complete. Scaling the model to three dimensions (e.g., $200 \times 200 \times 200$ domains) would require an order of magnitude more computational time and memory (at least). Such simulations would likely necessitate high-performance computing infrastructure. This is because the numerical solver is already highly optimised, the simulation was already run in parallel, and mesh and time-stepper adaptivity were already implemented.

Nevertheless, 3D simulations represent a crucial next step in validating the model's predictive capabilities. Only by directly observing the three-dimensional arrangement of voids can one confirm whether FCC or BCC superlattices are stabilised under different model conditions. Short of this, arguments for FCC formation based on 2D cross-sections or symmetry considerations remain speculative. Alternatively, one could attempt to identify 2D projections of FCC planes (e.g., [111] or [100] cuts), but this would still rely on indirect inference.

In short, the move to 3D is not only a technical milestone but a necessary one: the distinction between BCC and FCC void superlattices cannot be fully resolved without three-dimensional modelling and visualisation. Future work should therefore prioritise extending the model into 3D domains, especially in cases where the free energy equation or anisotropic diffusion mechanisms suggest the emergence of complex or multi-scale structures.

6.2.4 Void Superlattice Evolution Under Time-Varying Conditions

Experimental studies have firmly established that void and gas bubble superlattices can self-organise under sustained irradiation, transitioning from an initially disordered defect distribution into ordered periodic structures. These transitions are typically described under steady-state conditions, with fixed temperature, dose rate, and irradiation environment. However, it remains an open question whether already-formed superlattices are capable of reorganising or adapting their lattice parameters in response to dynamic changes in these external conditions.

Although temperature and dose rate are known to influence superlattice periodicity — with increased temperature typically yielding larger lattice spacings and higher dose rates promoting finer structures [144] — there is limited experimental or computational evidence exploring whether these changes can drive a transition within an already ordered lattice. In particular, scenarios where a void superlattice transitions from one lattice parameter to another in response to evolving irradiation conditions have not been systematically studied.

To investigate this behaviour, future simulations could explore how an established superlattice responds to time-dependent changes in the governing parameters. For example, a simulation could be initialised under conditions that are known to produce a stable void superlattice — with a fixed mobility ratio, source term c, and annihilation rate a — and allowed to evolve until a well-ordered lattice emerges. At this point, the simulation could be "paused," and the irradiation parameters adjusted to reflect

a change in environment (e.g., an increase in c or reduction in a to mimic a shift in dose rate or defect recombination dynamics or a change in the M_s/M_v ratio to mimic a shift in temperature). The simulation would then resume, and the evolution of the pre-existing lattice tracked.

This approach would test whether the system adapts to the new conditions by re-ordering into a new superlattice with a new lattice parameter, dissolving and reforming entirely, or disorder from its ordered state. It would also probe the existence of metastable states or tolerances within the phase-field model, offering insight into the resilience and flexibility of irradiated materials under realistic, time-varying environments.

Ultimately, such simulations would extend the applicability of the model from steady-state formation to dynamic reconfiguration, providing a valuable tool for interpreting experimental observations and informing the design of irradiation protocols that deliberately steer void superlattice morphology over time.

Appendix A

Python Code - Analytical Results

A.1 Searching the parameter space for Turing instabilities.

```
import pandas as pd
import numpy as np
import math
import matplotlib.pyplot as plt

def f_det_Aq_full(v, s, q):
    gs = 2 * (6 * s * (s - 1) + 1)
    gv = 2 * (6 * v * (v - 1) + 1)
    return (Mv * Ms * math.pow(q, 8)) + (Mv * Ms * (gs + gv) * math.pow(q, 6)) + (Mv * Ms *
         gs * gv + a * (Mv * v + Ms * s)) * math.pow(q, 4) + (a * (Mv * v * gv + Ms * s *
         gs) * math.pow(q, 2))

def f_tr_Aq_full(v, s, q):
    gs = 2 * (6 * s * (s - 1) + 1)
    gv = 2 * (6 * v * (v - 1) + 1)
```

```
    return - ((Ms + Mv) * math.pow(q, 4)) - ((Ms * gs + Mv * gv) * math.pow(q, 2)) - (a * (v
        + s))

l_Mv = []
l_Ms = []
l_v = []
l_s = []
l_q = []
l_det_Aq_full = []
l_tr_Aq_full = []
l_condition_1 = []
l_condition_2 = []

Mv = 1
a = 0.5

for Ms in [1, 2, 3, 4, 5, 10, 50, 100, 500, 1000, 5000, 10000]:

    for q in np.arange(0, 2*math.pi, 0.01):

        for v in np.arange(0, 0.5, 0.01):
            for s in np.arange(0, 0.5, 0.01):

                l_Mv.append(Mv)
                l_Ms.append(Ms)
                l_v.append(v)
                l_s.append(s)
                l_q.append(q)

                determinent = f_det_Aq_full(v, s, q)
                l_det_Aq_full.append(determinent)

                trace = f_tr_Aq_full(v, s, q)
                l_tr_Aq_full.append(trace)

                # Condition 1
                if (math.pow(trace, 2) - 4 * determinent) < 0 and trace > 0:
                    l_condition_1.append(True)
                else:
                    l_condition_1.append(False)
```

```
            # Condition 2
            if determinent < 0 and trace < 0:
                l_condition_2.append(True)
            else:
                l_condition_2.append(False)

df_results = pd.DataFrame({
    "Ms": l_Ms,
    "Mv": l_Mv,
    "v": l_v,
    "s": l_s,
    "q": l_q,
    "det_Aq_full": l_det_Aq_full,
    "tr_Aq_full": l_tr_Aq_full,
    "condition_1": l_condition_1,
    "condition_2": l_condition_2
    }
)

df_results["Ms"] = df_results["Ms"].astype(str)

df_results.head()
```

A.2 2D visualisation of the parameter space where Turing instabilities can exist.

```
for Ms in ["1", "2", "3", "4", "5", "10", "50", "100", "500", "1000", "5000", "10000"]:

    df_temp = df_results[df_results["Ms"] == Ms]

    df_temp_red = df_temp[df_temp["condition_2"] == True]

    print(f"For the Ms/Mv ratio {Ms}")

    fig, ax = plt.subplots()

    x, y = df_temp_red["v"], df_temp_red["s"]
```

```
    ax.scatter(x, y, alpha=0.1, edgecolors="none")

    #ax.legend()
    ax.grid(True)
    ax.set_title(f"Ms/Mv = {Ms}")
    ax.set_xlabel("v")
    ax.set_ylabel("s")

    plt.show()
```

A.3 3D visualisation of the parameter space where Turing instabilities can exist.

```
for Ms in ["1", "2", "3", "4", "5", "10", "50", "100", "500", "1000", "5000", "10000"]:

    df_temp = df_results[df_results["Ms"] == Ms]

    df_temp_red = df_temp[df_temp["condition_2"] == True]

    print(f"For the Ms/Mv ratio {Ms}")

    fig = plt.figure(figsize=(8, 6), dpi=80)
    ax = fig.add_subplot(projection='3d')

    x = df_temp_red["v"]
    y = df_temp_red["s"]
    z = df_temp_red["q"]
    ax.scatter(x, y, z, alpha=0.1)

    ax.set_xlabel("v")
    ax.set_ylabel("s")
    ax.set_zlabel("q")
    ax.zaxis.labelpad=-2
    ax.set_title(f"Ms/Mv = {Ms}")

    plt.show()
```

A.4 Plotting $det\mathbf{A_q}$ Against q^2.

```
l_Mv = []
l_Ms = []
l_qq = []
l_det_Aq = []
l_tr_Aq = []

Mv = 1

v = 0.25
s = 0.01

gs = 2 * (6 * s * (s - 1) + 1)
gv = 2 * (6 * v * (v - 1) + 1)

a = 0.5

def f_det_Aq(q):
    return (Mv * Ms * math.pow(q, 4)) + (Mv * Ms * (gs + gv) * math.pow(q, 3)) + ((Mv * Ms *
          gs * gv + a * (Mv * v + Ms * s)) * math.pow(q, 2)) + (a * (Mv * v * gv + Ms * s *
          gs) * math.pow(q, 1))

for Ms in [1, 2, 3, 4, 5, 10, 50, 100, 500, 1000, 5000, 10000]:

    for q in np.arange(-2*math.pi, 2*math.pi, 0.0001):

        l_Mv.append(1)
        l_Ms.append(Ms)
        l_qq.append(q)
        l_det_Aq.append(f_det_Aq(q))
        l_tr_Aq.append(f_tr_Aq(q))

df_results = pd.DataFrame({
    "Ms": l_Ms,
    "Mv": l_Mv,
    "q**2": l_qq,
    "det_Aq": l_det_Aq,
    "tr_Aq": l_tr_Aq
    }
```

```
)

df_results["Ms"] = df_results["Ms"].astype(str)

#####

f, ax = plt.subplots()

sns.lineplot(
    x="q**2",
    y="det_Aq",
    data=df_results,
    hue="Ms",
    hue_order = ["1", "2", "3", "4", "5", "10"]
)

# Define X and Y min/max
ax.set_xlim(xmin=-0, xmax=0.25)
ax.set_ylim(ymin=-0.04, ymax=0.04)
# Add a title
ax.set_title("Ms / Mv = 1, 2, 3, 4, 5, and 10")
# Put a legend to the right of the current axis
ax.legend(loc="center left", bbox_to_anchor=(1, 0.5))
# Add gridlines
plt.grid()
# Display the plot
plt.show()
```

A.5 Calculating and plotting the maximum eigenvalue of $\mathbf{A_q}$ for q^2 in the range $0 \leq q^2 \leq 2\pi$.

```
from numpy import linalg as LA

l_Mv = []
l_Ms = []
```

```
l_qq = []
l_det_Aq = []
l_tr_Aq = []
l_eig_1_Aq = []
l_eig_2_Aq = []
l_max_eig = []

Mv = 1

v = 0.25
s = 0.01

gs = 2 * (6 * s * (s - 1) + 1)
gv = 2 * (6 * v * (v - 1) + 1)

a = 0.5

for Ms in [1, 2, 3, 4, 5, 10, 50, 100, 500, 1000, 5000, 10000]:

    for q in np.arange(0, 2*math.pi, 0.001):

        l_Mv.append(1)
        l_Ms.append(Ms)
        l_qq.append(q)

        element_1 = (- (Ms * ( math.pow(q, 1) * gs + math.pow(q, 2))) - (a * v))
        element_2 = (- (a * s))
        element_3 = (- (a * v))
        element_4 = (- (Mv * ( math.pow(q, 1) * gv + math.pow(q, 2))) - (a * s))

        Aq = np.matrix([[element_1, element_2], [element_3,element_4 ]])

        eigenvalues, eigenvectors = LA.eig(Aq)
        l_eig_1_Aq.append(eigenvalues[0])
        l_eig_2_Aq.append(eigenvalues[1])
        l_max_eig.append(max(eigenvalues))

df_results = pd.DataFrame({
    "Ms": l_Ms,
    "Mv": l_Mv,
    "q**2": l_qq,
```

```
    "eigen_value_1": l_eig_1_Aq,
    "eigen_value_2": l_eig_2_Aq,
    "max_eigenvalue": l_max_eig
    }
)

df_results["Ms"] = df_results["Ms"].astype(str)

#####

f, ax = plt.subplots()

sns.lineplot(
    x="q**2",
    y="max_eigenvalue",
    data=df_results,
    hue="Ms",
    hue_order = ["1", "2", "3", "4", "5", "10", "50", "100", "500", "1000", "5000", "10000"]
)

# Define X and Y min/max
ax.set_xlim(xmin=-0, xmax=0.25)
ax.set_ylim(ymin=-0.01, ymax=0.015)
ax.set_title("Max eigenvalue of Aq Vs q**2 for increasing Ms/Mv mobility ratio.")
# Put a legend to the right of the current axis
ax.legend(loc="center left", bbox_to_anchor=(1, 0.5))
# Add gridlines
plt.grid()
# Display the plot
plt.show()
```

A.6 Searching the parameter space for "Descarte's Rule of Signs"

```

import pandas as pd
import numpy as np
import math
```

```
import matplotlib.pyplot as plt
import seaborn as sns

#####

def f_sign_changes(Mv, Ms, v, s, a, q):

    gv = 2 * (6 * v * (v - 1) + 1)
    gs = 2 * (6 * s * (s - 1) + 1)

    term_1 = (Mv * Ms * math.pow(q, 4))
    term_2 = (Mv * Ms * (gs + gv) * math.pow(q, 3))
    term_3 = (Mv * Ms * gs * gv + a * (Mv * v + Ms * s)) * math.pow(q, 2)
    term_4 = (a * (Mv * v * gv + Ms * s * gs) * math.pow(q, 1))

    def f_signs(value):
        if value > 0:
            return "+"
        elif value < 0:
            return "-"

    sign_1 = f_signs(term_1)
    sign_2 = f_signs(term_2)
    sign_3 = f_signs(term_3)
    sign_4 = f_signs(term_4)

    def f_num_sign_flip(sign_term_1, sign_term_2, sign_term_3, sign_term_4):
        counter = 0
        if sign_term_1 != sign_term_2:
            counter += 1
        if sign_term_2 != sign_term_3:
            counter += 1
        if sign_term_3 != sign_term_4:
            counter += 1
        return counter

    num_sign_changes = f_num_sign_flip(sign_1, sign_2, sign_3, sign_4)

    return (sign_1, sign_2, sign_3, sign_4), num_sign_changes

#####
```

```
def f_discriminant_4th(Mv, Ms, v, s, A, q):

    gv = 2 * (6 * v * (v - 1) + 1)
    gs = 2 * (6 * s * (s - 1) + 1)

    a = (Mv * Ms * math.pow(q, 4))
    b = (Mv * Ms * (gs + gv) * math.pow(q, 3))
    c = (Mv * Ms * gs * gv + A * (Mv * v + Ms * s)) * math.pow(q, 2)
    d = (A * (Mv * v * gv + Ms * s * gs) * math.pow(q, 1))
    e = 0

    discriminant = 256*math.pow(a, 3)*math.pow(e, 3)\
        - 192*math.pow(a, 2)*math.pow(b, 1)*math.pow(d, 1)*math.pow(e, 2)\
        - 128*math.pow(a, 2)*math.pow(c, 2)*math.pow(e, 2)\
        + 144*math.pow(a, 2)*math.pow(c, 1)*math.pow(d, 2)*math.pow(e, 1)\
        - 27*math.pow(a, 2)*math.pow(d, 4)\
        + 144*math.pow(a, 1)*math.pow(b, 2)*math.pow(c, 1)*math.pow(e, 2)\
        - 6*math.pow(a, 1)*math.pow(b, 2)*math.pow(d, 2)*math.pow(e, 1)\
        - 80*math.pow(a, 1)*math.pow(b, 1)*math.pow(c, 2)*math.pow(d, 1)*math.pow(e, 1) \
        + 18*math.pow(a, 1)*math.pow(b, 1)*math.pow(c, 1)*math.pow(d, 3)\
        + 16*math.pow(a, 1)*math.pow(c, 4)*math.pow(e, 1)\
        - 4*math.pow(a, 1)*math.pow(c, 3)*math.pow(d, 2)\
        - 27*math.pow(b, 4)*math.pow(e, 2)\
        + 18*math.pow(b, 3)*math.pow(c, 1)*math.pow(d, 1)*math.pow(e, 1)\
        - 4*math.pow(b, 3)*math.pow(d, 3)\
        - 4*math.pow(b, 2)*math.pow(c, 3)*math.pow(e, 1)\
        + math.pow(b, 2)*math.pow(c, 2)*math.pow(d, 2)
    return discriminant

#####

def f_det_Aq_full(Mv, Ms, v, s, A, q):
    gs = 2 * (6 * s * (s - 1) + 1)
    gv = 2 * (6 * v * (v - 1) + 1)
    return (Mv * Ms * math.pow(q, 8)) + (Mv * Ms * (gs + gv) * math.pow(q, 6)) + (Mv * Ms *
          gs * gv + a * (Mv * v + Ms * s)) * math.pow(q, 4) + (a * (Mv * v * gv + Ms * s *
          gs) * math.pow(q, 2))

#####
```

```
l_Mv = []
l_Ms = []
l_v = []
l_s = []
l_a = []
l_q = []
l_determinent = []
l_discriminant = []
l_sign_changes = []
l_num_sign_changes = []

Mv = 1
v = 0.25
s = 0.01
a = 0.5

for Ms in np.arange(0, 5, 0.001):
    for q in np.arange(0, 2*math.pi, 0.01):

        determinent = f_det_Aq_full(Mv, Ms, v, s, a, q)
        discriminant = f_discriminant_4th(Mv, Ms, v, s, a, q)
        sign_changes = f_sign_changes(Mv, Ms, v, s, a, q)

        l_Mv.append(Mv)
        l_Ms.append(Ms)
        l_v.append(v)
        l_s.append(s)
        l_a.append(a)
        l_q.append(q)
        l_determinent.append(determinent)
        l_discriminant.append(discriminant)
        l_sign_changes.append(sign_changes[0])
        l_num_sign_changes.append(sign_changes[1])

#####

df_results = pd.DataFrame({
    "Mv": l_Mv,
    "Ms": l_Ms,
    "v": l_v,
    "s": l_s,
```

```
    "a": l_a,
    "q": l_q,
    "determinent": l_determinent,
    "discriminant": l_discriminant,
    "sign_changes": l_sign_changes,
    "num_sign_changes": l_num_sign_changes
})

display(df_results.head())

df_results_mod = df_results[~df_results["sign_changes"].apply(lambda x: any(val is None for
     val in x))]

df_results_mod[df_results_mod["num_sign_changes"] == 2]["Ms"].min()
```

Appendix B

MOOSE Config Files

B.1 Initial Conditions: Random

```
[Mesh]
   [./Square]
      type = GeneratedMeshGenerator
      nx = 400
      ny = 400
      xmax = 200
      ymax = 200
      dim = 2
   [../]
[]

[BCs]
   [./Periodic]
      [./all]
         auto_direction = 'x y'
      [../]
   [../]
[]

[Modules]
   [./PhaseField]
      [./Conserved]
```

```
          [./s]
             solve_type = forward_split
             free_energy = F
             kappa = kappa
             mobility = Ms
             coupled_variables = v
          [../]
          [./v]
             solve_type = forward_split
             free_energy = F
             kappa = kappa
             mobility = Mv
             coupled_variables = s
          [../]
       [../]
   [../]
[]

[ICs]
   [./v_IC]
      type = RandomIC
      seed = 17
      max = 0.2525
      min = 0.2475
      variable = v
   [../]
   [./s_IC]
      type = RandomIC
      seed = 18
      max = 0.0101
      min = 0.0099
      variable = s
   [../]
[]

[Materials]
   [./constants]
      type = GenericConstantMaterial
      prop_names = 'kappa Ms Mv a'
      prop_values = '1 1000 1 -0.5'
   [../]
```

```
   [./annihilation_for_s]
      type = DerivativeParsedMaterial
      material_property_names = 'a'
      coupled_variables = v
      property_name = av
      expression = 'a * v'
   [../]
   [./annihilation_for_v]
      type = DerivativeParsedMaterial
      material_property_names = 'a'
      coupled_variables = s
      property_name = as
      expression = 'a * s'
   [../]
   [./f_bulk]
      type = DerivativeParsedMaterial
      property_name = F
      expression = 's^2 * (1 - s)^2 + v^2 * (1 - v)^2'
      coupled_variables = 's v'
   [../]
   [./creation_mask]
      type = DerivativeParsedMaterial
      property_name = creation_mask
      expression = '(1 - v)^2'
      coupled_variables = 'v'
   [../]
[]

[Kernels]
   [./s_creation]
       type = MaskedBodyForce
       value = 1.25e-3
       variable = s
       mask = creation_mask
       coupled_variables = v
    [../]
    [./v_creation]
       type = MaskedBodyForce
       value = 1.25e-3
       variable = v
       mask = creation_mask
```

```
        coupled_variables = s
    [../]
    [./s_recombination]
        type = MatReaction
        variable = s
        args = v
        mob_name = av
    [../]
    [./v_recombination]
        type = MatReaction
        variable = v
        args = s
        mob_name = as
    [../]
[]

[Preconditioning]
   [./SMP]
       type = SMP
       full = true
   [../]
[]

[Postprocessors]
   [./dt]
       type = TimestepSize
   [../]
   [./num_voids]
       type = FeatureFloodCount
       variable = v
       threshold = 0.5
       compute_var_to_feature_map = true
   [../]
   [./mesh_volume]
       type = VolumePostprocessor
       execute_on = 'initial'
   [../]
   [./porosity]
        type = FeatureVolumeFraction
        feature_volumes = void_volumes
        mesh_volume = mesh_volume
```

```
   [../]
   [./average_v_conc]
      type = ElementAverageValue
      variable = v
   [../]
   [./average_s_conc]
      type = ElementAverageValue
      variable = s
   [../]
 []

[VectorPostprocessors]
   [./void_volumes]
      type = FeatureVolumeVectorPostprocessor
      flood_counter = num_voids
      output_centroids = true
   [../]
[]

[Executioner]
   type = Transient
   scheme = bdf2
   solve_type = NEWTON
   end_time = 50000
   [./TimeStepper]
      type = IterationAdaptiveDT
      dt = 0.1
      optimal_iterations = 9
      growth_factor = 1.1
      cutback_factor = 0.5
      linear_iteration_ratio = 1000
   [../]
   petsc_options_iname = '-pc_type -sub_pc_type -pc_asm_overlap'
   petsc_options_value = 'asm lu 2'
   l_tol = 1e-4
   l_max_its = 250
   nl_rel_tol = 1e-8
   nl_abs_tol = 1e-9
   nl_max_its = 12
   automatic_scaling = true
   compute_scaling_once = false
```

```
   [./Predictor]
      type = SimplePredictor
      scale = 1.0
   [../]
[]

[Outputs]
   print_linear_residuals = false
   perf_graph = false
   [./exodus]
       type = Exodus
       file_base = "output-files/MsMv1000-200x200-exodus/output"
    [../]
    [./outfile]
       type = CSV
       file_base = "output-files/MsMv1000-200x200-csv/output"
    [../]
[]
```

B.2 Initial Conditions: Pre-Existing Voids

```
[Mesh]
   [./Square]
      type = GeneratedMeshGenerator
      nx = 400
      ny = 400
      xmax = 200
      ymax = 200
      dim = 2
   [../]
[]

[BCs]
   [./Periodic]
      [./all]
         auto_direction = 'x y'
      [../]
   [../]
[]
```

```
[Modules]
   [./PhaseField]
      [./Conserved]
         [./s]
            solve_type = forward_split
            free_energy = F
            kappa = kappa
            mobility = Ms
            coupled_variables = v
         [../]
         [./v]
            solve_type = forward_split
            free_energy = F
            kappa = kappa
            mobility = Mv
            coupled_variables = s
         [../]
      [../]
   [../]
[]

[ICs]
   [./v_IC]
      type = MultiSmoothCircleIC
      variable = v
      invalue = 1.0
      outvalue = 0.034
      bubspac = 15.0
      numbub = 65
      radius = 5.9
      int_width = 1.0
      rand_seed = 111
      radius_variation = 0
      radius_variation_type = normal
   [../]
   [./s_IC]
      type = MultiSmoothCircleIC
      variable = s
      invalue = 0.00688
      outvalue = 0.00692
```

```
      bubspac = 15.0
      numbub = 65
      radius = 5.9
      int_width = 1.0
      rand_seed = 111
      radius_variation = 0
      radius_variation_type = normal
   [../]
[]

[Materials]
   [./constants]
      type = GenericConstantMaterial
      prop_names = 'kappa Ms Mv a'
      prop_values = '1 1000 1 -0.5'
   [../]
   [./annihilation_for_s]
      type = DerivativeParsedMaterial
      material_property_names = 'a'
      coupled_variables = v
      property_name = av
      expression = 'a * v'
   [../]
   [./annihilation_for_v]
      type = DerivativeParsedMaterial
      material_property_names = 'a'
      coupled_variables = s
      property_name = as
      expression = 'a * s'
   [../]
   [./f_bulk]
      type = DerivativeParsedMaterial
      property_name = F
      expression = 's^2 * (1 - s)^2 + v^2 * (1 - v)^2'
      coupled_variables = 's v'
   [../]
   [./creation_mask]
      type = DerivativeParsedMaterial
      property_name = creation_mask
      expression = '(1 - v)^2'
      coupled_variables = 'v'
```

```
    [../]
[]

[Kernels]
    [./s_creation]
        type = MaskedBodyForce
        value = 1.25e-3
        variable = s
        mask = creation_mask
        coupled_variables = v
     [../]
     [./v_creation]
        type = MaskedBodyForce
        value = 1.25e-3
        variable = v
        mask = creation_mask
        coupled_variables = s
     [../]
     [./s_recombination]
        type = MatReaction
        variable = s
        args = v
        mob_name = av
     [../]
     [./v_recombination]
        type = MatReaction
        variable = v
        args = s
        mob_name = as
     [../]
[]

[Preconditioning]
    [./SMP]
       type = SMP
       full = true
    [../]
[]

[Postprocessors]
    [./dt]
```

```
      type = TimestepSize
   [../]
   [./num_voids]
      type = FeatureFloodCount
      variable = v
      threshold = 0.5
      compute_var_to_feature_map = true
   [../]
   [./mesh_volume]
      type = VolumePostprocessor
      execute_on = 'initial'
   [../]
   [./porosity]
       type = FeatureVolumeFraction
       feature_volumes = void_volumes
       mesh_volume = mesh_volume
   [../]
   [./average_v_conc]
      type = ElementAverageValue
      variable = v
   [../]
   [./average_s_conc]
      type = ElementAverageValue
      variable = s
   [../]
 []

[VectorPostprocessors]
   [./void_volumes]
      type = FeatureVolumeVectorPostprocessor
      flood_counter = num_voids
      output_centroids = true
   [../]
[]

[Executioner]
   type = Transient
   scheme = bdf2
   solve_type = NEWTON
   end_time = 50000
   [./TimeStepper]
```

```
      type = IterationAdaptiveDT
      dt = 0.1
      optimal_iterations = 9
      growth_factor = 1.1
      cutback_factor = 0.5
      linear_iteration_ratio = 1000
   [../]
   petsc_options_iname = '-pc_type -sub_pc_type -pc_asm_overlap'
   petsc_options_value = 'asm lu 2'
   l_tol = 1e-4
   l_max_its = 250
   nl_rel_tol = 1e-8
   nl_abs_tol = 1e-9
   nl_max_its = 12
   automatic_scaling = true
   compute_scaling_once = false
   [./Predictor]
      type = SimplePredictor
      scale = 1.0
   [../]
[]

[Outputs]
   print_linear_residuals = false
   perf_graph = false
   [./exodus]
       type = Exodus
       file_base = "output-files/MsMv1000-200x200-multiCircle65-exodus/output"
    [../]
    [./outfile]
       type = CSV
       file_base = "output-files/MsMv1000-200x200-multiCircle65-csv/output"
    [../]
[]
```

B.3 Coupled PDE and ODE

```
[Mesh]
   [./Square]
```

```
      type = GeneratedMeshGenerator
      nx = 400
      ny = 400
      xmax = 200
      ymax = 200
      dim = 2
   [../]
[]

[BCs]
   [./Periodic]
      [./all]
         auto_direction = 'x y'
      [../]
   [../]
[]

[Modules]
   [./PhaseField]
      [./Conserved]
         [./v]
            solve_type = forward_split
            free_energy = F
            kappa = kappa
            mobility = Mv
            coupled_variables = s
         [../]
      [../]
   [../]
[]

[ICs]
   [./v_IC]
      type = RandomIC
      seed = 17
      max = 0.2525
      min = 0.2475
      variable = v
   [../]
[]
```

```
[Variables]
   [./s_scalar]
      family = SCALAR
      order = FIRST
      initial_condition = 0.01
   [../]
[]

[AuxVariables]
   [./s]
   [../]
[]

[Materials]
   [./constants]
      type = GenericConstantMaterial
      prop_names = 'kappa Ms Mv a'
      prop_values = '1 1000 1 -0.5'
   [../]
   [./annihilation_for_v]
      type = DerivativeParsedMaterial
      material_property_names = 'a'
      coupled_variables = s
      property_name = annihilation_for_v
      expression = 'a * s'
   [../]
   [./f_bulk]
      type = DerivativeParsedMaterial
      property_name = F
      expression = 's^2 * (1 - s)^2 + v^2 * (1 - v)^2'
      coupled_variables = 's v'
   [../]
[]

[Kernels]
    [./v_creation]
       type = MaskedBodyForce
       value = 1.25e-3
       variable = v
    [../]
    [./v_recombination]
```

```
        type = MatReaction
        variable = v
        args = s
        mob_name = annihilation_for_v
    [../]
[]

[AuxKernels]
   [./s]
      type = FunctionAux
      variable = s
      function = s_func
      execute_on = 'INITIAL LINEAR TIMESTEP_END'
   [../]
[]

[ScalarKernels]
   [./s_scalar_dot]
      type = ODETimeDerivative
      variable = s_scalar
   [../]
   [./s_rest]
      type = ParsedODEKernel
      expression = '-(c - average_v_conc*s_scalar*a)'
      variable = s_scalar
      postprocessors = average_v_conc
      constant_names = 'c a'
      constant_expressions = '1.25e-3 0.5'
   [../]
[]

[Functions]
   [./s_func]
      type = ParsedFunction
      symbol_names = 's_scalar_reporter'
      symbol_values = 's_scalar_reporter'
      expression = 's_scalar_reporter'
      execute_on = 'INITIAL LINEAR'
   [../]
[]
```

```
[Preconditioning]
  [./SMP]
    type = SMP
    full = true
  [../]
[]

[Postprocessors]
  [./dt]
    type = TimestepSize
  [../]
  [./num_voids]
    type = FeatureFloodCount
    variable = v
    threshold = 0.5
    compute_var_to_feature_map = true
  [../]
  [./mesh_volume]
    type = VolumePostprocessor
    execute_on = 'initial'
  [../]
  [./porosity]
     type = FeatureVolumeFraction
     feature_volumes = void_volumes
     mesh_volume = mesh_volume
  [../]
  [./average_v_conc]
    type = ElementAverageValue
    variable = v
    execute_on = 'TIMESTEP_END'
  [../]
  [./average_s_conc]
    type = ElementAverageValue
    variable = s
  [../]
  [./s_scalar_reporter]
    type = ScalarVariable
    variable = s_scalar
    execute_on = 'INITIAL LINEAR TIMESTEP_END'
  [../]
[]
```

```
[VectorPostprocessors]
   [./void_volumes]
      type = FeatureVolumeVectorPostprocessor
      flood_counter = num_voids
      output_centroids = true
   [../]
[]

[Executioner]
   type = Transient
   scheme = bdf2
   solve_type = NEWTON
   end_time = 50000
   [./TimeStepper]
      type = IterationAdaptiveDT
      dt = 0.1
      optimal_iterations = 6
      linear_iteration_ratio = 300
   [../]
   petsc_options_iname = '-pc_type -sub_pc_type -pc_asm_overlap'
   petsc_options_value = 'asm lu 2'
   l_tol = 1e-4
   l_max_its = 20
   nl_rel_tol = 1e-8
   nl_abs_tol = 1e-9
   nl_max_its = 12
   automatic_scaling = true
   compute_scaling_once = false
   [./Predictor]
      type = SimplePredictor
      scale = 1.0
   [../]
[]

[Outputs]
   print_linear_residuals = false
   print_nonlinear_residuals = false
   perf_graph = false
   [./exodus]
       type = Exodus
```

```
        file_base = "output-files/MsMv1000-200x200-coupled-ODE-PDE-exodus/output"
    [../]
    [./outfile]
        type = CSV
        file_base = "output-files/MsMv1000-200x200-coupled-ODE-PDE-csv/output"
    [../]
[]
```

B.4 Single PDE with Constant s

```
[Mesh]
   [./Square]
      type = GeneratedMeshGenerator
      nx = 400
      ny = 400
      xmax = 200
      ymax = 200
      dim = 2
   [../]
[]

[BCs]
   [./Periodic]
      [./all]
         auto_direction = 'x y'
      [../]
   [../]
[]

[Modules]
   [./PhaseField]
      [./Conserved]
         [./v]
            solve_type = forward_split
            free_energy = F
            kappa = kappa
            mobility = Mv
         [../]
      [../]
```

```
    [../]
[]

[ICs]
    [./v_IC]
        type = RandomIC
        seed = 17
        max = 0.2525
        min = 0.2475
        variable = v
    [../]
[]

[Variables]
    [./s_scalar]
        family = SCALAR
        order = FIRST
        initial_condition = 0.01
    [../]
[]

[AuxVariables]
    [./average_v_conc]
    [../]
    [./s]
    [../]
[]

[Materials]
    [./constants]
        type = GenericConstantMaterial
        prop_names = 'kappa Mv a'
        prop_values = '1 1 -0.5'
    [../]
    [./annihilation_for_v]
        type = DerivativeParsedMaterial
        material_property_names = 'a'
        coupled_variables = s
        property_name = annihilation_for_v
        expression = 'a * s'
    [../]
```

```
   [./f_bulk]
      type = DerivativeParsedMaterial
      property_name = F
      expression = 's^2 * (1 - s)^2 + v^2 * (1 - v)^2'
      coupled_variables = 's v'
   [../]
[]

[Kernels]
    [./v_creation]
        type = MaskedBodyForce
        value = 1.25e-3
        variable = v
    [../]
    [./v_recombination]
        type = MatReaction
        variable = v
        args = s
        mob_name = annihilation_for_v
    [../]
[]

[AuxKernels]
   [./average_v_conc_kernel]
      type = FunctionAux
      variable = average_v_conc
      function = average_v_conc_function
      execute_on = 'INITIAL TIMESTEP_BEGIN'
   [../]
   [./s]
      type = ParsedAux
      variable = s
      coupled_variables = average_v_conc
      expression = '1.25e-3/(0.5*average_v_conc)'
   [../]
[]

[ScalarKernels]
   [./s_scalar_dot]
      type = ODETimeDerivative
      variable = s_scalar
```

```
    [../]
    [./s_rest]
        type = ParsedODEKernel
        expression = '-(c - average_v_conc*s_scalar*a)'
        variable = s_scalar
        postprocessors = average_v_conc
        constant_names = 'c a'
        constant_expressions = '1.25e-3 0.5'
    [../]
[]

[Functions]
    [./average_v_conc_func]
        type = ParsedFunction
        symbol_names = 'average_v_conc'
        symbol_values = 'average_v_conc'
        expression = 'average_v_conc'
    [../]
[]

[Preconditioning]
    [./SMP]
        type = SMP
        full = true
    [../]
[]

[Postprocessors]
    [./dt]
        type = TimestepSize
    [../]
    [./num_voids]
        type = FeatureFloodCount
        variable = v
        threshold = 0.5
        compute_var_to_feature_map = true
    [../]
    [./mesh_volume]
        type = VolumePostprocessor
        execute_on = 'initial'
    [../]
```

```
   [./porosity]
        type = FeatureVolumeFraction
        feature_volumes = void_volumes
        mesh_volume = mesh_volume
   [../]
   [./average_v_conc]
       type = ElementAverageValue
       variable = v
       execute_on = 'TIMESTEP_END'
   [../]
   [./average_s_conc]
       type = ElementAverageValue
       variable = s
   [../]
 []

[VectorPostprocessors]
   [./void_volumes]
       type = FeatureVolumeVectorPostprocessor
       flood_counter = num_voids
       output_centroids = true
   [../]
[]

[Executioner]
   type = Transient
   scheme = bdf2
   solve_type = NEWTON
   end_time = 50000
   [./TimeStepper]
       type = IterationAdaptiveDT
       dt = 0.1
       optimal_iterations = 6
       linear_iteration_ratio = 300
   [../]
   petsc_options_iname = '-pc_type -sub_pc_type -pc_asm_overlap'
   petsc_options_value = 'asm lu 2'
   l_tol = 1e-4
   l_max_its = 20
   nl_rel_tol = 1e-8
   nl_abs_tol = 1e-9
```

```
   nl_max_its = 12
   automatic_scaling = true
   compute_scaling_once = false
   [./Predictor]
      type = SimplePredictor
      scale = 1.0
   [../]
[]

[Outputs]
   print_linear_residuals = false
   print_nonlinear_residuals = false
   perf_graph = false
   [./exodus]
       type = Exodus
       file_base = "output-files/MsMv1000-200x200-Single-PDE-exodus/output"
    [../]
    [./outfile]
       type = CSV
       file_base = "output-files/MsMv1000-200x200-Single-PDE-csv/output"
    [../]
[]
```

Appendix C

Python Code - MOOSE Simulation Analysis

C.1 Example of Python Code to Convert ParaView images to FFT images

Followed the Fourier Transform tutorial on the OpenCV website: `https://opencv24-python-tutorials.readthedocs.io/en/latest/py_tutorials/py_imgproc/py_transforms/py_fourier_transform/py_fourier_transform.html` [248]

```
import cv2
import numpy as np
from matplotlib import pyplot as plt
import os

#####

l_directories = [
"/Users/mwn/DPhil/LaTeX/images/sim-paraview/PDE",
"/Users/mwn/DPhil/LaTeX/images/sim-paraview/MsMv1-200x200",
```

```
"/Users/mwn/DPhil/LaTeX/images/sim-paraview/MsMv2-200x200",
"/Users/mwn/DPhil/LaTeX/images/sim-paraview/MsMv4-200x200",
"/Users/mwn/DPhil/LaTeX/images/sim-paraview/MsMv5-200x200",
"/Users/mwn/DPhil/LaTeX/images/sim-paraview/MsMv10-200x200",
"/Users/mwn/DPhil/LaTeX/images/sim-paraview/MsMv100-200x200",
"/Users/mwn/DPhil/LaTeX/images/sim-paraview/MsMv1000-50x50",
"/Users/mwn/DPhil/LaTeX/images/sim-paraview/MsMv1000-100x100",
"/Users/mwn/DPhil/LaTeX/images/sim-paraview/MsMv1000-200x200",
"/Users/mwn/DPhil/LaTeX/images/sim-paraview/MsMv1000-200x200-multiCircle35",
"/Users/mwn/DPhil/LaTeX/images/sim-paraview/MsMv1000-200x200-multiCircle50",
"/Users/mwn/DPhil/LaTeX/images/sim-paraview/MsMv1000-200x200-multiCircle65",
"/Users/mwn/DPhil/LaTeX/images/sim-paraview/MsMv1000-200x200-multiCircle65+20perc",
"/Users/mwn/DPhil/LaTeX/images/sim-paraview/MsMv1000-200x200-multiCircle65+40perc",
"/Users/mwn/DPhil/LaTeX/images/sim-paraview/MsMv1000-200x200-multiCircle65+60perc",
"/Users/mwn/DPhil/LaTeX/images/sim-paraview/MsMv1000-200x200-multiCircle65+80perc",
"/Users/mwn/DPhil/LaTeX/images/sim-paraview/MsMv1000-200x200-multiCircle80",
"/Users/mwn/DPhil/LaTeX/images/sim-paraview/MsMv1000-200x200-multiCircle95",
"/Users/mwn/DPhil/LaTeX/images/sim-paraview/MsMv1000-300x300",
"/Users/mwn/DPhil/LaTeX/images/sim-paraview/MsMv1000-400x400",
"/Users/mwn/DPhil/LaTeX/images/sim-paraview/MsMv10000-200x200",
"/Users/mwn/DPhil/LaTeX/images/sim-paraview/ODE",
]

#####

for dir_path in l_directories:

    # list all files
    l_filenames = [os.path.join(dirpath,f) for (dirpath, dirnames, filenames) in
         os.walk(dir_path) for f in filenames if ".DS_Store" not in f]


    # extract the experiment folder
    l_experiment_folder = [f.split("/")[7] for f in l_filenames]

    # extract the timestamp
    l_timestamp = [f.split("/")[8] for f in l_filenames]

    for file_path, experiment, timestamp in zip(l_filenames, l_experiment_folder,
         l_timestamp):
```

```
    loaded_image = cv2.imread(file_path,0)
    fft_loaded_image = np.fft.fft2(loaded_image)
    fshift = np.fft.fftshift(fft_loaded_image)
    magnitude_spectrum = 20*np.log(np.abs(fshift))

    plt.imshow(magnitude_spectrum, cmap = 'gray')
    plt.savefig(f"/Users/mwn/DPhil/LaTeX/images/FFT-images/{experiment}/{timestamp}")
```

C.2 Example of Python Code to Generate Metric Plots from MOOSE Output Files

```
import pandas as pd
import numpy as np
import math
from scipy import stats

from os import listdir
from os.path import isfile, join

import seaborn as sns
import matplotlib.pyplot as plt

#####

exp_1 = "/Users/mwn/Downloads/MsMv1000-200x200-multiCircle65-correction-csv"
exp_2 = "/Users/mwn/Downloads/MsMv1000-200x200-multiCircle65+20perc-correction-csv"
exp_3 = "/Users/mwn/Downloads/MsMv1000-200x200-multiCircle65+40perc-correction-csv"
exp_4 = "/Users/mwn/Downloads/MsMv1000-200x200-multiCircle65+60perc-correction-csv"
exp_5 = "/Users/mwn/Downloads/MsMv1000-200x200-multiCircle65+80perc-correction-csv"

#####

def f_find_radius(val_area):
    """Calculates the radius of a circle given an area"""
    return math.sqrt(val_area/math.pi)

def f_walk_directory_sans_output(path):
    """Returns all file names in a directory"""
```

```
    l_tmp = []
    for item in listdir(path):
        if item != "output.csv":
            l_tmp.append(item)
    return sorted(l_tmp)

#####

l_exp_paths = [exp_1, exp_2, exp_3, exp_4, exp_5]

df_output = pd.DataFrame()

for exp in l_exp_paths:

    # Containers for stats
    l_tmp_void_radius_count = []
    l_tmp_void_radius_mean = []
    l_tmp_void_radius_std = []
    l_tmp_void_radius_max = []
    l_tmp_void_radius_min = []
    l_tmp_void_radius_median = []
    l_tmp_void_radius_Q1 = []
    l_tmp_void_radius_Q3 = []

    l_tmp_void_area_count = []
    l_tmp_void_area_mean = []
    l_tmp_void_area_std = []
    l_tmp_void_area_max = []
    l_tmp_void_area_min = []
    l_tmp_void_area_median = []
    l_tmp_void_area_Q1 = []
    l_tmp_void_area_Q3 = []

    l_tmp_radius_spread = []
    l_tmp_area_spread = []

    l_tmp_median_void_nn = []
    l_tmp_mean_void_nn = []
    l_tmp_spread_void_nn = []
    l_tmp_min_void_nn = []
    l_tmp_max_void_nn = []
```

```
for index, timestep_csv_file in enumerate(f_walk_directory_sans_output(exp)):

    df_tmp_output = pd.read_csv(exp + "/output.csv")
    df_tmp_output["initial_voids"] = 65
    try:
        df_tmp_output["variation"] = int(exp.split("multiCircle65+")[1].split("perc")[0])
    except Exception as e:
        df_tmp_output["variation"] = 0

    # Timestep data of the active voids
    tmp_num_voids = df_tmp_output["num_voids"].iloc[index]
    df_tmp_timestep = pd.read_csv(f"{exp}/{timestep_csv_file}")
    df_tmp_timestep = df_tmp_timestep.head(tmp_num_voids)

    # Calculate the radius
    df_tmp_timestep["radius"] = df_tmp_timestep["feature_volumes"].apply(f_find_radius)

    # Calculate the distances between centroids
    l_centroid_distances = []
    l_checked_pair = []

    for i in range(0, len(df_tmp_timestep), 1):
        x_1 = df_tmp_timestep["centroid_x"].iloc[i]
        y_1 = df_tmp_timestep["centroid_y"].iloc[i]
        radius = df_tmp_timestep["radius"].iloc[i]
        l_tmp_nearest_neighbours = []

        for j in range(0, len(df_tmp_timestep), 1):
            if not i==j:
                x_2 = df_tmp_timestep["centroid_x"].iloc[j]
                y_2 = df_tmp_timestep["centroid_y"].iloc[j]
                if not (x_1, y_1, x_2, y_2) in l_checked_pair:
                    distance = math.sqrt((x_2 - x_1)**2 + (y_2 - y_1)**2)
                    l_checked_pair.append((x_2, y_2, x_1, y_1))
                    if distance < radius:
                        pass
                    else:
                        l_tmp_nearest_neighbours.append(distance)

        l_tmp_nearest_neighbours = sorted(l_tmp_nearest_neighbours)[0:1]
```

```
        l_centroid_distances.extend(l_tmp_nearest_neighbours)

    mean_distance_nearest_neighbours = stats.tmean(l_centroid_distances) if
        l_centroid_distances else None
    median_distance_nearest_neighbours = np.percentile(l_centroid_distances, 50) if
        l_centroid_distances else None
    spread_distance_nearest_neighbours =
        stats.tstd(l_centroid_distances)/stats.tmean(l_centroid_distances) if
        l_centroid_distances else None
    min_distance_nearest_neighbours = min(l_centroid_distances) if l_centroid_distances
        else None
    max_distance_nearest_neighbours = max(l_centroid_distances) if l_centroid_distances
        else None

    l_tmp_mean_void_nn.append(mean_distance_nearest_neighbours)
    l_tmp_median_void_nn.append(median_distance_nearest_neighbours)
    l_tmp_spread_void_nn.append(spread_distance_nearest_neighbours)
    l_tmp_min_void_nn.append(min_distance_nearest_neighbours)
    l_tmp_max_void_nn.append(max_distance_nearest_neighbours)

    # describe() method to get stats of radius
    descriptive_stats_radius = df_tmp_timestep["radius"].describe()
    tmp_radius_count = descriptive_stats_radius.get("count", 0)
    tmp_radius_mean = descriptive_stats_radius.get("mean", 0)
    tmp_radius_std = descriptive_stats_radius.get("std", 0)
    tmp_radius_max = descriptive_stats_radius.get("max", 0)
    tmp_radius_min = descriptive_stats_radius.get("min", 0)
    tmp_radius_median = descriptive_stats_radius.get("50\%", 0)
    tmp_radius_Q1 = descriptive_stats_radius.get("25\%", 0)
    tmp_radius_Q3 = descriptive_stats_radius.get("75\%", 0)

    # Add to their container lists
    l_tmp_void_radius_count.append(tmp_radius_count)
    l_tmp_void_radius_mean.append(tmp_radius_mean)
    l_tmp_void_radius_std.append(tmp_radius_std)
    l_tmp_void_radius_max.append(tmp_radius_max)
    l_tmp_void_radius_min.append(tmp_radius_min)
    l_tmp_void_radius_median.append(tmp_radius_median)
    l_tmp_void_radius_Q1.append(tmp_radius_Q1)
    l_tmp_void_radius_Q3.append(tmp_radius_Q3)
```

```
        # describe() method to get stats of area
        descriptive_stats_area = df_tmp_timestep["feature_volumes"].describe()
        tmp_area_count = descriptive_stats_area.get("count", 0)
        tmp_area_mean = descriptive_stats_area.get("mean", 0)
        tmp_area_std = descriptive_stats_area.get("std", 0)
        tmp_area_max = descriptive_stats_area.get("max", 0)
        tmp_area_min = descriptive_stats_area.get("min", 0)
        tmp_area_median = descriptive_stats_area.get("50\%", 0)
        tmp_area_Q1 = descriptive_stats_area.get("25\%", 0)
        tmp_area_Q3 = descriptive_stats_area.get("75\%", 0)

        # Add to their container lists
        l_tmp_void_area_count.append(tmp_area_count)
        l_tmp_void_area_mean.append(tmp_area_mean)
        l_tmp_void_area_std.append(tmp_area_std)
        l_tmp_void_area_max.append(tmp_area_max)
        l_tmp_void_area_min.append(tmp_area_min)
        l_tmp_void_area_median.append(tmp_area_median)
        l_tmp_void_area_Q1.append(tmp_area_Q1)
        l_tmp_void_area_Q3.append(tmp_area_Q3)

    df_tmp_output["mean_void_distance_nearest_neighbours"] = l_tmp_mean_void_nn
    df_tmp_output["median_void_distance_nearest_neighbours"] = l_tmp_median_void_nn
    df_tmp_output["spread_void_distance_nearest_neighbours"] = l_tmp_spread_void_nn
    df_tmp_output["min_void_distance_nearest_neighbours"] = l_tmp_min_void_nn
    df_tmp_output["max_void_distance_nearest_neighbours"] = l_tmp_max_void_nn

    df_tmp_output["voids_radius_stats_count"] = l_tmp_void_radius_count
    df_tmp_output["voids_radius_stats_mean"] = l_tmp_void_radius_mean
    df_tmp_output["voids_radius_stats_std"] = l_tmp_void_radius_std
    df_tmp_output["voids_radius_stats_max"] = l_tmp_void_radius_max
    df_tmp_output["voids_radius_stats_min"] = l_tmp_void_radius_min
    df_tmp_output["voids_radius_stats_median"] = l_tmp_void_radius_median
    df_tmp_output["voids_radius_stats_Q1"] = l_tmp_void_radius_Q1
    df_tmp_output["voids_radius_stats_Q3"] = l_tmp_void_radius_Q3

    df_tmp_output["voids_area_stats_count"] = l_tmp_void_area_count
    df_tmp_output["voids_area_stats_mean"] = l_tmp_void_area_mean
    df_tmp_output["voids_area_stats_std"] = l_tmp_void_area_std
    df_tmp_output["voids_area_stats_max"] = l_tmp_void_area_max
    df_tmp_output["voids_area_stats_min"] = l_tmp_void_area_min
```

```
    df_tmp_output["voids_area_stats_median"] = l_tmp_void_area_median
    df_tmp_output["voids_area_stats_Q1"] = l_tmp_void_area_Q1
    df_tmp_output["voids_area_stats_Q3"] = l_tmp_void_area_Q3

    df_output = pd.concat([df_output, df_tmp_output])

display(df_output.head())

#####

sns.set_theme(style="ticks")

f, ax = plt.subplots()

g = sns.lineplot(
    x="time",
    y="num_voids",
    hue = "variation",
    hue_order = [0, 20, 40, 60, 80],
    data=df_output,
    palette="colorblind",
    legend=True
)

# Define X and Y min/max
ax.set_xlim(xmin=0, xmax=50000)
ax.set_ylim(ymin=0, ymax=70)

# Add a title and axes labels
ax.set_title("Number of Voids vs Time")
ax.set_xlabel("Time")
ax.set_ylabel("Number of Voids")

# Put a legend to the right of the current axis
plt.legend(title="Initial Void \nRadius Variation (\%)")
sns.move_legend(ax, "upper left", bbox_to_anchor=(1, 1))

# Add gridlines and remove spines
sns.despine()
plt.grid()
```

```
# Display the plot
plt.show(g)

#####

f, ax = plt.subplots()

g = sns.lineplot(
    x="time",
    y="num_voids",
    hue = "variation",
    hue_order = [0, 20, 40, 60, 80],
    data=df_output,
    palette="colorblind",
    legend=True
)

# Define X and Y min/max
ax.set_xlim(xmin=1, xmax=50000)
ax.set_ylim(ymin=1, ymax=1000)
ax.set_xscale("log")
ax.set_yscale("log")

# Define X and Y min/max
ax.set_xlim(xmin=0, xmax=50000)
ax.set_ylim(ymin=0, ymax=70)

# Add a title and axes labels
ax.set_title("Number of Voids vs Time as a log-log Plot")
ax.set_xlabel("Time")
ax.set_ylabel("Number of Voids")

# Put a legend to the right of the current axis
plt.legend(title="Initial Void \nRadius Variation (\%)")
sns.move_legend(ax, "upper left", bbox_to_anchor=(1, 1))

# Add gridlines and remove spines
sns.despine()
plt.grid()

# Display the plot
```

```
plt.show(g)
```

Bibliography

[1] S. Marc Cohen and C. D. C. Reeve. "Aristotle's Metaphysics". In: *The Stanford Encyclopedia of Philosophy*. Ed. by Edward N. Zalta. Winter 2021. Metaphysics Research Lab, Stanford University, 2021.

[2] M. Cross and H. Greenside. *Pattern Formation and Dynamics in Nonequilibrium Systems*. Cambridge University Press, 2009. DOI: https://doi.org/10.1017/CBO9780511627200.

[3] L. E. (Laurence E.) Sigler. *Fibonacci's Liber Abaci: A Translation into Modern English of Leonardo Pisano's Book of Calculation*. Sources and studies in the history of mathematics and physical sciences. pub-SV, 2002.

[4] Mario Livio. *The golden ratio: the story of phi, the world's most astonishing number*. New York : Broadway Books, 2003.

[5] P. Borckmans et al. "Turing Bifurcations and Pattern Selection". In: *Chemical Waves and Patterns*. Ed. by Raymond Kapral and Kenneth Showalter. Springer Netherlands, 1995, pp. 323–363. ISBN: 978-94-011-1156-0. DOI: https://doi.org/10.1007/978-94-011-1156-0_10.

[6] Daniel Walgraef. "Non Linear Dynamics, Pattern Formation and Materials Science". In: *Instabilities and Nonequilibrium Structures VII & VIII*.

Springer, 2004, pp. 355–370. DOI: https://doi.org/10.1007/978-1-4020-2149-7_27.

[7] Eberhard Bodenschatz, Walter Zimmermann, and Lorenz Kramer. "On electrically driven pattern-forming instabilities in planar nematics". In: *Journal de Physique* 49.11 (1988), pp. 1875–1899. DOI: https://doi.org/10.1051/jphys:0198800490110187500.

[8] Ingo Rehberg et al. "Pattern formation in a liquid crystal". In: *Festkörperprobleme 29: Plenary Lectures of the Divisions Semiconductor Physics Thin Films Dynamics and Statistical Physics Magnetism Metal Physics Surface Physics Low Temperature Physics of the German Physical Society (DPG), Münster, April 3 to 7, 1989* (1989), pp. 35–52. DOI: https://doi.org/10.1007/BFb0108006.

[9] FH Busse. "Non-linear properties of thermal convection". In: *Reports on Progress in Physics* 41.12 (1978), p. 1929. DOI: https://doi.org/10.1088/0034-4885/41/12/003.

[10] Friedrich H Busse and N Riahi. "Nonlinear convection in a layer with nearly insulating boundaries". In: *Journal of Fluid Mechanics* 96.2 (1980), pp. 243–256. DOI: https://doi.org/10.1017/S0022112080002091.

[11] GI Sivashinsky. "On cellular instability in the solidification of a dilute binary alloy". In: *Physica D: Nonlinear Phenomena* 8.1-2 (1983), pp. 243–248. DOI: https://doi.org/10.1016/0167-2789(83)90321-4.

[12] MQ López-Salvans et al. "Fingering in thin layer electrodeposition". In: *Materials Instabilities*. World Scientific, 2000, pp. 159–196. DOI: https://doi.org/10.1142/9789812793317_0003.

[13] H Neuhäuser. "Plastic instabilities and the deformation of metals". In: *Patterns, Defects and Materials Instabilities*. Springer, 1990, pp. 241–276. DOI: https://doi.org/10.1007/978-94-009-0593-1_19.

[14] J Kratochvil. "Dislocation pattern formation in metals". In: *Revue de physique appliquée* 23.4 (1988), pp. 419–429. DOI: https://doi.org/10.1051/rphysap:01988002304041900.

[15] J. H. Evans. "Observations of a regular void array in high purity molybdenum irradiated with 2 MeV nitrogen ions". In: *Nature* 229.5284 (1971), pp. 403–404. DOI: https://doi.org/10.1038/229403a0.

[16] SL Sass and BL Eyre. "Diffraction from void and bubble arrays in irradiated molybdenum". In: *Philosophical Magazine* 27.6 (1973), pp. 1447–1453. DOI: https://doi.org/10.1080/14786437308226898.

[17] M Seul and R Wolfe. "Evolution of disorder in magnetic stripe domains. II. Hairpins and labyrinth patterns versus branches and comb patterns formed by growing minority component". In: *Physical Review A* 46.12 (1992), p. 7534. DOI: https://doi.org/10.1103/PhysRevA.46.7534.

[18] Alan Mathison Turing. "The chemical basis of morphogenesis". In: *Bulletin of mathematical biology* 52 (1990), pp. 153–197. DOI: https://doi.org/10.1007/BF02459572.

[19] Otto Hahn and Fritz Strassmann. "Über den Nachweis und das Verhalten der bei der Bestrahlung des Urans mittels Neutronen entstehenden Erdalkalimetalle". In: *Naturwissenschaften* 27.1 (1939), pp. 11–15. DOI: https://doi.org/10.1007/BF01488241.

[20] Lise Meitner and Otto R Frisch. "Products of the fission of the uranium nucleus". In: *Nature* 143.3620 (1939), pp. 471–472. DOI: https://doi.org/10.1038/143471a0.

[21] W Schuettmann. "The discovery of uranium by Martin Heinrich Klaproth 200 years ago". In: *Kernenergie* 32.10 (1989), pp. 416–420.

[22] World Nuclear Association. *Outline History of Nuclear Energy*. 2023. URL: https://world-nuclear.org/information-library/current-and-future-generation/outline-history-of-nuclear-energy.aspx (visited on 09/21/2023).

[23] US Department of Energy. *The Manhatten Project and interactive history*. 2023. URL: https://www.osti.gov/opennet/manhattan-project-history/People/Scientists/leo-szilard.html (visited on 09/21/2023).

[24] Niels Bohr and John Archibald Wheeler. "The mechanism of nuclear fission". In: *Physical Review* 56.5 (1939), p. 426. DOI: https://doi.org/10.1103/PhysRev.56.426.

[25] Paul Breeze. "Chapter 17 - Nuclear Power". In: *Power Generation Technologies (Third Edition)*. Ed. by Paul Breeze. Third Edition. Newnes, 2019, pp. 399–429. ISBN: 978-0-08-102631-1. DOI: https://doi.org/10.1016/B978-0-08-102631-1.00017-1. URL: https://www.sciencedirect.com/science/article/pii/B9780081026311000171.

[26] LibreTexts: Chemistry. *21.6: Nuclear Fission*. 2023. URL: https://chem.libretexts.org/Bookshelves/General_Chemistry/Map%3A_Chemistry_-_The_Central_Science_(Brown_et_al.)/21%3A_Nuclear_Chemistry/21.06%3A_Nuclear_Fission (visited on 09/22/2023).

[27] World Nuclear Association. *Physics of Uranium and Nuclear Energy*. 2023. URL: https://world-nuclear.org/information-library/nuclear-fuel-cycle/introduction/physics-of-nuclear-energy.aspx (visited on 09/22/2023).

[28] N Sowmya and HC Manjunatha. "A study of binary fission and ternary fission". In: *Bulg. J. Phys* 46 (2019), pp. 16–27. URL: https://api.semanticscholar.org/CorpusID:172132297.

[29] R d E Atkinson and Friitz G Houtermans. "Zur Frage der Aufbaumöglichkeit der Elemente in Sternen". In: *Zeitschrift für Physik* 54.9-10 (1929), pp. 656–665. DOI: https://doi.org/10.1007/BF01341595.

[30] Marcus Laurence Elwin Oliphant, Paul Harteck, and Ernest Rutherford. "Transmutation effects observed with heavy hydrogen". In: *Proceedings of the Royal Society of London. Series A, Containing Papers of a Mathematical and Physical Character* 144.853 (1934), pp. 692–703. DOI: https://doi.org/10.1098/rspa.1934.0077.

[31] Hans Albrecht Bethe. "Energy production in stars". In: *Physical Review* 55.5 (1939), p. 434. DOI: https://doi.org/10.1103/PhysRev.55.434.

[32] Halopedia. *Pinch fusion reactor*. 2023. URL: https://www.halopedia.org/Pinch_fusion_reactor (visited on 09/22/2023).

[33] Matteo Barbarino. "A brief history of nuclear fusion". In: *Nature Physics* 16.9 (2020), pp. 890–893. DOI: https://doi.org/10.1038/s41567-020-0940-7.

[34] US Department of Energy. *DOE Explains...Tokamaks*. 2023. URL: https://www.energy.gov/science/doe-explainstokamaks (visited on 09/22/2023).

[35] Samuele Meschini et al. "Review of commercial nuclear fusion projects". In: *Frontiers in Energy Research* 11 (2023), p. 1157394. DOI: https://doi.org/10.3389/fenrg.2023.1157394.

[36] FL Ribe. "Fusion reactor systems". In: *Reviews of Modern Physics* 47.1 (1975), p. 7. DOI: https://doi.org/10.1103/RevModPhys.47.7.

[37] R. F. Post. "Nuclear Fusion". In: *Annual Review of Energy* 1.1 (1976), pp. 213–255. DOI: 10.1146/annurev.eg.01.110176.001241.

[38] AE Dabiri. "An overview of D-3He fusion reactors". In: *Nuclear Instruments and Methods in Physics Research Section A: Accelerators, Spectrometers, Detectors and Associated Equipment* 271.1 (1988), pp. 71–78. DOI: https://doi.org/10.1016/0168-9002(88)91127-8.

[39] MJ Monsler et al. "An overview of inertial fusion reactor design". In: *Nuclear Technology-Fusion* 1.3 (1981), pp. 302–358. DOI: https://doi.org/10.13182/FST81-A19936.

[40] J Ongena et al. "Magnetic-confinement fusion". In: *Nature Physics* 12.5 (2016), pp. 398–410. DOI: https://doi.org/10.1038/nphys3745.

[41] T Muroga, M Gasparotto, and SJ Zinkle. "Overview of materials research for fusion reactors". In: *Fusion engineering and design* 61 (2002), pp. 13–25. DOI: https://doi.org/10.1016/S0920-3796(02)00219-3.

[42] T Ihli et al. "Review of blanket designs for advanced fusion reactors". In: *Fusion Engineering and Design* 83.7-9 (2008), pp. 912–919. DOI: https://doi.org/10.1016/j.fusengdes.2008.07.039.

[43] K Lackner et al. "Long-term fusion strategy in Europe". In: *Journal of nuclear materials* 307 (2002), pp. 10–20. DOI: https://doi.org/10.1016/S0022-3115(02)00970-4.

[44] R Andreani and M Gasparotto. "Overview of fusion nuclear technology in Europe". In: *Fusion engineering and design* 61 (2002), pp. 27–36. DOI: https://doi.org/10.1016/S0920-3796(02)00110-2.

[45] Neil B Morley et al. "Overview of fusion nuclear technology in the US". In: *Fusion engineering and design* 81.1-7 (2006), pp. 33–43. DOI: https://doi.org/10.1016/j.fusengdes.2005.06.359.

[46] Satoru Tanaka. "Overview of research and development activities on fusion nuclear technologies in Japan". In: *Fusion engineering and design* 81.1-7 (2006), pp. 13–24. DOI: https://doi.org/10.1016/j.fusengdes.2005.07.025.

[47] ITER. *ADVANTAGES OF FUSION*. 2023. URL: https://www.iter.org/sci/Fusion (visited on 09/22/2023).

[48] G. S. Was. *Fundamentals of Radiation Materials Science: Metals and Alloys*. Springer-Verlag, Berlin Heidelberg, 2016. DOI: https://doi.org/10.1007/978-1-4939-3438-6.

[49] Mark C. Cross and Pierre C. Hohenberg. "Pattern formation outside of equilibrium". In: *Reviews of modern physics* 65.3 (1993), p. 851. DOI: 10.1103/RevModPhys.65.851.

[50] F. H. Busse and L. Kramer. *Nonlinear Evolution of Spatio-Temporal Structures in Dissipative Continuous Systems*. Springer New York, NY, 2003. DOI: https://doi.org/10.1007/978-1-4684-5793-3.

[51] Daniel Walgraef. *Spatio-Temporal Pattern Formation - With Examples from Physics, Chemistry, and Materials Science*. Springer New York, NY, 1997. DOI: https://doi.org/10.1007/978-1-4612-1850-0.

[52] Raúl A Enrique and Pascal Bellon. "Compositional patterning in systems driven by competing dynamics of different length scale". In: *Physical review letters* 84.13 (2000), p. 2885. DOI: https://doi.org/10.1103/PhysRevLett.84.2885.

[53] Qiangmin Wei et al. "Highly ordered Ga nanodroplets on a GaAs surface formed by a focused ion beam". In: *Physical review letters* 100.7 (2008), p. 076103. DOI: https://doi.org/10.1103/PhysRevLett.100.076103.

[54] SJ Zinkle and LL Snead. "Microstructure of copper and nickel irradiated with fission neutrons near 230 C". In: *Journal of nuclear materials* 225 (1995), pp. 123–131. DOI: https://doi.org/10.1016/0022-3115(94)00670-9.

[55] D Kaoumi and J Adamson. "Self-ordered defect structures in two model F/M steels under in situ ion irradiation". In: *Journal of nuclear materials* 448.1-3 (2014), pp. 233–238. DOI: https://doi.org/10.1016/j.jnucmat.2014.01.048.

[56] B Navinšek et al. "Radiation damage, annealing and thermal desorption in tungsten induced by low energy A+ ion bombardment". In: *Radiation Effects* 3.1 (1970), pp. 115–121. DOI: https://doi.org/10.1080/00337577008235623.

[57] DJ Mazey, RS Nelson, and PA Thackery. "Electron microscope examination of the surface topography of ion-bombarded copper". In: *Journal of Materials Science* 3 (1968), pp. 26–32. DOI: https://doi.org/10.1007/BF00550886.

[58] JO Stiegler and K Farrell. "Alignment of dislocation loops in irradiated metals". In: *Scripta Metallurgica* 8.6 (1974), pp. 651–655. DOI: https://doi.org/10.1016/0036-9748(74)90015-5.

[59] JB Whitley et al. "The depth dependent damage profile in nickel irradiated with nickel or copper ions". In: *Journal of Nuclear Materials* 79.1 (1979), pp. 159–169. DOI: https://doi.org/10.1016/0022-3115(79)90443-4.

[60] W. Jäger et al. "Periodic 001Walls of Defects in Proton-Irradiated Cu and Ni". In: *Materials Science Forum* 15-18 (1987), pp. 881–888. DOI: https://doi.org/10.4028/www.scientific.net/msf.15-18.881.

[61] JH Evans and DJ Mazey. "Evidence for solid krypton bubbles in copper, nickel and gold at 293K". In: *Journal of Physics F: Metal Physics* 15.1 (1985), p. L1. DOI: https://doi.org/10.1088/0305-4608/15/1/001.

[62] K Krishan. "Invited review article ordering of voids and gas bubbles in radiation environments". In: *Radiation Effects* 66.3-4 (1982), pp. 121–155. DOI: https://doi.org/10.1080/00337578208222474.

[63] JH Evans. "Irradiation-induced cavity lattice formation in metals". In: *Patterns, Defects and Materials Instabilities* (1990), pp. 347–370. DOI: https://doi.org/10.1007/978-94-009-0593-1_23.

[64] W Jäger and H Trinkaus. "Defect ordering in metals under irradiation". In: *Journal of nuclear materials* 205 (1993), pp. 394–410. DOI: https://doi.org/10.1016/0022-3115(93)90104-7.

[65] PB Johnson and DJ Mazey. "Gas-bubble superlattice formation in bcc metals". In: *Journal of nuclear materials* 218.3 (1995), pp. 273–288. DOI: https://doi.org/10.1016/0022-3115(94)00674-1.

[66] N. M. Ghoniem, Daniel Walgraef, and S. J. Zinkle. "Theory and experiment of nanostructure self-organization in irradiated materials". In: *Journal of computer-aided materials design* 8.1 (2001), pp. 1–38. DOI: https://doi.org/10.1023/A:1015062218246.

[67] Yongfeng Zhang. "A review of void and gas bubble superlattices self-organization under irradiation". In: *Frontiers in Nuclear Engineering* 2 (2023), p. 1110549. DOI: https://doi.org/10.3389/fnuen.2023.1110549.

[68] Michael Tonks et al. "Unit mechanisms of fission gas release: Current understanding and future needs". In: *Journal of Nuclear Materials* 504

(2018), pp. 300–317. DOI: https://doi.org/10.1016/j.jnucmat.2018.03.016.

[69] Di Chen et al. "Self-organization of helium precipitates into elongated channels within metal nanolayers". In: *Science advances* 3.11 (2017), eaao2710. DOI: https://doi.org/10.1126/sciadv.aao2710.

[70] Robert W Harrison et al. "Engineering self-organising helium bubble lattices in tungsten". In: *Scientific reports* 7.1 (2017), p. 7724. DOI: https://doi.org/10.1038/s41598-017-07711-w.

[71] Cheng Sun et al. "Formation window of gas bubble superlattice in molybdenum under ion implantation". In: *Physical Review Materials* 3.10 (2019), p. 103607. DOI: https://doi.org/10.1103/PhysRevMaterials.3.103607.

[72] Iuliia Ipatova et al. "Radiation-induced void formation and ordering in Ta-W alloys". In: *Journal of Nuclear Materials* 495 (2017), pp. 343–350. DOI: https://doi.org/10.1016/j.jnucmat.2017.08.029.

[73] BA Loomis, SB Gerber, and A Taylor. "Void ordering in ion-irradiated Nb and Nb-1% Zr". In: *Journal of Nuclear Materials* 68.1 (1977), pp. 19–31. DOI: https://doi.org/10.1016/0022-3115(77)90212-4.

[74] Cheng Sun et al. "Unveiling the interaction of nanopatterned void superlattices with irradiation cascades". In: *Acta Materialia* 239 (2022), p. 118282. DOI: https://doi.org/10.1016/j.actamat.2022.118282.

[75] J Gan et al. "Microstructural characterization of irradiated U–7Mo/Al–5Si dispersion fuel to high fission density". In: *Journal of Nuclear Materials* 454.1-3 (2014), pp. 434–445. DOI: https://doi.org/10.1016/j.jnucmat.2014.08.052.

[76] Cheng Sun et al. "Formation of tetragonal gas bubble superlattice in bulk molybdenum under helium ion implantation". In: *Scripta Materialia* 149 (2018), pp. 26–30. DOI: https://doi.org/10.1016/j.scriptamat.2018.01.023.

[77] Ericmoore Jossou et al. "Unraveling the early-stage ordering of krypton solid bubbles in molybdenum: a multimodal study". In: *The Journal of Physical Chemistry C* 125.42 (2021), pp. 23338–23348. DOI: https://doi.org/10.1021/acs.jpcc.1c05591.

[78] Aidan M Robinson et al. "The effect of temperature on bubble lattice formation in copper under in situ He ion irradiation". In: *Scripta Materialia* 131 (2017), pp. 108–111. DOI: https://doi.org/10.1016/j.scriptamat.2016.12.031.

[79] John Hedley Evans. "Simulations of the effects of 2-D interstitial diffusion on void lattice formation during irradiation". In: *Philosophical Magazine* 86.2 (2006), pp. 173–188. DOI: https://doi.org/10.1080/14786430500380134.

[80] PB Johnson and DJ Mazey. "The gas-bubble superlattice and the development of surface structure in He+ and H irradiated metals at 300 K". In: *Journal of Nuclear Materials* 93 (1980), pp. 721–727. DOI: https://doi.org/10.1016/0022-3115(80)90198-1.

[81] K. Malen and R. Bullough. "The void lattice in molybdenum". In: *Voids formed by irradiation of reactor materials*. 1971, pp. 109–119. DOI: 10.1680/vfbiorm.44623.0009.

[82] AG Khachaturyan. "Elastic Strains during Decomposition of Homogeneous Solid Solutions—Periodic Distribution of Decomposition Products". In: *physica status solidi (b)* 35.1 (1969), pp. 119–132. DOI: https://doi.org/10.1002/pssb.19690350109.

[83] AG Khachaturyan and VM Airapetyan. "Spatially periodic distributions of new phase inclusions caused by elastic distortions". In: *Physica status solidi (a)* 26.1 (1974), pp. 61–70. DOI: https://doi.org/10.1002/pssa.2210260104.

[84] AJE Foreman. *UK Atomic Energy Authority Harwell Report No.* Tech. rep. AERE, 1972.

[85] John W. Cahn and John E. Hilliard. "Free energy of a nonuniform system. I. Interfacial free energy". In: *The Journal of chemical physics* 28.2 (1958), pp. 258–267. DOI: https://doi.org/10.1063/1.1744102.

[86] C. H. Woo and W. Frank. "A theory of void-lattice formation". In: *Journal of Nuclear Materials* 137.1 (1985), pp. 7–21. DOI: https://doi.org/10.1016/0022-3115(85)90044-3.

[87] CH Woo and W Frank. "Limited growth, displacive stability and size uniformity of voids in a void lattice". In: *Journal of Nuclear Materials* 140.3 (1986), pp. 214–227. DOI: https://doi.org/10.1016/0022-3115(86)90204-7.

[88] CH Woo and W Frank. "The influence of temperature on void-lattice formation and swelling". In: *Journal of Nuclear Materials* 148.2 (1987), pp. 121–135. DOI: https://doi.org/10.1016/0022-3115(87)90104-8.

[89] CH Woo, AA Semenov, and BN Singh. "Analysis of microstructural evolution driven by production bias". In: *Journal of nuclear materials* 206.2-3 (1993), pp. 170–199. DOI: https://doi.org/10.1016/0022-3115(93)90123-G.

[90] J. H. Evans. "A computer simulation of the two-dimensional SIA diffusion model for void lattice formation". In: *Journal of Nuclear Materials* 132.2

(1985), pp. 147–155. DOI: https://doi.org/10.1016/0022-3115(85)90408-8.

[91] JH Evans and DJ Mazey. "Solid bubble formation in titanium injected with krypton ions". In: *Journal of Nuclear Materials* 138.2-3 (1986), pp. 176–184. DOI: https://doi.org/10.1016/0022-3115(86)90004-8.

[92] JH Evans. "Void and bubble lattice formation in molybdenum: A mechanism based on two-dimensional self-interstitial diffusion". In: *Journal of Nuclear Materials* 119.2-3 (1983), pp. 180–188. DOI: https://doi.org/10.1016/0022-3115(83)90195-2.

[93] VI Dubinko et al. "A mechanism of formation and properties of the void lattice in metals under irradiation". In: *Journal of Nuclear Materials* 161.1 (1989), pp. 57–71. DOI: https://doi.org/10.1016/0022-3115(89)90462-5.

[94] K Krishan. "Kinetics of void-lattice formation in metals". In: *Nature* 287.5781 (1980), pp. 420–421. DOI: https://doi.org/10.1038/287420a0.

[95] K Krishan. "Void ordering in metals during irradiation". In: *Philosophical Magazine A* 45.3 (1982), pp. 401–417. DOI: https://doi.org/10.1080/01418618208236179.

[96] Samuel Miller Allen and John W Cahn. "Ground state structures in ordered binary alloys with second neighbor interactions". In: *Acta Metallurgica* 20.3 (1972), pp. 423–433. DOI: https://doi.org/10.1016/0001-6160(72)90037-5.

[97] Ronald Bullough, B. L. Eyre, and K. Krishan. "Cascade damage effects on the swelling of irradiated materials". In: *Proceedings of the Royal So-*

ciety of London. A. Mathematical and Physical Sciences 346.1644 (1975), pp. 81–102. DOI: https://doi.org/10.1098/rspa.1975.0167.

[98] Michael R Tonks et al. "An object-oriented finite element framework for multiphysics phase field simulations". In: *Computational Materials Science* 51.1 (2012), pp. 20–29. DOI: https://doi.org/10.1016/j.commatsci.2011.07.028.

[99] Daniel Schwen et al. "Rapid multiphase-field model development using a modular free energy based approach with automatic differentiation in MOOSE/MARMOT". In: *Computational Materials Science* 132 (2017), pp. 36–45. DOI: https://doi.org/10.1016/j.commatsci.2017.02.017.

[100] Alexander D Lindsay et al. "2.0-MOOSE: Enabling massively parallel multiphysics simulation". In: *SoftwareX* 20 (2022), p. 101202. DOI: https://doi.org/10.1016/j.softx.2022.101202.

[101] Alexander Lindsay et al. "Automatic differentiation in MetaPhysicL and its applications in MOOSE". In: *Nuclear Technology* 207.7 (2021), pp. 905–922. DOI: https://doi.org/10.1080/00295450.2020.1838877.

[102] Daniel Schwen et al. "Rapid multiphase-field model development using a modular free energy based approach with automatic differentiation in MOOSE/MARMOT". In: *Computational Materials Science* 132 (2017), pp. 36–45. DOI: https://doi.org/10.1016/j.commatsci.2017.02.017.

[103] C Cawthorne and EJ Fulton. "Voids in irradiated stainless steel". In: *Nature* 216.5115 (1967), pp. 575–576. DOI: https://doi.org/10.1038/216575a0.

[104] Wiffin FW. In: *RADIATION-INDUCED VOIDS IN METALS. Proceedings of the 1971 Proceedings of the International Conference on Radiation-Induced Voids in Metals Held at Albany, New York, June 9–11, 1971.* 1971, p. 465. DOI: https://doi.org/10.2172/4694493.

[105] Evans JH Eyre BL. In: *Voids formed by irradiation of reactor materials.* Thomas Telford Publishing, 1971, p. 323. DOI: https://doi.org/10.1680/vfbiorm.44623.0034.

[106] GL Kulcinski, JL Brimhall, and HE Kissinger. "Production of voids in nickel with high energy selenium ions". In: *Journal of Nuclear Materials* 40.2 (1971), pp. 166–174. DOI: https://doi.org/10.1016/0022-3115(71)90130-9.

[107] Bullough R Evans JH and Stoneham AM. In: *RADIATION-INDUCED VOIDS IN METALS. Proceedings of the 1971 International Conference Held at Albany, New York, June 9–11, 1971.* 1972, p. 522. DOI: https://doi.org/10.2172/4694493.

[108] VK Sikka and J Moteff. "Superlattice of voids in neutron-irradiated tungsten". In: *Journal of Applied Physics* 43.12 (1972), pp. 4942–4944. DOI: https://doi.org/10.1063/1.1661050.

[109] VK Sikka and J Moteff. *OBSERVATION OF A VOID SUPERLATTICE CONTAINING A DISLOCATION IN NEUTRON IRRADIATED Mo–0.5 PERCENT Ti.* Tech. rep. Univ. of Cincinnati, 1972.

[110] Alain Risbet and Viviane Levy. "Ordre de cavites dans le magnesium et l'aluminium irradies aux neutrons rapides". In: *Journal of Nuclear Materials* 50.1 (1974), pp. 116–118. DOI: https://doi.org/10.1016/0022-3115(74)90069-5.

[111] FW Clinard Jr, JM Bunch, and WA Ranken. *Neutron irradiation damage in Al 2 O 3 and Y 2 O 3*. Tech. rep. 1976.

[112] LT Chadderton, E Johnson, and T Wohlenberg. "Observations of a regular void array in natural fluorite irradiated with 100 keV electrons". In: *Physica Scripta* 13.2 (1976), p. 127. DOI: https://doi.org/10.1088/0031-8949/13/2/012.

[113] LT Chadderton, E Johnson, and T Wohlenberg. "Void lattices". In: *Comments Solid State Phys.;(United Kingdom)* 7.5 (1976).

[114] A Jostsons and K Farrell. "Structural damage and its annealing response in neutron irradiated magnesium". In: *Radiation Effects* 15.3-4 (1972), pp. 217–225. DOI: https://doi.org/10.1080/00337577208234696.

[115] DJ Mazey, Susan Francis, and JA Hudson. "Observation of a partially-ordered void lattice in aluminium irradiated with 400 keV Al+ ions". In: *Journal of Nuclear Materials* 47.2 (1973), pp. 137–142. DOI: https://doi.org/10.1016/0022-3115(73)90095-0.

[116] A Horsewell and BN Singh. "Void hyperlattices in high-purity aluminium irradiated with fast neutrons". In: *Radiation effects* 102.1-4 (1987), pp. 1–5. DOI: https://doi.org/10.1080/00337578708222901.

[117] LJ Chen and AJ Ardell. "Void ordering in nitrogen-ion irradiated nickel—aluminum solid solutions". In: *Journal of Nuclear Materials* 75.1 (1978), pp. 177–185. DOI: https://doi.org/10.1016/0022-3115(78)90042-9.

[118] K Farrell and NH Packan. "A helium-induced shift in the temperature dependence of swelling". In: *Journal of Nuclear Materials* 85 (1979), pp. 683–687. DOI: https://doi.org/10.1016/0022-3115(79)90339-8.

[119] SJ Zinkle and BN Singh. "Microstructure of Cu–Ni alloys neutron irradiated at 210 ° C and 420 ° C to 14 dpa". In: *Journal of nuclear materials* 283 (2000), pp. 306–312. DOI: https://doi.org/10.1016/S0022-3115(00)00359-7.

[120] AT; Taylor A Santhanam and Harkness SD. In: *Proc. Int. Conf. on Defects and Defect Clusters in BCC Metals and Their Alloys, Nuclear Metallurgy Vol. 18, Arsenault R.J.(Ed.), National Bureau of Standards, Gaithersburg, MD*. 1973, p. 302.

[121] J Moteff, VK Sikka, and H Jang. "The physics of irradiation produced voids". In: *Consultant Symp. on the physics of irradiation produced voids*. 1975, p. 181.

[122] TH Ding, S Zhu, and LM Wang. "In situ TEM study of electron beam stimulated organization of three-dimensional void superlattice in CaF2". In: *Microscopy and Microanalysis* 11.S02 (2005), pp. 2064–2065. DOI: https://doi.org/10.1017/s1431927605503842.

[123] JH Evans. In: *Proceedings of the international conference on irradiation behaviour of metallic materials for fast reactor core components*. 1979, p. 225.

[124] JL Brimhall and EP Simonen. In: *Defects and defect clusters in bcc metals and their alloys. Proceedings of the 1973 international conference held at Gaithersburg, Maryland, August 14–16, 1973*. National Bureau of Standards, 1973, p. 321.

[125] GL Kulcinski and JL Brimhall. "Ordered defect structures in irradiated metals". In: *Effects of Radiation on Substructure and Mechanical Properties of Metals and Alloys*. American Society for Testing and Materials, 1973, pp. 258–271.

[126] PB Johnson and DJ Mazey. "Helium gas bubble lattices in face-centred-cubic metals". In: *Nature* 276.5688 (1978), pp. 595–596. DOI: https://doi.org/10.1038/276595a0.

[127] PB Johnson and DJ Mazey. "Observations of a fcc helium gas-bubble superlattice in copper, nickel, and stainless steel". In: *Radiation Effects* 53.3-4 (1980), pp. 195–202. DOI: https://doi.org/10.1080/00337578008207115.

[128] PB Johnson, RW Thomson, and DJ Mazey. "Large bubble-like features ordered on a macrolattice in helium-implanted gold". In: *Nature* 347.6290 (1990), pp. 265–267. DOI: https://doi.org/10.1038/347265a0.

[129] DJ Mazey and JH Evans. "Bubble lattice formation in titanium injected with krypton ions". In: *Journal of Nuclear Materials* 138.1 (1986), pp. 16–18. DOI: https://doi.org/10.1016/0022-3115(86)90248-5.

[130] JH Evans, AJE Foreman, and RJ McElroy. "Anisotropic diffusion of self-interstitials in zirconium". In: *Journal of Nuclear Materials* 168.3 (1989), pp. 340–342.

[131] Aidan M Robinson et al. "The effect of temperature on bubble lattice formation in copper under in situ He ion irradiation". In: *Scripta Materialia* 131 (2017), pp. 108–111. DOI: https://doi.org/10.1016/j.scriptamat.2016.12.031.

[132] Matheus Araujo Tunes et al. "Effect of He implantation on the microstructure of zircaloy-4 studied using in situ TEM". In: *Journal of nuclear materials* 493 (2017), pp. 230–238. DOI: https://doi.org/10.1016/j.jnucmat.2017.06.012.

[133] Sven Van den Berghe, Wouter Van Renterghem, and Ann Leenaers. "Transmission electron microscopy investigation of irradiated U–7 wt%

Mo dispersion fuel". In: *Journal of Nuclear Materials* 375.3 (2008), pp. 340–346. DOI: https://doi.org/10.1016/j.jnucmat.2007.12.006.

[134] Jian Gan et al. "Transmission electron microscopy characterization of irradiated U–7Mo/Al–2Si dispersion fuel". In: *Journal of Nuclear Materials* 396.2-3 (2010), pp. 234–239. DOI: https://doi.org/10.1016/j.jnucmat.2009.11.015.

[135] Daniele Salvato et al. "Pore pressure estimation in irradiated UMo". In: *Journal of Nuclear Materials* 510 (2018), pp. 472–483. DOI: https://doi.org/10.1016/j.jnucmat.2018.08.039.

[136] DJ Mazey et al. "A transmission electron microscopy study of molybdenum irradiated with helium ions". In: *Journal of Nuclear Materials* 64.1-2 (1977), pp. 145–156. DOI: https://doi.org/10.1016/0022-3115(77)90018-6.

[137] T Tanno et al. "Effects of transmutation elements on the microstructural evolution and electrical resistivity of neutron-irradiated tungsten". In: *Journal of Nuclear Materials* 386 (2009), pp. 218–221. DOI: https://doi.org/10.1016/j.jnucmat.2008.12.091.

[138] Yipeng Gao et al. "Theoretical prediction and atomic kinetic Monte Carlo simulations of void superlattice self-organization under irradiation". In: *Scientific reports* 8.1 (2018), p. 6629. DOI: https://doi.org/10.1038/s41598-018-24754-9.

[139] David J Sprouster et al. "Irradiation-dependent helium gas bubble superlattice in tungsten". In: *Scientific Reports* 9.1 (2019), p. 2277. DOI: https://doi.org/10.1038/s41598-019-39053-0.

[140] RW Harrison et al. "Chemical effects on He bubble superlattice formation in high entropy alloys". In: *Current Opinion in Solid State and Materials Science* 23.4 (2019), p. 100762. DOI: https://doi.org/10.1016/j.cossms.2019.07.001.

[141] Jian Gan et al. "Thermal stability of helium bubble superlattice in Mo under TEM in-situ heating". In: *Journal of Nuclear Materials* 505 (2018), pp. 207–211.

[142] Cheng Sun et al. "Disordering of helium gas bubble superlattices in molybdenum under ion irradiation and thermal annealing". In: *Journal of Nuclear Materials* 539 (2020), p. 152315. DOI: https://doi.org/10.1016/j.jnucmat.2020.152315.

[143] Yipeng Gao et al. "Formation and self-organization of void superlattices under irradiation: A phase field study". In: *Materialia* 1 (2018), pp. 78–88. DOI: https://doi.org/10.1016/j.mtla.2018.04.003.

[144] Yongfeng Zhang et al. "Symmetry breaking during defect self-organization under irradiation". In: *Materials Theory* 4 (2020), pp. 1–17. DOI: https://doi.org/10.1186/s41313-020-00021-1.

[145] MW Noble, MR Tonks, and SP Fitzgerald. "Turing instability in the solid state: Void lattices in irradiated metals". In: *Physical review letters* 124.16 (2020), p. 167401. DOI: https://doi.org/10.1103/PhysRevLett.124.167401.

[146] AM Stoneham. "Theory of regular arrays of defects: The void lattice". In: *Journal of Physics F: Metal Physics* 1.6 (1971), p. 778. DOI: https://doi.org/10.1088/0305-4608/1/6/311.

[147] E Johnson and Lewis T Chadderton. "Anion voidage and the void superlattice in electron irradiated CaF2". In: *Radiation effects* 79.1-4 (1983), pp. 183–233. DOI: https://doi.org/10.1080/00337578308207404.

[148] Hui-Chia Yu and Wei Lu. "Dynamics of the self-assembly of nanovoids and nanobubbles in solids". In: *Acta Materialia* 53.6 (2005), pp. 1799–1807. DOI: https://doi.org/10.1016/j.actamat.2004.12.029.

[149] MW Finnis. "The role of the interface in determining the orientation of solid rare gas bubbles in metals". In: *Acta Metallurgica* 35.10 (1987), pp. 2543–2547. DOI: https://doi.org/10.1016/0001-6160(87)90151-9.

[150] Yipeng Gao et al. "The effect of elastic anisotropy on the symmetry selection of irradiation-induced void superlattices in cubic metals". In: *Computational Materials Science* 206 (2022), p. 111252. DOI: https://doi.org/10.1016/j.commatsci.2022.111252.

[151] AA Semenov and CH Woo. "Void lattice formation as a nonequilibrium phase transition". In: *Physical Review B* 74.2 (2006), p. 024108. DOI: https://doi.org/10.1103/PhysRevB.74.024108.

[152] Shenyang Hu and Charles H Henager Jr. "Phase-field modeling of void lattice formation under irradiation". In: *Journal of Nuclear Materials* 394.2-3 (2009), pp. 155–159. DOI: https://doi.org/10.1016/j.jnucmat.2009.09.002.

[153] Shenyang Hu et al. "Formation mechanism of gas bubble superlattice in UMo metal fuels: Phase-field modeling investigation". In: *Journal of Nuclear Materials* 479 (2016), pp. 202–215. DOI: https://doi.org/10.1016/j.jnucmat.2016.07.012.

[154] Yipeng Gao et al. "Bifurcation and pattern symmetry selection in reaction-diffusion systems with kinetic anisotropy". In: *Scientific Reports* 9.1 (2019), p. 7835. DOI: https://doi.org/10.1038/s41598-019-44303-2.

[155] V. I. Dubinko et al. "The theory of gas bubble lattice". In: *Radiation effects* 100.1-2 (1986), pp. 85–104. DOI: https://doi.org/10.1080/00337578608208738.

[156] G Martin. "Long-range periodic decomposition of irradiated solid solutions". In: *Physical review letters* 50.4 (1983), p. 250. DOI: https://doi.org/10.1103/PhysRevLett.50.250.

[157] Daniel Walgraef, J Lauzeral, and NM Ghoniem. "Theory and numerical simulations of defect ordering in irradiated materials". In: *Physical Review B* 53.22 (1996), p. 14782. DOI: https://doi.org/10.1103/PhysRevB.53.14782.

[158] Daniel Walgraef and Nasr M Ghoniem. "Spatial instabilities and dislocation-loop ordering in irradiated materials". In: *Physical Review B* 39.13 (1989), p. 8867. DOI: https://doi.org/10.1103/PhysRevB.39.8867.

[159] JH Evans. In: *Patterns, Defects, and Materials Instabilities*. Kluwer Academic Publishers, 1990, p. 347.

[160] Philip Ball. "Ordering the void". In: *Nature Materials* 19.6 (2020), pp. 589–589. DOI: https://doi.org/10.1038/s41563-020-0695-7.

[161] T Suzudo, M Yamaguchi, and Akira Hasegawa. "Stability and mobility of rhenium and osmium in tungsten: first principles study". In: *Modelling and Simulation in Materials Science and Engineering* 22.7 (2014), p. 075006. DOI: https://doi.org/10.1088/0965-0393/22/7/075006.

[162] N Castin et al. "The effect of rhenium on the diffusion of small interstitial clusters in tungsten". In: *Computational Materials Science* 177 (2020), p. 109580. DOI: https://doi.org/10.1016/j.commatsci.2020.109580.

[163] SB Fisher and KR Williams. "Void spatial regularity in an electron-irradiated stainless steel". In: *Radiation Effects* 32.1-2 (1977), pp. 123–124. DOI: https://doi.org/10.1080/00337577708237467.

[164] DI Vainshtein, C Altena, and Henry W den Hartog. "Evidence of void lattice formation in heavily irradiated NaCl". In: *Materials Science Forum*. Vol. 239. 1997, pp. 607–610.

[165] PC Collins et al. "Microstructural control of additively manufactured metallic materials". In: *Annual Review of Materials Research* 46 (2016), pp. 63–91.

[166] AH Van Ommen, BH Koek, and MPA Viegers. "Ordering of oxide precipitates in oxygen implanted silicon". In: *Applied physics letters* 49.17 (1986), pp. 1062–1064. DOI: https://doi.org/10.1063/1.97475.

[167] Chao Jiang et al. "Ab initio theory of noble gas atoms in bcc transition metals". In: *Physical Chemistry Chemical Physics* 20.25 (2018), pp. 17048–17058. DOI: https://doi.org/10.1039/C8CP01817K.

[168] Chao Jiang et al. "Noble gas bubbles in bcc metals: Ab initio-based theory and kinetic Monte Carlo modeling". In: *Acta Materialia* 213 (2021), p. 116961. DOI: https://doi.org/10.1016/j.actamat.2021.116961.

[169] Yongfeng Zhang et al. "Molecular dynamics simulations of He bubble nucleation at grain boundaries". In: *Journal of Physics: Condensed Matter* 24.30 (2012), p. 305005. DOI: https://doi.org/10.1088/0953-8984/24/30/305005.

[170] Miaomiao Jin et al. "Dissociated prismatic loop punching by bubble growth in FCC metals". In: *Scientific reports* 11.1 (2021), p. 12839. DOI: https://doi.org/10.5281/zenodo.3970979.

[171] shipbuildingknowledge.wordpress.com. *MELTING POINT OF CARBON STEEL and STAINLESS STEEL*. 2023. URL: https://shipbuildingknowledge.wordpress.com/2019/01/05/melting-point-of-carbon-steel-stainless-steel/ (visited on 10/02/2023).

[172] Crystran. *Calcium Fluoride CaF2*. 2023. URL: https://www.crystran.co.uk/optical-materials/calcium-fluoride-caf2 (visited on 10/02/2023).

[173] Crystran. *Strontium Fluoride SrF2*. 2023. URL: https://www.crystran.co.uk/optical-materials/strontium-fluoride-srf2 (visited on 10/02/2023).

[174] University of Colarado Boulder. *Periodic Table of the Elements*. 2023. URL: https://home.cs.colorado.edu/~kena/classes/7818/f01/assignments/pt.html (visited on 10/02/2023).

[175] Crystran. *TZM Molybdenum Alloy*. 2023. URL: https://www.americanelements.com/tzm-molybdenum-alloy (visited on 10/02/2023).

[176] H Jang and J Moteff. "The Influence of Neutron Irradiation Temperature on the Void Characteristics of Niobium and Niobium-1% Zirconium Alloy,""" in: *Proc. 1975 Int. Conf. on Radiation Effects and*. 1976.

[177] Hyosim Kim et al. "Irradiation-induced swelling of pure chromium with 5 MeV Fe ions in the temperature range 450–650 ° C". In: *Journal of Nuclear Materials* 543.LA-UR-20-22579 (2020). DOI: https://doi.org/10.1016/j.jnucmat.2020.152585.

[178] JH Evans. "Observations of a regular void array in high purity molybdenum and TZM irradiated at high temperatures with 2MeV nitrogen ions". In: *Radiation Effects* 10.1-2 (1971), pp. 55–60. DOI: https://doi.org/10.1080/00337577108231071.

[179] GL Kulcinski, JL Brimhall, and HE Kissinger. In: *Radiation-induced voids in metals*. Atomic Energy Commission, 1972, p. 449.

[180] BA Loomis, A Taylor, and SB Gerber. *Void ordering in O-doped Nb and Nb–1 at.% Zr induced by 58 Ni+ bombardment*. Tech. rep. 1975.

[181] DRG Mitchell and SE Donnelly. "A TEM investigation of solid krypton bubbles formed in cobalt by ion implantation". In: *Radiation effects and defects in solids* 114.3 (1990), pp. 253–261. DOI: https://doi.org/10.1080/10420159008213102.

[182] Zhang-Jie Wang et al. "Mechanical behavior of copper containing a gas-bubble superlattice". In: *Acta Materialia* 121 (2016), pp. 78–84. DOI: https://doi.org/10.1016/j.actamat.2016.08.085.

[183] QM Wei and Lumin Wang. "Bubble formation in He implanted Cu and Au". In: *Microscopy and Microanalysis* 15.S2 (2009), pp. 1372–1373. DOI: https://doi.org/10.1017/S1431927609097426.

[184] PB Johnson and DJ Mazey. "Hydrogen gas-bubble structure in proton-irradiated copper at 300 K". In: *Journal of Nuclear Materials* 91.1 (1980), pp. 41–46. DOI: https://doi.org/10.1016/0022-3115(80)90030-6.

[185] JH Evans-Freeman. "The Role of Two-Dimensional Self-Interstitial Diffusion in Void Lattice Formation and Other Defect Phenomena in Metals". In: *Materials Science Forum*. Vol. 15. Trans Tech Publ. 1987, pp. 869–874. DOI: https://doi.org/10.4028/www.scientific.net/MSF.15-18.869.

[186] W Jäger and J Roth. "Microstructure of Ni and stainless steel after multiple energy He and D implantation". In: *Journal of Nuclear Materials* 93 (1980), pp. 756–766. DOI: https://doi.org/10.1016/0022-3115(80)90204-4.

[187] Si-Mian Liu, Shi-Hao Li, and Wei-Zhong Han. "Effect of ordered helium bubbles on deformation and fracture behavior of α-Zr". In: *Journal of Materials Science & Technology* 35.7 (2019), pp. 1466–1472. DOI: https://doi.org/10.1016/j.jmst.2019.03.015.

[188] Raymond Kapral and Kenneth Showalter. *Chemical waves and patterns*. Vol. 10. Springer Science & Business Media, 2012. DOI: https://doi.org/10.1007/978-94-011-1156-0.

[189] Pierre Borckmans et al. "Turing bifurcations and pattern selection". In: *Chemical waves and patterns* (1995), pp. 323–363. DOI: https://doi.org/10.1007/978-94-011-1156-0_10.

[190] Hannes Risken. "Fokker-Planck Equation". In: *The Fokker-Planck Equation: Methods of Solution and Applications*. Springer Berlin Heidelberg, 1996, pp. 63–95. DOI: https://doi.org/10.1007/978-3-642-61544-3_4.

[191] Joseph Frederick Scott. *The scientific work of René Descartes: 1596-1650*. Routledge, 2016.

[192] Eric W. Weisstein. *Polynomial Discriminant*. https://mathworld.wolfram.com/PolynomialDiscriminant.html. Accessed: 2023-09-04. 2023.

[193] Nikolas Provatas and Ken Elder. *Phase-field methods in materials science and engineering*. John Wiley & Sons, 2011. DOI: https://doi.org/10.1002/9783527631520.

[194] Olga Wodo and Baskar Ganapathysubramanian. "Computationally efficient solution to the Cahn–Hilliard equation: Adaptive implicit time schemes, mesh sensitivity analysis and the 3D isoperimetric problem". In: *Journal of Computational Physics* 230.15 (2011), pp. 6037–6060. DOI: http://doi.org/10.1016/j.jcp.2011.04.012.

[195] PETSc. *PETSc Overview*. 2023. URL: https://petsc.org/main/overview/ (visited on 09/10/2023).

[196] Idaho National Lab. *Executioner System*. 2023. URL: https://mooseframework.inl.gov/syntax/Executioner/ (visited on 09/10/2023).

[197] Idaho National Lab. *Solving Phase Field Models*. 2023. URL: https://mooseframework.inl.gov/modules/phase_field/Solving.html (visited on 09/10/2023).

[198] Idaho National Lab. *Installing MOOSE*. 2023. URL: https://mooseframework.inl.gov/getting_started/installation/conda.html (visited on 09/10/2023).

[199] Idaho National Lab. *New Users - Create an Application*. 2023. URL: https://mooseframework.inl.gov/getting_started/new_users.html (visited on 09/10/2023).

[200] Idaho National Lab. *Mesh System*. 2023. URL: https://mooseframework.inl.gov/syntax/Mesh/ (visited on 09/10/2023).

[201] Idaho National Lab. *GeneratedMeshGenerator*. 2023. URL: https://mooseframework.inl.gov/source/meshgenerators/GeneratedMeshGenerator.html (visited on 09/10/2023).

[202] Idaho National Lab. *BCs System*. 2023. URL: https://mooseframework.inl.gov/syntax/BCs/ (visited on 09/10/2023).

[203] Idaho National Lab. *Periodic System*. 2023. URL: https://mooseframework.inl.gov/syntax/BCs/Periodic/index.html (visited on 09/10/2023).

[204] Idaho National Lab. *Physics Modules*. 2023. URL: https://mooseframework.inl.gov/modules/ (visited on 09/10/2023).

[205] Idaho National Lab. *Phase Field Module*. 2023. URL: https://mooseframework.inl.gov/modules/phase_field/index.html (visited on 09/10/2023).

[206] Idaho National Lab. *ConservedAction*. 2023. URL: https://mooseframework.inl.gov/source/actions/ConservedAction.html (visited on 09/10/2023).

[207] Idaho National Lab. *TimeDerivative*. 2023. URL: https://mooseframework.inl.gov/source/kernels/TimeDerivative.html (visited on 09/10/2023).

[208] Idaho National Lab. *CoupledMaterialDerivative*. 2023. URL: https://mooseframework.inl.gov/source/kernels/CoupledMaterialDerivative.html (visited on 09/10/2023).

[209] Liangzhe Zhang et al. "A quantitative comparison between C0 and C1 elements for solving the Cahn–Hilliard equation". In: *Journal of Computational Physics* 236 (2013), pp. 74–80. DOI: https://doi.org/10.1016/j.jcp.2012.12.001.

[210] Idaho National Lab. *ICs System*. 2023. URL: https://mooseframework.inl.gov/syntax/ICs/ (visited on 09/10/2023).

[211] Idaho National Lab. *RandomIC*. 2023. URL: https://mooseframework.inl.gov/source/ics/RandomIC.html (visited on 09/10/2023).

[212] Idaho National Lab. *MultiSmoothCircleIC*. 2023. URL: https://mooseframework.inl.gov/source/ics/MultiSmoothCircleIC.html (visited on 09/16/2023).

[213] Idaho National Lab. *Materials System*. 2023. URL: https://mooseframework.inl.gov/syntax/Materials/ (visited on 09/10/2023).

[214] Idaho National Lab. *GenericConstantMaterial*. 2023. URL: https://mooseframework.inl.gov/source/materials/GenericConstantMaterial.html (visited on 09/10/2023).

[215] Idaho National Lab. *DerivativeParsedMaterial*. 2023. URL: https://mooseframework.inl.gov/source/materials/DerivativeParsedMaterial.html# (visited on 09/10/2023).

[216] Idaho National Lab. *Kernels System*. 2023. URL: https://mooseframework.inl.gov/syntax/Kernels/ (visited on 09/10/2023).

[217] Idaho National Lab. *MaskedBodyForce*. 2023. URL: https://mooseframework.inl.gov/source/kernels/MaskedBodyForce.html (visited on 09/10/2023).

[218] Idaho National Lab. *MatReaction*. 2023. URL: https://mooseframework.inl.gov/source/kernels/MatReaction.html (visited on 09/10/2023).

[219] Idaho National Lab. *Preconditioning System*. 2023. URL: https://mooseframework.inl.gov/syntax/Preconditioning/ (visited on 09/10/2023).

[220] Idaho National Lab. *Transient*. 2023. URL: https://mooseframework.inl.gov/source/executioners/Transient.html (visited on 09/10/2023).

[221] Idaho National Lab. *TimeStepper System*. 2023. URL: https://mooseframework.inl.gov/syntax/Executioner/TimeStepper/index.html (visited on 09/10/2023).

[222] Idaho National Lab. *Predictor System*. 2023. URL: https://mooseframework.inl.gov/syntax/Executioner/Predictor/ (visited on 09/11/2023).

[223] Johan Verbeke and Ronald Cools. "The newton-raphson method". In: *International Journal of Mathematical Education in Science and Technology* 26.2 (1995), pp. 177–193. DOI: https://doi.org/10.1080/0020739950260202.

[224] Idaho National Lab. *SMP*. 2023. URL: https://mooseframework.inl.gov/source/preconditioners/SingleMatrixPreconditioner.html (visited on 09/10/2023).

[225] Idaho National Lab. *BDF2*. 2023. URL: https://mooseframework.inl.gov/source/timeintegrators/BDF2.html (visited on 09/10/2023).

[226] Idaho National Lab. *IterationAdaptiveDT*. 2023. URL: https://mooseframework.inl.gov/source/timesteppers/IterationAdaptiveDT.html (visited on 09/10/2023).

[227] Idaho National Lab. *SimplePredictor*. 2023. URL: https://mooseframework.inl.gov/source/predictors/SimplePredictor.html (visited on 09/11/2023).

[228] Idaho National Lab. *Postprocessor System*. 2023. URL: https://mooseframework.inl.gov/syntax/Postprocessors/ (visited on 09/11/2023).

[229] Idaho National Lab. *VectorPostprocessors System*. 2023. URL: https://mooseframework.inl.gov/syntax/VectorPostprocessors/index.html (visited on 09/11/2023).

[230] Idaho National Lab. *TimestepSize*. 2023. URL: https://mooseframework.inl.gov/source/postprocessors/TimestepSize.html (visited on 09/11/2023).

[231] Idaho National Lab. *FeatureFloodCount*. 2023. URL: https://mooseframework.inl.gov/source/postprocessors/FeatureFloodCount.html (visited on 09/11/2023).

[232] Cody J Permann et al. "Scalable feature tracking for finite element meshes demonstrated with a novel phase-field grain subdivision model". In: *Nuclear Technology* 207.7 (2021), pp. 885–904. DOI: https://doi.org/10.1080/00295450.2020.1843893.

[233] Idaho National Lab. *VolumePostprocessor*. 2023. URL: https://mooseframework.inl.gov/source/postprocessors/VolumePostprocessor.html (visited on 09/11/2023).

[234] Idaho National Lab. *FeatureVolumeFraction*. 2023. URL: https://mooseframework.inl.gov/source/postprocessors/FeatureVolumeFraction.html (visited on 09/11/2023).

[235] Idaho National Lab. *ElementAverageValue*. 2023. URL: https://mooseframework.inl.gov/source/postprocessors/ElementAverageValue.html (visited on 09/16/2023).

[236] Idaho National Lab. *FeatureVolumeVectorPostprocessor System*. 2023. URL: https://mooseframework.inl.gov/source/vectorpostprocessors/FeatureVolumeVectorPostprocessor.html (visited on 09/11/2023).

[237] Idaho National Lab. *Output System*. 2023. URL: https://mooseframework.inl.gov/syntax/Outputs/index.html (visited on 09/11/2023).

[238] Idaho National Lab. *Exodus*. 2023. URL: https://mooseframework.inl.gov/source/outputs/Exodus.html (visited on 09/11/2023).

[239] Idaho National Lab. *CSV*. 2023. URL: https://mooseframework.inl.gov/source/outputs/CSV.html (visited on 09/11/2023).

[240] Idaho National Lab. *CommonOutputAction*. 2023. URL: https://mooseframework.inl.gov/source/actions/CommonOutputAction.html (visited on 09/11/2023).

[241] MPICH. *MPICH*. 2023. URL: https://www.mpich.org/ (visited on 09/15/2023).

[242] Idaho National Lab. *Step 7: Execute in Parallel*. 2023. URL: https://mooseframework.inl.gov/getting_started/examples_and_tutorials/tutorial01_app_development/step07_parallel.html (visited on 09/11/2023).

[243] William C Mills-Curran, Amy P Gilkey, and Dennis P Flanagan. *EXODUS: A finite element file format for pre-and postprocessing*. Tech. rep. Sandia National Lab.(SNL-NM), Albuquerque, NM (United States), 1988. DOI: https://doi.org/10.2172/6902151.

[244] ParaView. *Exodus*. 2023. URL: https://www.paraview.org/ParaView/index.php/Exodus (visited on 09/10/2023).

[245] ParaView. *ParaView - Home*. 2023. URL: https://www.paraview.org/ (visited on 09/10/2023).

[246] Junseok Kim et al. "Basic principles and practical applications of the Cahn–Hilliard equation". In: *Mathematical Problems in Engineering* 2016 (2016). DOI: https://doi.org/10.1155/2016/9532608.

[247] Takao Ohta and Kyozi Kawasaki. "Equilibrium morphology of block copolymer melts". In: *Macromolecules* 19.10 (1986), pp. 2621–2632. DOI: https://doi.org/10.1021/ma00164a028.

[248] OpenCV. *Fourier Transform*. 2023. URL: https://opencv24-python-tutorials.readthedocs.io/en/latest/py_tutorials/py_imgproc/py_transforms/py_fourier_transform/py_fourier_transform.html (visited on 09/30/2023).